

University of Southampton Research Repository ePrints Soton

Copyright © and Moral Rights for this thesis are retained by the author and/or other copyright owners. A copy can be downloaded for personal non-commercial research or study, without prior permission or charge. This thesis cannot be reproduced or quoted extensively from without first obtaining permission in writing from the copyright holder/s. The content must not be changed in any way or sold commercially in any format or medium without the formal permission of the copyright holders.

When referring to this work, full bibliographic details including the author, title, awarding institution and date of the thesis must be given e.g.

AUTHOR (year of submission) "Full thesis title", University of Southampton, name of the University School or Department, PhD Thesis, pagination

University of Southampton
Faculty of Engineering and Applied Science
Institute of Sound and Vibration Research

**ACTIVE CONTROL OF WAVES ON
ONE-DIMENSIONAL STRUCTURES**

by

Michael John Brennan

A Thesis submitted for the degree of
Doctor of Philosophy

November 1994

UNIVERSITY OF SOUTHAMPTON

ABSTRACT

FACULTY OF ENGINEERING AND APPLIED SCIENCE

INSTITUTE OF SOUND AND VIBRATION RESEARCH

Doctor of Philosophy

ACTIVE CONTROL OF WAVES ON ONE-DIMENSIONAL STRUCTURES

by

Michael John Brennan

This thesis is concerned with the active control of vibrations on one-dimensional structures. The main theme throughout is the use of waves to model the structures being investigated, which allows the study of both local and global dynamic behaviour. The coupling between the structure under control and the actuators and sensors is examined, as well as the effects of several control strategies. Two structures are chosen for the theoretical and experimental study; a slender aluminium beam and a water-filled perspex pipe.

The control strategies investigated involve explicit wave control, suppression of a flexural propagating wave using minimum effort, and strategies that use power as a controlling parameter; that of maximising the power absorbed by a secondary source and the minimization of the total power supplied to the structure. The effects of these control strategies are examined on both infinite and finite beams. Following on from the theoretical analysis, experimental work is carried out to validate the results.

The use of piezoceramic elements as vibration sensors and actuators for flexural and longitudinal motion on a beam is studied. These devices are compared with conventional transducers, and the situations when their use is advantageous is discussed. A non intrusive sensor and a non intrusive actuator for fluid waves in pipes are designed and tested. The sensor consists of several piezoelectric elements connected in series and fixed to the exterior of the pipe, and the actuator is a hydraulic device driven with a magnetostrictive element. A framework for coupling these transducers to the fluid motion is developed and the experimental predictions are confirmed by experimental observation.

CONTENTS

ACKNOWLEDGEMENTS	xxi
1 INTRODUCTION	1
2 ACTIVE CONTROL OF WAVES ON BEAM-LIKE STRUCTURES	6
2.1 Introduction	6
2.2 Control of Flexural Waves using Point Forces	7
2.2.1 Introduction	7
2.2.2 Model of the Secondary Force Array	8
2.2.3 Control Using a Single Secondary Force	11
2.2.4 Control Using Two Secondary Forces	14
2.2.5 Control Using Three Secondary Forces	19
2.2.6 Control Using Four Secondary Forces	23
2.3 Control of Flexural Waves Using Line Moments	25
2.3.1 Introduction	25
2.3.2 Model of the Secondary Moment Array	25
2.3.3 Control Using a Single Secondary Moment	26
2.3.4 Control Using Two Secondary Moments	28
2.3.5 Control Using Three Secondary Moments	29
2.3.6 Control Using Four Secondary Moments	30
2.4 Control of Flexural Waves Using Moment-Pairs	31
2.4.1 Introduction	31
2.4.2 Model of the Secondary Moment-Pair Array	31
2.4.3 Control Using a Single Secondary Moment-Pair	33
2.4.4 Control Using Two Secondary Moment-Pairs	33
2.4.5 Control Using Three Secondary Moment-Pairs	34
2.4.6 Control Using Four Secondary Moment-Pairs	36
2.4.7 Discussion	36

2.5	Active Control of Flexural Waves using Minimum Effort	37
2.5.1	Implementation on an Infinite Beam	37
2.5.2	Implementation on a Semi-Infinite Beam	44
2.6	Conclusions	48
3	ACTIVE CONTROL OF FLEXURAL WAVES USING POWER AS A CONTROLLING PARAMETER	51
3.1	Introduction	51
3.2	Control Strategies Applied to an Infinite Beam	52
3.2.1	Wave Suppression using a Single Secondary Force	52
3.2.2	Maximization of the Power Absorbed by the Secondary Force Array	55
3.2.2.1	Application of a Single Secondary Force	55
3.2.3	Minimization of the Total Power Supplied to the Beam	58
3.2.3.1	Application of a Single Secondary Force	58
3.2.4	Wave Suppression using Two Secondary Forces	64
3.2.5	Maximization of the Power Absorbed by the Secondary Forces	66
3.2.6	Minimization of the Total Power Supplied to the Beam using Two secondary Forces	68
3.3	Control Strategies using a Single Secondary Force on a Finite Beam	73
3.3.1	Wave Suppression	73
3.3.2	Maximization of the Power Absorbed by the Secondary Force	75
3.3.3	Minimization of the Total Power Supplied to the Beam	76
3.4	Control Strategies using Two Secondary Forces on a Finite Beam	81
3.4.1	Wave Suppression	81
3.4.2	Maximization of the Power Absorbed by the Secondary Forces	82
3.4.3	Minimization of the Total Power Supplied to the Beam	84
3.5	Discussion	89
3.6	Experimental Investigation	90
3.6.1	Introduction	90
3.6.2	Suppression of a Propagating Wave	91
3.6.3	Maximum Power Absorption by the Secondary Force	96

3.6.4	Minimization of Total Power Supplied to the Beam	100
3.7	Conclusions	104
4	DISTRIBUTED PIEZOELECTRIC SENSORS AND ACTUATORS FOR THE ACTIVE CONTROL OF WAVES ON A BEAM	106
4.1	Introduction	106
4.2	Review of Research into the use of Piezoelectric Devices as Vibration Sensors and Actuators	107
4.2.1	Introduction	107
4.2.2	Sensors	109
4.2.3	Actuators	110
4.2.3.1	PZT Actuators	111
4.2.3.2	PVDF Actuators	113
4.3	Piezoelectric Equations	114
4.4	Piezoelectric Sensors	118
4.4.1	Introduction	118
4.4.2	Sensor Sensitivity - Measurement of Flexural Vibration	121
4.4.2.1	Stiffening Effect of the Sensor	123
4.4.2.2	Calibration of the Sensor	125
4.4.3	Sensor Sensitivity - Measurement of Longitudinal Vibration	129
4.4.3.1	Stiffening Effect of the Sensor	131
4.4.4	Simultaneous Measurement of Longitudinal and Flexural Vibration.	131
4.4.4.1	Experimental Verification	132
4.4.5	Conclusions	134
4.5	Piezoelectric Actuators	134
4.5.1	Introduction	134
4.5.2	A flexural Vibration Actuator	137
4.5.2.1	Static Model of the Actuator	137
4.5.2.2	Coupling the Actuator into the Beam Dynamics	140
4.5.2.3	Complete Model of a PZT Flexural Vibration Actuator	141

4.5.2.4	Comparison Between the Simple and Complete Models of the PZT Flexural Vibration Actuator	145
4.5.2.5	Passive Effects of the PZT Flexural Vibration Actuator	147
4.5.2.6	Vibrational Power Supplied by a PZT Flexural Vibration Actuator	149
4.5.2.7	Experimental Validation	150
4.5.2.8	Uni-Directional Wave Generators	153
4.5.2.9	Spacing of Flexural PZT Actuators	157
4.5.3	A Longitudinal Vibration Actuator	159
4.5.3.1	Static Model of the Actuator	159
4.5.3.2	Coupling the Actuator into the Beam Dynamics	160
4.5.3.3	Complete Model of a PZT Longitudinal Vibration Actuator	161
4.5.3.4	Comparison Between the Simple and Complete Models of the PZT Longitudinal Vibration Actuator	164
4.5.3.5	Passive Effects of the PZT Longitudinal Vibration Actuator	166
4.5.3.6	Vibrational Power Supplied by a PZT Longitudinal Vibration Actuator	167
4.5.3.7	Experimental Validation	168
4.5.4	Conclusions	170
4.6	A Self Sensing Actuator	171
4.6.1	Introduction	171
4.6.2	Electrically Equivalent Model of the Self Sensing Actuator	171
4.6.3	Sensitivity of the Self Sensing Actuator	175
4.6.4	Experimental Investigation	177
4.6.5	Conclusions	181
4.7	Discussion and Conclusions	181
5	FEEDBACK OF FLEXURAL AND LONGITUDINAL WAVES ON A BEAM	184
5.1	Introduction	184

5.2	Feedback Control of Flexural Waves	186
5.2.1	Force Actuator as a Secondary Source	186
5.2.2	Moment Actuator as a Secondary Source	188
5.2.3	Moment-Pair Actuator as a Secondary Source	190
5.2.4	Comparison of Feedback Controllers	192
5.2.5	Practical Considerations	193
5.2.5.1	Practical Actuators and Sensors	193
5.2.5.2	Effects of Wave Reflections from Beam Terminations	198
5.2.5.3	Closed Loop Stability	200
5.2.6	Experimental Validation	201
5.2.7	Discussion	205
5.3	Feedback Control of Longitudinal Waves	207
5.3.1	Feedback Control Applied at the End of a Beam	207
5.3.2	Feedback Control Using an Actuator Integrated into the Beam	209
5.3.2.1	Theory	209
5.3.2.2	Practical Considerations	211
5.3.2.3	Experimental Validation	213
5.3.2.4	Discussion	218
5.4	Conclusions	219
6	ACTIVE CONTROL OF FLUID WAVES IN A PIPE	222
6.1	Introduction	222
6.2	Dynamic Behaviour of Fluid-Filled Pipes	223
6.3	Design of a Fluid Wave Actuator	233
6.3.1	Theory	233
6.3.2	Potential Types of Actuator	239
6.4	Design of a Fluid Wave Sensor	244
6.5	Experimental Design	246
6.6	Experimental Procedure	251
6.6.1	Measurement of the Mechanical Impedance of the Support Plates	252

6.6.2	Measurement of the Apparent Mass of the Piston used for Excitation of the Fluid	252
6.6.3	Measurement of the Frequency Response Functions using the Primary and Secondary Actuators	253
6.6.4	Active Control of Fluid Waves	254
6.7	Experimental Results	255
6.8	Discussion	269
6.9	Conclusions	278
7	GENERAL CONCLUSIONS	280
7.1	Conclusions	280
7.2	Recommendations for Further Work	284
	APPENDICES	285
A1	WAVE MOTION IN SOLIDS AND FLUIDS	285
A2	A WAVE MODEL FOR A BEAM	293
A2.1	Introduction	293
A2.2	Flexural Wave Generation	293
A2.2.1	Waves Generated by a Point Force	294
A2.2.2	Waves Generated by Line Moments	296
A2.3	Longitudinal Wave Generation	297
A2.3.1	Waves generated by In-Plane Forces	298
A2.4	Modelling of Finite Beams	300
A3	VIBRATIONAL POWER FLOW IN BEAMS	305
A3.1	Introduction	305
A3.2	Power Supplied by Various Actuators	305
A3.3	Power Based Control Strategies	312

A3.3.1	Maximizing the Power Absorbed by the Secondary Force Array	314
A3.3.2	Minimizing the Total Power Supplied by the Primary and Secondary Force Arrays	315
A3.4	Mechanisms of Power Absorption by a Force Actuator	317
A4	EXPERIMENTAL APPARATUS	319
A4.1	Beam Experiments	319
A4.1.1	Experimental Equipment	319
A4.1.2	Beam and PZT Elements	321
A4.2	Pipe Experiments	323
A4.2.1	Experimental Equipment	323
A4.2.2	Fluid Actuator Drawings	325
	GLOSSARY OF TERMS	331
	REFERENCES	334

LIST OF FIGURES

Figure 2.1	A Secondary Force Array on an Infinite Beam
Figure 2.2	Displacement of an Infinite Beam with One Secondary Force Applied to Suppress a Propagating Flexural Wave
Figure 2.3	Displacement of an Infinite Beam with a Single Secondary Force Configured to Pin the Beam
Figure 2.4	A Secondary Force Array with Two Actuators
Figure 2.5	Displacement of an Infinite Beam with the Incident and Negative-Going Propagating Waves Suppressed using Two Forces. $l_1/\lambda = 0.1$
Figure 2.6	Displacement of an Infinite Beam with the Incident Propagating Wave and Positive-Going Nearfield Wave Suppressed using Two Forces. $l_1/\lambda = 0.1$

- Figure 2.7** Displacement of an Infinite Beam with the Incident Propagating Wave and the Negative-Going Nearfield Wave Suppressed using Two Forces. $l_1/\lambda = 0.1$
- Figure 2.8** Secondary Force Effort for Cases 2.1 and 2.2 as a Function of Non-dimensionalised Distance between the Secondary Forces
- Figure 2.9** Secondary Force Array with Three Actuators
- Figure 2.10** Displacement of an Infinite Beam with Both Propagating Waves and the Positive Going Nearfield Wave Suppressed using Three Forces. $l/\lambda = 0.1$
- Figure 2.11** Displacement of an Infinite Beam with Both Propagating Waves and the Negative-Going Nearfield Wave Suppressed using Three Forces. $l/\lambda = 0.1$
- Figure 2.12** Displacement of an Infinite Beam with the Incident Propagating Wave and Both Nearfield Waves Suppressed using Three Forces. $l/\lambda = 0.1$
- Figure 2.13** Secondary Force Effort for Cases 3.1, 3.2 as a Function of Non-dimensionalised Distance between the Secondary Forces
- Figure 2.14** Displacement of an Infinite Beam with the Incident Propagating Wave, the Negative-Going Propagating Wave and both Nearfield Waves Suppressed using Four Forces. $l/\lambda = 0.1$
- Figure 2.15** Secondary Force Effort for Cases 2.1, 3.1 and 4 as a Function of Non-dimensionalised Distance between the Secondary Forces
- Figure 2.16** A Secondary Moment Array on an Infinite Beam
- Figure 2.17** Displacement of an Infinite Beam with a Single Secondary Moment Applied to Suppress a Propagating Wave
- Figure 2.18** Displacement of an Infinite Beam with a Single Secondary Moment Applied to give Zero Slope at the Secondary Moment Position
- Figure 2.19** Displacement of an Infinite Beam with the Incident and Negative-Going Propagating Waves Suppressed using Two Moments. $l_1/\lambda = 0.1$
- Figure 2.20** Displacement of an Infinite Beam with the Incident Propagating Wave and Positive-Going Nearfield Wave Suppressed using Two Moments. $l_1/\lambda = 0.1$
- Figure 2.21** Displacement of an Infinite Beam with the Incident Propagating Wave and the Negative-Going Nearfield Wave Suppressed using Two Moments. $l_1/\lambda = 0.1$
- Figure 2.22** Displacement of an Infinite Beam with Both Propagating Waves and the Positive Going Nearfield Wave Suppressed using Three Moments. $l/\lambda = 0.1$

- Figure 2.23** Displacement of an Infinite Beam with Both Propagating Waves and the Negative-Going Nearfield Wave Suppressed using Three Moments. $l/\lambda = 0.1$
- Figure 2.24** Displacement of an Infinite Beam with the Incident Propagating Wave and Both Nearfield Waves Suppressed using Three Moments. $l/\lambda = 0.1$
- Figure 2.25** Displacement of an Infinite Beam with the Incident Propagating Wave, the Negative-Going Propagating Wave and both Nearfield Waves Suppressed using Four Moments. $l/\lambda = 0.1$
- Figure 2.26** A Secondary Moment-Pair Array on an Infinite Beam
- Figure 2.27** Displacement of an Infinite Beam with a Single Secondary Moment-Pair Applied
- Figure 2.28** Displacement of an Infinite Beam with the Incident Propagating Wave and Positive-Going Nearfield Wave Suppressed using Two Moment-Pairs. $l_1/\lambda = 0.1$
- Figure 2.29** Displacement of an Infinite Beam with the Incident Propagating Wave and Positive-Going Nearfield Wave Suppressed using Two Moment-Pairs. $l_1/\lambda = 0.1$
- Figure 2.30** Displacement of an Infinite Beam with the Incident Propagating Wave and the Negative-Going Nearfield Wave Suppressed using Two Moment-Pairs. $l_1/\lambda = 0.1$
- Figure 2.31** Displacement of an Infinite Beam with Both Propagating Waves and the Positive Going Nearfield Wave Suppressed using Three Moment-Pairs. $l/\lambda = 0.1$
- Figure 2.32** Displacement of an Infinite Beam with Both Propagating Waves and the Negative-Going Nearfield Wave Suppressed using Three Moment-Pairs. $l/\lambda = 0.1$
- Figure 2.33** Displacement of an Infinite Beam with the Incident Propagating Wave and Both Nearfield Waves Suppressed using Three Moment-Pairs. $l/\lambda = 0.1$
- Figure 2.34** Displacement of an Infinite Beam with the Incident Propagating Wave, the Negative-Going Propagating Wave and both Nearfield Waves Suppressed using Four Moment-Pairs. $l/\lambda = 0.1$
- Figure 2.35** A Secondary Force Actuator Array Positioned on an Infinite Beam
- Figure 2.36** Displacement of an Infinite Beam with Two Secondary Forces Applied with a Control Strategy to Minimise the Secondary Effort
- Figure 2.37** Graphs of the Ratio of the Amplitude of Reflected Propagating Wave A_3 , to Incident propagating Wave A_i
- Figure 2.38** A Semi-infinite Beam with One Primary and Two Secondary Forces Applied

Figure 2.39	Ratio of the Secondary Forces when the Control Strategies are Implemented on a Semi-Infinite Beam
Figure 2.40	Secondary Effort Required for the Two Control Strategies
Figure 2.41	Ratio of the Effort with Two Secondary Forces Applied to the Effort with One Secondary Force Applied with the Minimum Effort Strategy Implemented
Figure 2.42	Displacement of the Beam Between the Primary and Secondary Forces with the Minimum Effort Control Strategy Implemented
Figure 2.43	Displacement of a Semi-Infinite Beam when the Minimum Effort Control Strategy is Implemented
Figure 3.1	An Infinite Beam with One Primary and One Secondary Force Applied
Figure 3.2	Normalized Magnitude of the Single Secondary Force Required to Implement Control Strategies on an Infinite Beam
Figure 3.3	Normalized Amplitudes of the Positive and Negative-Going Waves when One Secondary Force is Applied to an Infinite Beam
Figure 3.4	Ratios of the Power Supplied by Primary and Secondary Forces with Control to Power Supplied by the primary Force without Control using One Secondary Force on an Infinite Beam
Figure 3.5	An Infinite Beam with One Primary and Two Secondary Forces Applied
Figure 3.6	Normalized Magnitude of the Two Secondary Forces Required to Implement the Control Strategies on an Infinite Beam. $l = 10d$
Figure 3.7	Amplitude of the Propagating Waves with the Control Strategies Implemented on an Infinite Beam with Two Secondary Forces Applied. $l = 10d$
Figure 3.8	Ratios of Power Supplied by Forces with Control to the Power Supplied without Control with Two Secondary Forces Applied to an Infinite Beam. $l = 10d$
Figure 3.9	An Infinite Beam with One Primary and One Secondary Force Applied $l_1 = 0.2L, l_2 = 0.8L, l = 0.1\pi L$
Figure 3.10	Normalised Magnitude of the Single Secondary Force Required to Implement the Control Strategies on a Finite Beam
Figure 3.11	Normalised Displacement of a Finite Beam with One Secondary Force Applied.
Figure 3.12	Power Supplied by the Forces with Control with One Secondary Force Applied on a Finite Beam
Figure 3.13	An Infinite Beam with One Primary and Two Secondary Forces Applied $l_1 = 0.2L, l_2 = 0.8L, l = 0.1\pi L$ and $d = 0.1l$

Figure 3.14	Normalized Magnitudes of the Two Secondary Forces Required to Implement the Control Strategies on a Finite Beam
Figure 3.15	Normalised Displacement of a Finite Beam with Two Secondary Forces Applied
Figure 3.16	Power Supplied by the Forces with Control when Two Secondary Forces are Applied on a Finite Beam
Figure 3.17	Power Supplied by the Primary Forces with Control with Two Secondary Forces Applied on a Finite Beam
Figure 3.18	A semi-infinite Beam with One Primary and Two Secondary Forces Applied
Figure 3.19	Power Supplied by the Primary Force on a Semi-Infinite Beam with Two Secondary Forces Configured to Absorb Maximum Power
Figure 3.20	Experimental Set up with One Primary and One Secondary Force
Figure 3.21	Semi-infinite Beam Showing the Position of the Primary and Secondary Forces
Figure 3.22	Theoretical Ratio of the Secondary Force to the Primary Force Required to Suppress an Incident Flexural Propagating Wave on a Semi-Infinite Beam
Figure 3.23	Theoretical Power Supplied to the Beam by the Primary Force with and without Control
Figure 3.24	Measured Displacement per Unit Input Primary Force Downstream of the Secondary Force
Figure 3.25	Reduction in Measured Downstream Displacement
Figure 3.26	Measured Power Supplied to the Beam by the Primary Force with and without Control (c.f. figure 3.23)
Figure 3.27	Theoretical Secondary Force Required to Absorb Maximum Power
Figure 3.28	Theoretical Displacement of the Beam Downstream of the Secondary Force Adjusted to Absorb Maximum Power
Figure 3.29	Theoretical Change in Amplitude Downstream of the Secondary Force Adjusted to Maximize the Power Absorbed
Figure 3.30	Theoretical Power Supplied by the Primary Force with and without Control
Figure 3.31	Experimental Set Up for the Active Control Experiments using Power Based Control Strategies
Figure 3.32	Measured Displacement of the Beam Downstream of the Secondary Force Adjusted to Absorb Maximum Power
Figure 3.33	Measured Change in the Amplitude of the Beam Downstream of the Secondary Force Adjusted to Absorb Maximum Power

Figure 3.34	Measured Power Supplied by the Primary Force when the Secondary Force is Adjusted to Absorb Maximum Power
Figure 3.35	Theoretical Secondary Force Required to Minimize the Total Power Supplied to the Beam
Figure 3.36	Theoretical Displacement of the Beam Downstream of the Secondary Force Adjusted to Minimize the Total Power Supplied
Figure 3.37	Theoretical Change in the Displacement of the Beam Downstream of the Secondary Force Adjusted to Minimise the Total Power Supplied
Figure 3.38	Theoretical Power Supplied by the Primary Force with the Secondary Force Adjusted to Minimise the Total Power Supplied
Figure 3.39	Measured Displacement of the Beam Downstream of the Secondary Force when the Secondary Force is Adjusted to Minimize the Total Power Supplied
Figure 3.40	Change in the Measured Displacement of the Beam Downstream of the Secondary Force Adjusted to Minimise the Total Power Supplied
Figure 3.41	Measured Power Supplied by the Primary Force with the Secondary Force Adjusted to Minimise the Total Power Supplied
Figure 4.1	Construction of a Piezoelectric Element
Figure 4.2	Four Point Bending Test of a PZT Element
Figure 4.3	Relationship between LVDT Output Voltage and Load Applied
Figure 4.4	Deflected Shape of PZT Element
Figure 4.5	Experimental Set up to Measure the Piezoelectric Constant d_{31}
Figure 4.6	Measured and Theoretical Values of the Magnitude of the Piezoelectric Constant d_{31}
Figure 4.7	A Piezoelectric Sensor Fitted to a Beam
Figure 4.8	Equivalent Electrical Models of a Piezoelectric Sensor
Figure 4.9	Different Ways of Electrically Connecting Piezoelectric Elements to Measure Flexural and Longitudinal Motion of a Beam
Figure 4.10	Strain Distribution of a Flexural Sensor
Figure 4.11	Section through Beam and Sensor
Figure 4.12	Four Point Bending Test to check the Calibration of the Strain Gauges
Figure 4.13	Experimental Set Up to Measure the Sensitivity of a PZT Sensor - Plan View
Figure 4.14	Output from the Right-Hand Strain Gauge divided by the Output from the Left-Hand Strain Gauge

Figure 4.15	Output from PZT Sensor divided by the Output from the Left-Hand Strain Gauge
Figure 4.16	Strain Distribution of a Longitudinal Sensor
Figure 4.17	Electrical Connections for Simultaneous Longitudinal and Flexural Wave Measurement
Figure 4.18	Experimental Set Up to Measure Longitudinal and Flexural Motion Simultaneously
Figure 4.19	Surface Strain per Unit Input Lateral Force Measured using a PZT Sensor
Figure 4.20	Surface Strain per Unit Input Axial Force Measured using a PZT Sensor
Figure 4.21	A Flexural Vibration Actuator
Figure 4.22	Different Models Of Flexural Vibration Actuators
Figure 4.23	Strain Ratio against Thickness Ratio for A PZT Flexural Vibration Actuator Fitted to an Aluminium and a Steel Beam
Figure 4.24	Flexural Waves Generated by a PZT Actuator on a Beam
Figure 4.25	Sign Convention used with State Vector
Figure 4.26	Schematic Diagram of the PZT Flexural Actuator
Figure 4.27	Simple Block Diagram of the PZT Actuator
Figure 4.28	Propagating Wave Amplitude per unit Moment Applied
Figure 4.29	Ratios of Propagating Wave Amplitudes Calculated using the Simple and Complete Models
Figure 4.30	Phase Between Propagating Waves Calculated using the Simple and Complete Models
Figure 4.31	Wave Conversion by the PZT Actuator
Figure 4.32	Normalized Magnitude of the Reflected Evanescent A_1 Wave
Figure 4.33	Normalized Magnitude of the Transmitted Evanescent A_2 Wave
Figure 4.34	Normalized Magnitude of the Reflected Propagating A_3 Wave and the Transmitted A_4 Wave
Figure 4.35	Power Supplied to an 6.12 mm Thick Infinite Aluminium Beam by Different Actuators (Theoretical)
Figure 4.36	Experimental Set Up to Determine the Power Supplied to a Beam by a PZT Flexural Actuator
Figure 4.37	Theoretical Response of an Infinite and Semi-infinite Beam to Excitation by A PZT Flexural Vibration Actuator. Loss factor of 1 %

Figure 4.38	Comparison of the Theoretically Calculated Response of the Experimental Beam using the Complete and Simple Models of the Actuator
Figure 4.39	Response of the Experimental Beam to Excitation by a PZT Flexural Vibration Actuator - Theoretical and Experimental Results
Figure 4.40	A PZT Actuator Comprising Triangular PZT Elements
Figure 4.41	A Model of a General Distributed Flexural Actuator
Figure 4.42	Propagating Wave Amplitudes for Different Actuator Shapes
Figure 4.43	Phase Relationship between the Propagating Waves
Figure 4.44	Spacing of PZT Flexural Vibration Actuators
Figure 4.45	Simple Representation of Two Rectangular PZT Actuators Fitted to a Beam
Figure 4.46	Secondary Effort Required to Suppress the Incident and reflected Propagating Flexural Waves
Figure 4.47	A Longitudinal Vibration Actuator
Figure 4.48	Strain Distribution of Different Models of Longitudinal Vibration Actuators
Figure 4.49	Longitudinal Waves Generated by a PZT Actuator on a Beam
Figure 4.49	Sign Convention used with State Vector
Figure 4.50	Schematic Diagram of the PZT Longitudinal Actuator
Figure 4.51	Longitudinal Wave Amplitudes per unit Input Force
Figure 4.52	Ratio Longitudinal Wave Amplitude Calculated using the Simple and Complete Models
Figure 4.53	Phase Between Longitudinal Waves Calculated using the Simple and Complete Models
Figure 4.54	Wave Conversion by the PZT Actuator
Figure 4.55	Normalized Amplitudes of the Outgoing Waves from the Inactive PZT Longitudinal Actuator
Figure 4.56	Power Supplied to an 6.12 mm Thick Infinite Beam by a Longitudinal PZT Actuator
Figure 4.57	Experimental Set Up to Validate the Model of the Longitudinal PZT Actuator
Figure 4.58	Response of the Experimental Beam to Excitation by a PZT Longitudinal Vibration Actuator - Theoretical and Experimental Results
Figure 4.59	Electrical Equivalent Models of a Piezoelectric Actuator and Sensor

Figure 4.60	Electrical Bridge Circuit of the Self Sensing Actuator
Figure 4.61	Experimental Set Up to Measure the Electrical Impedance of the PZT Actuator
Figure 4.62	Experimental Results Showing the Magnitude of the Actuator Impedance
Figure 4.63	Experimental Results Showing the Phase of the Actuator Impedance
Figure 4.64	Magnitude of Input/Output Characteristic of a Self Sensing Actuator as a function of z_3/z_p
Figure 4.65	Phase of Input/Output Characteristic of a Self Sensing Actuator as a function of z_3/z_p
Figure 4.66	Diagram of the Self Sensing Circuit
Figure 4.67	Frequency Response (Magnitude) of the Self Sensing Circuit
Figure 4.68	Frequency Response (Phase) of the Self Sensing Circuit
Figure 4.69	Experimental Set Up to Test the Self Sensing Circuit
Figure 4.70	Response (Magnitude) of Beam per unit Moment Applied by the PZT Actuator and Measured with the Self Sensing Circuit
Figure 4.71	Response (Phase) of Beam per unit Moment Applied by the PZT Actuator and Measured with the Self Sensing Circuit
Figure 4.72	Receptance (Magnitude) of the Beam Measured with the Self Sensing Actuator, Showing the Effect of Changing C_3
Figure 4.73	Receptance (Phase) of the Beam Measured with the Self Sensing Actuator, Showing the Effect of Changing C_3
Figure 5.1	Feedback Control using a Force Actuator
Figure 5.2	Feedback Control using a Moment Actuator
Figure 5.3	Feedback Control using a Moment-Pair Actuator
Figure 5.4	Feedback Control using a PZT Actuator
Figure 5.5	Feedback Control using a PZT Actuator and Measuring Slope with Displacement Transducers
Figure 5.6	Normalized Moments Applied by the PZT Actuator
Figure 5.7	Change in Amplitude of the Propagating Wave when Moments M_1 and M_2 are Applied
Figure 5.8	Semi-Infinite Aluminium Beam with a Primary Force and a PZT Secondary Source
Figure 5.9	Change in the Magnitude of the Flexural Propagating Wave on a Semi-Infinite Beam with a Constant Feedback Gain
Figure 5.10	Block Diagram of the Feedback Control System

Figure 5.11	Experimental Set Up to Test the Effectiveness of a PZT Actuator in the Suppression of Flexural Propagating Waves
Figure 5.12	Experimental Set Up to Test the Effectiveness of the Feedback Control System in the Suppression of Flexural Propagating Waves
Figure 5.13	Measured Displacement of the Beam Downstream of the PZT Actuator
Figure 5.14	Reduction in Measured Downstream Displacement. Phase Reference Taken from the Primary Force
Figure 5.15	Measured Lateral Displacement of the Beam Downstream of the Secondary Source. Broadband Excitation and Feedback Control
Figure 5.16	Reduction in Measured Lateral Displacement of the Beam Downstream of the Secondary Source. Broadband Excitation and Feedback Control
Figure 5.17	Open Loop Transfer Function. The Numbers are Frequencies in Hz
Figure 5.18	Gain of the Transformer
Figure 5.19	Gain of the Phase Controller
Figure 5.20	Force Applied at the End of a Beam
Figure 5.21	Integrated Longitudinal Vibration Actuator
Figure 5.22	Changes in Axial Displacement when Axial Displacement and Axial Strain are Measured and fed back to an In-Plane Force
Figure 5.23	Change in Axial Displacement Downstream of the Actuator when Axial Displacement is Sensed and a Constant Feedback Gain H_1 is Used
Figure 5.24	Single PZT Element used as a Sensor and Actuator
Figure 5.25	Experimental Set Up to Test the Effectiveness of the PZT Actuator in the Suppression of Longitudinal Waves
Figure 5.26	Measured Displacement of the Beam Downstream of the Secondary Force Actuator
Figure 5.27	Reduction in the Measured Downstream Axial Displacement. Phase Reference Taken from the Primary Force
Figure 5.28	Ratio of the Secondary Force to Primary Force Applied to Suppress the Downstream Axial Displacement of the Beam
Figure 5.29	Experimental Set Up to Check the Effectiveness of the Feedback Control System to Suppress Longitudinal Waves
Figure 5.30	Positioning of the Capacitance Probe
Figure 5.31	Measured Axial Displacement of the Beam per Unit Input Force Downstream of the Secondary Source. Broadband Excitation and Feedback Control

Figure 5.32	Reduction in Measured Axial Displacement of the Beam Downstream of the Secondary Source. Broadband Excitation and Feedback Control
Figure 5.33	Open Loop Transfer Function. The Numbers are Frequencies in Hz
Figure 6.1	Fluid-Filled Pipe Co-ordinate System and Mode Shapes
Figure 6.2	Wavenumbers Derived by (a) Pavic [99], (b) Lin and Morgan [102] and (c) Pinnington and Briscoe [98] for a Water-Filled Perspex Pipe, $a = 72.5$ mm, $h = 5$ mm
Figure 6.3	Application of an External Pressure to an Infinite <i>In Vacuo</i> Pipe
Figure 6.4	Comparison Between the Actual Radial Displacement and Approximate Radial Displacement of a Pipe Due to External Pressure Loading
Figure 6.5	Fluid wave Actuator
Figure 6.6	Dynamic Stiffness of the Ring and Contained Fluid
Figure 6.7	Ratio of Internal to Applied Pressure for the Water-Filled Perspex Pipe
Figure 6.8	PVDF Actuator Fitted to a Ring
Figure 6.9	Equivalent Representation of a PVDF Wire Actuator Fitted to a Ring
Figure 6.10	Representation of a Hydraulic Actuator Driven by a Magnetostrictive Actuator
Figure 6.11	Line Diagram of the Fluid Wave Actuator
Figure 6.12	A PVDF Fluid Wave Sensor
Figure 6.13	Active Control of Fluid waves - Experimental Set Up
Figure 6.14	The Piston Assembly used to Excite the Fluid
Figure 6.15	Schematic Diagram of the Measurement of the Frequency Response Functions between the Primary Force and the Seven Sensors.
Figure 6.16	Schematic Diagram of the Measurements Taken during the Active Control Experiments
Figure 6.17	Real and Imaginary Components of the Measured Impedance of the Support Plates
Figure 6.18	Real and Imaginary Components of the Apparent Mass of the Primary Piston used to Excite the Fluid
Figure 6.19	Point Receptance of the Fluid-Filled Pipe with Excitation of the Fluid
Figure 6.20	Point Receptance of the Fluid-Filled Pipe with Excitation of the Pipe Wall
Figure 6.21	Pressure Measured by Hydrophone due to Excitation by Primary Force
Figure 6.22	Phase Angle between the Pressure Measured by the Hydrophone and the Primary Force (Fluid Excitation)

Figure 6.23	Phase Angle Between Accelerometers due to Excitation by Primary Force
Figure 6.24	Pressure Measured by Hydrophone and PVDF Sensor due to Excitation by Primary Force
Figure 6.25	Ratio between the Output from the PVDF Sensor and the Pressure Measured by Hydrophone due to Excitation by Primary Force
Figure 6.26	Phase Angle between the Output from the PVDF Sensor and the Pressure Measured by Hydrophone due to Excitation by Primary Force
Figure 6.27	Phase Angle between Accelerometers due to Excitation by Secondary Source
Figure 6.28	Pressure Measured by Hydrophone and PVDF Sensor due to Excitation by Secondary Source
Figure 6.29	Ratio of the Output from the PVDF Sensor and the Pressure measured by Hydrophone due to Excitation by the Secondary Source
Figure 6.30	Phase Angle between the Output from the PVDF Sensor and the Pressure Measured by Hydrophone due to Excitation by the Secondary Source
Figure 6.31	Pressure Measured using the Hydrophone with and without Control
Figure 6.32	Change in Pressure Measured using the Hydrophone with Control
Figure 6.33	Pressure Measured using the PVDF Sensor with and without Control
Figure 6.34	Change in Pressure Measured using PVDF Sensor with Control
Figure 6.35	Graph Showing How Effective Active Control of the Fluid Waves Could be if the PVDF Sensor was used as the Error Sensor
Figure 6.36	Magnitude of Secondary Effort Required to Minimise the Downstream Pressure
Figure 6.37	Phase Angle between the Secondary and Primary Sources when the Downstream Pressure is Minimised
Figure 6.38	Sum of the Squared Radial Acceleration Levels of the Pipe
Figure 6.39	Change in the Sum of the Squared Acceleration Levels of the Pipe
Figure 6.40	Phase Angle between Accelerometers with Control
Figure A1.1	Notation for the Equations of Motion
Figure A1.2	Wavenumber Diagram for Sound and Structural Waves
Figure A2.1	Flexural Waves Generated by a Lateral Force on a Semi-Infinite Beam
Figure A2.3	Flexural Waves Generated by a Moment on an Infinite Beam
Figure A2.4	Flexural Waves Generated by a Pair of Moments on an Infinite Beam

Figure A2.5	Longitudinal Waves Generated by an In-Plane Force on an Infinite Beam
Figure A2.6	Longitudinal Waves Generated by a Pair of In-Plane Forces on an Infinite Beam
Figure A2.7	Forced Vibration of a Finite Beam
Figure A2.8	Pictorial Representation of Equation (A2.24)
Figure A2.9	Pictorial Representation of Equation (A2.25)
Figure A3.1	Force Excitation of a General Structure
Figure A3.2	Power Input into an Infinite Uniform Beam by a Point Force
Figure A3.3	Power Input into an Infinite Uniform Beam by a Point Moment
Figure A3.4	Power Supplied to an Infinite Uniform Beam by a Pair of Moments
Figure A3.5	Power Supplied to an Infinite Beam by Different Actuators
Figure A3.6	Power Supplied to an Infinite Uniform Beam by a Pair of In-Plane Forces
Figure A3.7	Power Supplied to an Infinite Uniform Beam by a Longitudinal PZT Actuator
Figure A3.8	A Primary and Secondary Array Positioned on a Beam
Figure A3.9	Excitation of a Beam by a Lateral Force
Figure A3.10	Power Supplied to- and Absorbed from the beam as a Function of the Phase Angle between the Displacement and the Force Applied
Figure A4.1	Beam used in Experiments - Plan View
Figure A4.2	A Piezoceramic Element
Figure A4.3	PZT Elements Fixed to the Beam
Figure A4.4	Data Sheet for Piezoceramic Elements
Figure A4.5	Fluid Actuator Assembly
Figure A4.6	Item 1 Magnetostrictive Actuator Outline Drawing
Figure A4.7	Item 2 Actuator Clamp
Figure A4.8	Item 3 Cylinder
Figure A4.9	Item 4 Piston
Figure A4.10	Item 5 Cylinder Ring

LIST OF PLATES

Plate 6.1	Experimental Rig used for the Control of Fluid Waves
Plate 6.2	The Fluid Wave Actuator
Plate 6.3	Photograph Showing the Hydrophone (inside the pipe), the Radial and Axial PVDF Sensors and the Accelerometers

LIST OF TABLES

Table 2.1	The Secondary Effort E , Required for the Different Control Strategies for Various Distances between the Two Secondary Forces
Table 2.2	The Secondary Effort E , Required for the Different Control Strategies for Various Distances between the Three Secondary Forces
Table 2.3	The Secondary Effort E , Required for Various Distances between the Four Secondary Forces
Table 4.1	Properties of PZT and PVDF
Table 4.2	Strain Gauge Calibration Test
Table 4.3	Comparison Between Strain-Energy and Pin-Force Static Models of PZT Actuators [74]
Table 5.1	Transfer Functions of the Feedback Controllers fro Various Collocated Sensor and Actuator Combinations which Suppress Propagating Flexural Waves
Table 6.1	Material Properties of the Perspex Pipe and Water
Table 6.2	Ratios of Variables due to the "Fluid" Wave to those due to the "Structural" Wave for Different Excitations of the Experimental Water-Filled Perspex Pipe at a Frequency of 500 Hz
Table 6.3	Properties of PVDF Wire
Table 6.4	Material Properties of PVDF Film Elements
Table 6.5	Effect of Fluid-Structure Interaction on Wave Speeds

ACKNOWLEDGEMENTS

I would like to express my sincere gratitude to my Supervisors, Professor Stephen Elliott and Dr Roger Pinnington for their inspirational guidance and help throughout this project.

The assistance of Mr Mick Day at the Royal Naval Engineering College is also gratefully acknowledged. His invaluable help with the design and manufacture of the experimental rigs ensured a successful outcome to the practical work.

Finally, I would like to thank my wife, Laura, and daughter, Emma, for their indulgence and tolerance shown to me whilst I have been engaged in this endeavour.

CHAPTER 1

1 INTRODUCTION

Practical engineering structures are often fabricated from a number of components held together by structural elements that can be modelled as one-dimensional waveguides. Examples of such structures are truss beams in large space-structures and bridges, antenna booms, and struts and tie-bars found in machinery installations in ships, submarines and helicopters. Pipework systems, which are found in many engineering installations, also behave as one-dimensional waveguides at low frequencies. These waveguides act as noise and vibration transmission paths from sources to receivers, for example the gearbox support struts in a helicopter couple the gearbox (source) to the cabin (receiver) [1]. It is the control of vibrations along one-dimensional structures such as these, that is the subject of this thesis. Before considering this in detail, however, various methods of vibration control are first reviewed.

The transmission of noise and vibration is generally undesirable, and there are three established ways of combatting it; these are passive, semi-active and active control. Until about 1990, passive control measures were generally applied to practical engineering systems, and the theory underlying these measures is well documented, for example [2]. Semi-active vibration control involves passively generating a secondary force, by actively changing the properties of the system, such as stiffness and damping. This strategy is found in automobile applications, where damping is controlled, for example [3][4], and in some building earthquake response systems [5], where stiffness is controlled. Damping can be controlled by using adjustable orifices in hydraulic dampers [4], or by electrorheological fluids [6][7]. Another semi-active control device is a tuned mass damper. These are employed extensively in Japan, where they are fitted to high-rise buildings as a seismic control measure [8]. On a much smaller scale, a tunable vibration absorber has been developed for use in machinery installations, where the stiffness is controlled by changing the air pressure

in a set of rubber bellows [9]. Shape memory alloys have also been used in the semi-active control of composite plate vibrations [10]. Nitinol fibre wires are integrated into the plate, and these wires can be activated to change the stiffness of the plate and shift resonant frequencies away from troublesome excitation frequencies.

The active control of noise and vibration involves cancelling unwanted disturbances by deliberately adding secondary controlled disturbances. In the active control of sound, the secondary sources are generally loudspeakers, and in the active control of vibration, actuators that generate forces or moments are used. The concept of active control is not a new idea. The earliest work was done in the active control of sound in 1934 by Leug [11], and there has been a significant amount of research since, culminating in a text book [12], to which the reader is referred for further information. The active control of vibrations or structure-borne sound is less well developed, however, as structures behave in a much more complex manner than sound in air. This is because many more wave types can potentially propagate in a structure [13].

The development of an active control system for the control of structure-borne sound may be divided into two parts. The first part involves an analysis of the physical system to be controlled. This includes the way in which vibration sensors and actuators couple into the dynamics of the structure, and the determination of the behaviour of the system when the control strategies are implemented. The second part involves the development of the electronic control system, which needs to be designed such that the vibration levels achieved are as close as possible to the theoretically achievable levels determined in the first part. This thesis is primarily concerned with the first part; the physical analysis of the control of structure-borne sound in one-dimensional structures. In order to conduct experiments to confirm the theoretical predictions of the physical limits, two simple controllers were used. The first was a feedforward system in which the amplitude and phase of the signal driving the secondary actuator was manually adjusted to minimise some measured cost function. The second was a feedback system using a simple analogue controller.

There are two contemporary ways of modelling the dynamical behaviour of a structure. The first involves a modal description, where the dynamics are described in terms of structural modes and natural frequencies [14], and the second involves describing the structure in terms of waves [13][15][16]. Although these two formulations are formally equivalent it is convenient to describe some approaches to active control in terms of modes and others in terms of waves.

Global control of a structure has been formulated in modal space by several researchers, for example [17][18]. These have generally been treated analytically by way of a modal decomposition, with a finite number of modes being retained in the analytical model. This is of necessity, as a real structure will have an infinite number of modes, which cannot all be controlled in reality. The effects of the uncontrolled and unmodelled modes are detrimental to the performance of the system in practice [17]. Firstly observation spillover occurs, in that the response of these modes contributes to the measured displacement and hence to the control forces. Secondly there is control spillover. This is where the control forces, which are intended to control specific modelled modes, excite unmodelled modes unless the control forces are positioned on nodal points of these modes. Clearly this control strategy requires accurate and detailed knowledge of the dynamic behaviour of the structure to be controlled. Thus, this type of control strategy is only appropriate if there are very few modes excited in the structure. Von Flotow [19] discusses the inherent limitation of global control when there are many modes contributing to the response of the structure. He demonstrates the extreme sensitivity of the mode shapes to small modelling errors in this frequency range, and the difficulty in designing a stable system to control these ill-defined modes.

Rather than adopt global control of the system dynamics, another approach is to prevent the transmission of vibrational power between the structural components. For this type of local control, a modal model of the structure is inappropriate, and the system dynamics can better be described by a wave model. In general, three wave types will be present in connecting elements between the structural components; flexural, or out-of-plane waves, longitudinal, or in-plane waves and torsional waves

[13]. Additionally, in most pipework systems there will be fluid-borne as well as structure-borne waves [20]. Local control of these waves can be achieved by placing actuators along the waveguides, and commercially available devices to generate the control forces and moments are electromagnetic, magnetostrictive and piezoelectric actuators.

The active control of structure-borne sound using wave models has been discussed by several researchers, for example Miller *et al* [21], and Pines and Von Flotow [22], who designed controllers based on wave models. In their analysis, they coupled the actuators to the structure under control by relating structural wave-modes to the physical quantities of forces, moments, displacements and rotations at the interfaces between the actuators (junctions) and waveguides. Wave models have also been used by Pan and Hansen to analyse various aspects of active vibration control on a beam [23][24], and other researchers have discussed the active control of flexural waves on a beam using secondary control forces [25][26][27][28]. Elliott and Billet [29] highlighted fundamental low and high frequency limitations in the practical implementation of the feedforward control of these waves.

This thesis is concerned with several aspects of the active control of structure- and fluid-borne sound in one-dimensional structures, and uses wave models to describe the dynamic behaviour of the systems under investigation. Two structures are used as a vehicle for both the analytical and experimental studies and these are a slender beam and a fluid-filled pipe. Much of the thesis is concerned with the control of flexural and longitudinal waves on the beam, where insight is gained into the control of these waves, and this can be applied to any structure provided its dimensions are such that it behaves in a beam-like manner.

Chapter 2 contains a theoretical analysis into the control of flexural waves using different types of secondary sources, and investigates the relationship between the number and disposition of the sources, and the number and types of waves that can be controlled. Also contained in this chapter is an investigation into the control strategy where flexural waves are suppressed using minimum secondary effort.

Control of these waves using power as a cost function is the subject of Chapter 3, which contains a theoretical analysis into the physical effects of these control strategies. Experimental results which validate the theory are also presented in this chapter. Chapter 4 is a major part of this thesis, and contains a comprehensive theoretical and experimental investigation into the use of piezoelectric sensors and actuators in the active control of vibration on a beam. Piezoceramic actuators are used in Chapter 5 in the implementation of some simple feedback control strategies, involving flexural and longitudinal waves on a beam. Chapter 6 extends the analysis of wave control to a fluid-filled pipe. A design of fluid wave actuator is proposed and a framework which couples the actuator to the fluid is developed. This non intrusive actuator was built and tested along with a non intrusive fluid wave sensor made up of piezoelectric elements. The results of the experiments proving these devices are also presented. Finally, Chapter 7 summarises the main conclusions from this thesis and makes recommendations for further work.

CHAPTER 2

2 ACTIVE CONTROL OF WAVES ON BEAM-LIKE STRUCTURES

2.1 Introduction

It was mentioned in Chapter 1 that a convenient way of describing the dynamic behaviour of a one-dimensional structure is in terms of the waves that can potentially exist in the structure. On long slender structures, longitudinal, torsional and flexural waves may propagate, depending on the excitation mechanisms [13]. There are two longitudinal and torsional waves that can propagate in such a structure, one from left to right and the other from right to left. There are four flexural waves, however; in addition to the two propagating waves, there are left and right-going nearfield waves. These waves decay away exponentially from the source of excitation, and only need to be considered at low frequencies or close to discontinuities. Thus, the most complicated wave field consists of flexural waves, and if control of these waves is understood, then the control of the other waves can be readily inferred using the same formulation by ignoring the nearfield waves. A summary of the nature of wave propagation in solids and fluids is given in Appendix 1, and the way in which waves can be used to model the dynamical behaviour of a beam is described in Appendix 2.

The control of flexural waves on beams has been investigated by other researchers. Mace [25], considered two systems; the first involved the application of a force and a moment to suppress a propagating flexural wave, and the second involved the application of two forces to achieve the same result. McKinnell [30] designed a feedforward controller to suppress a flexural propagating wave using two secondary forces on a cantilever beam. Scheuren [27] demonstrated that four forces are required to completely suppress an incident propagating wave, but if nearfield waves

are neglected then only two forces are necessary. He further showed that if a finite beam is considered, the same effect can be achieved by the application of one force at the end of the beam [28].

This chapter is concerned with the active control of flexural waves on an Euler-Bernoulli beam. An analysis is conducted into the physical effects of various wave control strategies, and to simplify this initially, the beam is assumed to be infinitely long; i.e., there are no boundaries or discontinuities either side of the secondary sources. Secondary source arrays consisting of forces, moments, or pairs of moments which are generated by piezoceramic actuators, are modelled as wave generators, and the ways in which these arrays couple into and control flexural waves are examined. The analysis is conducted in the frequency domain which is appropriate for deterministic disturbances. How control of the secondary actuators is implemented, i.e., how the magnitude and phase of the signal fed to each actuator can be adjusted in practice is not addressed. The chapter is arranged into six sections. Following this introduction, individual sections are devoted to wave suppression using forces, moments and moment-pairs, and then section 2.5 discusses a wave control strategy whereby a flexural propagating wave is suppressed using minimum control effort. The final section discusses the main conclusions from the analysis.

2.2 Control of Flexural Waves using Point Forces

2.2.1 Introduction

In this section an investigation is carried out into the ways in which harmonic secondary forces can be applied to an Euler-Bernoulli beam to suppress a propagating flexural wave. A general framework is first developed, so that when the secondary forces are applied, the displacement of any point on the beam can be determined. A secondary force array consisting of up to four secondary force actuators is considered. This was chosen because four forces are required to suppress an incident propagating wave without generating any residual nearfield or propagating waves [27]. An

exhaustive investigation is conducted into the effects that the application of one, two, three and four secondary forces can have on the lateral displacement of an infinite beam when a flexural propagating wave is incident on the secondary array.

2.2.2 Model of the Secondary Force Array

The secondary force array is shown in **figure 2.1**. The forces are assumed to have the same frequency as the tonal incident wave A_i , and the magnitude and phase is represented by a complex number. Each of these complex forces $f_{s1} \rightarrow f_{s4}$ generates four waves, two nearfield and two propagating, as discussed in

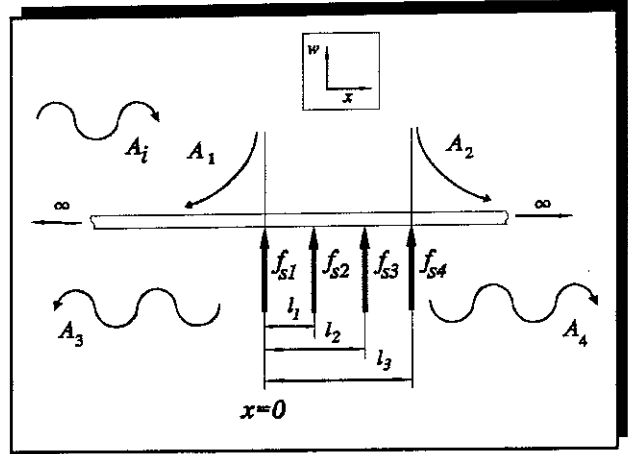


Figure 2.1 A Secondary Force Array on an Infinite Beam

Appendix 2. In addition, there is a propagating wave A_i , incident on the array. The complex lateral displacement at any point on the beam is the linear superposition of these waves and can be described by the equation:

$$w(x) = A_1 e^{k_b x} + A_2 e^{-k_b x} + A_3 e^{jk_b x} + A_4 e^{-jk_b x} + A_i e^{-jk_b x} \quad (2.1a)$$

where k_b is the flexural wavenumber given in Appendix 1, and the A 's are complex wave amplitudes. *The $e^{j\omega t}$ time dependence is suppressed for clarity* and no energy loss in the beam is assumed. As the beam is infinite, waves generated by the secondary force array can only propagate away and decay away from the array. Thus, to the left of the secondary force array when $x \leq 0$, the displacement is given by:

$$w(x) = A_1 e^{k_b x} + A_3 e^{jk_b x} + A_i e^{-jk_b x} \quad (2.1b)$$

and to the right of the array when $x \geq l_3$, the displacement is given by:

$$w(x) = A_2 e^{-k_b x} + A_4 e^{-jk_b x} + A_1 e^{-jk_b x} \quad (2.1c)$$

The wave amplitudes A_1 , A_2 , A_3 and A_4 in these regions of the beam, where $x \leq 0$ and $x \geq l_3$ can be determined using the matrix equation:

$$\begin{bmatrix} A_1 \\ A_2 \\ A_3 \\ A_4 \end{bmatrix} = -\frac{1}{4EI k_b^3} \begin{bmatrix} 1 & e^{-k_b l_1} & e^{-k_b l_2} & e^{-k_b l_3} \\ 1 & e^{k_b l_1} & e^{k_b l_2} & e^{k_b l_3} \\ j & j e^{-jk_b l_1} & j e^{-jk_b l_2} & j e^{-jk_b l_3} \\ j & j e^{jk_b l_1} & j e^{jk_b l_2} & j e^{jk_b l_3} \end{bmatrix} \begin{bmatrix} f_{s1} \\ f_{s2} \\ f_{s3} \\ f_{s4} \end{bmatrix} \quad (2.2)$$

where E is the Young's modulus of the beam and I is the second moment of area about the neutral axis. These complex wave amplitudes can be substituted into equations (2.1b, c) to give the lateral displacement of the beam either side of the secondary array in response to the secondary forces. The wave amplitudes within the array can be calculated using three similar relationships to equation (2.2). These are:

for $0 \leq x \leq l_1$

$$\begin{bmatrix} A_1 \\ A_2 \\ A_3 \\ A_4 \end{bmatrix} = -\frac{1}{4EI k_b^3} \begin{bmatrix} 0 & e^{-k_b l_1} & e^{-k_b l_2} & e^{-k_b l_3} \\ 1 & 0 & 0 & 0 \\ 0 & j e^{-jk_b l_1} & j e^{-jk_b l_2} & j e^{-jk_b l_3} \\ j & 0 & 0 & 0 \end{bmatrix} \begin{bmatrix} f_{s1} \\ f_{s2} \\ f_{s3} \\ f_{s4} \end{bmatrix} \quad (2.3)$$

for $l_1 \leq x \leq l_2$

$$\begin{bmatrix} A_1 \\ A_2 \\ A_3 \\ A_4 \end{bmatrix} = -\frac{1}{4EI k_b^3} \begin{bmatrix} 0 & 0 & e^{-k_b l_2} & e^{-k_b l_3} \\ 1 & e^{k_b l_1} & 0 & 0 \\ 0 & 0 & j e^{-jk_b l_2} & j e^{-jk_b l_3} \\ j & j e^{jk_b l_1} & 0 & 0 \end{bmatrix} \begin{bmatrix} f_{s1} \\ f_{s2} \\ f_{s3} \\ f_{s4} \end{bmatrix} \quad (2.4)$$

for $l_2 \leq x \leq l_3$

$$\begin{bmatrix} A_1 \\ A_2 \\ A_3 \\ A_4 \end{bmatrix} = -\frac{1}{4EIk_b^3} \begin{bmatrix} 0 & 0 & 0 & e^{-k_b l_3} \\ 1 & e^{k_b l_1} & e^{k_b l_2} & 0 \\ 0 & 0 & 0 & j e^{-jk_b l_3} \\ j & j e^{jk_b l_1} & j e^{jk_b l_2} & 0 \end{bmatrix} \begin{bmatrix} f_{s1} \\ f_{s2} \\ f_{s3} \\ f_{s4} \end{bmatrix} \quad (2.5)$$

These are general equations and can be used for any number of secondary forces up to a maximum of four. Should a greater number of forces be applied, then the system of matrices can be extended to accommodate these relatively easily. The purpose of the secondary force array is to generate a set of waves such that the incident propagating wave is suppressed, so that the displacement in the far-field downstream of the array is zero. The wave amplitudes either side of the secondary force array, including the incident wave, may be determined by the equation:

$$\begin{bmatrix} A_1 \\ A_2 \\ A_3 \\ A_4 \end{bmatrix} = -\frac{1}{4EIk_b^3} \begin{bmatrix} 1 & e^{-k_b l_1} & e^{-k_b l_2} & e^{-k_b l_3} \\ 1 & e^{k_b l_1} & e^{k_b l_2} & e^{k_b l_3} \\ j & j e^{-jk_b l_1} & j e^{-jk_b l_2} & j e^{-jk_b l_3} \\ j & j e^{jk_b l_1} & j e^{jk_b l_2} & j e^{jk_b l_3} \end{bmatrix} \begin{bmatrix} f_{s1} \\ f_{s2} \\ f_{s3} \\ f_{s4} \end{bmatrix} + \begin{bmatrix} 0 \\ 0 \\ 0 \\ A_i \end{bmatrix} \quad (2.6)$$

As mentioned above, if four forces are applied, the nearfield A_1 and A_2 waves and the negative-going A_3 propagating wave can be suppressed as well as the incident propagating wave. In this case we require:

$$\begin{bmatrix} A_1 \\ A_2 \\ A_3 \\ A_4 \end{bmatrix} = -\frac{1}{4EIk_b^3} \begin{bmatrix} 1 & e^{-k_b l_1} & e^{-k_b l_2} & e^{-k_b l_3} \\ 1 & e^{k_b l_1} & e^{k_b l_2} & e^{k_b l_3} \\ j & j e^{-jk_b l_1} & j e^{-jk_b l_2} & j e^{-jk_b l_3} \\ j & j e^{jk_b l_1} & j e^{jk_b l_2} & j e^{jk_b l_3} \end{bmatrix} \begin{bmatrix} f_{s1} \\ f_{s2} \\ f_{s3} \\ f_{s4} \end{bmatrix} = \begin{bmatrix} 0 \\ 0 \\ 0 \\ -A_i \end{bmatrix} \quad (2.7)$$

which can be re-arranged to give the required secondary forces:

$$\begin{bmatrix} f_{s1} \\ f_{s2} \\ f_{s3} \\ f_{s4} \end{bmatrix} = -4EI k_b^3 \begin{bmatrix} 1 & e^{-k_b l_1} & e^{-k_b l_2} & e^{-k_b l_3} \\ 1 & e^{k_b l_1} & e^{k_b l_2} & e^{k_b l_3} \\ j & j e^{-jk_b l_1} & j e^{-jk_b l_2} & j e^{-jk_b l_3} \\ j & j e^{jk_b l_1} & j e^{jk_b l_2} & j e^{jk_b l_3} \end{bmatrix}^{-1} \begin{bmatrix} 0 \\ 0 \\ 0 \\ -A_i \end{bmatrix} \quad (2.8)$$

This equation can be reduced in size depending on how many secondary forces are applied. In this chapter, the effects of applying up to four secondary forces are considered.

2.2.3 Control Using a Single Secondary Force

Two control strategies are considered with the application of one secondary force. The first strategy involves the suppression the incident propagating wave and the second involves bringing the beam to rest at the point of application of the secondary force.

Case 1.1 Suppression of the Incident Propagating Wave

If the incident propagating wave is to be suppressed, equation (2.8) can be used, and when only one secondary force is applied, it reduces to:

$$f_s = -j4EI k_b^3 A_i \quad (2.9)$$

Upstream of the secondary force, the resulting displacement of the beam normalised to the amplitude of the incident wave is:

$$\frac{w_-(x)}{A_i} = j e^{k_b x} - e^{jk_b x} + e^{-jk_b x} \quad (2.10)$$

which can also be written as:

$$\frac{w_-(x)}{A_i} = j(e^{k_b x} - 2\sin k_b x) \quad (2.11)$$

This shows that the displacement of the beam upstream of the secondary force

consists of a nearfield and a standing wave. Similarly the displacement of the beam downstream of the secondary force is given by:

$$\frac{w_+(x)}{A_i} = j e^{-kx} \quad (2.12)$$

which is a nearfield wave only.

The displacement of the beam, which is described by equations (2.11) and (2.12) is plotted in

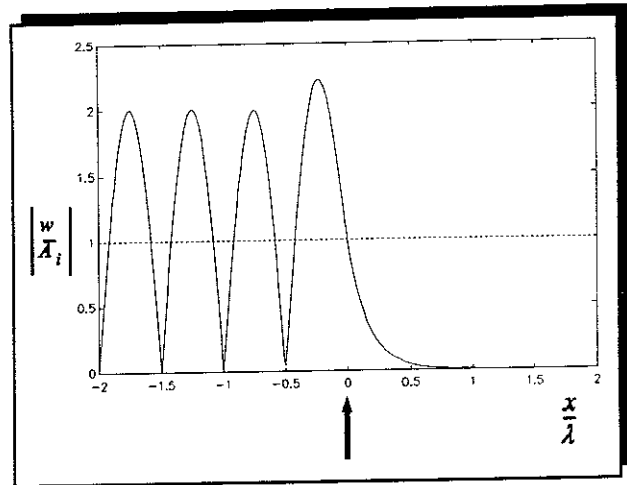


Figure 2.2 Displacement of an Infinite Beam with One Secondary Force Applied to Suppress a Propagating Flexural Wave

figure 2.2. It should be noted that only one secondary force is required to suppress the incident propagating wave. This wave is effectively reflected into a negative-going propagating wave, and combines with the incident wave to form a standing wave upstream of the secondary force. This can clearly be seen in **figure 2.2**. The discontinuities (sharp minima) are nodal points where there is no motion, and their position is dependent on frequency. It can also be seen that nearfield waves are generated either side of the secondary force at $x = 0$. In the far-field, to the right of the secondary force, the displacement of the beam is zero, as expected. Thus, although the beam has been brought to rest downstream of the secondary force, the vibration of the beam upstream has increased.

Case 1.2 Use of a Single Secondary Force to Pin the Beam

Rather than use a control strategy to suppress the incident propagating wave, it is possible to pin the beam at the secondary force position, i.e., to prevent lateral motion of the beam at that point. In this case the incident propagating wave is not suppressed, but is reduced by a factor of the square root of two, and the reflected wave is not as large as in the previous case. The displacement of an infinite beam with a pinned discontinuity is discussed by Mead [15]. The required secondary force can be calculated by applying the boundary condition at secondary force position:

$$w_+(0) = w_-(0) \quad (2.13)$$

which results in a secondary force of:

$$f_s = \frac{4EI k_b^3}{(1+j)} A_i \quad (2.14)$$

If this is applied, then the displacement of the beam upstream of the secondary force is given by:

$$\frac{w_-(x)}{A_i} = -\frac{e^{k_b x}}{(1+j)} + \frac{2\sin k_b x + e^{-j k_b x}}{(1+j)} \quad (2.15)$$

and the displacement of the beam downstream of the secondary force is given by:

$$\frac{w_+(x)}{A_i} = -\frac{e^{-k_b x}}{(1+j)} + \frac{e^{-j k_b x}}{(1+j)} \quad (2.16)$$

The displacement of the beam with this pinned condition imposed at the secondary force position is shown in **figure 2.3**. The pinned condition can clearly be seen at $x = 0$, and the amplitude of the propagating wave downstream of the actuator is $\sqrt{2}A_i$. The upstream wave is not now a pure standing wave as in the previous case, but two nearfield waves are again generated. It is unlikely that this

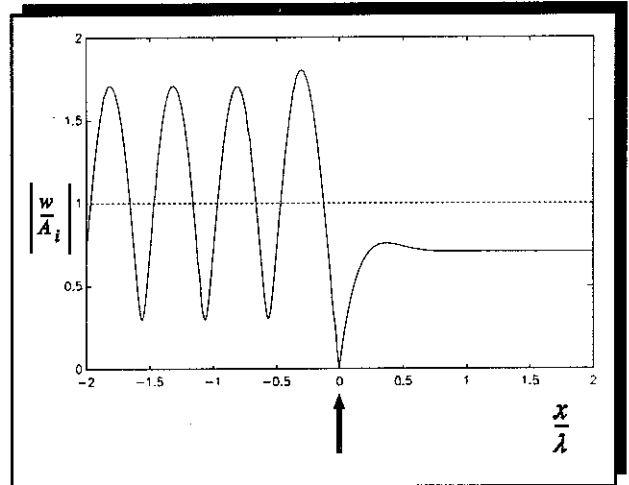


Figure 2.3 Displacement of an Infinite Beam with a Single Secondary Force Configured to Pin the Beam

control strategy would be deliberately used in practice but it can be unwittingly implemented. Execution of the wave suppression control strategy requires an error sensor downstream of the secondary force, positioned so that it does not sense the nearfield wave. At low frequencies, however, the nearfield wave decays over a large distance and it is thus likely to be measured by the error sensor, and the effect is

similar to that shown in **figure 2.3**. This means that there is a fundamental low frequency limit on the practical implementation of the wave suppression control strategy and this has been experimentally verified by Elliott and Billet [29].

2.2.4 Control Using Two Secondary Forces

The secondary array containing two secondary forces is shown in **figure 2.4**. When two secondary forces are applied, it is possible to suppress another wave in addition to the incident propagating wave. This can be either the negative-going propagating wave or one of the nearfield waves, and it is the suppression of these waves that is

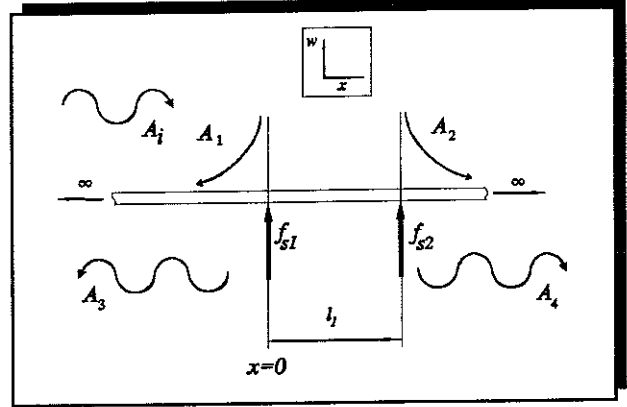


Figure 2.4 A Secondary Force Array with Two Actuators

considered in this section. The equations to determine the required secondary forces and the amplitudes of the waves generated for the various control strategies can be derived by partitioning the matrices in equations (2.2) - (2.8).

Case 2.1 Suppression of the Incident and Negative-Going Propagating Waves

The matrix equation describing the positive and negative-going propagating waves either side of the secondary force array is a partition of equation (2.6) and is given by:

$$\begin{bmatrix} A_3 \\ A_4 \end{bmatrix} = -\frac{1}{4EI k_b^3} \begin{bmatrix} j & j e^{-jk_b l_1} \\ j & j e^{jk_b l_1} \end{bmatrix} \begin{bmatrix} f_{s1} \\ f_{s2} \end{bmatrix} + \begin{bmatrix} 0 \\ A_i \end{bmatrix} \quad (2.17)$$

If both propagating waves are suppressed then A_3 and A_4 are set to zero, and equation (2.17) can be rearranged to give the required secondary forces:

$$\begin{bmatrix} f_{s1} \\ f_{s2} \end{bmatrix} = -4EI k_b^3 \begin{bmatrix} j & j e^{-jk_b l_1} \\ j & j e^{jk_b l_1} \end{bmatrix}^{-1} \begin{bmatrix} 0 \\ -A_i \end{bmatrix} \quad (2.18)$$

This expands to give:

$$f_{s1} = \frac{4EI k_b^3 e^{-jk_b l}}{2 \sin k_b l} A_i \quad (2.19)$$

and

$$f_{s2} = -\frac{4EI k_b^3}{2 \sin k_b l} A_i \quad (2.20)$$

The similarity should be noted between these equations and those resulting from the use of two loudspeakers to absorb an incident acoustic wave in a duct [12]. The wave amplitudes can be determined by substituting the secondary forces required into equations (2.2) - (2.5) and setting f_{s3} and f_{s4} to zero. The displacement of the beam can then be determined by substituting the wave amplitudes into equation (2.1)

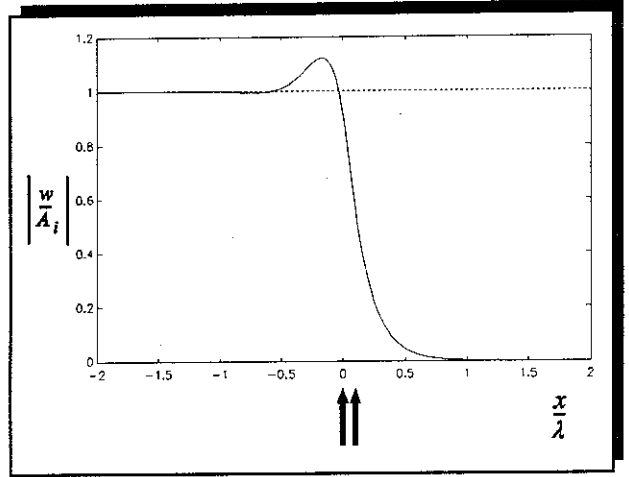


Figure 2.5 Displacement of an Infinite Beam with the Incident and Negative-Going Propagating Waves Suppressed using Two Forces. $l_1/\lambda = 0.1$

which is plotted in **figure 2.5** for the non-dimensionalised distance between the secondary forces of $l_1/\lambda = 0.1$, where λ is a wavelength of the incident propagating flexural wave. This figure shows that upstream of the secondary forces there is the incident propagating wave and a nearfield wave generated by the secondary forces. Downstream there is a nearfield wave only. Examination of the expressions for the secondary forces, equations (2.19) and (2.20), reveals that when the distance between the forces is an integer number of half-wavelengths of the incident propagating wave, then the forces required to suppress the incident propagating wave becomes infinite. This results in an infinite displacement of the beam. Clearly this cannot happen in

practice, as actuators have a finite force capacity and therefore the incident wave will not be suppressed. However, this analysis does show that there are frequencies when the incident and the negative-going propagating waves cannot both be suppressed, and that this is a function of the distance between the actuators.

Case 2.2 Use of Two Secondary Forces to Suppress the Incident Propagating Wave and One of the Nearfield Waves

If the incident propagating wave and the positive-going nearfield wave are to be suppressed, the appropriate matrix equation that describes the amplitudes of these waves is a partition of equation (2.6) and is given by:

$$\begin{bmatrix} A_2 \\ A_4 \end{bmatrix} = -\frac{1}{4EI k_b^3} \begin{bmatrix} 1 & e^{k_b l_1} \\ j & j e^{j k_b l_1} \end{bmatrix} \begin{bmatrix} f_{s1} \\ f_{s2} \end{bmatrix} + \begin{bmatrix} 0 \\ A_i \end{bmatrix} \quad (2.21)$$

Setting A_2 and A_4 to zero and rearranging this equation, gives the secondary forces required:

$$\begin{bmatrix} f_{s1} \\ f_{s2} \end{bmatrix} = -4EI k_b^3 \begin{bmatrix} 1 & e^{k_b l_1} \\ j & j e^{j k_b l_1} \end{bmatrix}^{-1} \begin{bmatrix} 0 \\ -A_i \end{bmatrix} \quad (2.22)$$

The wave amplitudes can be determined by substituting these secondary forces into equations (2.2) - (2.5) and setting f_{s3} and f_{s4} to zero. The displacement of the beam can then be determined by substituting the wave amplitudes into equation (2.1), which is plotted in figure 2.6 for the non-dimensionalised distance between the secondary forces of $l_1/\lambda = 0.1$.

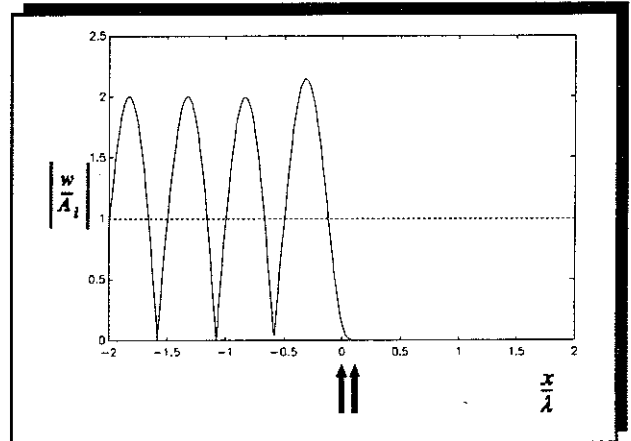


Figure 2.6 Displacement of an Infinite Beam with the Incident Propagating Wave and Positive-Going Nearfield Wave Suppressed using Two Forces. $l_1/\lambda = 0.1$

Examination of this figure shows that the incident propagating wave and the positive-

going nearfield wave have been suppressed. The resulting displacement of the beam upstream of the secondary force array is a standing wave with an amplitude which is twice that of the incident propagating wave, and a nearfield wave generated by the secondary forces. In this case the secondary forces are not infinitely large when the distance between the secondary forces is an integer number of half-wavelengths.

If the incident propagating wave and the negative-going nearfield wave are to be suppressed, the appropriate matrix equation is given by:

$$\begin{bmatrix} A_1 \\ A_4 \end{bmatrix} = -\frac{1}{4EI k_b^3} \begin{bmatrix} 1 & e^{-k_b l_1} \\ j & j e^{j k_b l_1} \end{bmatrix} \begin{bmatrix} f_{s1} \\ f_{s2} \end{bmatrix} + \begin{bmatrix} 0 \\ A_i \end{bmatrix} \quad (2.23)$$

and the secondary forces required to suppress these waves are given by:

$$\begin{bmatrix} f_{s1} \\ f_{s2} \end{bmatrix} = -4EI k_b^3 \begin{bmatrix} 1 & e^{-k_b l_1} \\ j & j e^{j k_b l_1} \end{bmatrix}^{-1} \begin{bmatrix} 0 \\ -A_i \end{bmatrix} \quad (2.24)$$

Again equations (2.2) - (2.3) can be used to determine the wave amplitudes and equation (2.1) used to determine the beam's displacement. This is plotted in **figure 2.7** for the non-dimensionalised distance between the secondary forces of $l_1/\lambda = 0.1$.

This figure should be compared with **figure 2.6** where it can be seen that the only difference is with the nearfield waves.

It was noted above, that when the incident and negative-going propagating waves are suppressed then the secondary forces required become very large at certain frequencies. However when the

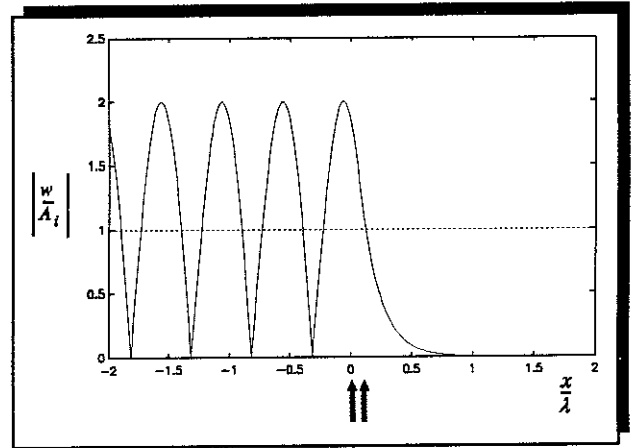


Figure 2.7 Displacement of an Infinite Beam with the Incident Propagating Wave and the Negative-Going Near-field Wave Suppressed using Two Forces. $l_1/\lambda = 0.1$

incident propagating wave and one of the nearfield waves are suppressed then this is not the case. To compare these two strategies, the secondary force requirements are

calculated. Referring to equation (2.9), it can be seen that the force required to generate a propagating wave is:

$$f_p = j4Ek^3 A_i \quad (2.25)$$

where f_p is termed the primary force. To quantify the secondary control effort required for each of the control strategies, the following relationship is determined as a function of non-dimensionalised distance (l_1/λ), between the secondary forces:

$$E = \frac{\sum_{n=1}^N |f_{sn}|^2}{|f_p|^2} \quad (2.26)$$

where E is defined as the secondary force effort normalised to the primary force and N is the number of secondary forces applied. When a propagating wave is suppressed

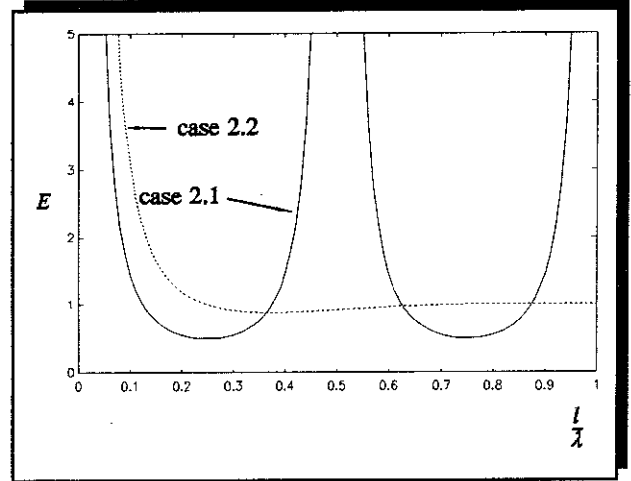


Figure 2.8 Secondary Force Effort for Cases 2.1 and 2.2 as a Function of Non-dimensionalised Distance between the Secondary Forces

using a single secondary force, the magnitude of that secondary force f_s , is equal to the magnitude of the primary force f_p , so that $E = 1$. The graph of E as a function of non-dimensionalised distance between the secondary forces is plotted in **figure 2.8** and tabulated in **Table 2.1** for the case when two secondary forces are applied ($l = l_1$). It can be seen that provided the distance between the secondary forces is less than a quarter of a wavelength, the secondary force required in both cases increases as the distance between the secondary forces is reduced. The minimum effort required is in case 2.1 when both propagating waves are suppressed; it reaches a minimum value of 0.5 when distance between the secondary forces is an odd integer number of quarter wavelengths. However, as discussed above, it goes to infinity (with no damping included in the beam) when the distance between the secondary forces is an integer number of half-wavelengths of the incident propagating wave. In case 2.2, when the incident propagating wave and one of the nearfield waves are suppressed, this is not the case, and the secondary effort levels off at unity when the

distance between the secondary forces is greater than half a wavelength. This is because the solution is then similar to when only one secondary force is applied.

CASES	DISTANCE BETWEEN THE TWO SECONDARY FORCE ACTUATORS					
	0.1λ	0.25λ	0.5λ	0.7λ	0.9λ	1λ
2.1	1.45	0.5	∞	0.55	1.45	∞
2.2	3.05	1	0.92	0.99	1	1

Table 2.1 The Secondary Effort E , Required for the Different Control Strategies for Various Distances between the Two Secondary Forces

2.2.5 Control Using Three Secondary Forces

The use of three secondary forces is now considered, and the secondary force array is shown in **figure 2.9**. When three secondary forces are applied, it is possible to suppress two other waves in addition to the incident propagating wave. Again, the expressions for the secondary forces required and the wave amplitudes generated can be determined by partitioning the matrices in equations (2.2) - (2.8).

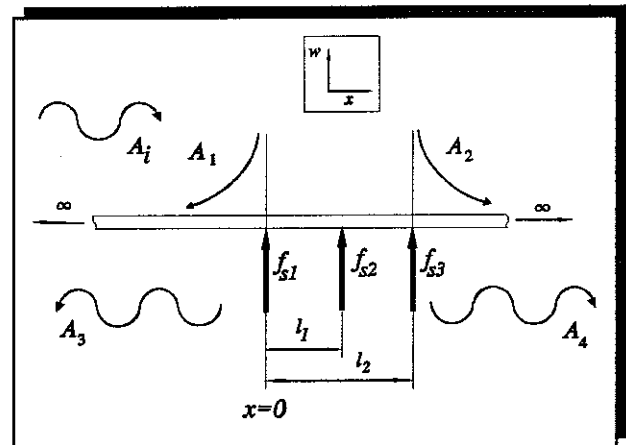


Figure 2.9 Secondary Force Array with Three Actuators

Case 3.1 Use of Three Secondary Forces to Suppress the Incident and Negative-Going Propagating Waves, and one of the NearField Waves

The matrix equation describing both propagating waves and the positive-going nearfield wave outside of the array is a partition of equation (2.6) and is given by:

$$\begin{bmatrix} A_2 \\ A_3 \\ A_4 \end{bmatrix} = -\frac{1}{4EIk_b^3} \begin{bmatrix} 1 & e^{k_b l_1} & e^{k_b l_2} \\ j & j e^{-jk_b l_1} & j e^{-jk_b l_2} \\ j & j e^{jk_b l_1} & j e^{jk_b l_2} \end{bmatrix} \begin{bmatrix} f_{s1} \\ f_{s2} \\ f_{s3} \end{bmatrix} + \begin{bmatrix} 0 \\ 0 \\ A_i \end{bmatrix} \quad (2.27)$$

If the waves are set to zero, equation (2.27) can be rearranged to give the secondary forces required:

$$\begin{bmatrix} f_{s1} \\ f_{s2} \\ f_{s3} \end{bmatrix} = -4EIk_b^3 \begin{bmatrix} 1 & e^{k_b l_1} & e^{k_b l_2} \\ j & j e^{-jk_b l_1} & j e^{-jk_b l_2} \\ j & j e^{jk_b l_1} & j e^{jk_b l_2} \end{bmatrix}^{-1} \begin{bmatrix} 0 \\ 0 \\ -A_i \end{bmatrix} \quad (2.28)$$

By putting $f_{s4} = 0$, equations (2.2) - (2.5) can be used to determine the wave amplitudes in the various sections of the beam and equation (2.1) used to determine the beam's displacement. This is plotted in **figure 2.10** for the non-dimensionalised distance between each of the secondary forces of $l/\lambda = 0.1$. Referring to **figure 2.9**, $l_2 = 2l_1$, so that the secondary forces are equally spaced. Examination of

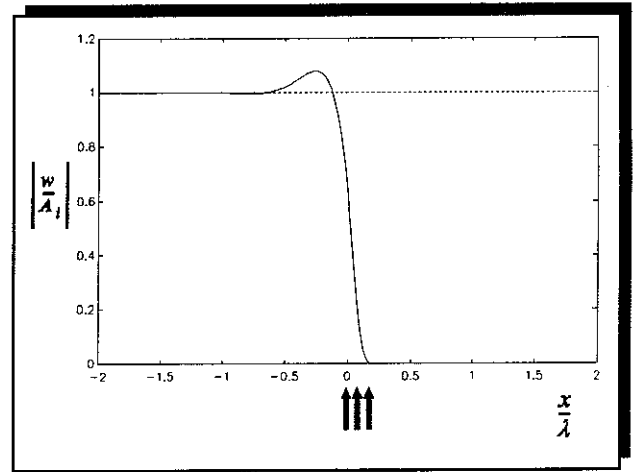
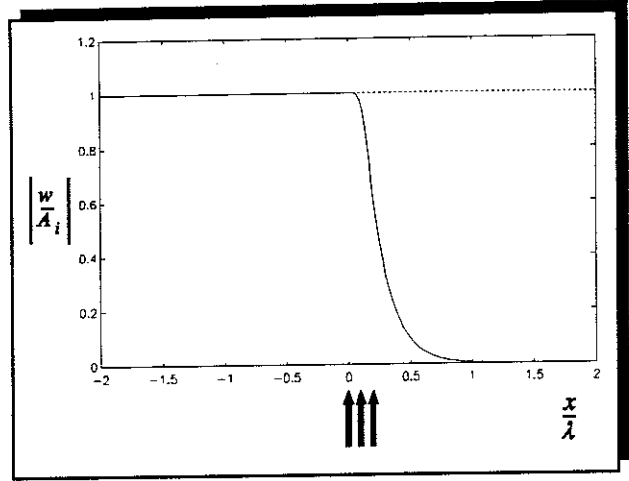


Figure 2.10 Displacement of an Infinite Beam with Both Propagating Waves and the Positive Going Nearfield Wave Suppressed using Three Forces. $l/\lambda = 0.1$

figure 2.10 shows that the resulting displacement of the beam is very similar to that in case 2.1, but in this case the positive-going nearfield wave generated by the

secondary force array is additionally suppressed. Again the secondary forces required are infinite when the distance between them is an integer number of half-wavelengths of the incident propagating wave.



If the negative-going nearfield wave is suppressed instead of the positive-going nearfield wave, a similar way of calculating the

Figure 2.11 Displacement of an Infinite Beam with Both Propagating Waves and the Negative-Going Nearfield Wave Suppressed using Three Forces. $l/\lambda = 0.1$

secondary forces can be employed to that discussed above, and the resulting displacement of the beam is plotted in **figure 2.11**. Comparing this figure with **Figure 2.10**, it can be seen that the displacements of the beam are very similar, the only difference being the nearfield waves.

Case 3.2 Use of Three Secondary Forces to Suppress the Incident Propagating Wave and the Positive and Negative-Going Nearfield Waves

Although the suppression of this combination of wave types is an unlikely control strategy it is included for completeness. As before, equation (2.6) can be partitioned to describe the amplitudes of the waves either side of the secondary force array to give:

$$\begin{bmatrix} A_1 \\ A_2 \\ A_4 \end{bmatrix} = -\frac{1}{4EI k_b^3} \begin{bmatrix} 1 & e^{-k_b l_1} & e^{-k_b l_2} \\ 1 & e^{k_b l_1} & e^{k_b l_2} \\ j & j e^{j k_b l_1} & j e^{j k_b l_2} \end{bmatrix} \begin{bmatrix} f_{s1} \\ f_{s2} \\ f_{s3} \end{bmatrix} + \begin{bmatrix} 0 \\ 0 \\ A_i \end{bmatrix} \quad (2.29)$$

The secondary forces required to suppress these waves are thus given by:

$$\begin{bmatrix} f_{s1} \\ f_{s2} \\ f_{s3} \end{bmatrix} = -4EI k_b^3 \begin{bmatrix} 1 & e^{-k_b l_1} & e^{-k_b l_2} \\ 1 & e^{k_b l_1} & e^{k_b l_2} \\ j & j e^{j k_b l_1} & j e^{j k_b l_2} \end{bmatrix}^{-1} \begin{bmatrix} 0 \\ 0 \\ -A_i \end{bmatrix} \quad (2.30)$$

By putting $f_{s4} = 0$, equations (2.2) - (2.5) can be used to determine the wave amplitudes in the various sections of the beam, and equation (2.1) used to determine the beam's displacement. This is plotted in **figure 2.12** for the non-dimensionalised distance between each of the secondary forces of l/λ 0.1. Examination of this figure shows that the resulting displacement of the beam is very similar to case 2.2 (**figures 2.6 and 2.7**), but in this case both the nearfield waves have been suppressed. As with case 2.2, the secondary forces required are not infinitely large when the distance between the secondary forces is an integer number of half-wavelengths. The secondary force effort as a function of the non-dimensionalised distance between the secondary forces is calculated using equation (2.26), and is plotted in **figure 2.13** and tabulated in **Table 2.2**. It can be seen that provided the distance between the secondary forces is less than a quarter of a wavelength, the effort required in both cases increases as the distance between the secondary forces is reduced.

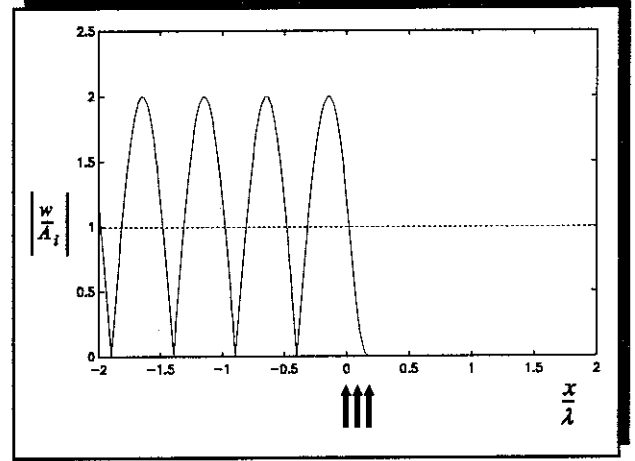


Figure 2.12 Displacement of an Infinite Beam with the Incident Propagating Wave and Both Nearfield Waves Suppressed using Three Forces. $l/\lambda = 0.1$

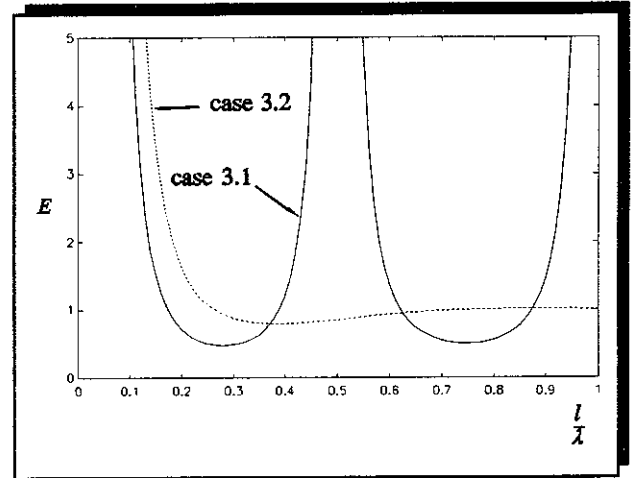


Figure 2.13 Secondary Force Effort for Cases 3.1, 3.2 as a Function of Non-dimensionalised Distance between the Secondary Forces

CASES	DISTANCE BETWEEN EACH OF THE THREE SECONDARY FORCE ACTUATORS						
	0.1λ	0.25λ	0.28λ	0.5λ	0.7λ	0.9λ	1λ
3.1	5.89	0.5	0.47	∞	0.55	1.46	∞
3.2	12.5	1.08	0.94	0.85	0.96	1.01	1

Table 2.2 The Secondary Effort E , Required for the Different Control Strategies for Various Distances between the Three Secondary Forces

The minimum effort required is in case 3.1 when both propagating waves are suppressed. It reaches a minimum value of just below 0.5 when the non-dimensionalised distance between the secondary forces is between 0.25 and 0.3 (approx 0.28). However, as discussed above, it becomes infinite (with no damping included in the beam) when the distance between the secondary forces is an integer number of half-wavelengths of the incident propagating wave. In case 3.2, when the incident propagating wave and both nearfield waves are suppressed, this is not the case and the effort levels off at unity when the distance between the secondary forces is greater than about half a wavelength.

2.2.6 Control Using Four Secondary Forces

As discussed by Scheuren [27], when four secondary forces are applied as shown in **figure 2.1**, the incident propagating wave is suppressed, and no waves are generated outside the secondary force array. The forces required can be calculated using equation (2.8), the wave amplitudes using equations (2.2)-(2.5) and the beam's displacement with equation (2.1). This is plotted in **figure 2.14** for the non-dimensionalised distance between each of the secondary forces of $l/\lambda = 0.1$.

The secondary force effort required to suppress all the waves is calculated using equation (2.26) and is plotted in **figure 2.15** together with the effort required in cases 2.1 and 3.1 for comparison. The secondary effort is also tabulated in **Table 2.3**. It

can be seen that provided the distance between the secondary forces is less than a quarter of a wavelength, the effort required in all cases increases as the distance between the secondary forces is reduced. It should be noted, however, that a greater number of forces considerably increases the total effort required for a given distance between the forces in the array provided this distance is less than about a quarter of a wavelength. As the distance between the forces approaches zero, or an integer number of half-wavelengths, then the forces required become prohibitively large. The minimum effort required in each case reaches a minimum value of approximately 0.5 when the non-dimensionalised distance between the secondary forces is between 0.25 and 0.3 (Tables 2.1, 2.2 and 2.3).

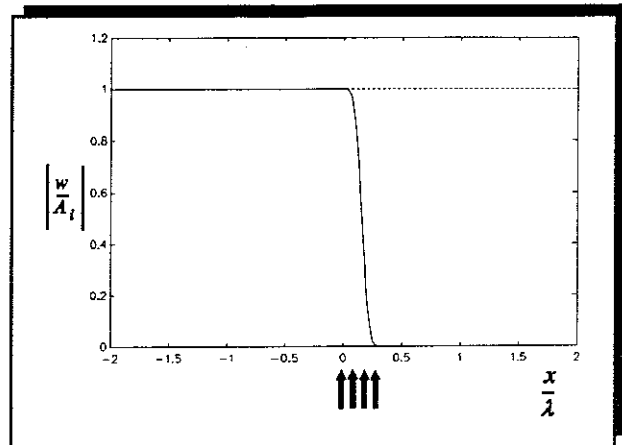


Figure 2.14 Displacement of an Infinite Beam with the Incident Propagating Wave, the Negative-Going Propagating Wave and both Nearfield Waves Suppressed using Four Forces. $l/\lambda = 0.1$

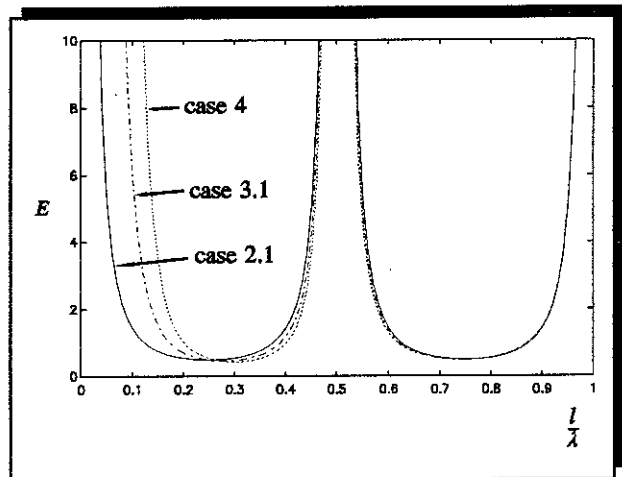


Figure 2.15 Secondary Force Effort for Cases 2.1, 3.1 and 4 as a Function of Non-dimensionalised Distance between the Secondary Forces

CASE	DISTANCE BETWEEN EACH OF THE FOUR SECONDARY FORCE ACTUATORS						
	0.1λ	0.25λ	0.3λ	0.5λ	0.7λ	0.9λ	1λ
4	27.13	0.54	0.44	∞	0.54	1.47	∞

Table 2.3 The Secondary Effort E , Required for Various Distances between the Four Secondary Forces

If the secondary forces are spaced non-uniformly, the propagating and nearfield waves can still be suppressed in a similar manner to that described in this chapter, however the maximum and minimum effort E , will occur at different frequencies, as the secondary effort is a function of the spacing of the forces.

2.3 Control of Flexural Waves Using Line Moments

2.3.1 Introduction

In the previous section it was shown that point forces can be applied to a beam to suppress a propagating flexural wave. Line moments can also be used as secondary sources, and can be positioned in a secondary array similar to the forces. Although moment actuators are not commercially available at present, the suppression of a propagating flexural wave using moments is considered in this section for the sake of completeness. However, a detailed analysis is not undertaken, but a model of the secondary array and computer simulations are presented that show that line moments can control the motion of the beam in a similar way to point forces.

2.3.2 Model of the Secondary Moment Array

The general arrangement of the secondary moment array is shown in **figure 2.16**. Each moment generates four waves in a similar way to a point force, and the magnitude and phase of these waves per unit applied moment is given in Appendix 2. As with the force array, these waves combine to generate the A_1 and A_2 nearfield

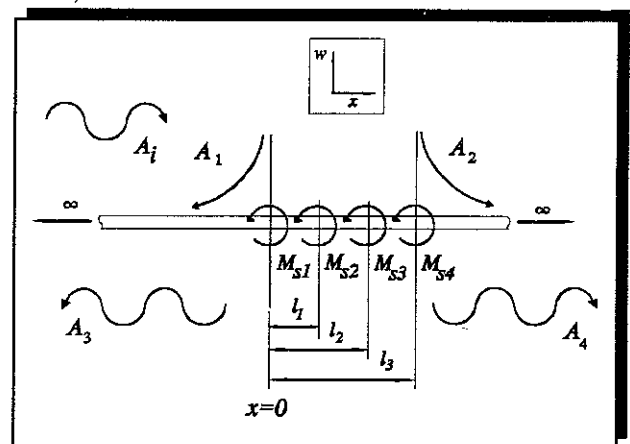


Figure 2.16 A Secondary Moment Array on an Infinite Beam

waves and the A_3 and A_4 propagating waves outside the array. The relationship

between these waves and the moments (including the incident propagating wave) is given by:

$$\begin{bmatrix} A_1 \\ A_2 \\ A_3 \\ A_4 \end{bmatrix} = \frac{1}{4EI k_b^2} \begin{bmatrix} 1 & e^{-k_b l_1} & e^{-k_b l_2} & e^{-k_b l_3} \\ -1 & -e^{k_b l_1} & -e^{k_b l_2} & -e^{k_b l_3} \\ -1 & -e^{-jk_b l_1} & -e^{-jk_b l_2} & -e^{-jk_b l_3} \\ 1 & e^{jk_b l_1} & e^{jk_b l_2} & e^{jk_b l_3} \end{bmatrix} \begin{bmatrix} M_{s1} \\ M_{s2} \\ M_{s3} \\ M_{s4} \end{bmatrix} + \begin{bmatrix} 0 \\ 0 \\ 0 \\ A_i \end{bmatrix} \quad (2.31)$$

As with the secondary force array, the amplitudes of the waves within the moment array may be calculated; in this case by modifying equation (2.31) to give equations similar to (2.3) - (2.5). If all four waves are to be suppressed then these waves can be set to zero in equation (2.31), which can then be rearranged to give the secondary moments required:

$$\begin{bmatrix} M_{s1} \\ M_{s2} \\ M_{s3} \\ M_{s4} \end{bmatrix} = 4EI k_b^2 \begin{bmatrix} 1 & e^{-k_b l_1} & e^{-k_b l_2} & e^{-k_b l_3} \\ -1 & -e^{k_b l_1} & -e^{k_b l_2} & -e^{k_b l_3} \\ -1 & -e^{-jk_b l_1} & -e^{-jk_b l_2} & -e^{-jk_b l_3} \\ 1 & e^{jk_b l_1} & e^{jk_b l_2} & e^{jk_b l_3} \end{bmatrix}^{-1} \begin{bmatrix} 0 \\ 0 \\ 0 \\ -A_i \end{bmatrix} \quad (2.32)$$

This equation can be reduced in size depending on how many secondary moments are applied.

2.3.3 Control Using a Single Secondary Moment

If only one secondary moment is used to suppress the incident propagating wave, equation (2.32) reduces to:

$$M_s = -4EI k_b^2 A_i \quad (2.33)$$

If this moment is applied to the beam, the resulting displacement normalised to the amplitude of the incident wave is plotted in **figure 2.17**. It can be seen that, as in the case of the single secondary force, if the incident propagating wave is suppressed, then there is a standing wave upstream of the secondary moment and a nearfield wave either side. As with a single secondary force, when a secondary moment is applied,

it is possible to adopt a different strategy rather than reducing the far-field downstream displacement to zero. When a force is applied, the beam can be pinned at the secondary force position, as discussed in the previous section. However, when a moment is applied, it is possible to bring the slope of the beam to zero at the position where the secondary moment is applied, as shown in **figure 2.18**. The secondary moment required is given by the equation [31]:

$$M_s = \frac{j4EI k_b^2}{1 - j} A_i \quad (2.34)$$

Figure 2.18 shows that although the slope of the beam is zero at $x = 0$, the displacement downstream is not zero but $\sqrt{2}A_i$, as in the case when a single secondary force is applied to pin the beam. The displacement upstream of the secondary moment is a partial standing wave. When this strategy is adopted, the secondary moment actuator acts like a very stiff rotary spring and the power transmitted along the beam is reduced by 50%. This is because the power transmitted by the bending moment is brought to zero at this point, but the power transmitted by the shear force is unaffected.

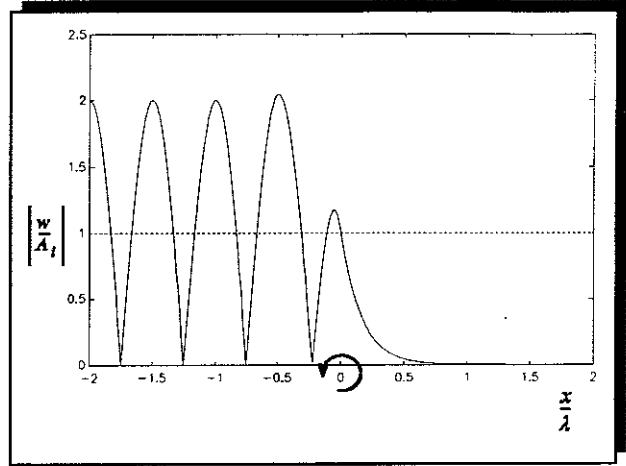


Figure 2.17 Displacement of an Infinite Beam with a Single Secondary Moment Applied to Suppress a Propagating Wave

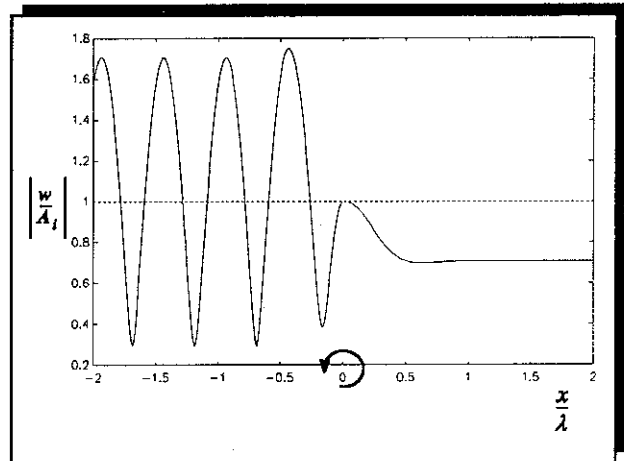


Figure 2.18 Displacement of an Infinite Beam with a Single Secondary Moment Applied to give Zero Slope at the Secondary Moment Position

2.3.4 Control Using Two Secondary Moments

If two secondary moments are applied, another wave can be suppressed in addition to the incident propagating wave. This can be the negative-going propagating wave, or one of the positive-going or negative-going nearfield waves. The displacements of the beam for these three cases are shown in **figures 2.19 - 2.21** respectively. These cases are very similar to when two forces are applied and should be compared with **figures 2.5 - 2.7**.

The secondary effort required when using moments can be calculated in a similar manner to the secondary effort when forces are used. However in this case the effort is defined as:

$$E = \frac{\sum_{n=1}^N |M_{sn}|^2}{|M_p|^2} \quad (2.35)$$

where M_p is the moment required to generate the incident propagating wave and is given by [31]:

$$M_p = -4EI k_b^2 A_i \quad (2.36)$$

When moments are used, the secondary effort is *identical* to the effort when forces are used, which is plotted in **figure 2.8** and tabulated in **Table 2.1**.

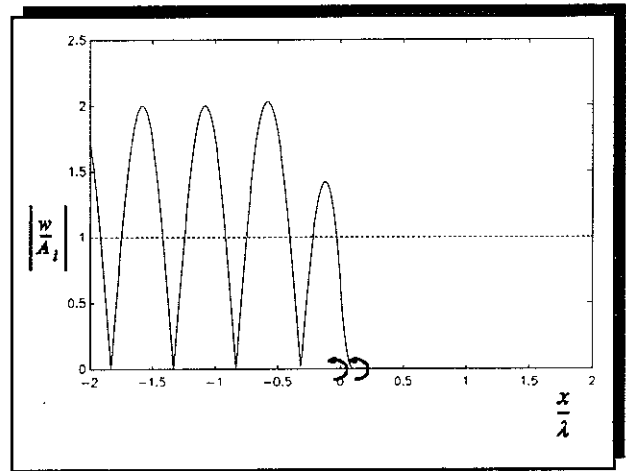


Figure 2.19 Displacement of an Infinite Beam with the Incident and Negative-Going Propagating Waves Suppressed using Two Moments. $l_1/\lambda = 0.1$

Figure 2.20 Displacement of an Infinite Beam with the Incident Propagating Wave and Positive-Going Nearfield Wave Suppressed using Two Moments. $l_1/\lambda = 0.1$

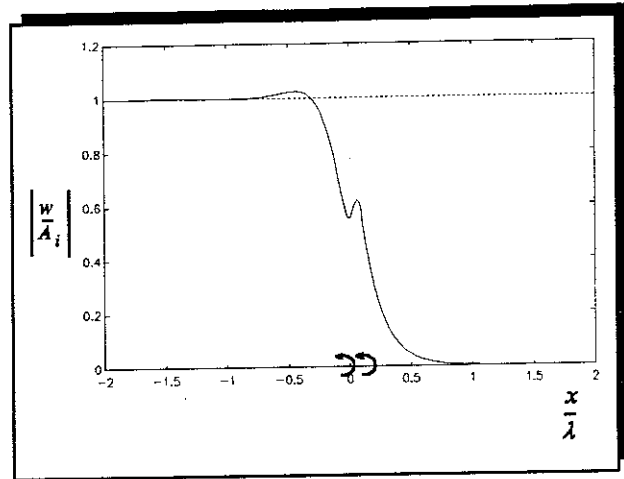
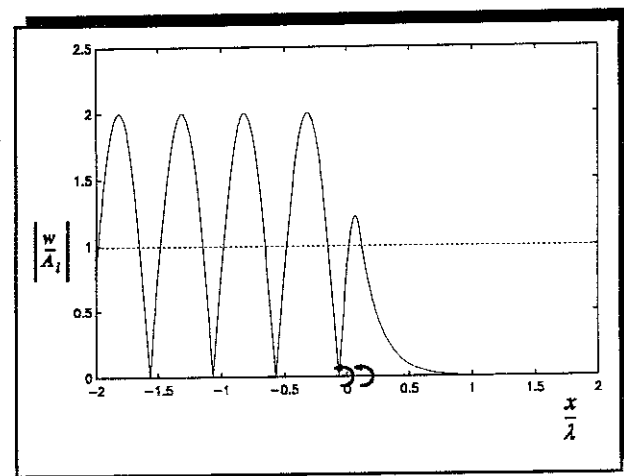


Figure 2.21 Displacement of an Infinite Beam with the Incident Propagating Wave and the Negative-Going Nearfield Wave Suppressed using Two Moments. $l_1/\lambda = 0.1$



2.3.5 Control Using Three Secondary Moments

If three secondary moments are applied, then two other waves can be suppressed in addition to the incident propagating wave. The displacement of the beam when these control moments are positioned one tenth of a wavelength apart, are shown for the three possible control strategies in **figures 2.22 - 2.24**.

The displacements of the beam shown in **figures 2.22 - 2.24** are similar to when three forces are applied, except within the secondary array, and should be compared with **figures 2.10 - 2.12**. The secondary effort can be calculated using equation (2.35), and this is identical to when three forces are applied which is plotted in **figure 2.13** and tabulated in **Table 2.2**.

Figure 2.22 Displacement of an Infinite Beam with Both Propagating Waves and the Positive Going Nearfield Wave Suppressed using Three Moments. $l/\lambda = 0.1$

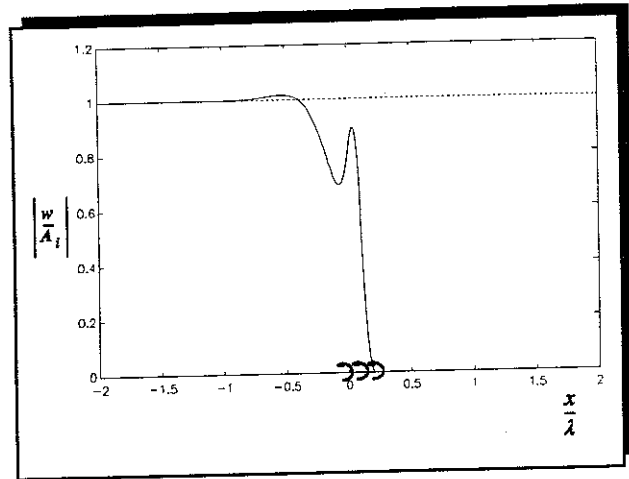


Figure 2.23 Displacement of an Infinite Beam with Both Propagating Waves and the Negative-Going Nearfield Wave Suppressed using Three Moments. $l/\lambda = 0.1$

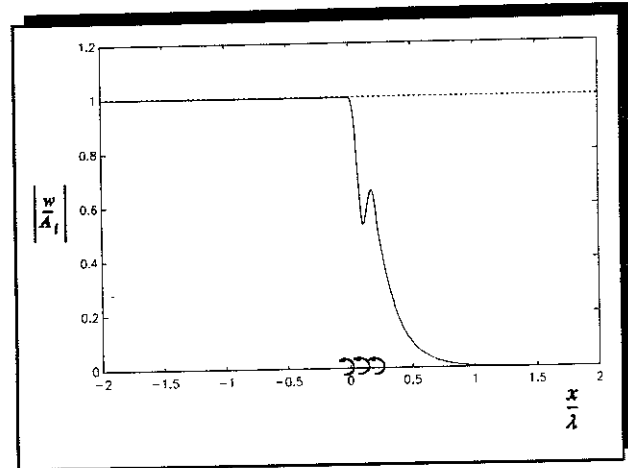
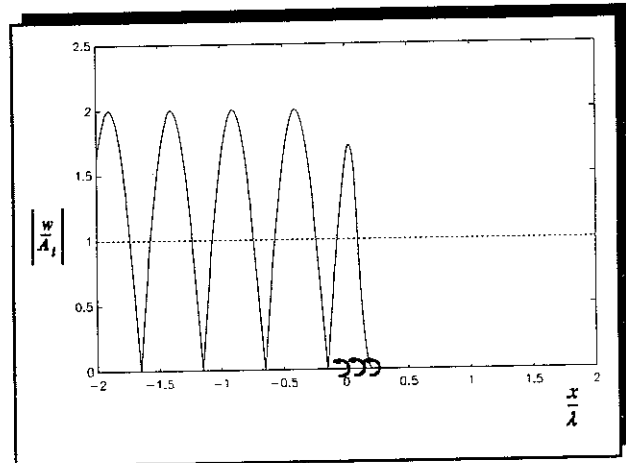


Figure 2.24 Displacement of an Infinite Beam with the Incident Propagating Wave and Both Nearfield Waves Suppressed using Three Moments. $l/\lambda = 0.1$



2.3.6 Control Using Four Secondary Moments

As mentioned previously, if four moments are applied then all the waves can be suppressed. The secondary moments required in this case are given by equation

(2.32), and the displacement of the beam when these are applied is shown in **figure 2.25**. This differs from the case when four forces are applied in that the displacement of the beam within the array has increased under the action of the secondary moments. The secondary effort calculated using equation (2.35) is exactly the same as that calculated for four forces, which is plotted in **figure 2.5** and tabulated in **Table 2.3**.

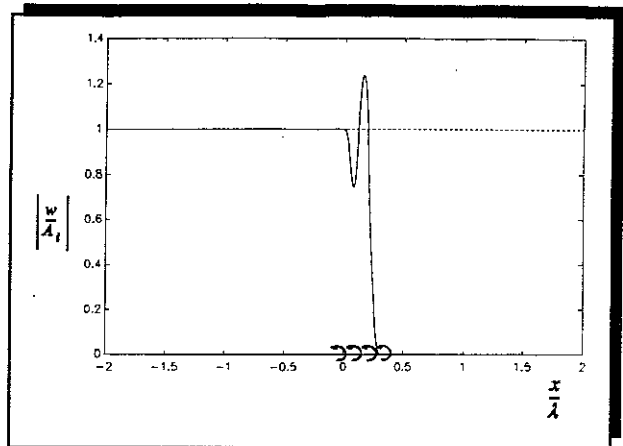


Figure 2.25 Displacement of an Infinite Beam with the Incident Propagating Wave, the Negative-Going Propagating Wave and both Nearfield Waves Suppressed using Four Moments. $l/\lambda = 0.1$

2.4 Control of Flexural Waves Using Moment-Pairs

2.4.1 Introduction

An actuator that has potential for use as a secondary source in the active control of waves on a beam is a piezoceramic (PZT) actuator, which is discussed in detail in Chapter 4. In this section the actuator is incorporated into an array in the same way as the force and moment actuators discussed previously.

2.4.2 Model of the Secondary Moment-Pair Array

A PZT actuator applies moments at the ends of the actuator [32], and when four of them are positioned in array they can be modelled as shown in **figure 2.26**. Each actuator has length d and generates four waves that decay or propagate away from the actuator. When an array of four of these is considered, the model is quite complex. To simplify the model, the length of each of the actuators is taken to be small compared to a flexural wavelength as discussed in Appendix 2, and thus the moments

are deemed to act along a line. The relationship between the A_1 and A_2 nearfield waves, the A_3 and A_4 propagating waves outside the array and the moment-pairs (including the incident propagating wave) is given by:

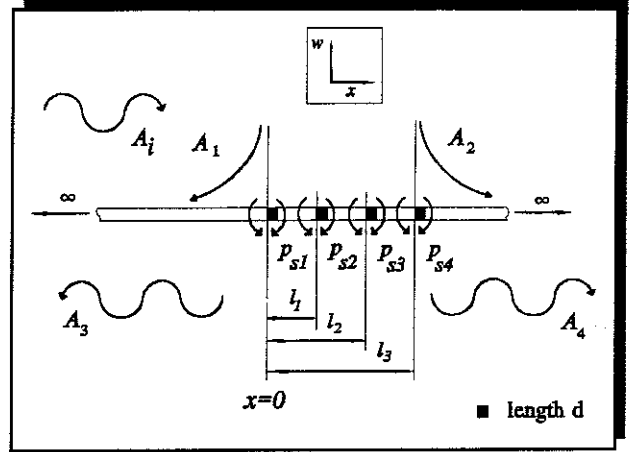


Figure 2.26 A Secondary Moment-Pair Array on an Infinite Beam

$$\begin{bmatrix} A_1 \\ A_2 \\ A_3 \\ A_4 \end{bmatrix} = \frac{1}{4EI k_b} \begin{bmatrix} 1 & e^{-k_b l_1} & e^{-k_b l_2} & e^{-k_b l_3} \\ 1 & e^{k_b l_1} & e^{k_b l_2} & e^{k_b l_3} \\ -j & -j e^{-j k_b l_1} & -j e^{-j k_b l_2} & -j e^{-j k_b l_3} \\ -j & -j e^{j k_b l_1} & -j e^{j k_b l_2} & -j e^{j k_b l_3} \end{bmatrix} \begin{bmatrix} P_{s1} \\ P_{s2} \\ P_{s3} \\ P_{s4} \end{bmatrix} + \begin{bmatrix} 0 \\ 0 \\ 0 \\ A_i \end{bmatrix} \quad (2.37)$$

where P , a moment-pair is equal to an applied moment M , multiplied by the length of the actuator d . As with the secondary force and moment arrays, the amplitudes of the waves within the moment-pair array may be calculated; in this case by modifying equation (2.37) to give equations similar to (2.3) - (2.5). If all four waves are to be suppressed then these waves can be set to zero in equation (2.37), which can then be rearranged to give the secondary moment-pairs required:

$$\begin{bmatrix} P_{s1} \\ P_{s2} \\ P_{s3} \\ P_{s4} \end{bmatrix} = 4EI k_b \begin{bmatrix} 1 & e^{-k_b l_1} & e^{-k_b l_2} & e^{-k_b l_3} \\ 1 & e^{k_b l_1} & e^{k_b l_2} & e^{k_b l_3} \\ -j & -j e^{-j k_b l_1} & -j e^{-j k_b l_2} & -j e^{-j k_b l_3} \\ -j & -j e^{j k_b l_1} & -j e^{j k_b l_2} & -j e^{j k_b l_3} \end{bmatrix}^{-1} \begin{bmatrix} 0 \\ 0 \\ 0 \\ -A_i \end{bmatrix} \quad (2.38)$$

This matrix equation can be reduced in size depending on how many secondary moment-pairs are generated and as before all the possible cases are considered.

2.4.3 Control Using a Single Secondary Moment-Pair

If only one secondary moment-pair is used to suppress the incident propagating wave, equation (2.38) reduces to:

$$P_s = j4EI k_b A_i \quad (2.39)$$

When this moment-pair is applied to the beam, the resulting displacement is shown in figure 2.27. It can be seen that, as in the cases of the single secondary force

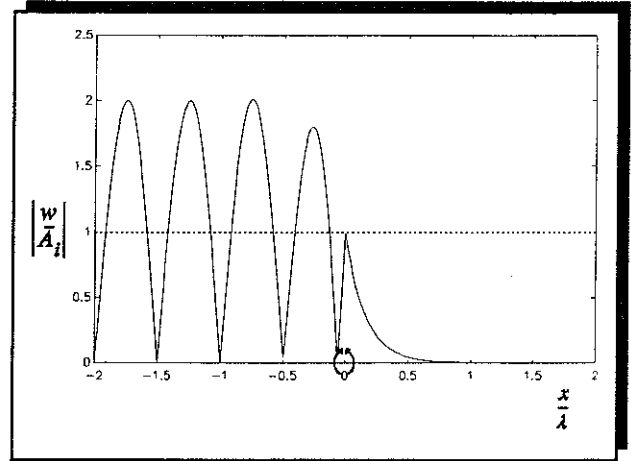


Figure 2.27 Displacement of an Infinite Beam with a Single Secondary Moment-Pair Applied

and moment, the incident propagating wave is effectively reflected, resulting in a standing wave upstream of the secondary moment-pair. A discontinuity in transverse displacement and slope of the beam is evident at $x = 0$. This occurs because of the low frequency approximation that the length of the actuator is small compared to a flexural wavelength. Thus, the model does not contain any information about the displacement of the section of beam underneath the actuator. Physically these discontinuities cannot exist, but the displacement of the beam predicted by the model in the far-field should be representative of a real beam fitted with moment-pair actuators.

2.4.4 Control Using Two Secondary Moment-Pairs

As with the forces and moments, three control strategies are possible when two secondary moment-pairs are applied to the beam. The displacements of the beam when these control sources are positioned one tenth of a wavelength apart, are shown for the three possible control strategies in figures 2.28 - 2.30.

Figure 2.28 Displacement of an Infinite Beam with the Incident Propagating Wave and Positive-Going 'Nearfield' Wave Suppressed using Two Moment-Pairs. $l_i/\lambda = 0.1$

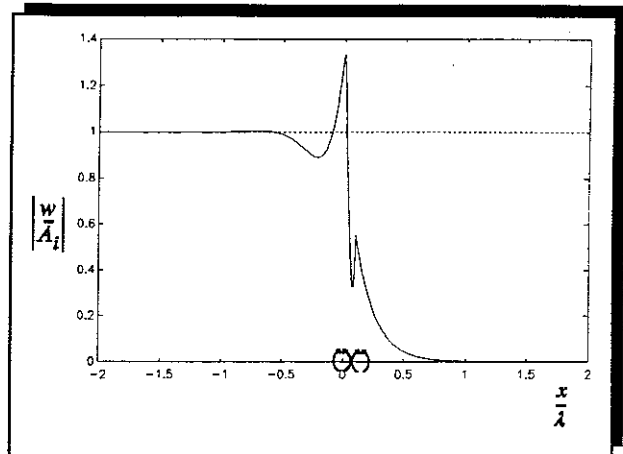


Figure 2.29 Displacement of an Infinite Beam with the Incident Propagating Wave and Positive-Going Nearfield Wave Suppressed using Two Moment-Pairs. $l_i/\lambda = 0.1$

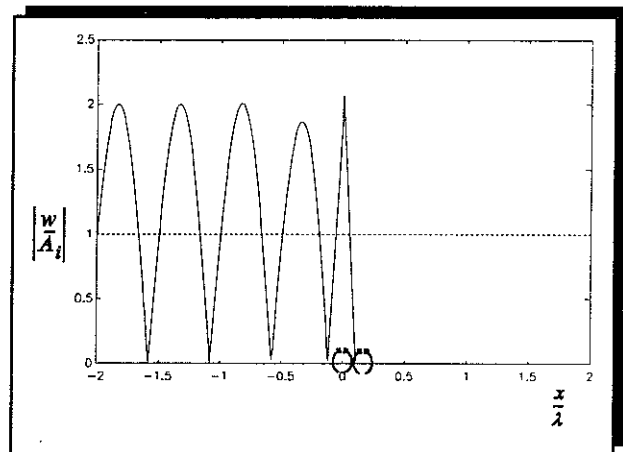
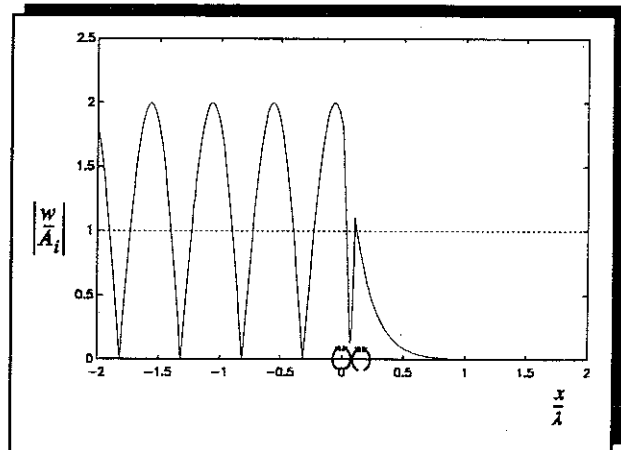


Figure 2.30 Displacement of an Infinite Beam with the Incident Propagating Wave and the Negative-Going Nearfield Wave Suppressed using Two Moment-Pairs. $l_i/\lambda = 0.1$



2.4.5 Control Using Three Secondary Moment-Pairs

As before, three control strategies are possible when three secondary sources are applied to the beam. The displacements of the beam when three moment-pairs are

positioned one tenth of a wavelength apart, are shown for the three possible control strategies in **figures 2.31 - 2.33**.

Figure 2.31 Displacement of an Infinite Beam with Both Propagating Waves and the Positive Going Nearfield Wave Suppressed using Three Moment-Pairs. $l/\lambda = 0.1$

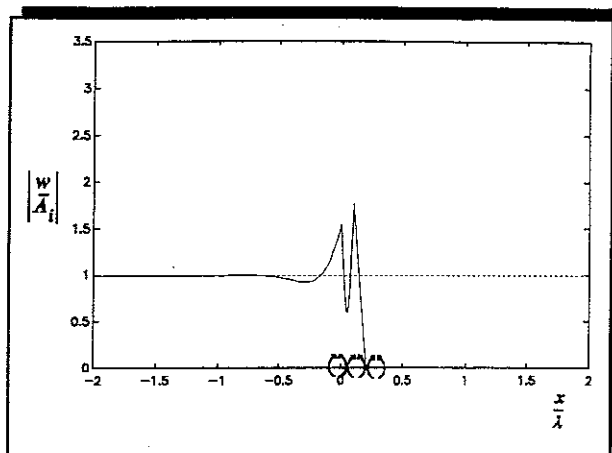


Figure 2.32 Displacement of an Infinite Beam with Both Propagating Waves and the Negative-Going Nearfield Wave Suppressed using Three Moment-Pairs. $l/\lambda = 0.1$

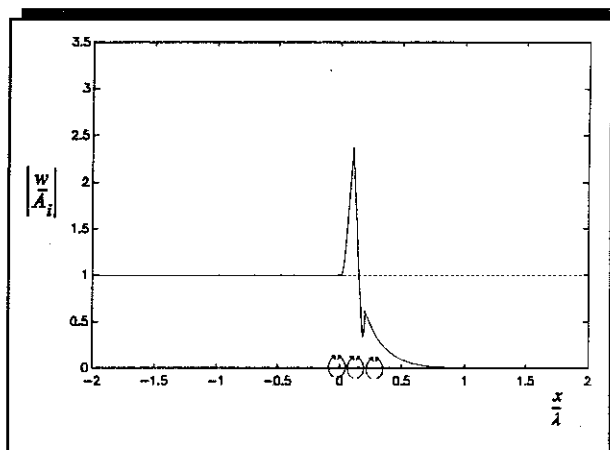
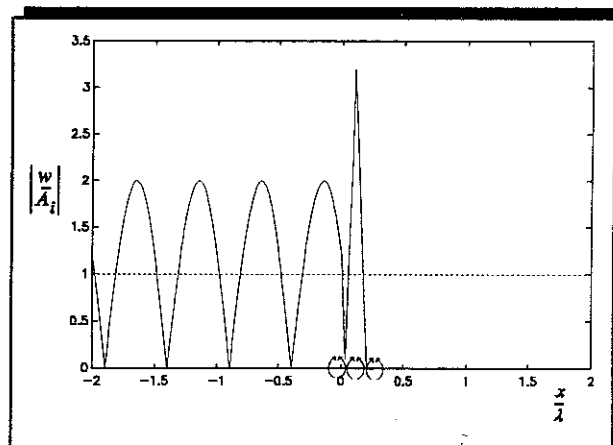


Figure 2.33 Displacement of an Infinite Beam with the Incident Propagating Wave and Both Nearfield Waves Suppressed using Three Moment-Pairs. $l/\lambda = 0.1$



2.4.6 Control Using Four Secondary Moment-Pairs

As mentioned previously, if four secondary sources are applied then all the waves can be suppressed. The secondary moment-pairs required in this case are given by equation (2.38), and the displacement of the beam when these are applied is shown in figure 2.34.

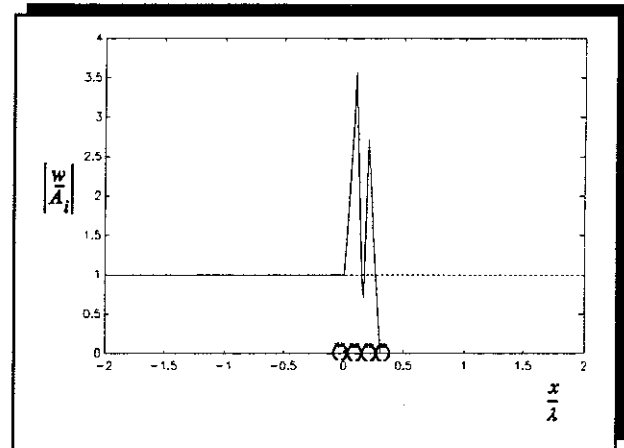


Figure 2.34 Displacement of an Infinite Beam with the Incident Propagating Wave, the Negative-Going Propagating Wave and both Nearfield Waves Suppressed using Four Moment-Pairs. $l/\lambda = 0.1$

2.4.7 Discussion

It can be seen that when two or more moment-pairs are applied, then the amplitude of vibration within the secondary array generally increases by a substantial amount. It is observed that this also increases with the number of actuators. Although the required displacement outside the actuator array can be achieved using the moment-pair actuators, the displacement within the actuator array is much more complicated than if moments or forces are applied. This is because the actuators induce a change in the curvature of the beam rather than the displacement directly. The secondary effort for all the cases considered is identical to the effort calculated for the corresponding control strategies for forces and moments discussed previously.

2.5 Active Control of Flexural Waves using Minimum Effort

The strategies for controlling flexural waves on a beam discussed so far involve suppression of as many waves as there are secondary sources. Another strategy for the control of flexural waves on a beam is the suppression of a single propagating wave using minimum effort. It has been shown previously that the effort required for wave suppression is dependent upon the number and spacing of the secondary sources. In this section, a theoretical analysis is conducted into wave suppression using minimum effort where forces are used as secondary sources. The author has also conducted the same analysis using moments and moment-pairs as secondary sources [31], and similar results were obtained. This control strategy poses a constrained optimisation problem such as that discussed in general optimisation textbooks, for example [33]. The method of solving such a problem involves the use of the Lagrange function. This is the sum of the objective function, which in this case is the sum of the squares of the secondary forces, and the product of the Lagrange multiplier μ , with the imposed constraint.

2.5.1 Implementation on an Infinite Beam

Consider a secondary force array with N forces positioned at $x = 0$, l_2, \dots, l_N on the beam as shown in figure 2.35. The N secondary forces may be represented as a vector, given by:

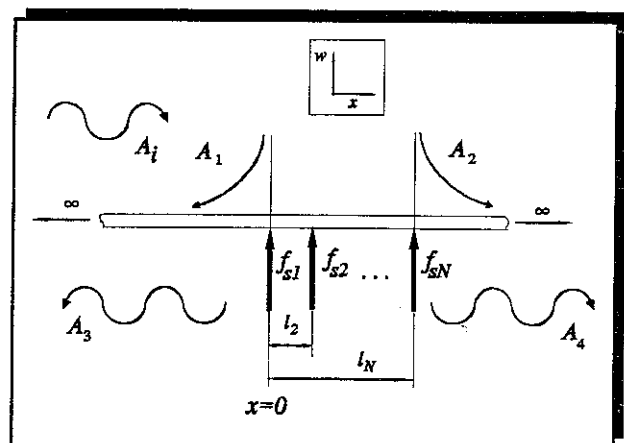


Figure 2.35 A Secondary Force Actuator Array Positioned on an Infinite Beam

$$\underline{F}_s^T = [f_{s1}(0) \ f_{s2}(l_2) \ f_{s3}(l_3) \ \dots \ f_{sN}(l_N)] \quad (2.40)$$

and the positive-going propagating A_4 wave generated by the secondary force array is given by:

$$A_4 = \underline{Z} \underline{F}_s \quad (2.41)$$

where:

$$\underline{Z} = \frac{-j}{4EI k_b^3} [1 \ e^{jk_b l_2} \ e^{jk_b l_3} \ \dots \ e^{jk_b l_N}] \quad (2.42)$$

The lateral displacement of the beam in the far-field, downstream of the secondary force array, where the amplitude of the nearfield wave is negligible, is given by:

$$w(x) = (A_4 + A_i) e^{-jkx} \quad (2.43)$$

where the $e^{j\omega t}$ time dependence is omitted for clarity. Substituting for A_4 from equation (2.41) into equation (2.43) results in:

$$w(x) = (\underline{Z} \underline{F}_s + A_i) e^{-jkx} \quad (2.44)$$

The object is to minimise the secondary effort, $\underline{F}_s^H \underline{F}_s$ subject to the constraint that the far-field downstream displacement is zero, i.e., $\underline{Z} \underline{F}_s + A_i = 0$, where H denotes the hermitian transpose, which is the transpose of the complex conjugate. The Lagrange function (cost function) is thus [12]:

$$J = \underline{F}_s^H \underline{F}_s + \mu^* (\underline{Z} \underline{F}_s + A_i) + \mu (\underline{Z} \underline{F}_s + A_i)^* \quad (2.45)$$

where μ is the complex Lagrange multiplier. The problem has now been modified and the constraint has been incorporated in the cost function which has to be minimised. Noting that equation (2.45) is of hermitian quadratic form in both \underline{F}_s and μ , the complex derivatives of J with respect to both the real and imaginary parts of these quantities are:

$$\frac{\partial J}{\partial \mu_R} + j \frac{\partial J}{\partial \mu_I} = 2(\underline{Z}\underline{F}_s + A_i) \quad (2.46)$$

and

$$\frac{\partial J}{\partial \underline{F}_{sR}} + j \frac{\partial J}{\partial \underline{F}_{sI}} = 2\underline{F}_s + 2\mu\underline{Z}^H \quad (2.47)$$

where the subscripts R and I denote real and imaginary parts. The minimum value of \underline{F}_s within the constraint is given by setting both equations (2.46) and (2.47) to zero to give:

$$\underline{Z}\underline{F}_s + A_i = 0 \quad (2.48)$$

and

$$\underline{F}_s + \mu\underline{Z}^H = 0 \quad (2.49)$$

Equations (2.48) and (2.49) combine to give the Lagrange multiplier that gives the optimum solution:

$$\mu = \frac{A_i}{\underline{Z}\underline{Z}^H} \quad (2.50)$$

and hence the optimum secondary force vector is given by:

$$\underline{F}_{so} = -\frac{\underline{Z}^H A_i}{\underline{Z}\underline{Z}^H} \quad (2.51)$$

where \underline{F}_{so} is the minimum secondary force effort that has to be applied to achieve zero displacement in the far-field downstream of the secondary forces. It should be noted that a more general problem of this type occurs in the active control of a sound field where there are fewer microphones (error sensors) than loudspeakers (secondary sources). In this case the Lagrange multiplier turns out to be a vector and the reader is referred to reference [12] for a full explanation on how to deal with a problem of this type.

To find the optimum secondary force vector in terms of the incident propagating

wave, \underline{Z} can be substituted from equation (2.42) into equation (2.51) to give:

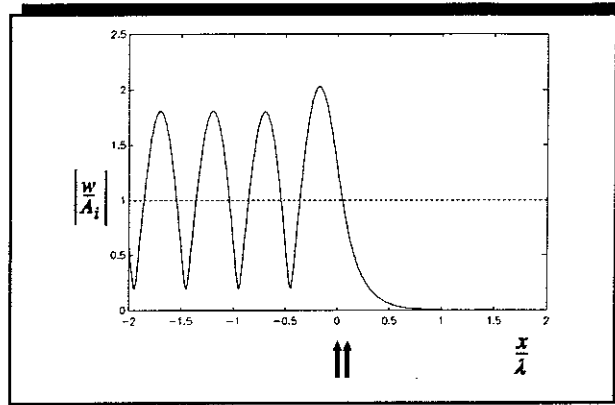
$$\underline{F}_{so} = -\frac{j4EI k_b^3}{N} \begin{bmatrix} 1 & e^{-jk_b l_2} & e^{-jk_b l_3} & \dots & e^{-jk_b l_N} \end{bmatrix}^T A_i \quad (2.52)$$

The force (primary force) required to generate a propagating wave with amplitude A_i is given by equation (2.25). This can be substituted into equation (2.52) and the square of the modulus calculated to give the expression for the sum of the squared minimum secondary forces:

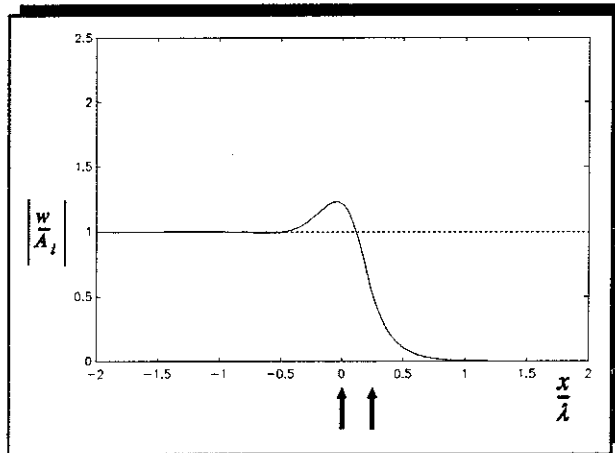
$$\sum_{n=1}^N |F_n|^2 = \underline{F}_{so}^H \underline{F}_{so} = \frac{|f_p|^2}{N} \quad (2.53)$$

This rather surprising result shows that *the minimum secondary force vector required to suppress an incident propagating wave is independent of the distance between the secondary forces, and the secondary effort reduces as the number of secondary forces N increases.*

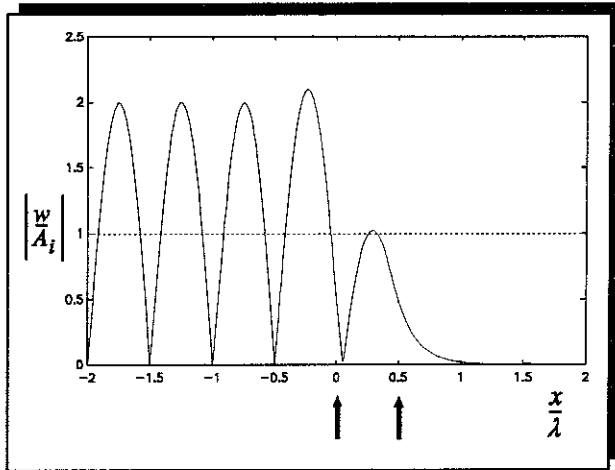
The displacement of an infinite beam when the minimum effort control strategy is implemented using two secondary forces, a distance l apart, is shown in **figures 2.36a-c** for distances between the secondary forces of 0.1, 0.25 and 0.5 of a wavelength of the incident propagating wave.



(a) l/λ Between Secondary Forces = 0.1



(b) l/λ Between Secondary Forces = 0.25



(c) l/λ Between Secondary Forces = 0.5

Figure 2.36 Displacement of an Infinite Beam with Two Secondary Forces Applied with a Control Strategy to Minimise the Secondary Effort

Examination of **figures 2.36a-c** shows that the incident propagating wave is suppressed as required by the constraint imposed. It can also be seen that the amplitude of the reflected propagating wave, which combines with the incident propagating wave upstream of the secondary force array ($x/\lambda < 0$), is dependent upon the distance between the secondary forces. This dependency, and the relationship between the amplitude of the negative-going propagating wave and the number of secondary forces is investigated next.

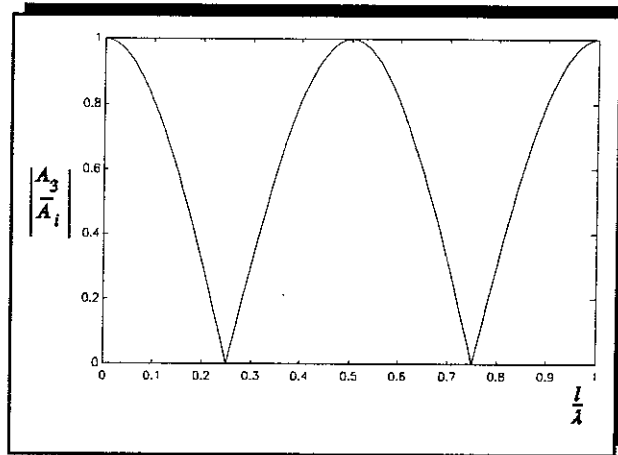
The negative-going propagating (reflected) wave generated by the secondary force array is given by:

$$A_3 = -\frac{j}{4EI k_b^3} \begin{bmatrix} 1 & e^{-jk_b l_2} & e^{-jk_b l_3} & \dots & e^{-jk_b l_N} \end{bmatrix} \begin{bmatrix} f_{s1} \\ f_{s2} \\ f_{s3} \\ \vdots \\ f_{sN} \end{bmatrix} \quad (2.54)$$

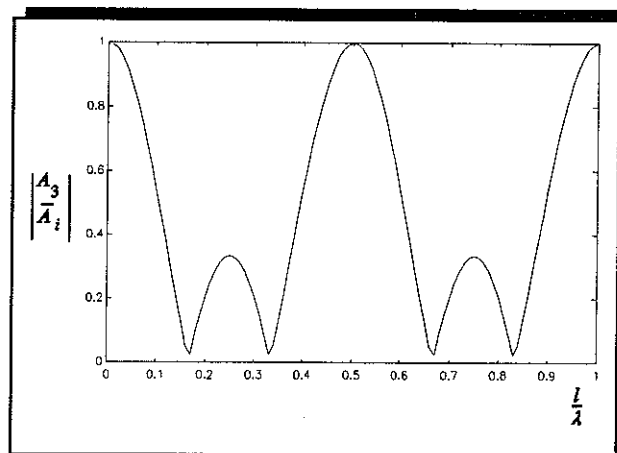
Substituting for the minimum secondary force vector from equation (2.52) gives the relationship between the reflected and the incident wave, which is:

$$\frac{A_3}{A_i} = -\frac{1}{N} \left[1 + e^{-j2k_b l_2} + e^{-j2k_b l_3} + \dots + e^{-j2k_b l_N} \right] \quad (2.55)$$

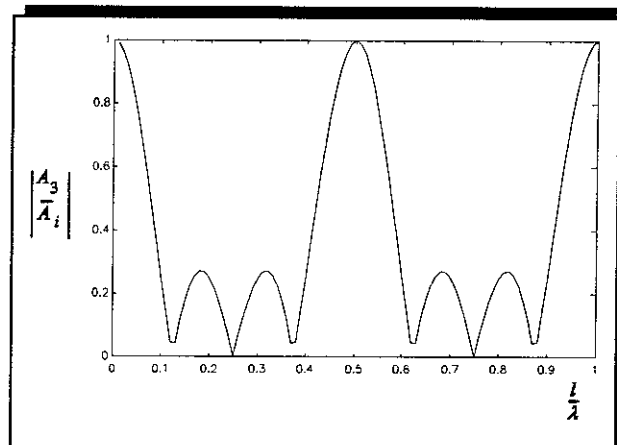
The modulus of this ratio is plotted as a function of the spacing between the secondary forces for two, three and four secondary forces in **figure 2.37**, where l is the distance between each of the secondary forces.



(a) Two Secondary Forces Applied



(b) Three Secondary Forces Applied



(c) Four Secondary Forces Applied

Figure 2.37 Graphs of the Ratio of the Amplitude of the Reflected Propagating Wave A_3 , to the Incident Propagating Wave A_i

If no wave is reflected by the secondary array, then the displacement of the beam upstream of the secondary array is not affected by the array and the incident propagating wave is effectively absorbed by the secondary array. As discussed previously, if this occurs, then the vibration of the beam upstream of the array is not increased by the action of the secondary forces. It can be seen from **figures 2.37a-c** that the amplitude of the reflected wave is dependent upon the number and the spacing of the secondary forces. At frequencies when the distances between the secondary forces is an integer number of half-wavelengths, the amplitude of the reflected wave is equal to that of the incident wave, resulting in a pure standing wave upstream of the secondary force array. An example of this can be seen in **figure 2.36c**. It can also be seen from **figures 2.37a-c** that the frequency range over which the amplitude of the reflected wave is relatively small in comparison with the incident wave, increases with the number of secondary forces.

It can be concluded from the analysis conducted in this section, that if this control strategy is implemented on an infinite beam, then as the number of secondary forces increases, the effort required decreases. As the number of equidistant secondary forces increases, the relative amplitude of the reflected wave is much diminished over an ever wider range of frequencies. Although this analysis has been conducted using secondary forces, the results are similar for the application of moments and moment-pairs.

2.5.2 Implementation on a Semi-Infinite Beam

It can be seen in **figure 2.37** that although the incident propagating wave is suppressed there is a reflected A_3 wave at most frequencies. If the beam is not infinite, and there is a boundary upstream of the secondary force array (a semi-infinite beam), then this wave will be reflected and combine with the incident wave which is to be suppressed by the secondary force array. This is effectively a feedback system. If only one secondary force is applied, then the effort required to suppress the incident wave becomes very large at frequencies when the negative-going

wave generated by the secondary force is reflected by the upstream boundary and destructively interferes with the positive-going propagating wave generated by the same force. This is because only a small residual wave remains to suppress the incident wave.

It is thus prudent to investigate the effects of the minimum effort control strategy on a system with an upstream boundary. On a finite beam there will also be a boundary downstream of the secondary force array, but as the strategy involves suppression of the propagating wave, this boundary can be neglected. The beam considered in this section is shown in **figure 2.38**.

To demonstrate that the effects of this control strategy are different on a semi-infinite beam, the application of two secondary forces is considered. Although the general framework is essentially the same as in the infinite beam case,

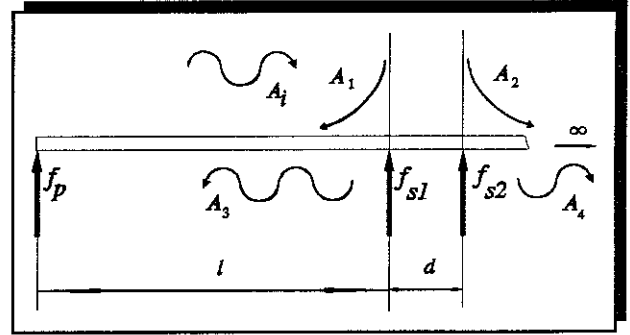


Figure 2.38 A Semi-infinite Beam with One Primary and Two Secondary Forces Applied

the relationship \underline{Z} , between the positive-going propagating wave and the secondary forces differs. With a semi-infinite beam there is an additional component due to the A_3 wave which is generated by the secondary force and reflected from the free boundary. Hence the vector \underline{Z} is given by:

$$\underline{Z} = \frac{-j}{4EI k_b^3} \begin{bmatrix} 1 - j e^{-j2k_b l} & e^{jk_b d} - j e^{-jk_b d} e^{-j2k_b l} \end{bmatrix} \quad (2.56)$$

Substituting this into equation (2.51) gives the minimum secondary forces required to suppress the propagating flexural wave. It was shown in section 2.2.4, that when both propagating waves are suppressed, then both secondary forces are equal in magnitude but there is a phase difference between them. With the minimum effort strategy implemented on a semi-infinite beam this is not the case, and the ratio of the secondary forces is plotted in **figure 2.39**, where $l = 10d$. It can be seen that ratio of the forces is dependent upon the distance between the secondary forces and the boundary, and also the distance between the secondary forces. The control strategy

requires that the magnitudes of the secondary forces are *always* less than or equal to the magnitude of a single secondary force applied to suppress the incident propagating wave. The best way of quantifying this is by determining the secondary effort by combining equations (2.51), (2.53) and (2.56) to give:

$$\text{effort} = \frac{|f_{s1}|^2 + |f_{s2}|^2}{\frac{|f_p|^2}{8}} = \frac{4}{2 - \sin 2k_b l - \sin 2k_b (l + d)} \quad (2.57)$$

The factor of 8 occurs because the force required to generate a propagating wave on an infinite beam is $\sqrt{8}$ times greater than the same amplitude of wave generated on a semi-infinite beam (the square of the modulus of the force is eight times greater). The effort is written in this form so that it is easier to make a direct comparison between the minimum effort required to suppress a propagating wave on an infinite and a semi-infinite beam. The secondary effort is calculated for the minimum effort and wave suppression strategies when $l = 10d$ and these are plotted together for comparison in **figure 2.40**.

Examining this figure and equation (2.57), it can be seen that the effort required with the minimum effort control strategy is not independent of frequency and distance between the secondary forces, as in the infinite beam case. The effort required has a complicated dependency on frequency, the

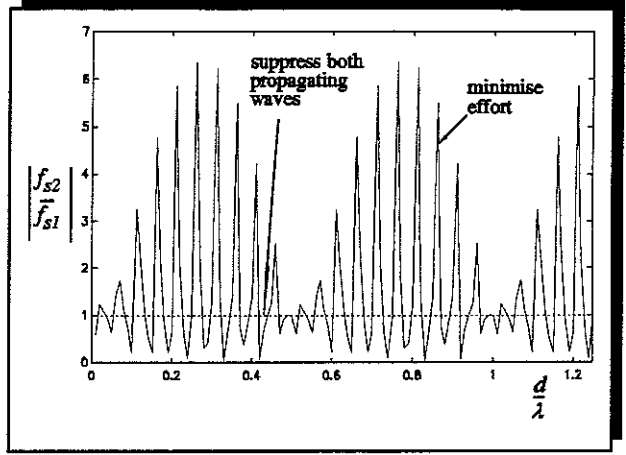


Figure 2.39 Ratio of the Secondary Forces when the Control Strategies are Implemented on a Semi-Infinite Beam

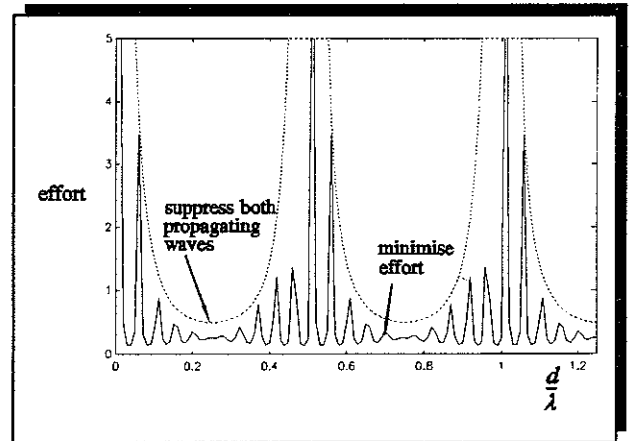


Figure 2.40 Secondary Effort Required for the Two Control Strategies

distance between the secondary forces and the distance between the secondary array and the left-hand boundary. The effort when both propagating waves are suppressed is the same as that discussed in section 2.2.4, which has a minimum value of 0.5 when the distance between the secondary forces is an odd integer number of quarter-wavelengths. As expected, when the minimum effort strategy is implemented, the effort is always less than the effort required with the wave suppression strategy; it does, however, follow the same general trend. As mentioned above, the effort when two forces are applied is always less than or equal to the effort when one secondary force is applied and the minimum effort strategy is implemented, and this is confirmed by the graph plotted in **figure 2.41**.

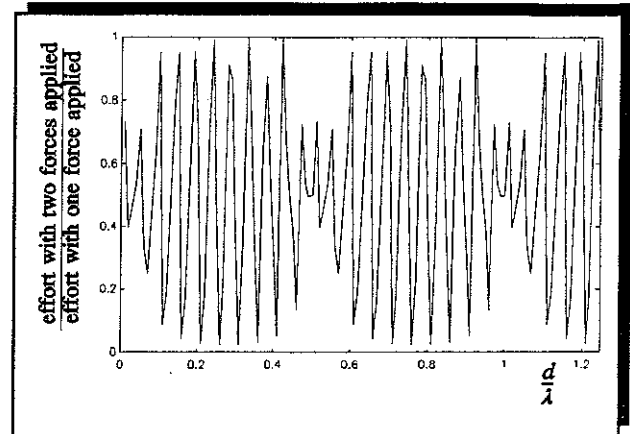


Figure 2.41 Ratio of the Effort with Two Secondary Forces Applied to the Effort with One Secondary Force Applied with the Minimum Effort Strategy Implemented

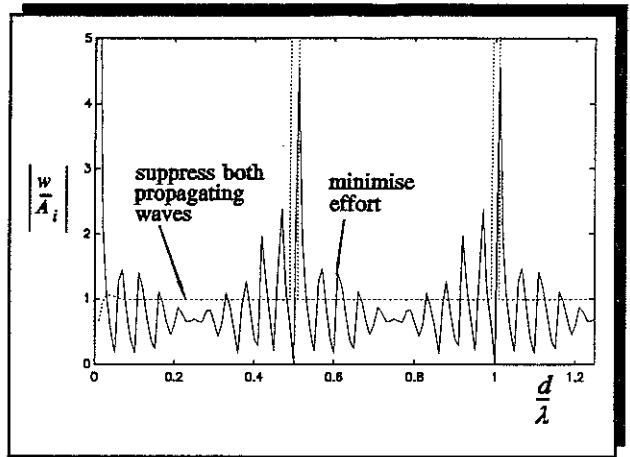


Figure 2.42 Displacement of the Beam Between the Primary and Secondary Forces with the Minimum Effort Control Strategy Implemented

The displacement of the beam at a point between the primary and secondary forces is plotted in **figure 2.42**. It can be seen that when both propagating waves are suppressed, the displacement is due only to the propagating wave generated by the primary force, and a very small contribution from the nearfield wave generated by the primary and secondary forces. Discontinuities occur when the distance between the secondary forces is an integer number of half-wavelengths as discussed in section 2.2.4. The displacement of the beam between the primary and secondary forces when

the minimum effort strategy is implemented is sometimes smaller than that without control and sometimes greater, depending on the frequency of excitation. An example of the beam's displacement when the distance between the secondary forces is a quarter of a wavelength is shown in **figure 2.43**. The standing wave upstream of the secondary force is evident.

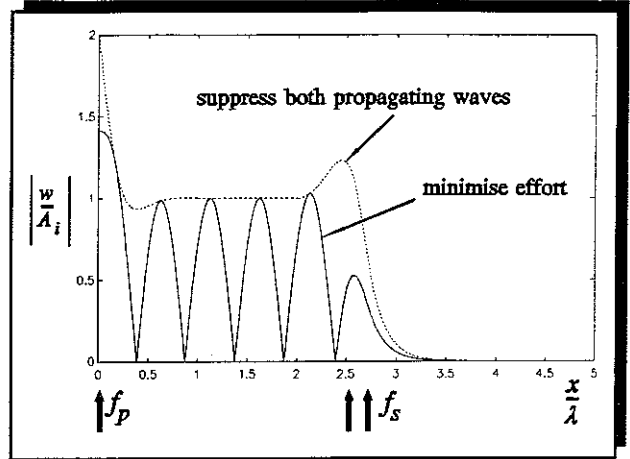


Figure 2.43 Displacement of a Semi-infinite Beam when the Minimum Effort Control Strategy is Implemented

The analysis conducted in this section shows that although there are differences in the effects of the minimum effort control strategy when applied to infinite and semi-infinite beams, it is an effective control strategy in both cases. In a practical situation it is a sensible control strategy if the capacity of the secondary actuators is limited. Even though the secondary effort is large at frequencies close to when the distance between the secondary forces is an integer number of half-wavelengths, the secondary effort is less than that required with the wave suppression control strategy. Hence smaller actuators can be used.

2.6 Conclusions

Wave control strategies using up to four secondary sources have been discussed. It was shown that with one secondary source, a propagating flexural wave can be reflected, resulting in a pure standing wave upstream of the secondary source, that is twice the amplitude of the incident wave. Additionally, there are two residual nearfield waves, one either side of the secondary source. If two secondary sources are used, the incident propagating wave can be suppressed without generating a negative-going propagating wave, but again nearfield waves are generated. If three

secondary sources are used, one of these nearfield waves can additionally be suppressed, and with four actuators all waves can be suppressed. This is in agreement with the results presented by Scheuren [27].

The relationship between the secondary effort and the number and spacing of the secondary sources has been investigated. The smallest effort required in all cases occurs when the distance between the secondary sources is close to an odd integer number of quarter-wavelengths. The effort is infinite when the positive and negative-going propagating waves are suppressed, and the distance between each of the secondary sources is an integer number of half-wavelengths of the incident propagating wave. This is because the contributions from the two secondary sources become self cancelling.

The use a secondary force array causes the transverse displacement in the array to change more smoothly than with either moment or moment-pair arrays. The displacement within the array becomes increasingly complicated with moment and moment-pair actuators, and with number of actuators in the array. The reason for this is believed to be that force actuators induce a change in displacement directly, whereas moment actuators induce a change in slope, and moment-pair actuators induce a change in curvature. The change in displacement is then associated with these changes in slope and curvature. The disadvantage of using force actuators in a practical situation, however, is that they either have to act against another structure or an inertial mass. The application of a moment is difficult to realise practically, and any moment actuator will suffer the same constraints as a force actuator. The moment-pair actuator can be realised practically by using piezoceramic elements glued to either side of the structure (this actuator is discussed at length in Chapter 4). The main advantage of this type of actuator is that it does not require an inertial mass, because it acts against the structure that is being controlled and is thus extremely compact. One further consideration in the design of an actuator array, is the frequency range over which it has to operate. Appendix 3 shows that in general, a force actuator is more appropriate for low frequencies, and a moment-pair actuator is more appropriate for high frequencies.

The final topic discussed in this chapter was the suppression of a flexural propagating wave using minimum effort. It was shown that the effort required to suppress a propagating wave on an infinite beam decreases as the number of secondary sources increases. The way in which a finite beam behaves when this control strategy is implemented using two secondary forces was analysed. There are differences in the behaviour of a finite and an infinite beam when the minimum effort control strategy is implemented, and this emphasises the importance of conducting analysis on finite structures once basic insight has been gained using infinite structure models.

CHAPTER 3

3 ACTIVE CONTROL OF FLEXURAL WAVES USING POWER AS A CONTROLLING PARAMETER

3.1 Introduction

Active control strategies using power as the controlling parameter have been explored at some length in the active control of sound fields [34][35][36], and there has also been some work carried out in the application of these strategies to beams [23][37][38][39] and plates [40]. Two power based control strategies have been proposed [36]; that of maximizing the power absorbed by the secondary sources and the minimization of total power supplied by all the sources. As vibrational and acoustic power can be relatively difficult to measure in practical situations, particularly power supplied by a primary uncontrolled force, ways of implementing control without directly measuring this have been investigated by Johnson and Elliott [41]. This chapter is concerned with the application of active control strategies to infinite and finite beams using power as a cost function. The effects of implementing these strategies are discussed for infinite and finite beams and are compared with the wave control strategies discussed in Chapter 2. In this chapter it was shown that four secondary forces can control four flexural waves. However two of these are nearfield waves that do not transmit power unless they interfere with other nearfield waves that are generated at discontinuities. Thus in this chapter only a secondary force array with at most two forces is considered. In the computer simulations presented a loss factor of 0.1% was included for the infinite beam and 1% for the finite beam. Without damping singularities appear in the equations for the secondary forces and the results are difficult to interpret [42]; hence the loss factor of 0.1% for the infinite beam. 1% was chosen as a realistic value of damping for the finite beam. As in Chapter 2 all the analysis is conducted in the frequency domain which is appropriate

for deterministic disturbances. To validate the theory, some experimental results of the control strategies implemented on a slender aluminium beam using one secondary force are presented.

3.2 Control Strategies Applied to an Infinite Beam

The effects of the control strategies are first considered on an infinite beam, as this gives insight into the physical effects of active control without the added complexities of wave reflections from boundaries and beam resonances.

3.2.1 Wave Suppression using a Single Secondary Force

Consider the beam shown in figure 3.1 with one primary and one secondary force applied. The amplitudes of the waves shown in this figure can be calculated using a similar formulation to that described in Chapter 2, and are given by the equation:

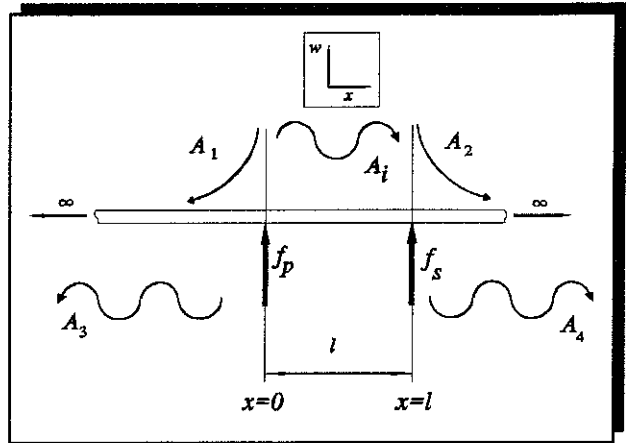


Figure 3.1 An Infinite Beam with One Primary and One Secondary Force Applied

$$\begin{bmatrix} A_1 \\ A_2 \\ A_3 \\ A_4 \end{bmatrix} = -\frac{1}{4EI k_b^3} \begin{bmatrix} 1 & e^{-k_b l} \\ 1 & e^{k_b l} \\ j & j e^{-j k_b l} \\ j & j e^{j k_b l} \end{bmatrix} \begin{bmatrix} f_p \\ f_s \end{bmatrix} \quad (3.1)$$

The amplitude of vibration upstream of the primary force is given by:

$$w(x) = A_1 e^{k_b x} + A_3 e^{jk_b x} \quad (3.2)$$

and the amplitude of vibration downstream of the secondary force is given by:

$$w(x) = A_2 e^{-k_b x} + A_4 e^{-jk_b x} \quad (3.3)$$

where k_b is the flexural wavenumber given in Appendix 1 and the $e^{j\omega t}$ time dependence is suppressed for clarity. Damping is included by way of a complex Young's modulus. If the incident wave is suppressed, the secondary force is just an inverted delayed version of the primary force given by the equation:

$$f_s = e^{-jk_b l} f_p \quad (3.4)$$

the magnitude of which is equal to that of the primary force and is shown in **figure 3.2a** on page 61 for the sake of completeness. To determine the amplitude of the upstream propagating wave, the required secondary force f_s , is substituted from equation (3.4) into equation (3.1) to give:

$$A_3 = -\frac{j}{4EI k_b^3} (1 - e^{-2jk_b l}) f_p \quad (3.5)$$

Now, the amplitude of the propagating wave in the absence of control is:

$$A_i = \frac{-j f_p}{4EI k_b^3} \quad (3.6)$$

which can be substituted into equation (3.5) to give the amplitude of negative-going propagating wave normalised to the incident propagating wave:

$$\frac{|A_3|}{|A_i|} = 2 \sin k_b l \quad (3.7)$$

which is plotted in **figure 3.3a** on page 62. The power supplied to the beam by the primary and secondary forces when control is implemented can be determined from the expression derived in Appendix 3, which is:

$$P = -\frac{\omega}{2} \text{Im} \{f^* w\} \quad (3.8)$$

where Im denotes the imaginary part. The displacement of the beam at the primary force position with control, $w(0)$, can be determined by combining equations (3.1), (3.2) and (3.4) which can then be substituted into equation (3.8) to give the power supplied by the primary force of:

$$P_p = \frac{\omega |f_p|^2}{8EI k_b^3} \{ e^{-k_b l} \sin k_b l + 1 - \cos 2k_b l \} \quad (3.9)$$

and similarly the power supplied by the secondary force can be calculated to be:

$$P_s = \frac{-\omega |f_p|^2}{8EI k_b^3} e^{-k_b l} \sin k_b l \quad (3.10)$$

Now, the power supplied to the beam by the primary force in the absence of any control force is derived in Appendix 3 and is given by:

$$P_p = \frac{\omega |f_p|^2}{8EI k_b^3} \quad (3.11)$$

Thus, the ratios of the powers supplied to the beam by the primary and secondary forces to the power supplied by the primary force without control can be calculated by dividing equations (3.9) and (3.10) by equation (3.11), and these are plotted in **figure 3.4a** on page 63. It can be seen that the secondary force absorbs the power supplied by the primary force due to the interaction of the nearfield waves generated by the primary and secondary forces. However, at higher frequencies, when the interaction between the nearfield waves is negligible, the secondary force neither absorbs nor supplies power. The incident propagating wave is effectively reflected by the secondary force and either constructively or destructively interferes with the negative-going propagating wave generated by the primary force depending on frequency. Thus the power supplied by the primary force oscillates between zero and twice the power supplied without control. The high frequency behaviour is similar

to that found in the analogous acoustic case as discussed by Nelson and Elliott [12].

3.2.2 Maximization of the Power Absorbed by the Secondary Force Array

This control strategy has been investigated theoretically by Curtis [37] for an infinite lossless beam, and experimentally by Redman-White *et al* [38], for a beam which has anechoic terminations fitted to each end. Curtis concluded that the suppression of both propagating waves using two secondary forces, as discussed in the Chapter 2, and the maximization of the power absorbed by two secondary forces are equivalent. The aim in this thesis is to explore the effects of implementing this control strategy using one and two secondary forces on a beam which is modelled with damping included. This control strategy has also been investigated by Elliott *et al* [36] for acoustic sources in an enclosure.

3.2.2.1 Application of a Single Secondary Force

The structure considered in this section is that shown in **figure 3.1**, an infinite beam with one primary and one secondary force applied. The magnitude and phase of the secondary force required to maximize the power absorbed is given by the equation, derived in Appendix 3:

$$f_s = \frac{j}{2} X_{ss}^{-1} \alpha_{sp} f_p \quad (3.12)$$

where X_{ss} is the imaginary part of the point receptance of the beam at the secondary force position, and α_{sp} is the complex transfer receptance between the primary force and the displacement at the secondary force position. Using this relationship, the secondary force can be written in terms of the primary force as:

$$f_s = \frac{1}{2} (j e^{-k_b l} - e^{-j k_b l}) f_p \quad (3.13)$$

whose magnitude normalised to the primary force is plotted in **figure 3.2b** on page 61. This shows that at high frequencies, when the interaction between the nearfield waves generated by the primary and secondary forces is negligible, the magnitude of the secondary force is half that of the primary force. Equation (3.13) can be combined with equation (3.1) to give the amplitudes of the propagating waves upstream of the primary force and downstream of the secondary force array, which are given by:

$$A_3 = -\frac{j f_p}{4 E I k_b^3} \left\{ \frac{e^{-2 j k_b l}}{2} - \frac{e^{-k_b l} e^{-j k_b l}}{2} \right\} \quad (3.14)$$

and

$$A_4 = -\frac{f_p}{4 E I k_b^3} \left\{ \frac{j}{2} - \frac{e^{-k_b l} e^{-j k_b l}}{2} \right\} \quad (3.15)$$

The amplitudes of these waves normalised to the incident propagating wave are shown in **figure 3.3b** on page 62. It can be seen that the amplitudes of the propagating waves converge to $1/\sqrt{2}$ of the amplitude of the incident wave at zero frequency. At high frequencies when the interaction between the nearfield waves is negligible, the magnitude of the propagating wave downstream of the secondary force is half of what it is without control. The upstream propagating wave oscillates between half and twice the magnitude of the upstream wave without control, depending on frequency. This is because the negative-going waves generated by the primary and secondary forces either constructively or destructively interfere. As in the previous section, equation (3.8) can be used to calculate the powers supplied by the primary and secondary forces to give the equations:

$$P_p = \frac{\omega |f_p|^2}{8 E I k_b^3} \left\{ e^{-k_b l} \sin k_b l + 1 - \frac{\cos 2 k_b l}{2} + \frac{e^{-2 k_b l}}{2} \right\} \quad (3.16)$$

and

$$P_s = \frac{-\omega |f_p|^2}{8EI\bar{k}_b^3} \left\{ \frac{e^{-\bar{k}_b l} \sin \bar{k}_b l}{2} + \frac{1}{4} + \frac{e^{-2\bar{k}_b l}}{4} \right\} \quad (3.17)$$

where \bar{k}_b is the real part of the flexural wavenumber, and the decaying standing waves which are generated as a result of the inclusion of damping (as explained by Cremer *et al* [13]), are ignored. It should be noted that it is the inclusion of damping that causes the wavenumber to be complex. Equations (3.16) and (3.17) are plotted in **figure 3.4b** on page 63 as ratios of the power supplied by the primary force without control. Examination of this figure shows that at high frequencies the power absorbed by the secondary force is 25% of the power supplied by the primary force before control. The power supplied by the primary force follows the trend of the negative-going propagating wave oscillating between 0.5 and 1.5 times the power supplied before control. It is interesting to note that *this control strategy could be implemented in principle by attaching variable passive elements instead of applying a secondary force* [42]. The modulus of the mechanical impedance of the combined passive elements required is equal to the modulus of the mechanical impedance of the beam. This can be realized with a stiffness which has a spring rate of $2EI\bar{k}_b^3$ in parallel with a visco-elastic damper with a damping coefficient $2\rho S c_f$, where ρ is the density of the beam, S is the cross-sectional area of the beam and c_f is the flexural wave speed. It should be noted that *the values of stiffness and damping are frequency dependent, and thus can only be realised by passive elements at one frequency*.

It is clear that when one secondary force is applied, this strategy is markedly different from the wave suppression control strategy discussed in the previous section, and it is difficult to see what practical use it could have, as the amplitude of vibration downstream of the secondary force is only halved. However, the physical insight into the effects of this control strategy is useful in the investigation of the same strategy when two secondary forces are applied, which is discussed later.

3.2.3 Minimization of the Total Power Supplied to the Beam

This is another power based control strategy. It has been thoroughly investigated for the acoustic case [34][35] and has received some attention in its application to beams and plates [40]. As with the other two control strategies discussed in this chapter, the effects of this strategy are examined for up to two secondary forces applied to a beam, and a physical explanation for the resulting behaviour of the beam is offered. Elliott *et al* [36] showed that when this strategy is applied to any general system, the power output by each of the secondary sources is zero, provided that all the primary sources are in phase. The physical effects are thus significantly different from the power absorption control strategy. In this case, the impedance of the beam at the primary force positions is modified under the action of control, such that the power supplied to the beam by *all* the forces is minimized.

3.2.3.1 Application of a Single Secondary Force

The structure considered in this section is shown in **figure 3.1**. The magnitude of the secondary force required is given by the equation derived in Appendix 3:

$$f_s = -X_{ss}^{-1} X_{sp} f_p \quad (3.18)$$

where X_{ss} is the imaginary part of the point receptance at the secondary force position and X_{sp} is the imaginary part of the transfer receptance between the primary force and the secondary force position. Equation (3.18) expands to give:

$$f_s = -\cos k_b l f_p \quad (3.19)$$

where the decaying standing wave is again ignored. This is plotted in **figure 3.2c** on page 61. The normalised amplitudes of the propagating waves upstream of the primary force and downstream of the secondary force array can be determined by combining equations (3.1), (3.6) and (3.19) to give:

$$\left| \frac{A_4}{A_i} \right| = \left| \frac{A_3}{A_i} \right| = |\sin k_b l| \quad (3.20)$$

which are plotted in **figure 3.3c** on page 62. In this case, the normalised upstream and downstream displacements never exceed one. Thus, at frequencies when there is an integer number of half-wavelengths between the primary and secondary force, the secondary force is driven to zero because at these frequencies any magnitude of secondary force would result in an increase in power being supplied to the beam. The power supplied by the primary force can again be determined using equation (3.8) which results in the expression:

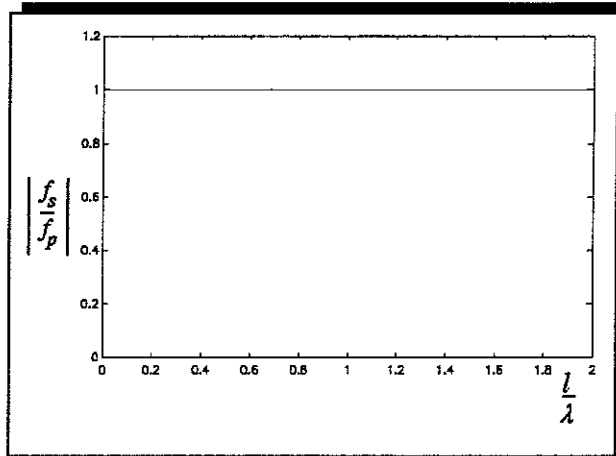
$$P_p = \frac{\omega |f_p|^2}{8EI k_b^3} \sin^2 k_b l \quad (3.21)$$

where the decaying nearfield standing waves are again ignored. This is plotted in **figure 3.4c** on page 63 as a ratio of the power supplied by the primary force without control. It can be seen that the secondary force supplies no power and the normalised power supplied by the primary force oscillates between zero and one as expected. It is interesting to note that this control strategy has the same effect on both the upstream and downstream propagating waves, unlike the other two strategies. As with the power absorption control strategy implemented using one secondary force, this control strategy is not generally a practical proposition unless the distance between the forces can be arranged to be an integer number of half-wavelengths, but again it does give insight into the physical effects when two forces are employed, as shown in the next section.

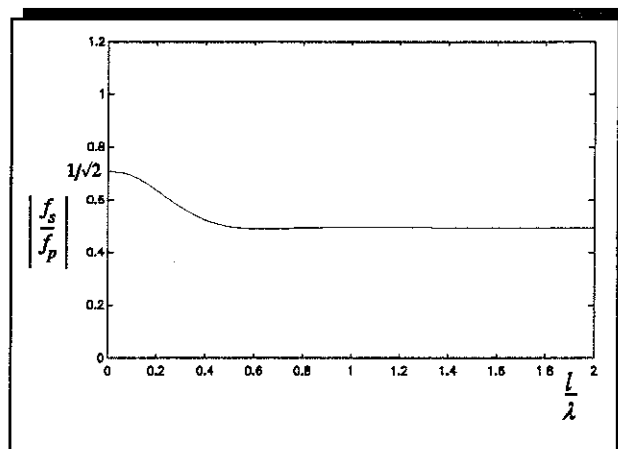
As with the power absorption control strategy, the same effect could also be implemented using variable passive elements. In this case, however, the impedance of the passive elements required is purely reactive (no power supplied or absorbed) and is given by the expression:

$$z = \frac{4EI\bar{k}_b^3 \cos \bar{k}_b l (\sin \bar{k}_b l - \cos \bar{k}_b l)}{j\omega(1 - \sin 2\bar{k}_b l)} \quad (3.22)$$

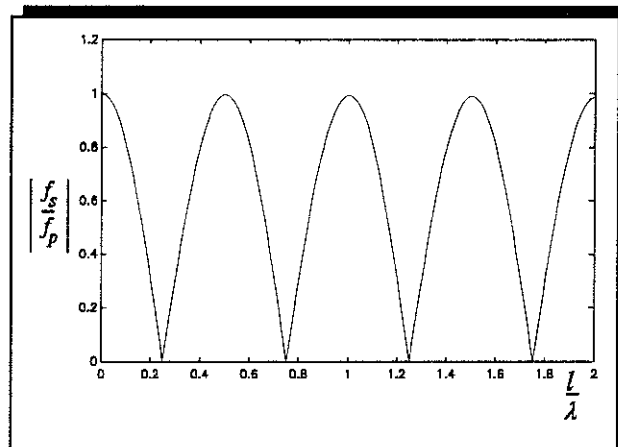
which alternates between a mass-like and a spring-like element with increasing frequency. It is difficult to see how this could be implemented over a wide frequency range, but it could be achieved with a variable stiffness device over a limited frequency range.



(a) Control Strategy: Suppress the Incident Propagating Wave

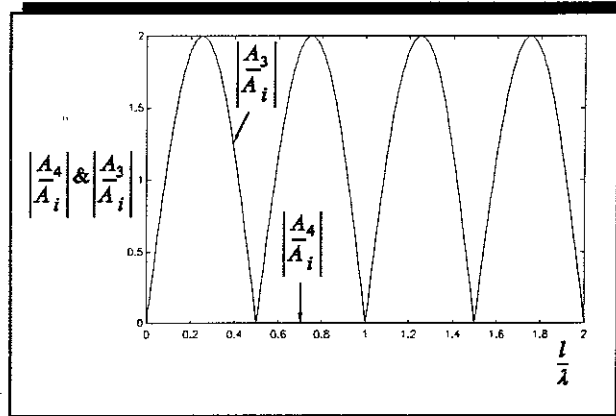


(b) Control Strategy: Maximize the Power Absorbed by the Secondary Force.

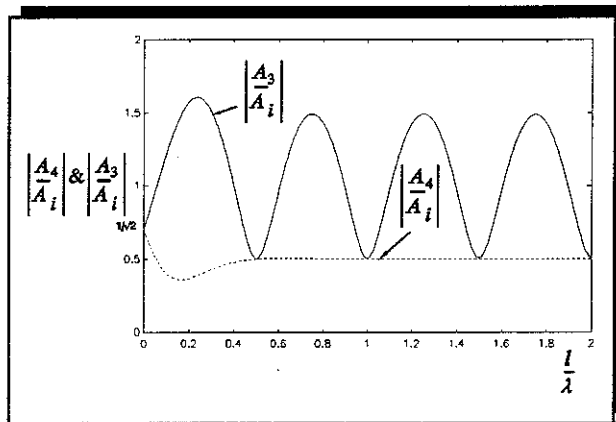


(c) Control Strategy: Minimize the Total Power Supplied to the Beam

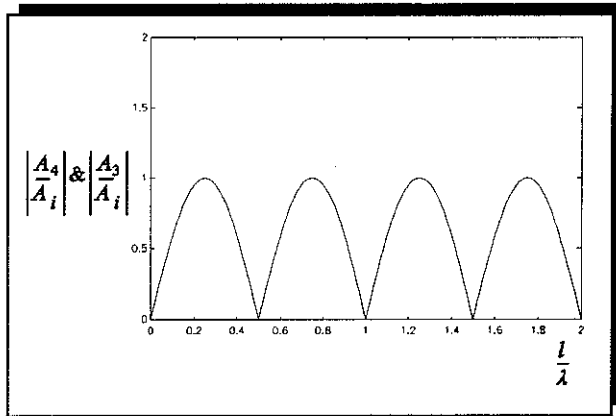
Figure 3.2 Normalised Magnitude of the Single Secondary Force Required to Implement Control Strategies on an Infinite Beam



(a) Control Strategy: Suppress the Incident Propagating Wave

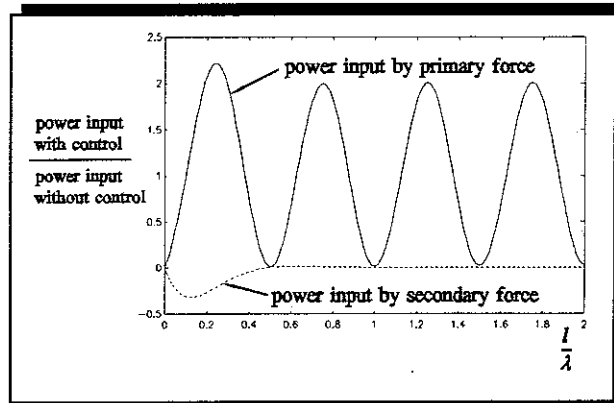


(b) Control Strategy: Maximize the Power Absorbed by the Secondary Force.

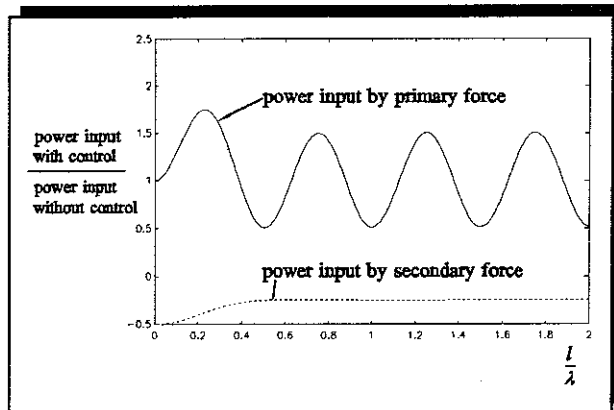


(c) Control Strategy: Minimize the Total Power Supplied to the Beam

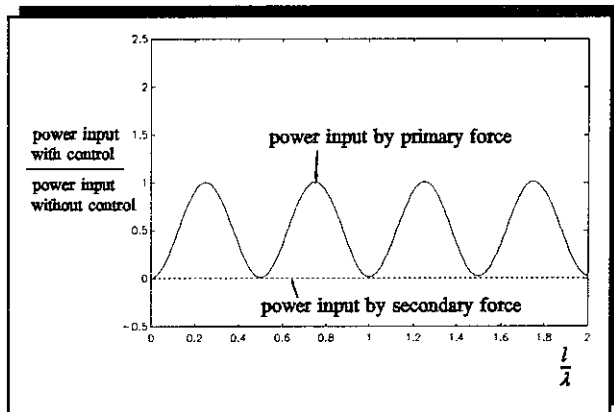
Figure 3.3 Normalised Amplitudes of the Positive and Negative-Going Waves when One Secondary Force is Applied to an Infinite Beam



(a) Control Strategy: Suppress the Incident Propagating Wave



(b) Control Strategy: Maximize the Power Absorbed by the Secondary Force.



(c) Control Strategy: Minimize the Total Power Supplied to the Beam

Figure 3.4 Ratios of the Power Supplied by Primary and Secondary Forces with Control to Power Supplied by the Primary Force without Control using One Secondary Force on an Infinite Beam

3.2.4 Wave Suppression using Two Secondary Forces

This control strategy was discussed in Chapter 2, but the analysis is summarized here for convenience. If two secondary forces are applied to a beam as shown in **figure 3.5**, and the positive and negative-going propagating waves away from the secondary array are suppressed, the secondary forces required are given by:

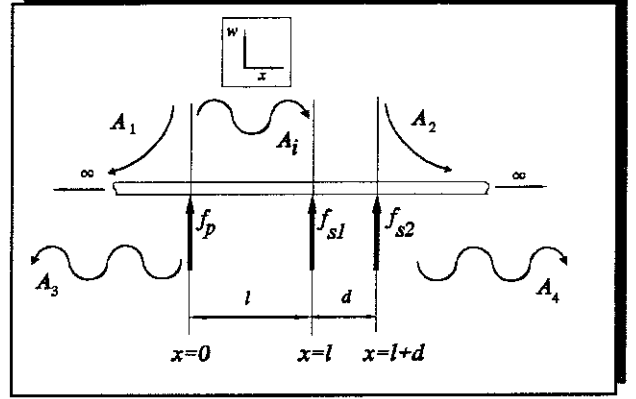


Figure 3.5 An Infinite Beam with One Primary and Two Secondary Forces Applied

$$\begin{bmatrix} f_{s1} \\ f_{s2} \end{bmatrix} = -4EI k_b^3 \begin{bmatrix} j & j e^{-jk_b d} \\ j & j e^{jk_b d} \end{bmatrix}^{-1} \begin{bmatrix} 0 \\ -A_i \end{bmatrix} \quad (3.23)$$

Using the relationship between the incident propagating wave and the primary force given in equation (3.6), the secondary force can be written in terms of the primary force as:

$$f_{s1} = \frac{-j f_p}{2 \sin k_b d} e^{-jk_b(l+d)} \quad (3.24)$$

and

$$f_{s2} = \frac{j f_p}{2 \sin k_b d} e^{-jk_b l} \quad (3.25)$$

The magnitudes of these secondary forces are plotted as ratios of the primary force in **figure 3.6a** on page 70. Examination of equations (3.24) and (3.25) and **figure 3.6a** shows that the secondary forces required are very large when the distance between the secondary forces equals an integer number of half-wavelengths of the incident propagating wave as noted in Chapter 2. Thus, it is not possible to suppress both the incident propagating wave and a negative-going propagating wave generated

by the secondary array at these frequencies. The amplitudes of the positive and negative-going propagating waves when this control strategy is implemented are shown in **figure 3.7a** on page 71.

The power supplied by the primary and secondary forces can be determined using equation (3.8), with the displacement at the primary force position being determined using equations (3.1), (3.2), (3.24) and (3.25). The resulting power supplied by the primary force with control is given by:

$$P_p = \frac{\omega |f_p|^2}{8EI k_b^3} \left\{ 1 - \frac{e^{-k_b l} \cos k_b (l + d)}{2 \sin k_b d} + \frac{e^{-k_b (l + d)} \cos k_b l}{2 \sin k_b d} \right\} \quad (3.26)$$

and the power supplied by the secondary forces are given by:

$$P_{s1} = \frac{-\omega |f_p|^2}{16EI k_b^3} \left\{ 1 + \frac{e^{-k_b d}}{2 \sin k_b d} - \frac{e^{-k_b l} \cos k_b (l + d)}{\sin k_b d} \right\} \quad (3.27)$$

and

$$P_{s2} = \frac{\omega |f_p|^2}{16EI k_b^3} \left\{ \frac{e^{-k_b d}}{2 \sin k_b d} - \frac{e^{-k_b (l + d)} \cos k_b l}{\sin k_b d} \right\} \quad (3.28)$$

These are plotted as ratios of the primary power supplied in the absence of control in **figure 3.8a** on page 72. It can be seen that the power supplied by the primary force is largely unaffected by the action of the secondary forces, except at low frequencies, when there is a slight increase due to the interaction of the nearfield waves. The secondary force f_{s1} , absorbs all the power that is carried in the propagating wave incident on the secondary force array (50% of the power supplied by the primary force). It should be noted that this decreases slightly with frequency, as the power dissipated in the beam increases with frequency. This is because the loss factor generated by a complex wavenumber is defined as energy dissipated per unit wavelength. f_{s2} generally neither supplies nor absorbs power, except at very low frequencies, due to the nearfield interaction between the two secondary forces. Its function appears to be to modify the impedance at the position of f_{s1} such that f_{s1} can absorb all the power carried in the incident propagating wave (it was shown in

section 3.2.2 that a single secondary force can absorb only 25% of the power in an incident propagating wave). At frequencies when the distance between the secondary forces is an integer number of half-wavelengths, the forces become very large (as noted above), and f_{s1} actually supplies power. f_{s2} also supplies power to the beam at these frequencies, and this power is dissipated in a very large standing wave generated between the secondary forces. It is clear that if this type of wave suppression control strategy is adopted, then frequencies when the distance between the secondary forces is an integer number of half-wavelengths must be avoided.

3.2.5 Maximization of the Power Absorbed by the Two Secondary Forces

In this case, the vector of secondary forces which maximizes the power absorbed by the secondary forces is derived in Appendix 3 and is given by:

$$\underline{F}_s = \frac{j}{2} \underline{X}_{ss}^{-1} \underline{\alpha}_{sp} f_p \quad (3.29)$$

which is the vector equivalent of equation (3.12). The imaginary part of the point receptance between the secondary forces and the displacements at the secondary force positions is given by:

$$\underline{X}_{ss} = \text{Im} \left\{ \frac{-1}{4EI k_b^3} \begin{bmatrix} 1 + j & e^{-k_b d} + j e^{-j k_b d} \\ e^{-k_b d} + j e^{-j k_b d} & 1 + j \end{bmatrix} \right\} \quad (3.30)$$

and the transfer receptance matrix between the primary force and the secondary force positions is given by:

$$\underline{\alpha}_{sp} = \frac{-1}{4EI k_b^3} \begin{bmatrix} j e^{-j k_b l} + e^{-k_b l} \\ j e^{-j k_b (l+d)} + e^{-k_b (l+d)} \end{bmatrix} \quad (3.31)$$

The secondary forces can be calculated using equations (3.29) - (3.31) and are plotted as ratios of the primary force in **figure 3.6b** on page 70. This figure should be compared with **figure 3.6a**, which is a plot of the secondary forces applied in the

wave suppression control strategy. It can be seen that these figures are similar, except at frequencies close to where the distance between the secondary forces is an integer number of half-wavelengths. When the wave suppression control strategy is implemented, the secondary forces become very large at these frequencies, with a resulting large standing wave between the secondary forces which dissipates a large amount of energy. In a power based control strategy such as this one, energy must be accounted for. Consequently, the secondary force f_{s2} , which supplies the power, reduces to zero at these frequencies, and the control strategy acts as though only one force is applied and the structure behaves as discussed in section 3.2.1.

The amplitudes of the propagating waves upstream of the primary force and downstream of the secondary force array normalised to the amplitude of the propagating wave incident on the secondary force array are shown in **figure 3.7b** on page 71. This shows that the propagating wave upstream of the primary force, A_3 , is largely the same as it is in the absence of control, except at low frequencies and at frequencies where the distance between the secondary forces is an integer number of half-wavelengths. At these frequencies it reduces by a factor of about two. The downstream propagating wave reduces to zero, except at these frequencies, where it rises to about the same magnitude of the upstream propagating wave. **Figure 3.8b** on page 72 shows the power input by the primary and secondary forces and should be compared with **figure 3.8a**. It can be seen that the two figures are very similar, except at the frequencies mentioned above. The strategy of maximizing the power absorbed by the secondary forces has the effect of limiting the magnitude of the control forces at these frequencies, as it accounts for the power supplied by these forces, whereas the wave suppression control strategy does not.

The main conclusion that can be drawn about this control strategy when two secondary forces are applied to an infinite damped beam is that the net effect is very similar to the wave suppression control strategy. They differ at low frequencies where there is interaction between the primary and secondary nearfield waves, and at frequencies close to when the distance between the secondary forces is an integer number of half-wavelengths. Maximizing the secondary power absorption thus

appears to be a good way of implementing wave absorption using measurements local to the secondary source. This was noted by Curtis [37] and it prompted the experiments of Redman-White [38].

3.2.6 Minimization of the Total Power Supplied to the Beam using Two Secondary Forces

In this case, the vector of secondary forces required is derived in Appendix 3 and is given by:

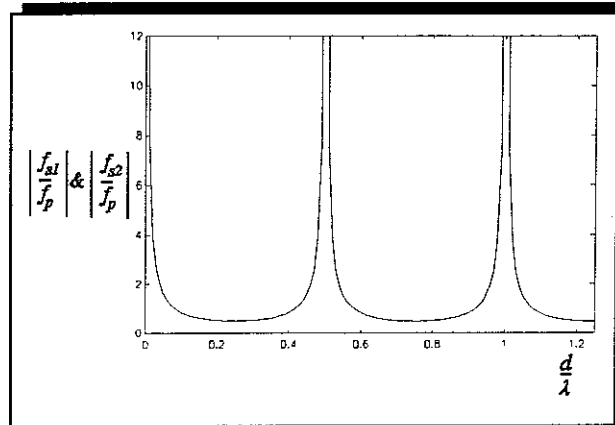
$$\underline{F}_s = - \underline{X}_{ss}^{-1} \underline{X}_{sp} f_p \quad (3.32)$$

where \underline{X}_{ss} is given by equation (3.30) and \underline{X}_{sp} is determined by taking the imaginary part of equation (3.31). The calculated secondary forces are plotted in **figure 3.6c** on page 70. It can be seen that these results are significantly different than with the other two control strategies, and this reflects the fact that this strategy works in a completely different way to wave suppression and power absorption. It has the effect of changing the impedance at the primary force position so that the primary force supplies much less power to the beam, rather than the secondary forces absorbing power. The reduction in the secondary force magnitudes at frequencies where the distance between these forces is an integer number of half-wavelengths should be noted.

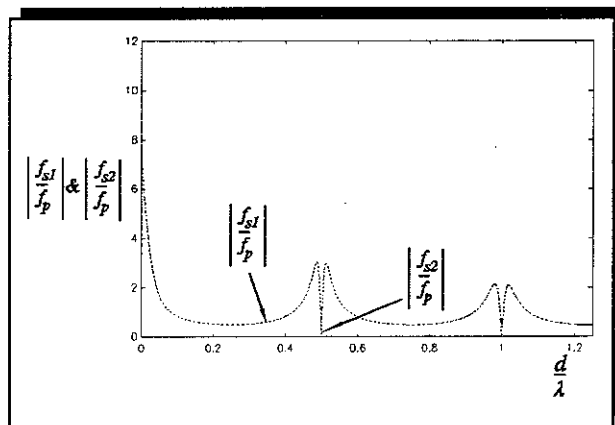
The propagating waves resulting from the implementation of this control strategy are plotted as functions of non-dimensional frequency in **figure 3.7c** on page 71. This shows that at frequencies other than those close to where the distance between the secondary forces is an integer number of half-wavelengths, the downstream wave has largely been suppressed. The amplitude of the propagating wave upstream of the primary force, however, increases with frequency, and the reason for this is again due to energy accounting by the control algorithm. The energy dissipated in the standing wave between the primary and secondary forces is balanced with the energy carried in the upstream propagating wave, such that the power supplied at any

frequency is a minimum. As frequency increases, less power is carried in the small upstream propagating wave than is dissipated in the standing wave. It is interesting to note that if the forces are placed either side of the primary force, rather than on one side, then both the upstream and downstream propagating waves are zero at all frequencies, other than those close to frequencies at which the distance between the two secondary forces is an integer number of half-wavelengths. As noted above, because there is only one primary force, the power supplied by each of the secondary forces is zero. The power supplied by the primary force when (a), the secondary forces are both placed downstream of the primary force and (b), the secondary forces are placed symmetrically either side of the primary force with the same spacing between them, are shown in **figure 3.8c** on page 72. The power supplied in case (b) is generally less over the frequency range considered, as the secondary forces are placed 20 times closer to the primary force than in (a), and thus the standing wave between the primary and secondary forces occupies a much smaller section of beam, and thus dissipates less energy over the frequency range considered.

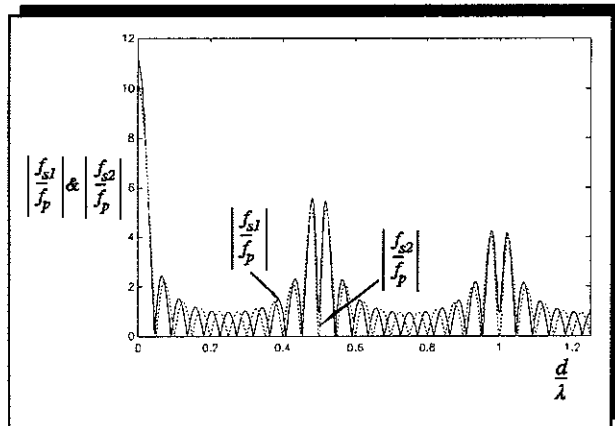
The strategy of minimizing the total power supplied has been demonstrated to be an effective control strategy on an infinite beam, as vibration away from the controlled region of the beam, upstream of the primary force and downstream of the secondary forces is reduced. It is also apparent that this control strategy is equivalent to minimizing the far-field displacement of the beam when the secondary forces are placed either side of the primary force. Thus, to implement the control strategy, displacement can be measured instead of power, which may be much easier in a practical situation, where the measurement of the power supplied by the primary force may be difficult.



(a) Control Strategy: Suppress the A_3 and A_4 Waves

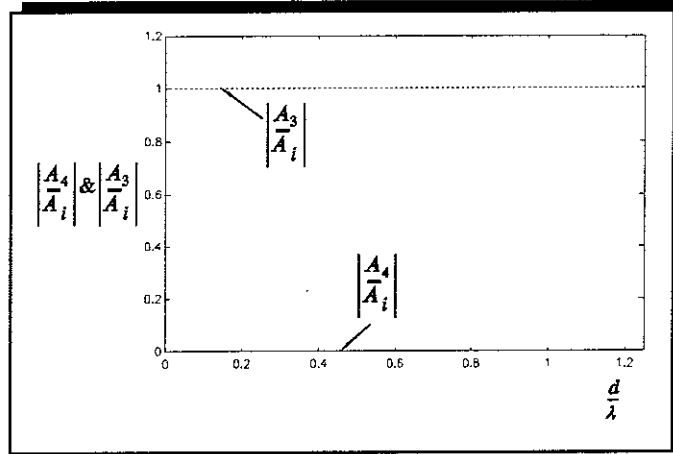


(b) Control Strategy: Maximize the Power Absorbed by the Secondary Forces.

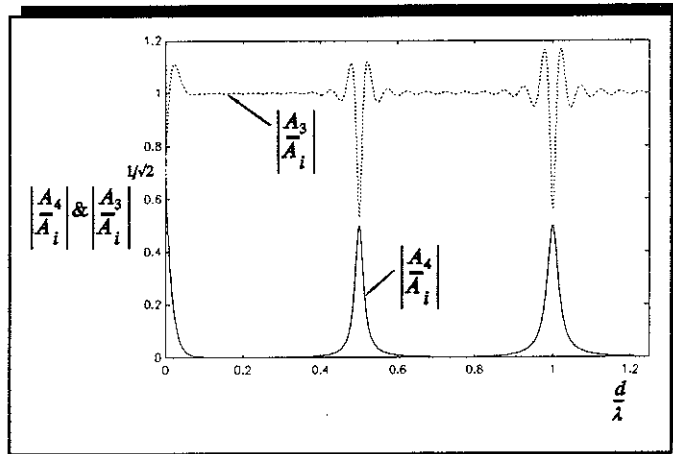


(c) Control Strategy: Minimize the Total Power Supplied to the Beam

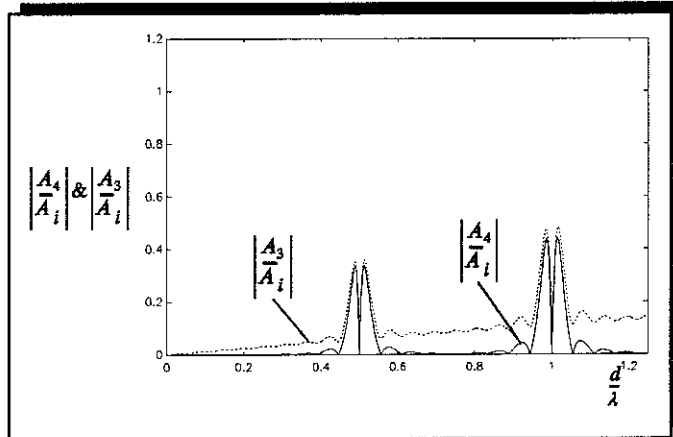
Figure 3.6 Normalised Magnitude of the Two Secondary Forces Required to Implement the Control Strategies on an Infinite Beam. $l = 10d$.



(a) Control Strategy: Suppress the A_3 and A_4 Waves

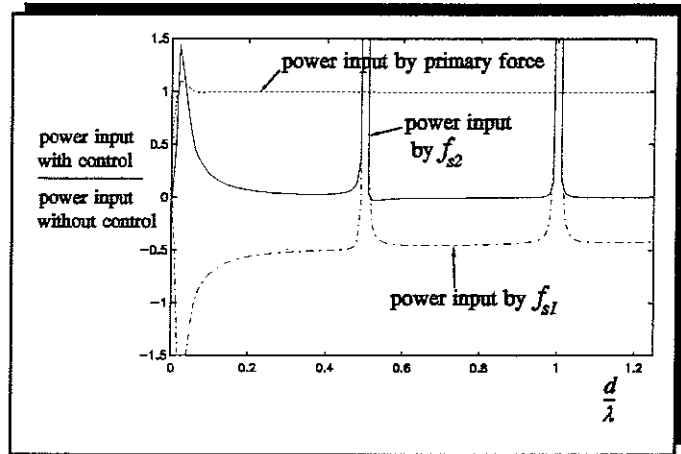


(b) Control Strategy: Maximize the Power Absorbed by the Secondary Forces.

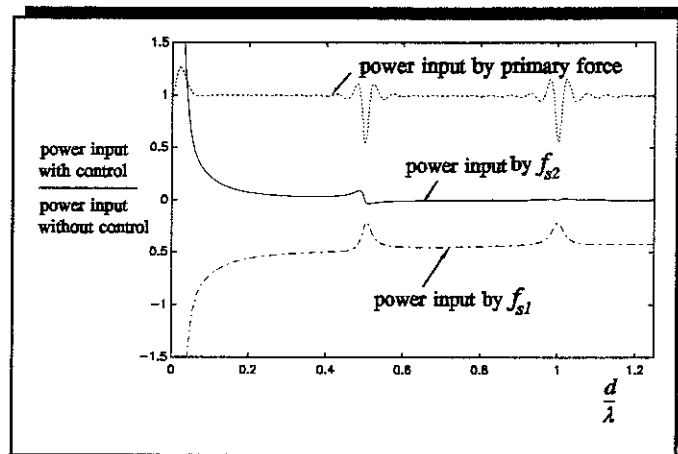


(c) Control Strategy: Minimize the Total Power Supplied to the Beam

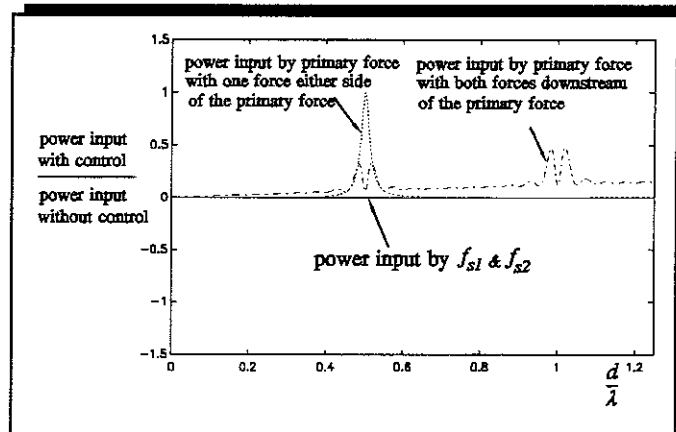
Figure 3.7 Amplitudes of the Propagating Waves with the Control Strategies Implemented on an Infinite Beam with Two Secondary Forces Applied. $l = 10d$.



(a) Control Strategy: Suppress the A_3 and A_4 Waves.



(b) Control Strategy: Maximize the Power Absorbed by the Secondary Forces.



(c) Control Strategy: Minimize the Total Power Supplied to the Beam

Figure 3.8 Ratios of Power Supplied by Forces with Control to the Power Supplied without Control with Two Secondary Forces Applied to an Infinite Beam. $l = 10d$.

3.3 Control Strategies using a Single Secondary Force on a Finite Beam

In this section the effects of boundaries on the control strategies are investigated. The dynamics of the beam are still modelled with waves and the boundaries are modelled using reflection coefficients, as discussed by Mace [16]. This enables the analysis and numerical modelling to be consistent with the infinite beam model discussed hitherto. As mentioned previously, waves reflected from boundaries interfere with the direct waves generated by the primary and secondary forces, producing a complicated wave-field on the beam. A theoretical framework that enables finite beams to be modelled using waves is developed in Appendix 2. The algebraic expressions describing the vibration quantities for a finite system are prohibitively large, so in this section the results are only displayed graphically. As before, three control strategies are considered; wave suppression and the two power based control strategies. A simply supported beam was chosen as the structure on which to apply these control strategies. This type of structure was chosen for simplicity, as there are no nearfield waves generated at the boundaries, and it is the effects of the reflected propagating waves on the control strategies that are of most interest. Other boundaries have more complex interactions between propagating and nearfield waves and unnecessarily complicate the analysis which is being used to establish the physical mechanisms at work.

3.3.1 Wave Suppression

The effects of this control strategy are discussed for a single secondary force as in section 3.2.1. As we are considering a finite beam which has resonance frequencies, the displacement of the beam is shown with the control strategy implemented at a resonance and an off-resonance frequency. The simply supported beam of length L is shown in **figure 3.9**, where the distance between the left-hand boundary and the primary force is $l_1 = 0.2L$ and the distance between the primary and secondary forces is $l = 0.1\pi L$. The secondary force required to suppress the incident wave A_i can be

calculated in a similar way to that for the infinite beam. However, in this case the waves reflected from the left-hand boundary generated by both the primary and secondary forces must be taken into consideration. Figure 3.10a on page 78 is a plot of the secondary force required as a function of non-dimensional frequency. This shows

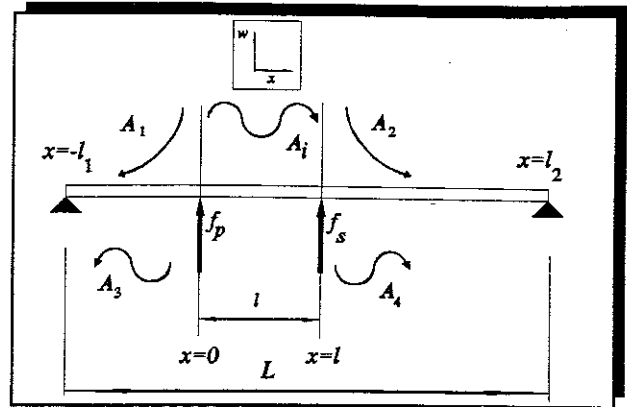


Figure 3.9 An Infinite Beam with One Primary and One Secondary Force Applied $l_1 = 0.2L$, $l_2 = 0.8L$, $l = 0.1\pi L$

that the magnitude of the force required changes with frequency, unlike in the infinite beam case. The peaks occur at frequencies where the distance between the secondary force and left-hand boundary is an integer number of half-wavelengths. This is because the downstream propagating wave generated by the secondary force has two components; a direct wave and a reflected wave. At the frequencies mentioned above these two waves destructively interact, leaving only a small residual wave to suppress the wave generated by the primary force. This situation improves with increasing frequency as the reflected wave reduces in magnitude due to the damping in the beam, leaving a larger residual wave to interact with the wave generated by the primary force. At a frequency of $L/\lambda = 2.5$, the secondary force required is zero, and this is because the primary force is at a node and the beam is not excited.

The normalised displacements of the beam when it is being forced at a resonant and an off-resonant frequency with and without control are shown in **figures 3.11a** and **b** on page 79. It can be readily seen that the control strategy has most affect at resonance, when the displacements at almost all positions on the beam are reduced and the displacement downstream of the secondary force is reduced to zero. Off-resonance, the displacement downstream of the secondary force is also reduced to zero, as required by the control strategy, but upstream of the secondary force there is a slight increase in vibration level in the form of a standing wave. What these figures do not show are the new resonance frequencies created by the action of the secondary force. These frequencies occur when the distance between the secondary

force and the left-hand boundary equals an integer number of half-wavelengths. From the point of view of the primary force the beam has been shortened by approximately a factor of two ($l_1 + l = 0.514L$), as the propagating wave is stopped at the position of the secondary force. These "new" resonances can be seen on the graph of power supplied to the beam in **figure 3.12a** on page 80. Clearly, the closer that the secondary force can be placed to the primary force the better. As well as restricting the vibration to a smaller area around the primary force, the number of resonances on the active part of the beam will be reduced and the fundamental resonance frequency will be pushed higher. In contrast to the infinite beam case, the secondary force now supplies power to the beam at all frequencies.

3.3.2 Maximization of the Power Absorbed by the Secondary Force

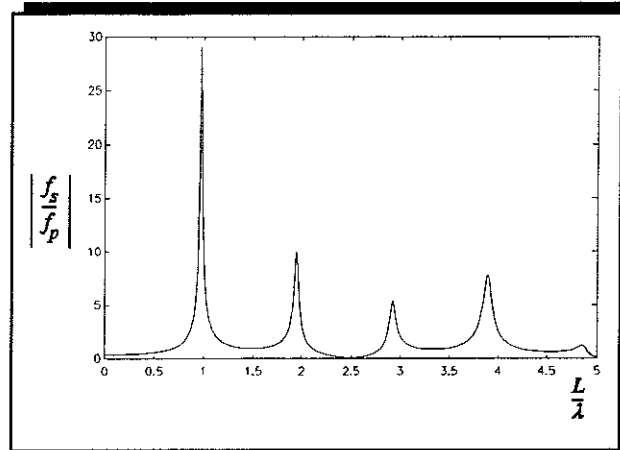
This strategy was applied to an infinite beam in section 3.2, where it was shown that it was very similar to the wave suppression control strategy when two secondary forces are applied. The question addressed in this section is whether this is still the same on a finite beam. The structure considered is shown in **figure 3.9**. The magnitude and phase of the secondary force required to maximize the power absorbed is given by equation (3.12). As before, X_{ss} is the imaginary part of the point receptance of the beam at the secondary force position, and α_{sp} is the transfer receptance between the primary force and the displacement at the secondary force position. However, these receptances now include the direct waves and the waves reflected from the boundaries. The force has a complicated frequency dependency and its normalised magnitude is shown in **figure 3.10b** on page 78. The resulting beam displacement both off-resonance ($L/\lambda=3.25$) and at resonance ($L/\lambda=3.5$) are shown in **figures 3.11c** and **d** on page 79. It is evident that this control strategy is detrimental when the beam is excited off-resonance, as the displacement is increased at practically all positions on the beam. At resonance there is some benefit, as the beam displacement is reduced by a factor of two as can be seen in **figure 3.11d**.

The power supplied by the forces is shown in **figure 3.12b** on page 80. This shows that when control is implemented, the power supplied by the primary force is significantly increased at all frequencies, other than those close to the resonance frequencies. It can also be seen that the power absorbed by the secondary force follows the same trend. This control strategy demands that the secondary force absorb as much power as it can, and in this case the way in which the secondary force can meet this demand is for it to cause the primary force to supply more power. It does this by using the boundaries to direct the appropriate waves to change the impedance of the beam at the primary force position such that more power can be supplied. Some of this power is, of course, absorbed by the secondary force, and some is dissipated by the internal damping mechanisms in the beam. This phenomenon is further discussed later in this chapter. This control strategy does not appear to be a practical proposition for a finite beam, since it generally has a detrimental rather than beneficial effect on the overall response of the beam.

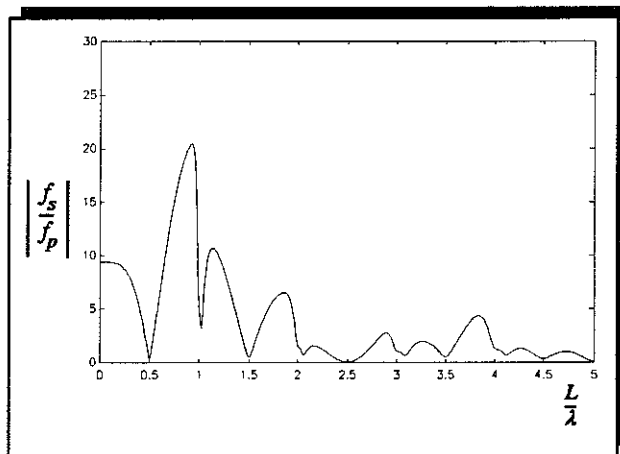
3.3.3 Minimization of the Total Power Supplied to the Beam

The structure considered in this section is shown in **figure 3.9**. The secondary force required is determined using equation (3.18) and is plotted in **figure 3.10c** on page 78. It can be seen that there is again a complicated dependence of the secondary force on frequency, but the magnitude of force required is considerably less than that with the other two control strategies (c.f. with **figures 3.10a & b**). The displacement of the beam under off-resonance and resonance conditions are shown in **figures 3.11e and f** on page 79. It can be seen that the effect is similar to the wave suppression control strategy (**figures 3.11a and b**), but the displacement downstream of the secondary force is not zero. The power supplied by the forces are plotted in **figure 3.12c** on page 80. This shows that this control strategy is effective in the respect that the overall power level is not increased at any frequency and that there is resonance suppression for alternate modes.

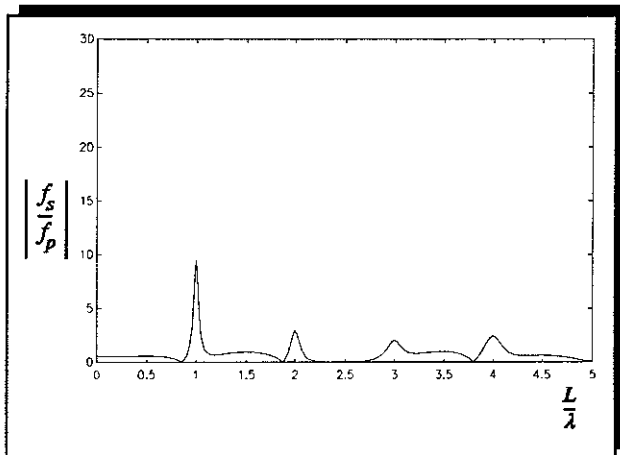
It is interesting to note that some work has been conducted on the implementation of this control strategy for the acoustic case. Johnson and Elliott [41] made use of the fact when the total power supplied to a system is minimized, the power supplied by the secondary source is zero (as can be seen in **figure 3.12c**). By only having phase knowledge of the primary source, they were able to implement control by monitoring the power supplied by the secondary source only. This makes the implementation of this control strategy much easier and significantly helps in a practical situation where the direct measurement of the power supplied by the primary force may be difficult. This method was used to implement control in the experimental study discussed later in this chapter.



(a) Control Strategy: Suppress the Incident Propagating Wave

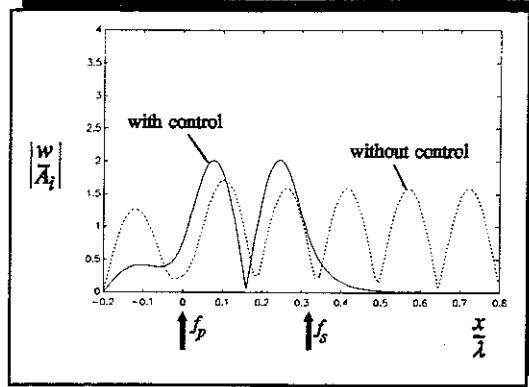


(b) Control Strategy: Maximize the Power Absorbed by the Secondary Force.

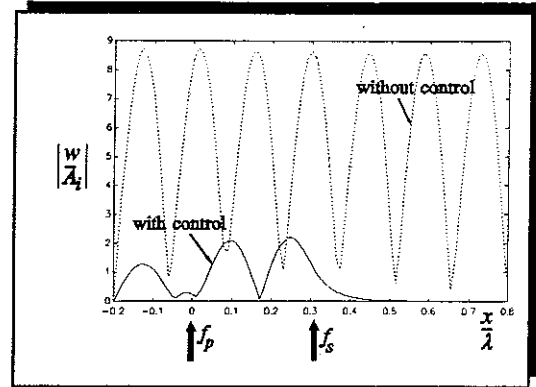


(c) Control Strategy: Minimize the Total Power Supplied to the Beam

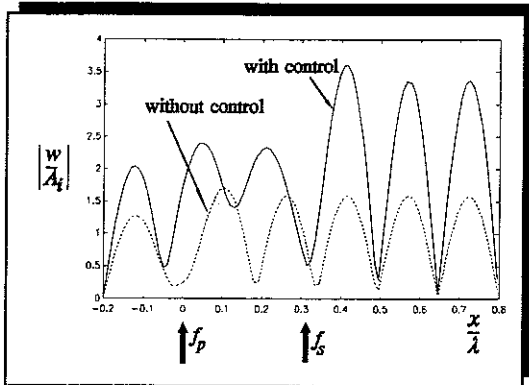
Figure 3.10 Normalised Magnitude of the Single Secondary Force Required to Implement the Control Strategies on a Finite Beam



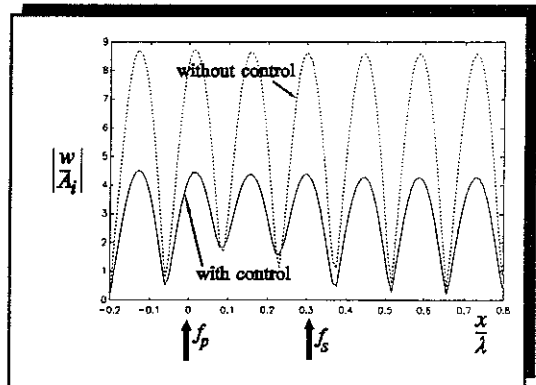
(a) Wave Suppression, $L/\lambda = 3.25$



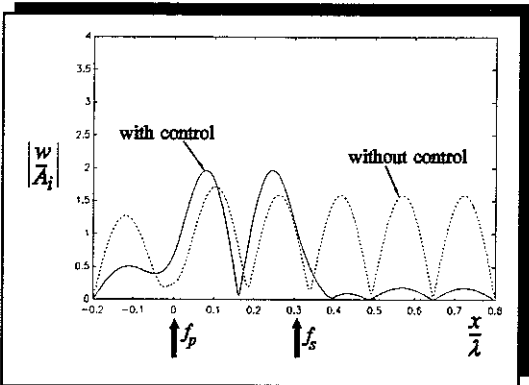
(b) Wave Suppression, $L/\lambda = 3.5$



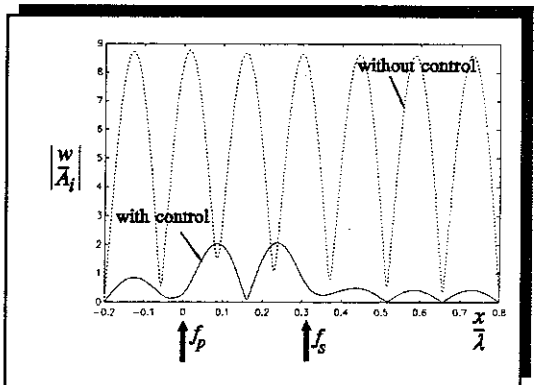
(c) Power Absorption, $L/\lambda = 3.25$



(d) Power Absorption, $L/\lambda = 3.5$

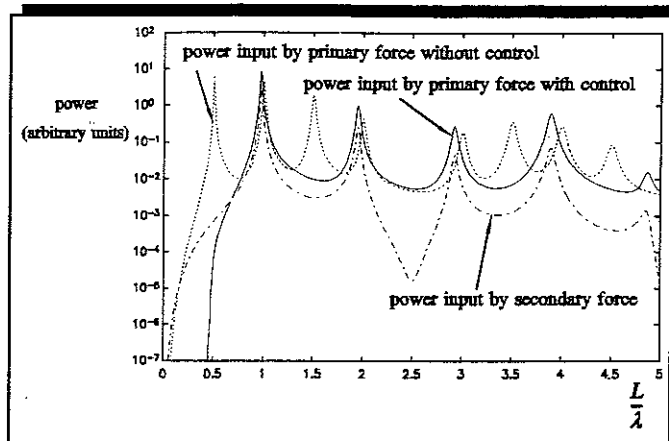


(e) Power Minimization, $L/\lambda = 3.25$

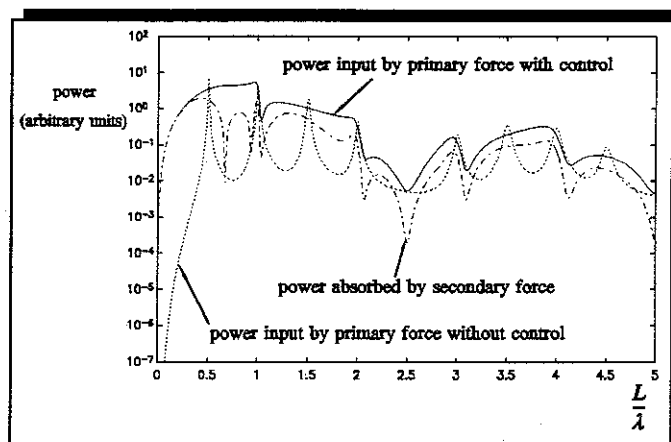


(f) Power Minimization, $L/\lambda = 3.5$

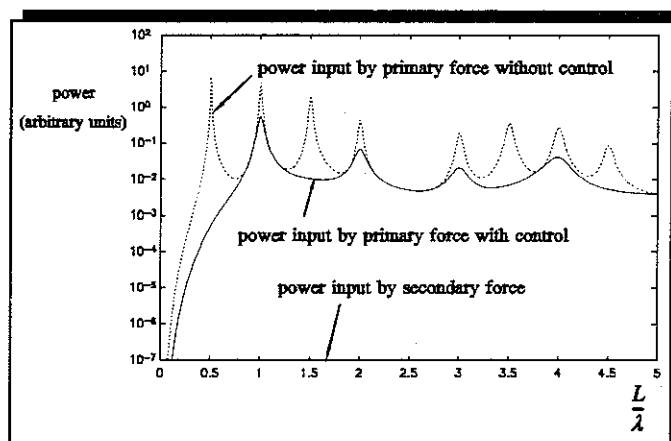
Figure 3.11 Normalised Displacement of a Finite Beam with One Secondary Force Applied.



(a) Control Strategy: Suppress the Incident Propagating Wave



(b) Control Strategy: Maximize the Power Absorbed by the Secondary Force.



(c) Control Strategy: Minimize the Total Power Supplied to the Beam

Figure 3.12 Power Supplied by the Forces with Control with One Secondary Force Applied on a Finite Beam

3.4 Control Strategies using Two Secondary Forces on a Finite Beam

The structure considered in this section is shown in **figure 3.13** and is configured in a similar way to the structure discussed in the previous section. It has two simply supported ends, but there is an additional secondary force applied at a distance $d = 0.1l$ from the other secondary force.

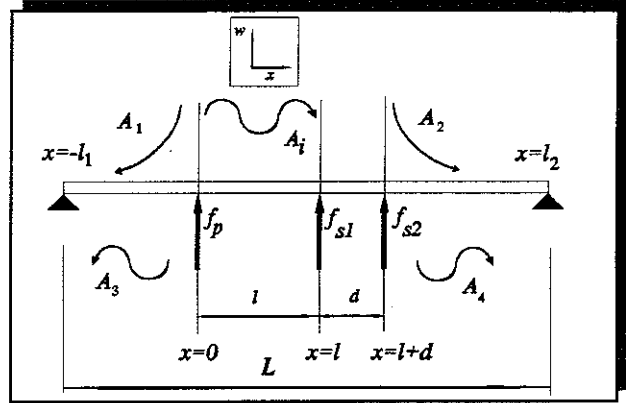


Figure 3.13 An Infinite Beam with One Primary and Two Secondary Forces Applied $l_1 = 0.2L$, $l_2 = 0.8L$, $l = 0.1\pi L$ and $d = 0.1l$.

3.4.1 Wave Suppression

This control strategy suppresses the positive and negative-going waves propagating waves away from the secondary force array. The magnitudes of the secondary forces required are calculated in a similar way to the infinite beam case, but taking into consideration the reflected waves from the left-hand boundary. They are plotted in **figure 3.14a** on page 85. It is interesting to note that in the low frequency limit, the magnitude of the secondary forces are finite, unlike the infinite beam case, and tend towards "the static case", as expected. These forces become very large when the distance between them is an integer number of half-wavelengths, but this occurs at a higher frequency than is shown on this figure. As two secondary forces are applied, there is no negative-going wave generated by the secondary force array. Thus, unlike the case where one secondary force is applied, there is no reflected wave from the left-hand boundary to cause problems with generating a wave downstream to destructively interfere with the wave generated by the primary force. Therefore, there are not the same peaks and troughs in the magnitudes of the secondary forces required as in the single force case. This is quite important when it comes to

implementing these control strategies in practice, as *the capacity of the actuators required with two secondary forces is much less than if a single secondary force is used.*

The displacement of the beam when it is forced off-resonance and at resonance are shown in **figures 3.15a and b** on page 86. The effects are similar to when a single secondary force is applied, but now the standing wave between the primary and secondary force array is suppressed.

The power supplied by the forces with control is shown in **figure 3.16a** on page 87, where it can be seen that as in the infinite beam case, f_{s1} absorbs power, but now f_{s2} supplies power to the beam. As discussed before, the effect of f_{s2} is to change the impedance at the position of f_{s1} such that it can absorb all the power carried in a propagating wave. **Figure 3.17** on page 88 provides perhaps the best way of comparing the three control strategies described in this section. **Figure 3.17a** shows the power supplied by the primary force only with and without control, and indicates that the secondary forces have the effect of making the beam appear semi-infinite to the primary force. As there are no negative-going propagating waves generated by the secondary force array, the primary force is not influenced by the right-hand boundary, but it is, however, influenced by the finite length of beam to the left. The net result is that the primary force supplies less power at the original resonance frequencies, but supplies more power to the beam at the original off-resonance frequencies.

3.4.2 Maximization of the Power Absorbed by the Secondary Forces

In this case the forces required are derived using equation (3.29) and are plotted in **figure 3.14b** on page 85. The magnitudes of these forces are considerable and should be compared with those in the wave suppression case shown in **figure 3.14a**. The displacement of the beam for off-resonance and resonance conditions are plotted in

figures 3.15c and d on page 86. In both cases the displacement of the beam downstream of the secondary force is considerably reduced, but in the off-resonance case the displacement upstream of the secondary force array is significantly increased. Under resonance conditions, the upstream displacement is largely unaffected by the secondary forces. Recalling the infinite beam case, the strategies of wave suppression and power absorption result in similar beam displacements. In this case, however, there is considerable difference which can be seen by comparing **figures 3.15c and d** with **3.15a and b**.

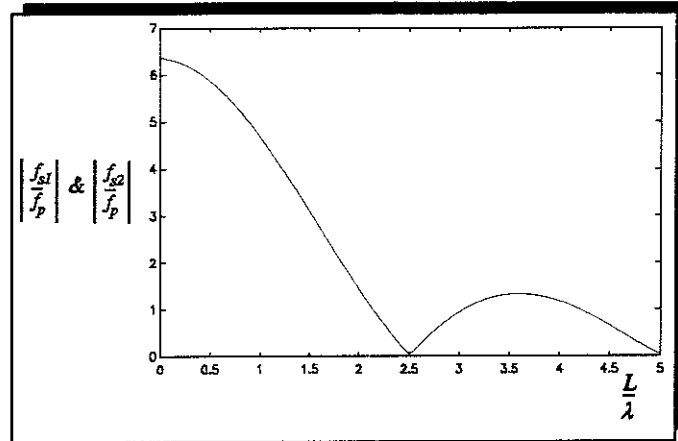
The power supplied by the forces are shown in **figure 3.16b** on page 87. It can be seen that this is similar to **figure 3.16a**, the wave suppression control strategy, but the powers that are supplied and absorbed are an order of magnitude larger. **Figure 3.17b** on page 88 shows the power supplied by the primary force with and without control. It can be seen that the power supplied by the primary force is increased at all frequencies other than at the resonance frequencies. The primary force effectively "sees" a beam that has the impedance of an uncontrolled beam *at resonance*.

This control strategy, which appeared encouraging on an infinite beam, is thus not so attractive on a finite beam. Although the displacement downstream of the secondary forces is reduced, the vibration levels upstream are increased, and the primary force supplies much more power to the beam. One way of overcoming this problem is to measure the "de-reverberated" power absorbed by the secondary forces instead of the total power. The "de-reverberated" power is the power absorbed by the secondary forces computed using the anechoic input impedance of the beam and thus excludes the power increases due to the reverberant beam behaviour. Thus, the secondary forces effectively see an infinite beam, and the behaviour of the beam under control is similar to that discussed in section 3.2. A similar technique to this was used by MacMartin and Hall [43], where they used the de-reverberated drive point mobility at a single point as a local model of the dynamics of a beam, and has recently been discussed for transverse waves on a string by Hiram [44].

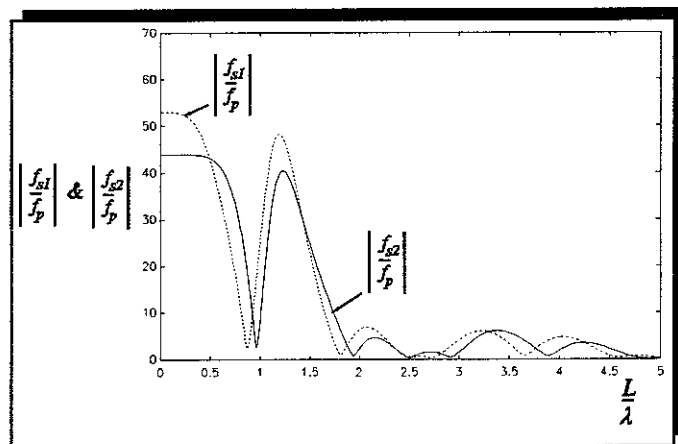
3.4.3 Minimization of the Total Power Supplied to the Beam

In this case the control forces can be determined using equation (3.32) and are plotted in **figure 3.14c** on page 85. This figure should be compared with **figures 3.14a** and **b**, where it can be seen that the magnitudes of the forces required to implement this control strategy are generally less than those required for the other two strategies. As mentioned previously, this can be an important issue when considering implementation of the control strategy, as smaller actuators can be used.

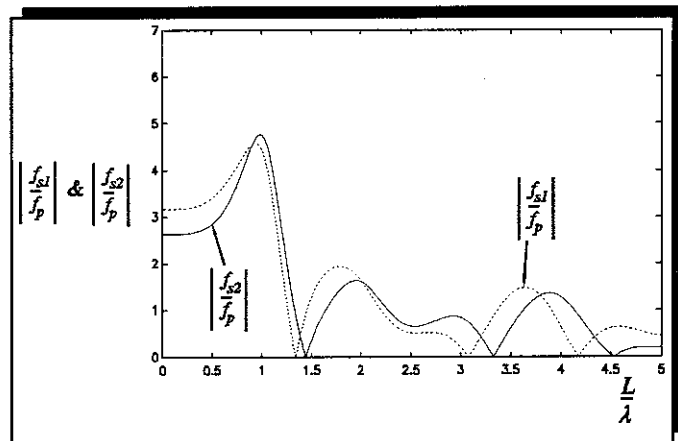
The displacement of the beam off-resonance and at resonance can be seen in **figures 3.15e** and **f** on page 86. These figures show that the displacement upstream of the primary force and downstream of the secondary force array has been reduced, but in the off-resonance condition the amplitude of vibration between the primary and secondary forces has marginally increased. The boundaries, in this case, only have a slight affect on the behaviour of the controlled beam and the power supplied by the primary force is very small as can be seen by examining **figure 3.16c** on page 87. As with the infinite beam case, the implementation of this control strategy could be approximated by minimizing the displacement of the beam upstream of the primary force and downstream of the secondary force. The residual vibration of the structure would then be restricted to the section of beam between the primary and secondary forces. It should be noted that if the displacement of the beam either side of the secondary forces is minimized, instead of measuring, and minimizing the power supplied directly, then there is the practical issue of observability when placing transducers to monitor displacement on a finite beam. The main advantage of this control strategy can be seen by examining **figure 3.17c** on page 88, the power supplied by the primary force with and without control. Less power is supplied at all frequencies when control is implemented. Rather than absorb power or suppress waves, this control strategy actively changes the impedance at the primary force position such that less power is supplied to the beam by the primary force, as the impedance seen by the primary force is always that of an "anti-resonant" beam.



(a) Control Strategy: Suppress the Incident Propagating Wave

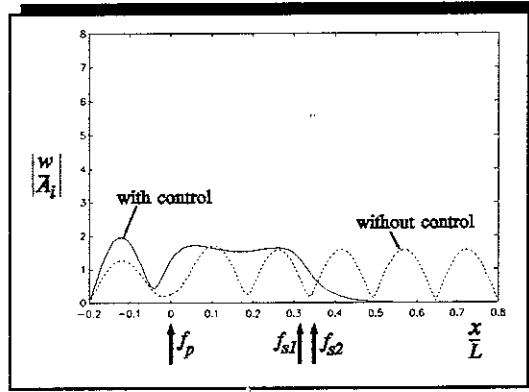


(b) Control Strategy: Maximize the Power Absorbed by the Secondary Force. (note the change in scale)

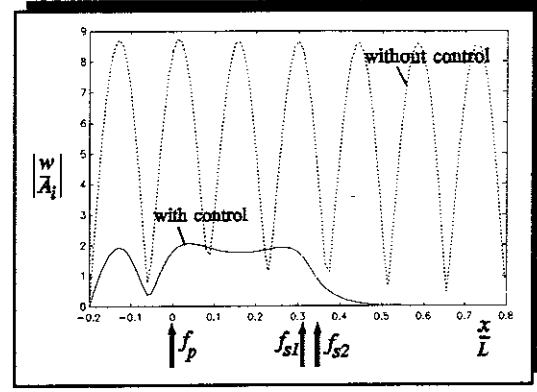


(c) Control Strategy: Minimize the Total Power Supplied to the Beam

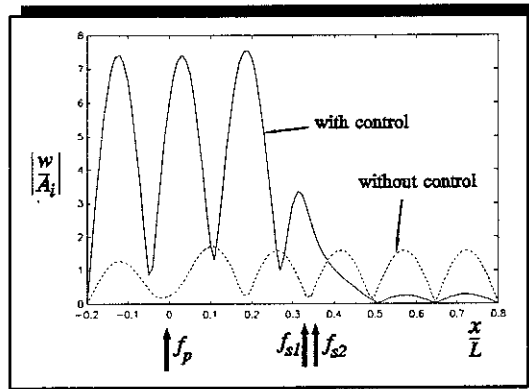
Figure 3.14 Normalised Magnitudes of the Two Secondary Forces Required to Implement the Control Strategies on a Finite Beam



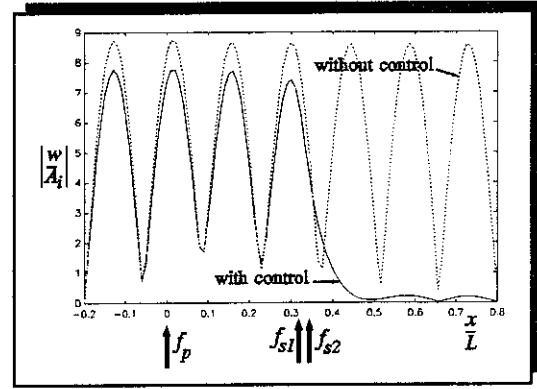
(a) Wave Suppression, $L/\lambda = 3.25$



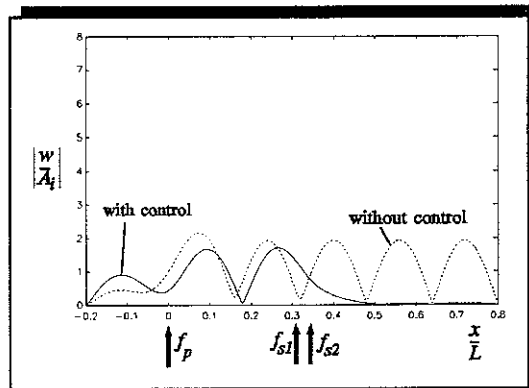
(b) Wave Suppression, $L/\lambda = 3.5$



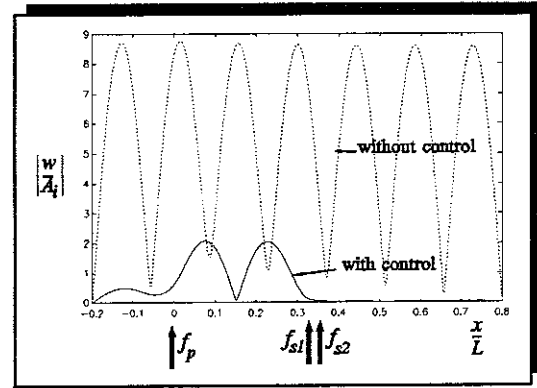
(c) Power Absorption, $L/\lambda = 3.25$



(d) Power Absorption, $L/\lambda = 3.5$

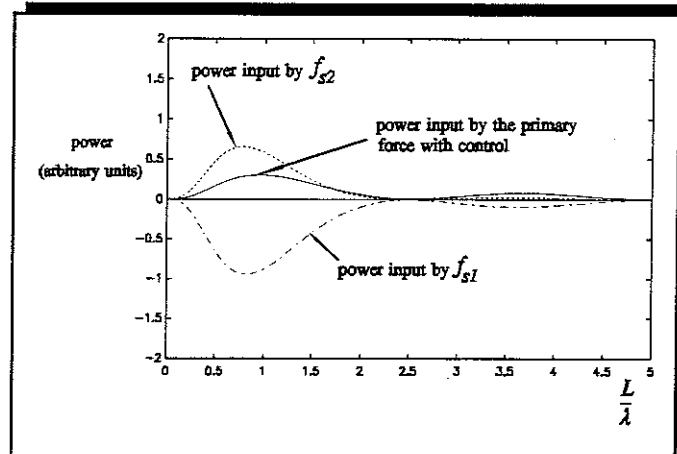


(e) Power Minimization, $L/\lambda = 3.25$

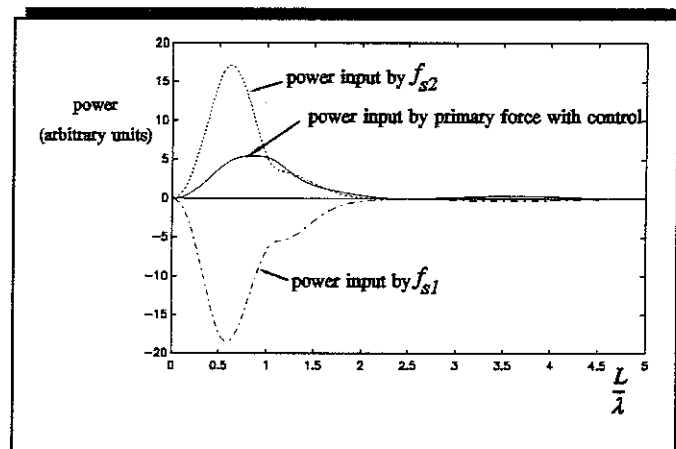


(f) Power Minimization, $L/\lambda = 3.5$

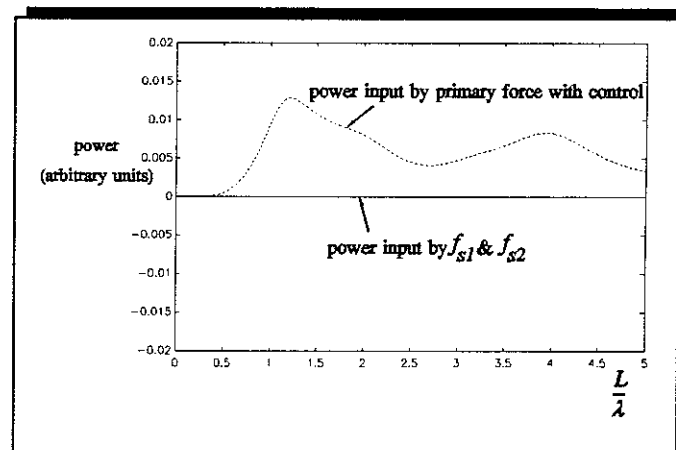
Figure 3.15 Normalised Displacement of a Finite Beam with Two Secondary Forces Applied



(a) Control Strategy: Suppress the Incident Propagating Wave

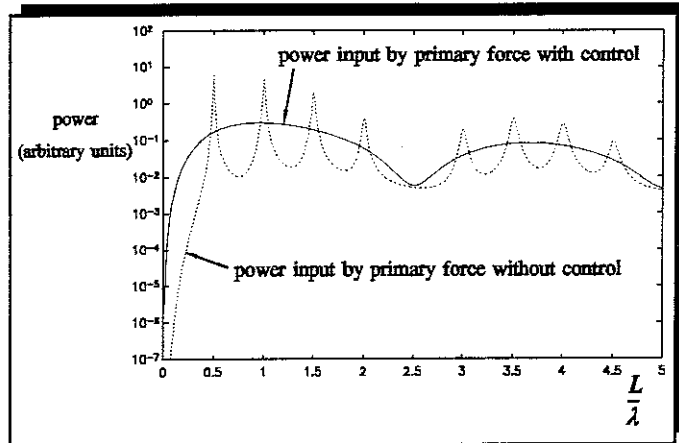


(b) Control Strategy: Maximize the Power Absorbed by the Secondary Force.

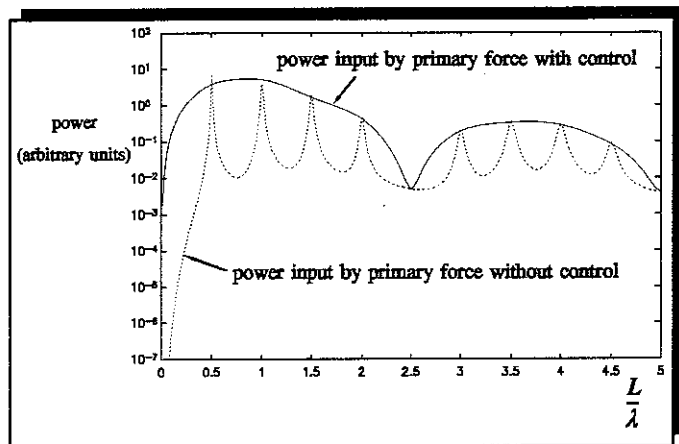


(c) Control Strategy: Minimize the Total Power Supplied to the Beam

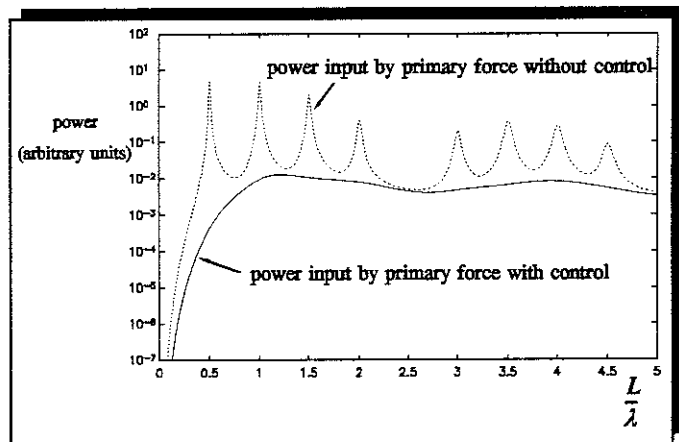
Figure 3.16 Power Supplied by the Forces with Control when Two Secondary Forces are Applied on a Finite Beam



(a) Control Strategy: Suppress the Incident Propagating Wave



(b) Control Strategy: Maximize the Power Absorbed by the Secondary Force.



(c) Control Strategy: Minimize the Total Power Supplied to the Beam

Figure 3.17 Power Supplied by the Primary Forces with Control with Two Secondary Forces Applied on a Finite Beam

3.5 Discussion

The analysis conducted in this chapter has shown that in general, a finite beam behaves rather differently than an infinite beam when control forces are applied. On an infinite beam, the local control strategy of maximum power absorption using two secondary forces has been shown to be very similar to wave suppression, effectively absorbing a propagating flexural wave. However, when this strategy is employed on a finite beam it changes the impedance of the beam at the primary force position to that of a resonant beam at all frequencies, resulting in more power being supplied by the primary force under the action of control. To examine the cause of this, the effects of this strategy on a semi-infinite beam with two secondary forces applied,

such as that shown in **figure 3.18**, was explored, where the primary force is applied at the free end of the beam. The distance between the primary and secondary forces l is ten times the distance between the secondary forces, d . The power supplied by the forces normalised to the power supplied by the primary force without control is shown in **figure 3.19**. This figure should be compared with **figure 3.8b** in which the normalised powers are an order of magnitude smaller. It can be seen that the power supplied by the primary force has increased substantially due to the presence of the boundary. It is clear that it is

the upstream boundary that allows the secondary sources to couple in so strongly to the primary source that its power output can be increased, to allow large power

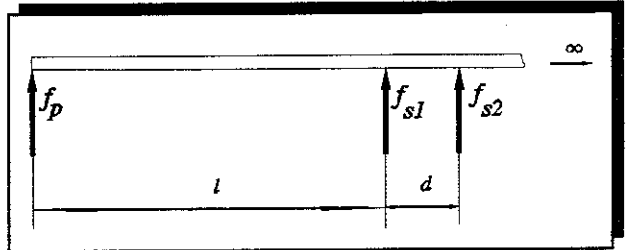


Figure 3.18 A semi-infinite Beam with One Primary and Two Secondary Forces Applied

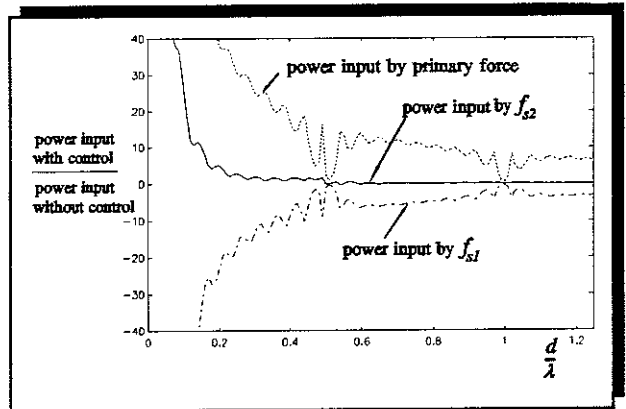


Figure 3.19 Power Supplied by the Primary Force on a Semi-Infinite Beam with Two Secondary Forces Configured to Absorb Maximum Power

absorption by the secondary sources.

The advantages of using the power minimization control strategy on a finite beam when one and two forces are applied have been clearly demonstrated. When either one or two secondary forces are applied, the control effort is less than with the other two control strategies, potentially resulting in smaller actuators. It has been shown that this strategy is similar to minimizing the far-field displacement away from the secondary force actuators. This appears attractive as it is generally easier to measure displacement rather than power flow into a structure. However, there is a low frequency limit imposed with this method due to the presence of a nearfield wave at the sensor position as discussed in Chapter 2.

The physical effects of the three control strategies using a pair of secondary forces on a finite beam are most clearly summarized in **figure 3.17**, which shows the power output of the primary force with and without control for the three cases. For wave control the beam effectively becomes semi-infinite, and the power supplied by the primary force is reduced at the original resonance frequencies, and increased at the original off-resonance frequencies. In the power absorption control strategy the power supplied by the primary force is increased at all frequencies other than at the original resonance frequencies, and the primary force effectively sees a beam that has the impedance of an uncontrolled beam at resonance. With the power minimization strategy the impedance at the primary force position is modified to that of an "anti-resonant" beam so less power is supplied to the beam by the primary force at all frequencies.

3.6 Experimental Investigation

3.6.1 Introduction

To validate the theoretical analysis concerning the active control of beam dynamics discussed in this chapter, some simple experiments were carried out. The wave

suppression and power control strategies were implemented on a slender aluminium beam with an anechoic flexural termination at one end. The anechoic termination had a measured reflection coefficient of less than 0.1 [45], and the specification for the beam is given in Appendix 4. Three experiments were conducted; the implementation of the wave suppression and the two power control strategies using one secondary force only. The implementation of the control strategies experimentally with two secondary sources is an attractive possibility, but it would be difficult to achieve by hand and would thus require an automatic controller; it was therefore not attempted.

A 4 m x 30 mm x 6.12 mm aluminium beam, that was free at one end and anechoically terminated at the other end was suspended from pieces of cord attached to a supporting structure. A type VP2 Derritron force shaker driven by a 25 watt amplifier was fitted at the free end which acted as the primary force to excite the beam laterally. The secondary force was generated by a similar shaker. This configuration is shown in **figure 3.20**. The power supplied by the primary force was

calculated from measurements at the primary source position made using a B&K type 4368 accelerometer and a B&K type 8200 force transducer. The acceleration downstream of the secondary source was measured with a B&K type 4369 accelerometer and was integrated twice to give displacement. A full list of the experimental equipment is given in Appendix 4.

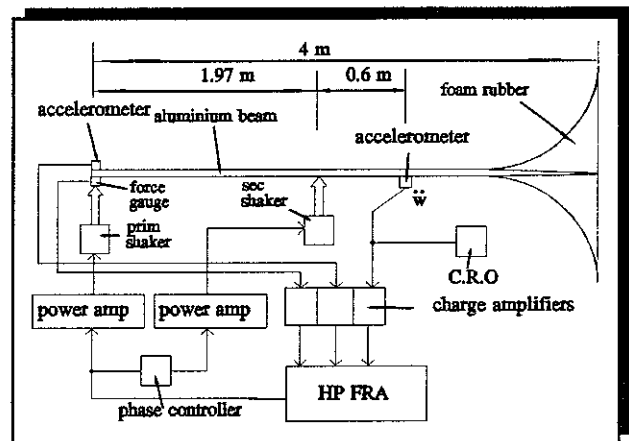


Figure 3.20 Experimental Set up with One Primary and One Secondary Force

3.6.2 Suppression of a Propagating Wave

As the beam considered in this chapter is "semi-infinite", and as only frequencies greater than 100 Hz are of concern (frequency range of interest is 100 Hz - 1 kHz),

there is only a flexural propagating wave on the uncontrolled beam at the secondary force position, as the nearfield wave generated by the primary force will have decayed to a negligible amplitude. Thus, the problem of reducing the far-field vibration downstream of the secondary source is the same as that of suppressing the incident propagating flexural wave. The control effort required on a semi-infinite beam is different than that required on the infinite beam, discussed in section 3.2, as it changes with frequency. At frequencies when the distance between the secondary force and the free end equals an integer number of half-wavelengths, then the required force is very large. This is because the negative-going propagating wave generated by the secondary force is reflected from the free end and destructively interferes with the positive-going propagating wave generated by the secondary force. Thus, at these frequencies there is only a small residual wave to destructively interfere with the positive-going propagating wave generated by the primary force.

In this section the experiment to suppress a propagating flexural wave using a secondary force actuator is discussed. The theory is briefly presented in order to allow comparison with experimental results.

Consider the semi-infinite beam shown in **figure 3.21**. The positive-going propagating wave A_4 , has contributions from the primary and secondary forces f_p and f_s , and is given by the expression:

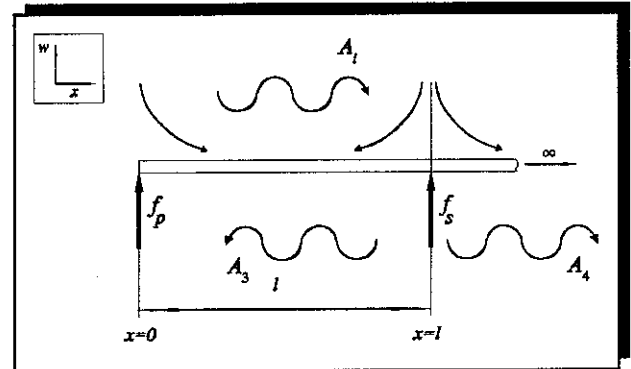


Figure 3.21 Semi-infinite Beam Showing the Position of the Primary and Secondary Forces

$$A_4 = \frac{-j f_p}{2 E I k_b^3} (1 - j) e^{-j k_b l} - \frac{j f_s}{4 E I k_b^3} (1 - j e^{-j 2 k_b l}) \quad (3.33)$$

To determine the secondary force required to reduce the far-field vibration downstream of the secondary force to zero, A_4 can be set to zero in this equation,

which can then be rearranged to give:

$$\frac{f_s}{f_p} = \frac{2}{\sin k_b l - \cos k_b l} \quad (3.34)$$

The modulus of this over the frequency range 100 Hz to 1 kHz is plotted in **figure 3.22**, for the aluminium beam. This figure shows that the secondary force requirements are very large at certain frequencies as discussed above, and therefore the secondary force has to have a much greater capacity than the primary force.

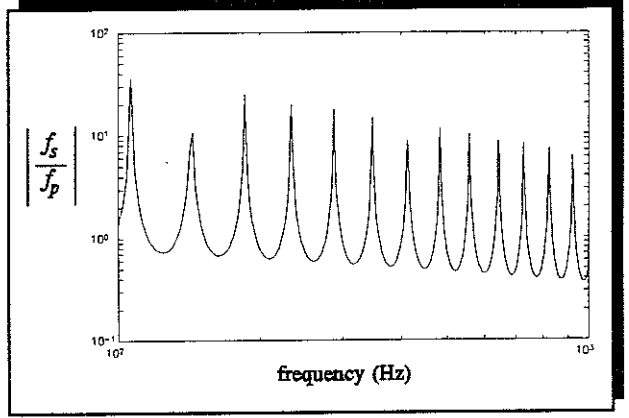


Figure 3.22 Theoretical Ratio of the Secondary Force to the Primary Force Required to Suppress an Incident Flexural Propagating Wave on a Semi-Infinite Beam

The Power supplied by the primary force P_p can be calculated from the expression:

$$P_p = -\frac{\omega}{2} \text{Im}\{f_p^* w(0)\} \quad (3.35)$$

where * stands for the complex conjugate and $w(0)$ is the lateral displacement at the primary force position. The action of the secondary force changes this

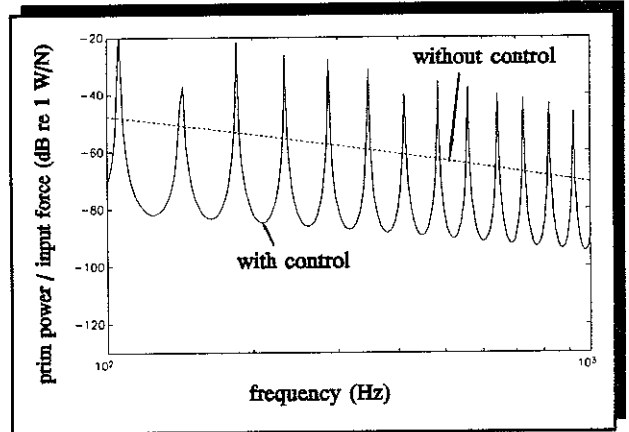


Figure 3.23 Theoretical Power Supplied to the Beam by the Primary Force with and without Control

displacement as discussed previously, and thus the power supplied by the primary force changes under the influence of the secondary force. The power supplied by the primary force per unit input force with and without control as a function of frequency is plotted in **figure 3.23**. This figure clearly shows that the effect of the secondary control force is to change the impedance of the beam as seen by the primary force. It changes from a semi-infinite beam to a finite beam of length l , which is evident by the resonant behaviour. Although the far-field displacement of the beam downstream

of the secondary force is reduced to zero under the action of the secondary force, there are frequencies where there is an increase in the power supplied to the structure by the primary force. This power is dissipated by internal damping mechanisms in the standing wave between the primary and secondary forces. A small amount of power is supplied by the secondary force which is also dissipated in the beam.

An experiment was set up as shown in **figure 3.20**. The response of the beam in the absence of the secondary force was first measured, with the secondary force shaker attached to the beam but inactive. The beam was excited at frequencies between 100 Hz and 1 kHz at 10 Hz intervals using the swept sine technique with a Hewlett Packard type 3566A Frequency Response Analyzer. The point acceleration at the primary force position and the transfer acceleration between the primary force and the acceleration downstream of the secondary force were measured. Having recorded the dynamic response of the beam in the absence of active control, it was then necessary to test the effects of applying a controlled secondary force. The beam was excited using the primary shaker at discrete frequencies between 100 Hz and 1 kHz at intervals of 10 Hz. At each single frequency, when the response of the beam had reached a steady state, the secondary force was applied using the secondary shaker. The amplitude and phase of the electrical power supply to this shaker were adjusted using the gain control on the power amplifier and a locally manufactured phase controller [46], until the downstream acceleration of the beam was a minimum as measured by the accelerometer and displayed on an oscilloscope. Once this condition was achieved, the frequency response functions of primary point acceleration and transfer acceleration between the primary force and the downstream acceleration were measured. On completion of this measurement, the excitation frequency was incremented by 10 Hz and the process of adjusting the secondary force to minimize the downstream displacement was repeated.

The displacement of the beam downstream of the secondary force per unit input primary force with and without control is plotted in **figure 3.24**. Overlaid on this graph is the theoretically calculated displacement in the absence of the secondary force; the theoretical downstream displacement when control is implemented is, of

course zero.

The effectiveness of the active control can be seen by plotting the change in the amplitude of vibration downstream of the secondary force, when the secondary force is applied, as shown in **figure 3.25**.

Active control using power as a controlling parameter is implemented in later sections. In order that those control strategies can be compared with the control strategy of suppressing a propagating wave, the power supplied by the primary force with and without control is plotted. The primary power was computed using the imaginary part of the measured primary point acceleration and the primary force with and without control, and is shown in **figure 3.26**.

The results in this section have demonstrated that the control strategy of minimizing the downstream displacement of the beam downstream of the secondary source can be achieved with a simple force actuator. Reductions in

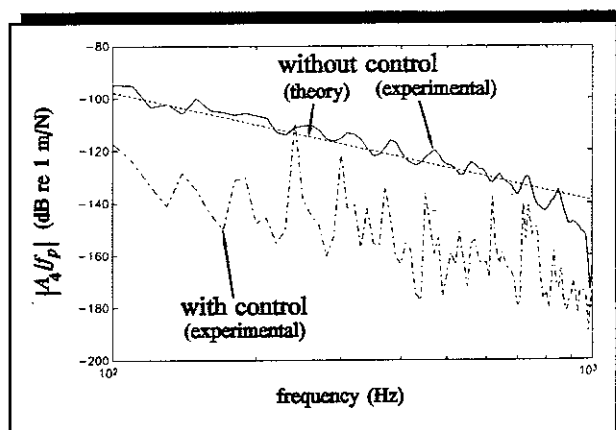


Figure 3.24 Measured Displacement per Unit Input Primary Force Downstream of the Secondary Force

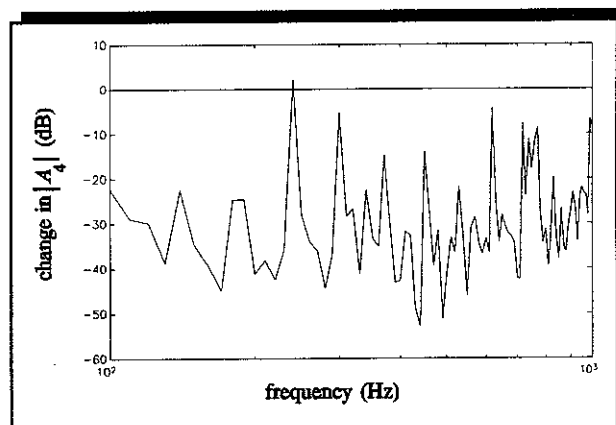


Figure 3.25 Reduction in Measured Downstream Displacement

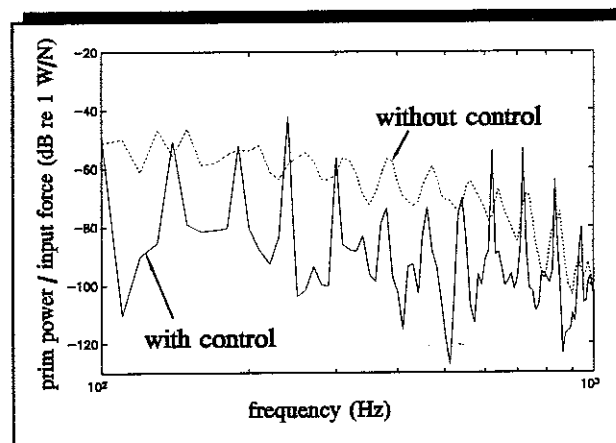


Figure 3.26 Measured Power Supplied to the Beam by the Primary Force with and without Control (c.f. **figure 3.23**)

the downstream displacement of up to 50 dB were achieved. However, examination of **figure 3.25** shows that there were frequencies when only a small reduction in downstream displacement was achieved. These frequencies were close to those when the distance l , between the secondary force and the free end was an integer number of half-wavelengths of the generated propagating wave. Thus, very large forces were required to reduce the downstream displacement to zero and these forces could not be generated by the secondary shaker.

The passive effect of the shaker is evident in **figure 3.26**. The power supplied to the beam without control is predicted to be a straight line as shown in **figure 3.23**. However, the measured power supplied does not have a straight line characteristic and this can be attributed to the reflections caused by the mass loading of the beam by the inactive secondary shaker. It is clear from **figure 3.26** that power supplied by the primary force does change when the secondary force is applied, and there are frequencies at which the primary force supplies more power when control is implemented. As mentioned before this occurs at frequencies when there is a large standing wave between the primary and secondary forces which dissipates the energy.

3.6.3 Maximum Power Absorption by the Secondary Force

The analysis conducted in section 3.3 concluded that provided a beam is not infinite, then the control strategy to maximise the power absorbed by the secondary force changes the impedance at the primary force position such that the primary force supplies more power to the beam. In this section, the effect of this control strategy implemented using a single secondary force on a "semi-infinite" beam is investigated experimentally, with a brief initial discussion of the theoretical result included for comparison.

Consider the beam shown in **figure 3.21**, which shows the position of the primary and secondary forces on the semi-infinite beam. The secondary force required to

maximize the power absorbed by the secondary force is given by equation (3.12). In this case, provided nearfield waves are ignored, the transfer receptance between the primary force and the displacement at the secondary force position, is given by:

$$\alpha_{sp} = \frac{-(1 + j)}{2EI k_b^3} e^{-jk_b l} \quad (3.36)$$

The imaginary part of the point receptance of the secondary force is given by:

$$X_{ss} = \frac{\sin 2k_b l - 1}{4EI k_b^3} \quad (3.37)$$

where nearfield waves are again ignored. The secondary force normalised to the primary force can be calculated by combining equations (3.12), (3.36) and (3.37), and is plotted in **figure 3.27** for an aluminium beam having the dimensions of those used in the experiments. The theoretical displacement of the beam downstream of the secondary force when this control strategy is implemented is shown in **figure 3.28**. The calculated change in the displacement due to the action of

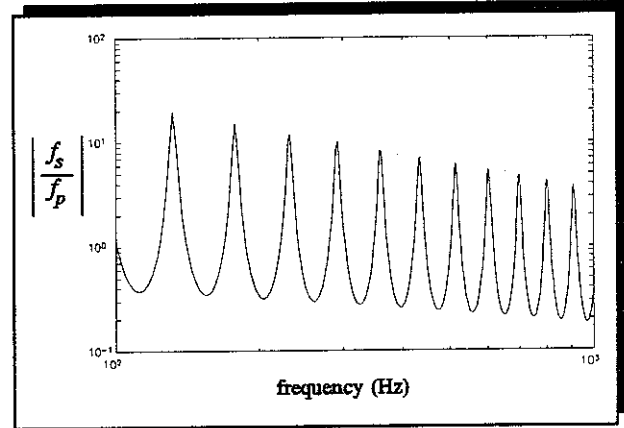


Figure 3.27 Theoretical Secondary Force Required to Absorb Maximum Power

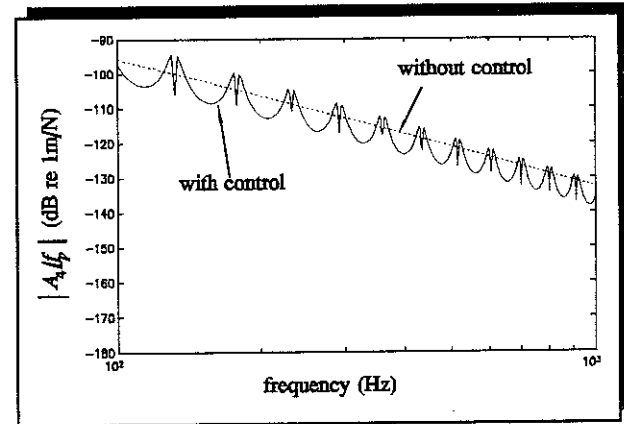


Figure 3.28 Theoretical Displacement of the Beam Downstream of the Secondary Force Adjusted to Absorb Maximum Power

the secondary force is shown in **figure 3.29**, and the power supplied by the primary force, with and without control is shown in **figure 3.30**.

The experiment was conducted using the same beam and force actuators as the wave suppression experiment. As the aim of the experiment was to investigate the effects

of implementing the power absorption control strategy, the measurement of the power supplied by the secondary force actuator was required. This was achieved by measuring the force and acceleration at the secondary force position, using a Solartron 1200 two channel frequency response analyzer. The imaginary part of the cross-spectrum of force and acceleration was computed, and displayed on the screen of the Solartron analyser, and was used to indicate when the secondary actuator was absorbing maximum power. The experiment was conducted in a similar way to the wave suppression experiment, and the experimental set up is shown in **figure 3.31**. The beam was excited at discrete frequencies between 100 Hz and 1 kHz with 10 Hz intervals. At each frequency the magnitude and phase of the secondary force were adjusted by hand until the power absorbed by the secondary force actuator, as indicated on the screen of the Solartron signal analyzer, was a maximum. When this condition was achieved, the power supplied by the primary

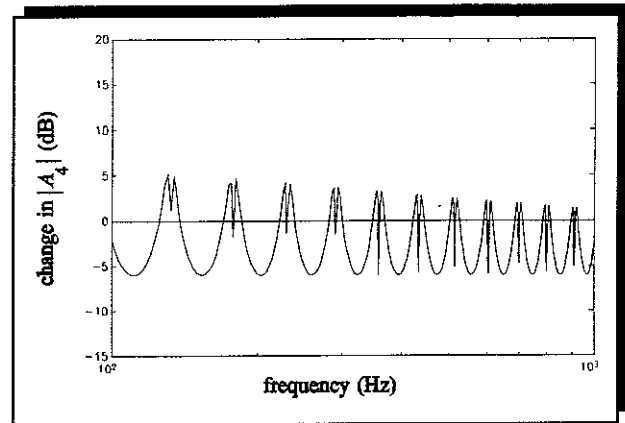


Figure 3.29 Theoretical Change in Amplitude Downstream of the Secondary Force Adjusted to Absorb Maximum Power

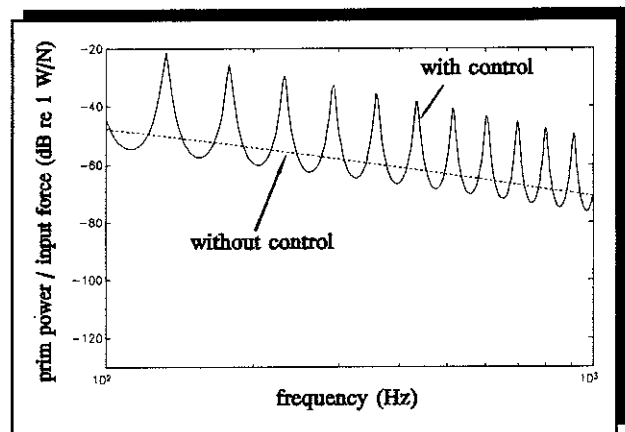


Figure 3.30 Theoretical Power Supplied by the Primary Force with and without Control

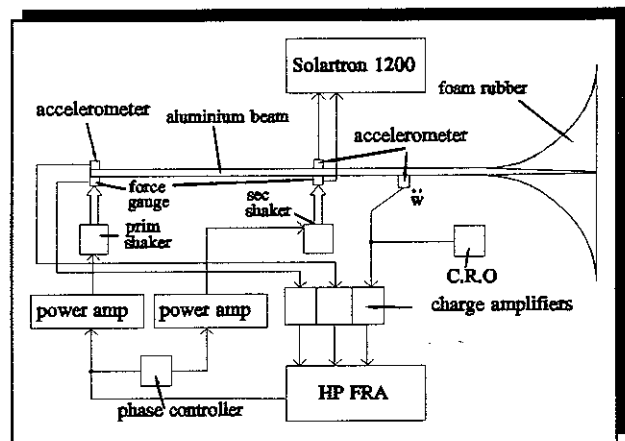


Figure 3.31 Experimental Set Up for the Active Control Experiments using Power Based Control Strategies

force and the displacement of the beam downstream of the secondary force were measured.

The displacement of the beam per unit input primary force downstream of the secondary force is shown with and without control in **figure 3.32**. The change in the displacement due to the secondary force is shown in **figure 3.33** and the power supplied by the primary force is shown in **figure 3.34**. These results demonstrate that the control strategy of maximizing the power absorbed by a single secondary force on a semi-infinite beam is quite different from the wave suppression control strategy discussed in the previous section. Examining **figures 3.32** and **3.33**, it can be seen that although the amplitude of the propagating wave has changed, it is not by very much, and at some frequencies it is greater than when no control force is applied. The power supplied by the primary force is plotted in **figure 3.34**. This shows that, in general, there is an increase in the power supplied by the primary force when the secondary force is

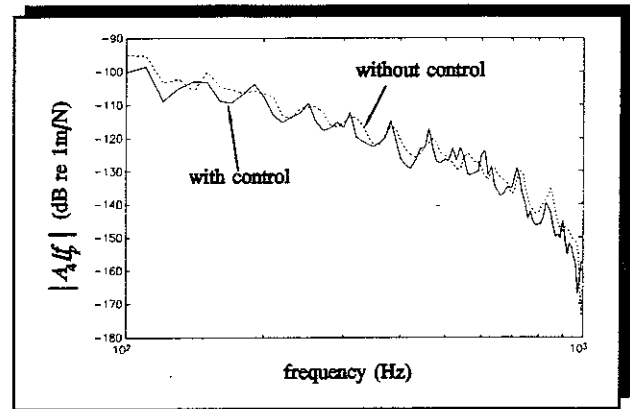


Figure 3.32 Measured Displacement of the Beam Downstream of the Secondary Force Adjusted to Absorb Maximum Power

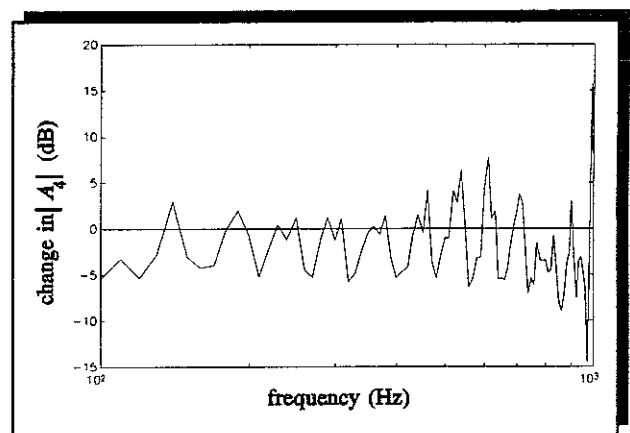


Figure 3.33 Measured Change in the Amplitude of the Beam Downstream of the Secondary Force Adjusted to Absorb Maximum Power

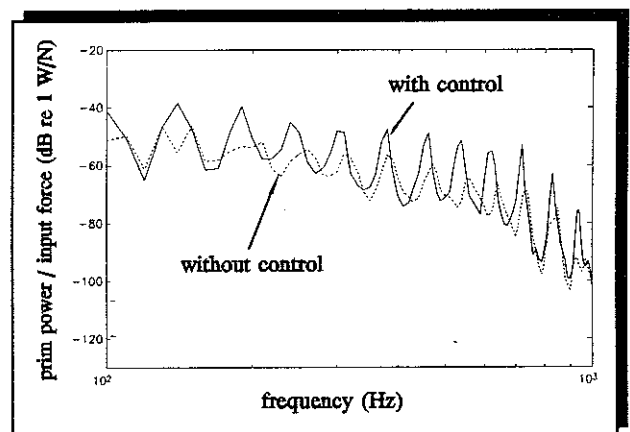


Figure 3.34 Measured Power Supplied by the Primary Force when the Secondary Force is Adjusted to Absorb Maximum Power

adjusted to absorb maximum power. It appears therefore, that this is not a useful control strategy to employ if global control of the structure is required.

3.6.4 Minimization of Total Power Supplied to the Beam

This experiment involved minimising the total power supplied to the aluminium beam by the primary and secondary forces in a similar way to that discussed in sections 3.2 and 3.3. Thus, this requires knowledge of the power supplied by the primary *and* secondary forces, and therefore requires more information than the power absorption strategy. The method used in this section however, does not involve direct measurement of the total power supplied by the primary and secondary forces but is the simplified method described by Johnson and Elliott [41]. It requires the monitoring of power supplied by the secondary force only and the use of a phase reference from the primary force.

The secondary force required to minimize the total power supplied to the beam can be calculated using equation (3.18), where X_{ss} is given by equation (3.37) and X_{sp} can be determined by taking the imaginary part of equation (3.36). The calculated normalised secondary force is plotted in **figure 3.35** and the predicted displacement of the beam downstream of the secondary

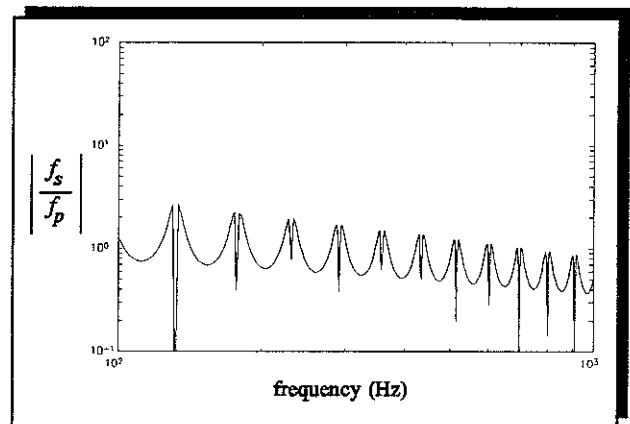


Figure 3.35 Theoretical Secondary Force Required to Minimize the Total Power Supplied to the Beam

force, when this control strategy is implemented is shown in **figure 3.36**. The predicted change in the displacement due to the action of the secondary force is shown in **figure 3.37**, and the power supplied by the primary force, with and without control is shown in **figure 3.38**.

The experiment was conducted using the same aluminium beam and force actuators as in the previous experiments and the aim was to examine the effects of implementing the power minimization control strategy. The power supplied by the secondary force was measured using a Solartron 1200 two channel analyzer as with the absorption experiment, and the experimental arrangement is shown in figure 3.31. Instead of measuring the total power supplied to the beam and then minimizing this quantity, only the power supplied by the secondary force actuator was measured. The following method, based on that discussed by Johnson and Elliott [41], was adopted to ensure that at each frequency the minimum power was supplied to the beam:

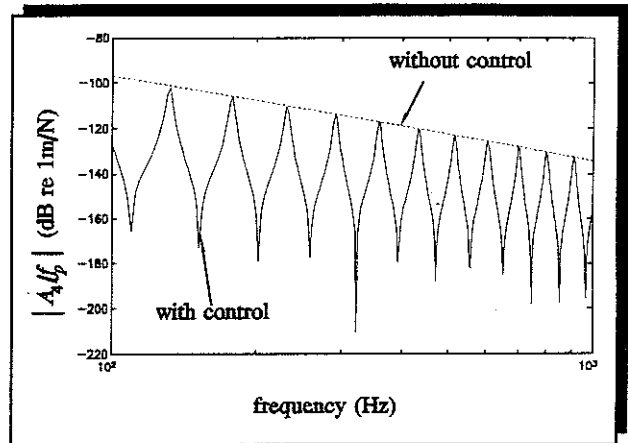


Figure 3.36 Theoretical Displacement of the Beam Downstream of the Secondary Force Adjusted to Minimize the Total Power Supplied

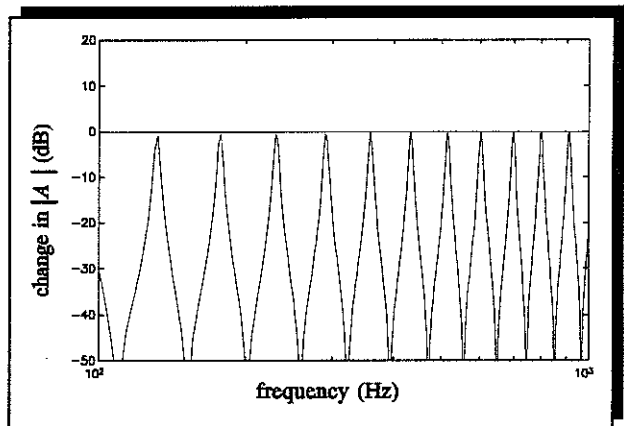


Figure 3.37 Theoretical Change in the Displacement of the Beam Downstream of the Secondary Force Adjusted to Minimise the Total Power Supplied

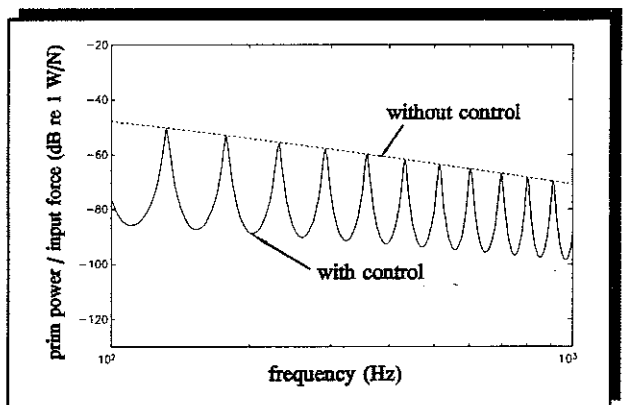


Figure 3.38 Theoretical Power Supplied by the Primary Force with the Secondary Force Adjusted to Minimise the Total Power Supplied

1. The beam was excited by the primary force at discrete frequencies (100 Hz -1 k Hz in 10 Hz steps).
2. The phase of the supply to the secondary force was arranged so that it was out of phase with the primary force.
3. At each frequency the secondary force was gradually increased. The secondary force actuator then started to absorb power as monitored using the Solartron Signal Analyzer.
4. As the magnitude of the secondary force was increased, the secondary force initially started to absorb power and then gradually reduced to zero, before starting to supply power. When the secondary force actuator neither absorbed nor supplied power, this was deemed to be the point at which the minimum power was being supplied to the beam, as discussed by Elliott *et al* [36].
5. When the force was increased as in step 4, if the secondary force actuator supplied rather absorbed power, then the phase of the supply to the secondary force actuator was reversed, and the force increased until the power supplied was zero.
6. When minimum power was being supplied to the beam, the power supplied by the primary force and the displacement of the beam downstream of the secondary force were measured.

The displacement of the beam downstream of the secondary force per unit input primary force is plotted with and without control in **figure 3.39**. The change in the displacement due to the application of the secondary force is shown in **figure 3.40** and the power supplied by the primary force is shown in **figure 3.41**. The experimental results show that this is an effective

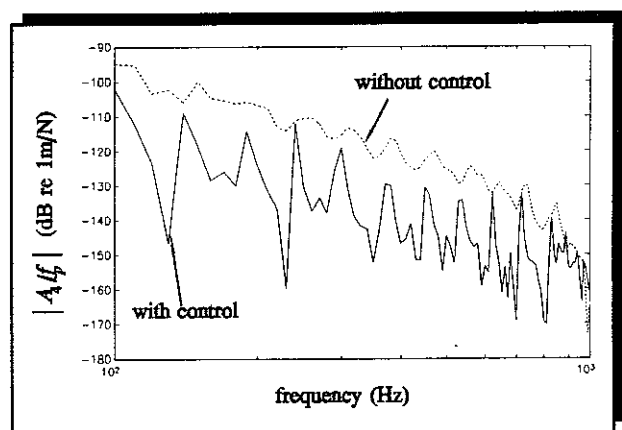


Figure 3.39 Measured Displacement of the Beam Downstream of the Secondary Force when the Secondary Force is Adjusted to Minimize the Total Power Supplied

control strategy in reducing the downstream displacement and ensures that no more power is supplied to the beam by the primary force when the secondary force is applied.

This control strategy has been shown to be the same as the wave suppression control strategy for a *lossless* semi-infinite beam [42].

The fundamental difference between the two control strategies on a damped beam can be seen by examining the secondary force requirements shown in figures 3.22 and 3.35. In the wave control strategy the secondary force required becomes very large at frequencies when the distance between the secondary force and the free end equals an integer number of half-wavelengths. At these frequencies there is a large standing wave between the primary and secondary forces, which dissipates power. In the power control strategy, this power is accounted for and the secondary force reduces to a very small level as can be seen in figure 3.35. This strategy therefore has the following advantages over the wave control strategy; (a) a smaller capacity secondary force actuator is required, and (b) the strategy is guaranteed not to increase the power supplied to the beam by the primary force. The penalty, however, is a smaller reduction in the amplitude of the beam downstream of the secondary force actuator, as can be seen by examining figures 3.25 and 3.40. The method of measuring the power supplied by the secondary force only, and setting this to zero, worked well and validated the method proposed by Johnson and Elliott [41]

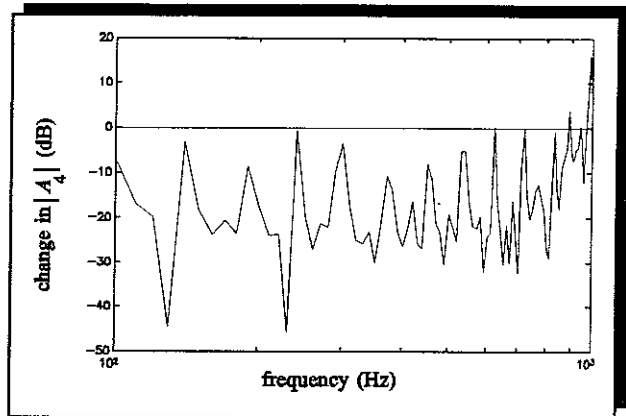


Figure 3.40 Change in the Measured Displacement of the Beam Downstream of the Secondary Force Adjusted to Minimise the Total Power Supplied

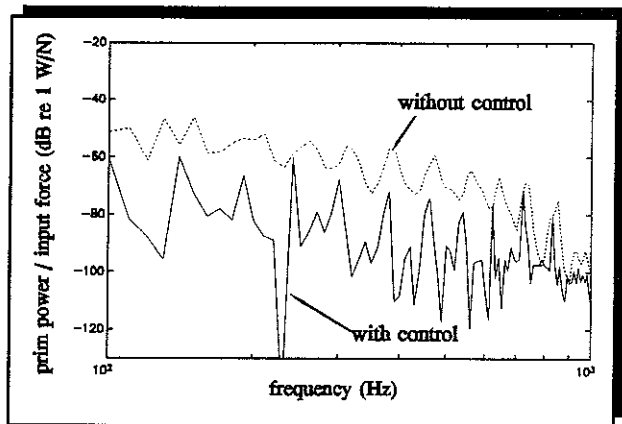


Figure 3.41 Measured Power Supplied by the Primary Force with the Secondary Force Adjusted to Minimise the Total Power Supplied

in structural control.

3.7 Conclusions

This chapter has discussed two power based active control strategies applied to a beam; that of maximizing the power absorbed by secondary forces and minimizing the total power supplied to the beam. These control strategies have been considered for infinite and finite beams and compared with a wave control strategy. It was found that the local control strategy of power absorption is very similar to wave suppression on an infinite beam, effectively absorbing a propagating wave incident on the secondary force array. However, when this strategy is employed on a finite beam it changes the impedance of the beam at the primary force position to that of a resonant beam *at all frequencies*. The net effect is that displacement of the beam downstream of the secondary force array is much reduced but the displacement of the beam upstream of the secondary force array is greatly increased at most frequencies. The power minimization strategy is effective on both finite and infinite beams, but it can cause an increase in vibration between the primary and secondary forces. This control strategy is global and can be implemented by either monitoring the power supplied by the primary and secondary forces, or the far-field displacements upstream of the primary force and downstream of the secondary force array. Care must be taken on a finite beam, however, to ensure that the motion of the beam is observable by the transducers.

These control strategies have been implemented on a slender semi-infinite aluminium beam. Reductions in the amplitude of the beam downstream of the secondary force of up to 50 dB were achieved using the wave suppression control strategy. The magnitude of the secondary force required to achieve this varied with frequency, and reached a maximum when the distance between the secondary force and the free end of the beam was an integer number of half-wavelengths. As the control effort required was very large at these frequencies, and the secondary force actuator lacked the capacity to generate the required motion, the amplitude of the beam downstream

of the secondary force was at a maximum at these frequencies. If this control strategy is to be successfully adopted over a wide range of frequencies, then a large secondary force actuator is required. Alternatively, a smaller actuator could be used over a limited frequency band. Implementation of the power control strategies at discrete frequencies was achieved by monitoring the power supplied by the secondary source using a two channel signal analyzer. With the power absorption control strategy, the magnitude and phase of the secondary force were adjusted until it absorbed maximum power, and with the power minimization control strategy, the secondary force was adjusted until it neither supplied nor absorbed power. It was shown that the power absorption control strategy was an ineffective global control strategy as it caused an increase in the power supplied to the beam. There was, however, a halving in the amplitude of the propagating wave downstream of the secondary force at some frequencies. The main advantage of the power minimisation control strategy is that it does not require large forces, unlike the wave suppression control strategy, which means that the secondary actuator can be made much smaller. Although the reduction in amplitude of the beam, downstream of the secondary force, was not as great as when the propagating wave was suppressed, reductions of up to 40 dB were achieved.

The experimental results of the implementation of the three control strategies correlate well the theoretical predictions and thus validate the theoretical models developed.

CHAPTER 4

4 DISTRIBUTED PIEZOELECTRIC SENSORS AND ACTUATORS FOR THE ACTIVE CONTROL OF WAVES ON A BEAM

4.1 Introduction

During the past decade there has been tremendous interest in the use of piezoelectric sensors and actuators in the active control of structural vibrations. This is part of a wider area of study of so called "smart structures", which adapt to their environment. The study of smart structures and intelligent systems is now a recognised area of research and has prompted several International Conferences, for example [47][48] and two International Journals [49][50]. Piezoelectric materials have been used as elements in vibration sensors for many years and can be found in most makes of accelerometers. In the smart structure concept the sensors and actuators are embedded into the structure and become an integral part of that structure. The use of integrated piezoelectric sensors and actuators in vibration control is a relatively new concept and is very much in the early stages of research.

The aim of the work reported in this chapter was to investigate the use of piezoelectric devices as vibration sensors and actuators, specifically on one-dimensional structures. Flexural and longitudinal motion only were considered, and appropriate theoretical models of the sensors and actuators were developed and validated by way of simple experiments. In Chapter 2 a framework was proposed, whereby secondary actuator arrays are coupled into a beam using waves to model the beam dynamics, and considering the secondary control forces as wave generators. In this chapter piezoceramic vibration actuators are considered as wave generators, and this framework is used to integrate the actuators into the beam dynamics.

The chapter comprises several sections which contain integrated analytical and experimental work. Following the introduction, a review is conducted of the contemporary literature on the use of piezoelectric devices in active vibration control. This is followed by a short description of piezoelectric devices, and then there are sections on sensors and actuators. Current static models of flexural and longitudinal vibration actuators are discussed and the limitations of these relatively simple models are compared with more complicated models. The penultimate section describes how a piezoelectric element can be used as both an actuator and a sensor, and shows that there are significant difficulties in using this type of device in practice. Finally, the chapter is concluded with some general observations and conclusions on the use of piezoelectric devices in active vibration control.

4.2 Review of Research into the use of Piezoelectric Devices as Vibration Sensors and Actuators

4.2.1 Introduction

The piezoelectric effect, whereby an electric field is generated due to a change in dimensions of a material, was discovered by the Curie brothers over 100 years ago. They found the effect in several materials, some of which were quartz, cane sugar and Rochelle salt, and they reported their results in the French Journal *Comptes Rendus* [51]. The converse piezoelectric effect, that is a change in dimensions of a material due to the application of an electric field, was verified by the Curies five years later. The history of piezoelectric materials and applications from their discovery to 1981 are reported in a series of papers published in the *Journal of the Acoustical Society of America*. [52][53][54][55][56][57]. It is only in the relatively recent past, however, that piezoelectric materials have been used in the active control of vibrations.

There are two commonly used types of piezoelectric material; ceramics of the PZT family (lead zirconate titanate) and plastic film made of polyvinylidene fluoride

(PVDF) and related polymers. Piezoceramics and piezopolymers are both usually produced in thin sheets with films of metal deposited on opposite faces as electrodes. However, PZT elements can now be produced in a variety of shapes such as tubes, rings and hemispheres [58], and there are wires fabricated from PVDF [59]. Integrated piezoelectric sensors can be made by firmly attaching an electroded piece of piezoelectric material directly to the surface of a vibrating structure, usually with adhesive. The wires from the piezoelectric element are fed to a high electrical impedance device such as a voltage follower. Alternatively, the piezoelectric material can be embedded in a composite structure. However, care must be taken not to expose piezoelectric elements to temperatures higher than the Curie temperature, which is the temperature above which the material loses its piezoelectric properties, and PZT typically has Curie temperatures in the range 200 to 350°C and PVDF in the range 80 to 100°C.

Table 4.1 summarises typical pertinent properties of PVDF and PZT. It can be seen that the ceramic is about twenty times stiffer than PVDF and it will be shown that this

is an important parameter to be considered when selecting the material to be used as a sensor or an actuator. A sensor requires a small stiffness so that it adds a minimum local stiffening to the host structure, and an actuator requires a large stiffness for effective mechanical coupling to the structure. The piezoelectric constant, which relates the free strain of a piezoelectric element

PROPERTY	PZT (PCSH) type V1	PVDF
Curie Temperature (°C)	210	100
Longitudinal Young's Modulus (Nm ⁻²)	59.5 x 10 ⁹	3 x 10 ⁹
Dielectric Constant - d ₃₁ (mV ⁻¹)	212 x 10 ⁻¹²	23 x 10 ⁻¹²
Max E-field (Vm ⁻¹)	0.4 x 10 ⁶	40 x 10 ⁶

Table 4.1 Properties of PZT and PVDF

to the applied voltage, is an order of magnitude greater for PZT than for PVDF. These two properties imply that PZT is the more appropriate material for actuator applications. However, the maximum electrical field that can be applied to PVDF

is about one hundred times greater than for PZT which means that provided the voltage capacity is available, PVDF elements can also be used as actuators. Applications of PZT and PVDF as sensors and actuators are described in the following subsections

4.2.2 Sensors

PVDF has been the preferred integrated sensor material to date, as it is generally less intrusive than the ceramic. As discussed above, it has less of a stiffening effect on the structure and it is generally thinner, but it is 10 times less sensitive; however, it is relatively easy to cut into the required shapes. Nonetheless when considered against other strain sensors, such as resistive strain gauges, PVDF still offers significant improvements in sensitivity, even after amplification of the strain gauge signals. Two piezoelectric elements can be fitted either side of a beam and the sum of their outputs is proportional to the longitudinal, or in-plane motion, and the difference is proportional to the flexural, or out-of-plane motion of the beam. Gibbs *et al* [60] used two such sensors (4 elements) spaced a distance apart on a beam to decompose the vibrational field into flexural and longitudinal travelling waves. Rex [61], following on from the work from Burke and Hubbard [62], showed that shaping or shading a one-dimensional piezoelectric element can affect its output. He considered four simple cases, firstly a rectangular element which measures local curvature at the ends of the sensor; secondly a sensor with a linear-slope "tent" weighting which measures double the transverse displacement at its centre, minus the displacement at its ends; thirdly a quadratically weighted sensor which measures the integral of the structures transverse displacement over the sensors length; and fourthly a modally weighted sensor which senses single modes dependent upon its shape. Lee and Moon [63] have constructed modal sensors from sheets of PVDF laid on a cantilever beam. They weighted the sensitivity of each PVDF sheet by varying the width of one of the electrodes. Some of these ideas have been extended to plates. Johnson and Elliott [64] have used two-dimensional quadratically shaped sensors to measure the acoustic volume velocity from a plate, and Larson and Larson [65] have

shaped PVDF modal sensors as spatial filters to measure specific modal amplitudes of a plate. Lefebvre *et al* [66] conducted active control experiments on a plate using PVDF strips as error sensors. They compared the use of PVDF strips as error sensors laid onto a plate with conventional accelerometers. It was shown that as the PVDF strips spatially integrates the plate's displacement, their positioning is not as crucial as for accelerometers. Rex and Elliott *et al* [67] used a piece of PVDF wire (piezowire) as a quadratically weighted strain integrating sensor and introduced the concept of a surface microphone. A novel idea by Briscoe and Pinnington [68] involves the use of PVDF wire wrapped around a fluid filled pipe to measure fluid pulsations in the pipe. A similar sensor to this is constructed to measure fluid pressure in a pipe and is discussed in Chapter 6.

PZT elements are particularly versatile and have been used in some experimental work [69][70] as sensors. They can, however, be used as actuators as well as sensors, which is the case in this work. Dosch *et al* [71] describe an arrangement where the same elements have been used simultaneously as both actuator and sensor. The "self sensing actuator" was used in a feedback loop on a cantilever beam to control two modes of vibration. Circuits to measure strain and strain rate with the "self sensing actuator" were described, but the experiments they conducted used strain rate feedback. Some practical issues concerning this "self-sensing actuator" are discussed later in this chapter.

4.2.3 Actuators

In the past few years there has been a tremendous growth of research into the use of piezoelectric devices as vibration actuators. This growth has been spurred on by the need for compact actuators for use in active vibration control systems. Again, as with the sensors, PVDF and PZT are both used and have been reported on extensively in the literature. PVDF actuators tend to be long strips of material, whereas PZT actuators tend to be much smaller in length.

4.2.3.1 PZT Actuators

The mechanical coupling of a piezoceramic actuator to a beam was first reported by Crawley and de Luis [32]. They conducted a detailed investigation into the effects of an imperfect bonding layer between the actuator and the beam, and also developed relationships between induced strain at the surface of the beam and applied voltage for surface mounted and embedded actuators, symmetrically bonded to each side of the beam. This work has been recognised as the first rigorous study of induced strain piezoelectric actuators, but there have been one or two modifications to the basic theory subsequently. It was shown in this work, that provided the bonding layer is perfect, i.e., there is no relative motion between the actuator and the beam at the interface, then there is effectively a longitudinal point force applied to the beam at the ends of the actuator on the surface of the beam. In practice, this has been generally shown to be a reasonable physical model of the actuator for beam displacements away from the actuator and this is borne out in this thesis. Pan *et al* [72] assert that the static model of the actuator and beam proposed by Crawley and de Luis is inadequate for describing the beam dynamics close to the actuator, especially at high frequencies. They proposed a complex dynamic model which includes stiffness and inertia effects of the actuator and presented some preliminary experimental results validating their theory.

The analysis undertaken by Crawley and de Luis did not differentiate between bending and pure extension of the beam, when considering strain distribution in the piezoelectric elements. They used a simple model which assumed constant strain in the actuator elements. Subsequent work by Crawley and Anderson [73] showed that this was not a valid assumption when the thickness of the beam was not significantly greater than the thickness of the PZT elements. A more complex model of the actuators is required for relatively thick PZT elements, and this model assumes Euler-Bernoulli bending strain distribution in the PZT elements. Crawley and Anderson validated their findings with a finite element model, and this refined model is checked against experimental observations in this thesis. In the case of pure extension,

Crawley and de Luis assumed a constant strain distribution at a cross-section through the actuator and the beam. This was shown by Wang and Rogers [74] to be a good approximation if the beam was thin compared to the actuators, but not such a good approximation if the beam was relatively thick. In this case the centre of the beam strained less than the surface, and in the model developed by Crawley and de Luis, the force applied by the piezoceramic elements was overestimated. A more appropriate strain distribution was a linearly varying one induced by each piezoceramic element. This modified model postulated by Wang and Rogers was found to be more accurate, according to experimental observations in this thesis. These models of piezoelectric actuators are discussed in more detail later in this chapter

PZT actuators have been used effectively in wave control on one-dimensional structures. Fuller *et al* [70] and Clark *et al* [75] used PZT actuators to simultaneously control longitudinal and flexural power flow in a beam, and Gibbs and Fuller [69] and Pines and Von flotow [76] have successfully demonstrated the use of PZT actuators to suppress propagating flexural waves on a beam. Fanson and Caughey [77] used PZT actuators and sensors to demonstrate a technique called "positive position feedback", a modal based active control system using a co-located actuator and sensor, to control the first six modes of a cantilever beam. The thrust of their work was to test their control technique which avoided control "spillover" [78], and they used piezoceramic actuators and sensors in their experiments. de Luis and Crawley [79] extended their previous work with one actuator and tested a prototype "intelligent structure" with sixteen embedded piezoceramic actuators (32 elements). The structure was a 1.2 m free-free composite beam made from epoxy resin and was modelled using finite element analysis with analytical models for the PZT elements. Control of the first five modes of the beam was achieved.

The theoretical study of PZT actuators has been extended to two dimensions. Dimitriadis *et al* [80] formulated a static coupling model of two-dimensional PZT patches bonded either side of a thin elastic structure. They extended their work to include an analysis of the dynamic coupling of various sizes of actuator to a simply

supported undamped thin rectangular plate. Although the actuators excited the plate, they found that the size and placing of the actuators had a strong influence on their ability to excite certain modes. PZT elements can also be assembled into a stack. Palazzolo *et al* [81] developed a vibration exciter by assembling a stack which they used to control radial vibrations of a rotor bearing in a squirrel cage electric motor. Sung *et al* [82] demonstrated the use of PZT elements to sense and control torsional vibrations. They conducted experiments on a torsional pendulum made of phenolic and pyrex and used ring shaped sensors and actuators to control three modes using velocity feedback.

4.2.3.2 PVDF Actuators

As mentioned in the introduction to this section, PVDF actuators tend to be distributed over a much larger area than PZT actuators. There have been several experiments conducted using this material, notably some early work conducted by Bailey and Hubbard [83], who bonded a piece of PVDF to one side of a cantilever beam and used it as an active distributed damper, which in theory could control all the modes of vibration. They conducted some experiments, feeding back a voltage proportional to the angular velocity of the tip of the beam, and achieved order of magnitude increases in modal loss factors. Some Interesting work by Burke and Hubbard [62] on the shaping of PVDF actuators followed. They showed that by tailoring the shape of the PVDF film, both forces and moments could be applied by the actuator. Their general observation was that discontinuities of slope in the actuator shape produced point forces, and discontinuities in size (width) produced point moments. The shaping of PZT actuators is discussed in some detail later in this chapter. As with PZT actuators the research moved on to investigate more sophisticated arrangements. Tzou and Gadre [84] conducted an analysis of the coupling of multiple layers of PVDF film to a thin cylindrical shell and recently Charon *et al* [85], described a composite structure made up of carbon fibre and several layers of PVDF film. Their tests involved open loop control of a composite cantilever beam where they minimised the tip displacement of the two lowest modes

of vibration. A novel PVDF actuator has been proposed by Harper and Leung [86]. They embedded helical strips of piezowire into a rubber pipe element and used them to control two flexural waves, a longitudinal wave and a torsional wave propagating in the pipe.

It is clear from the discussion above that there are many groups working on the use of piezoelectric materials as vibration sensors and actuators. Most of the work to date has been confined to the laboratory but it is probably only a matter of time before these so called "smart materials" find their way into commercially available products.

4.3 Piezoelectric Equations

The constitutive equations governing the electromechanical behaviour of a piezoelectric material are given in reference [87]. When discussing isotropic elements (rectangular), as shown in **figure 4.1**, that are connected to a beam which strains in the 1 direction, then the stress in the piezoelectric element is confined to the normal stress in the 1 direction. In this case the electromechanical equations reduce to the scalar equations, written in the conventional notation, as:

$$\epsilon_1 = s_{11}^E \sigma_1 + d_{31} E_3 \quad (4.1)$$

$$D_3 = d_{31} \sigma_1 + \xi_{33} E_3 \quad (4.2)$$

where

ϵ = Strain (no units), E = field (Vm^{-1}), σ = Stress (Nm^{-2})

d = piezoelectric constant (mV^{-1} or CN^{-1}), ξ = permittivity (Fm^{-1})

D = Dielectric displacement, i.e., charge per unit area (Cm^{-2})

s^E = $1/\text{modulus of elasticity measured at constant electric field}$ (m^2N^{-1})

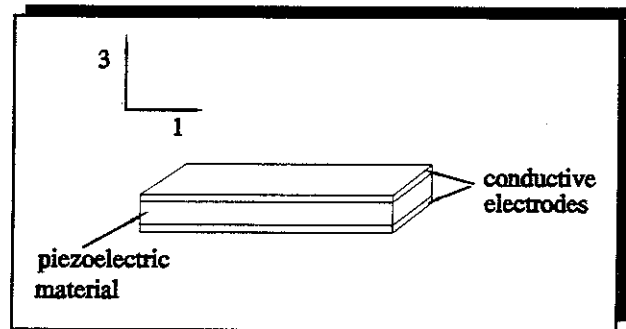


Figure 4.1 Construction of a Piezoelectric Element

The subscripts 1 and 3 refer to the directions shown in **figure 4.1**. Equation (4.1) can be thought of as the actuator equation. The strain in the PZT element in the 1 direction is proportional to the applied stress in the 1 direction (Hooke's law) and the applied voltage (the product of the electric field and the thickness of the element) in the 3 direction. It can be seen that a larger piezoelectric constant d_{31} results in a larger strain for a given applied voltage. Equation (4.2) is the sensor equation. The charge per unit area of electrode is proportional to the stress applied to the element in the 1 direction (the piezoelectric effect) and the applied electric field in the 3 direction.

It was decided to use PZT elements (Matroc Unilator PC5H) as vibration actuators *and* sensors on a beam. Before fitting them to the beam it was decided to experimentally measure the Young's modulus and piezoelectric constant of one of the elements. The element measured 100 mm x 20 mm x 1.52 mm and had the properties tabulated in Appendix 4.

A four point bending test was carried out on the PZT element to experimentally determine the modulus of elasticity and the experimental set up can be seen in **figure 4.2**. The PZT element was taped to two carbon fibre elements and laid on two small cylinders.

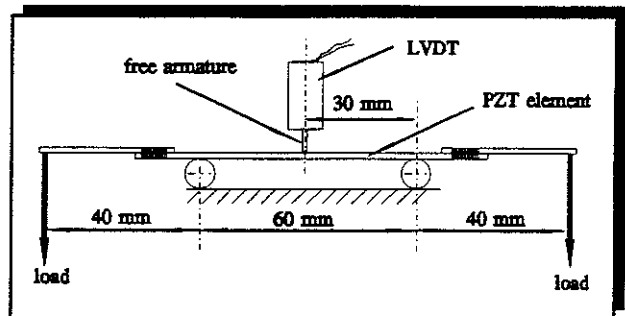


Figure 4.2 Four Point Bending Test of a PZT Element

Incremental masses were loaded on the ends of the carbon fibre strips and the lateral deflection in the centre of the PZT element measured with an LVDT. The LVDT had been calibrated previously using a micrometer and was found to have a sensitivity of 0.7686 Vmm^{-1} . The following calculations were done to determine the modulus of elasticity of the PZT element.

Dimensions of the PZT element (mm):	$l \times b \times d = 100 \times 20 \times 1.52$ (measured)
2 nd Moment of Area, I :	$bd^3/12 = 5.85 \times 10^{-12} \text{ m}^4$

The graph showing the relationship between the LVDT output voltage and the load applied to the carbon fibre strips is shown in **figure 4.3**. From the straight line characteristic of shown in this figure, the LVDT voltage for a 50 gm load is 0.019379 V. The central deflection for 50 g is therefore $0.019379 \times 1/0.7686 = 0.0252$ mm. The radius of curvature R can be determined using the intersecting chord theorem. Consider the deflected PZT element shown in **figure 4.4**. The radius of curvature is related to the deflection x by the following expression:

$$x(2R - x) = 30^2 \quad (4.3)$$

Substituting for $x = 0.0252$ mm gives $R = 4.4625$ m. The bending moment M between the supporting cylinders is the product of the weight (50 g) and the distance from the application of the weight and the cylinder (40 mm). Hence $M = 0.04 \times 0.05 \times 9.81 = 0.01962$ Nm. The modulus of elasticity for the PZT element can be determined using the Euler-Bernoulli bending equation:

$$\frac{M}{I} = \frac{E_p}{R} \quad (4.4)$$

Substituting for M , I and R gives $E_p = 59.84$ GNm⁻². This value compares favourably with the manufacturers data (see Appendix 4) of 59.5 GNm⁻².

Another experiment was conducted to measure the piezoelectric constant. The relationship between the piezoelectric constant d_{31} , the strain of a PZT element and

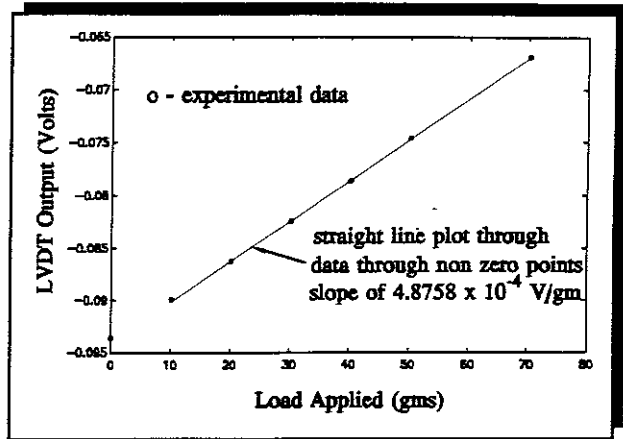


Figure 4.3 Relationship between LVDT Output Voltage and Load Applied

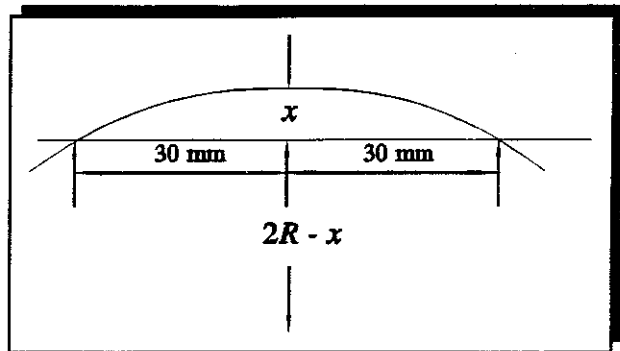


Figure 4.4 Deflected Shape of PZT Element

the applied electric field was given in equation (4.1). Noting that $s_{11}^E = 1/E_p$, where E_p is the Young's modulus of the PZT discussed above, and the electric field, $E_3 = V_3/t_p$, where V_3 is the voltage applied and t_p is the thickness of the PZT element, equation (4.1) can be written as:

$$\epsilon_1 = \frac{\sigma_1}{E_p} + d_{31} \frac{V_3}{t_p} \quad (4.5)$$

In the absence of any applied longitudinal stress, the piezoelectric constant can be related to the applied voltage, the thickness of the PZT element and the induced strain:

$$d_{31} = \frac{\epsilon_1 t_p}{V_3} \quad (4.6)$$

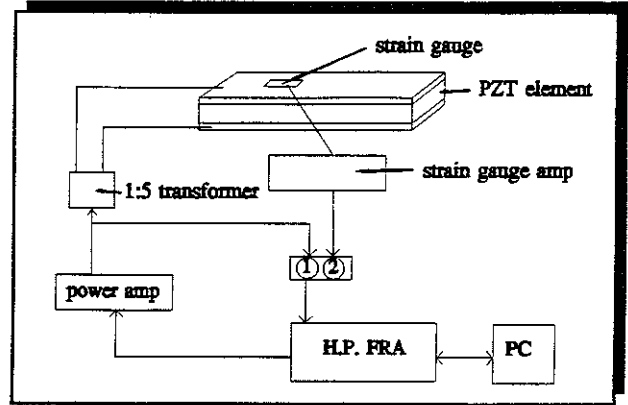


Figure 4.5 Experimental Set up to Measure the Piezoelectric Constant d_{31}

As the thickness of the PZT element and the strain resulting from an applied voltage can be measured, the piezoelectric constant can be calculated from experimental data. Thus an experiment was set up to measure the piezoelectric constant d_{31} and the arrangement is shown in figure 4.5. A PZT element was positioned free in space and excited over a frequency range 50 to 250 Hz using the stepped sine measuring technique with 2 Hz steps. The motion of the element was measured using a strain gauge bonded to one of the electrodes. The measured signal was amplified with a Sangamo Western Controls, Modular Carrier Amplifier type C56. This had an upper frequency limit of 400 Hz. The frequency response function of dynamic strain/voltage applied was measured and multiplied by the thickness of the element (1.52 mm), which gives the piezoelectric constant d_{31} and the magnitude is shown in figure 4.6. The measured frequency response function had to be post-processed to determine the piezoelectric constant d_{31} . This consisted of the following multiplication:

$$d_{31} = \frac{1.52 * 10^{-3}}{5 * 19.85 * 10^3} * \frac{V_e}{V_m} \quad (4.7)$$

where V_e is the output voltage from the strain gauge, V_m is the voltage applied to the transformer exciting the PZT element. $1.52 * 10^{-3}$ is the thickness of the PZT element, 5 is the gain of the transformer and $19.95 * 10^3$ is the gain of the strain gauge amplifier. It can be seen that the experimental result compares well with the d_{31}

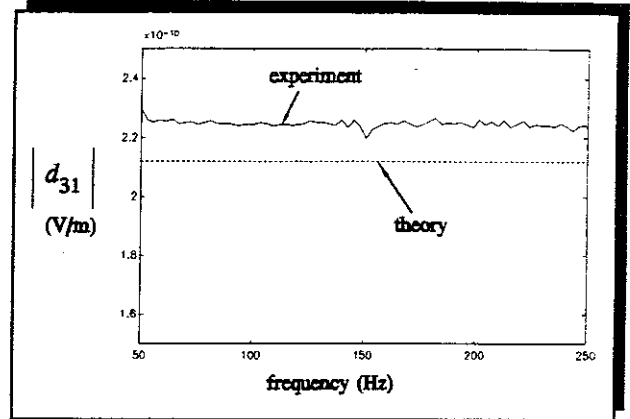


Figure 4.6 Measured and Theoretical Values of the Magnitude of the Piezoelectric Constant

constant given on the manufactures data sheet shown in Appendix 4. The measured magnitude was within 8% of that quoted by the manufacturer. The PZT element under test was thus found to have a Young's modulus and piezoelectric constant similar to that quoted by the manufacturer and the manufacturers data sheet could thus be used with confidence.

4.4 Piezoelectric Sensors

4.4.1 Introduction

This section describes how piezoelectric elements can be used as sensors to detect the motion of a slender beam. Equations of motion describing the sensitivities of various sensors (the relationship between the sensor output voltage to the strain in the beam) are derived and validated by simple experiments. Although the theoretical development in this section is applicable to both PZT and PVDF elements the practical work involved using PZT elements only.

Piezoelectric elements can be glued to a beam and configured to measure strain

spatially integrated over the area they occupy. With elements fitted to opposite sides of the beam they can detect longitudinal motion, flexural motion, or both simultaneously, depending on the way they are connected electrically. These sensors strain when the structure vibrates and generate an electrical charge by the direct piezoelectric effect. This charge is proportional to the strain and is thus a measure of the motion of the beam. The sensor considered in this chapter consists of two piezoelectric elements bonded to opposite sides of a beam as shown in figure 4.7. Using two elements allows discrimination between longitudinal and flexural motion.

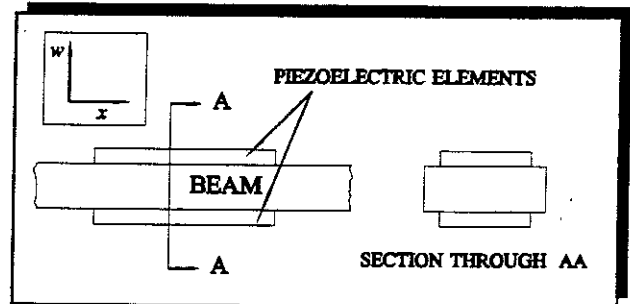


Figure 4.7 A Piezoelectric Sensor Fitted to a Beam

If a longitudinal wave impinges on the sensor, both piezoelectric elements strain by the same amount and in the same sense. The sum of the voltages generated by these two elements gives a measure of the beam's longitudinal motion. However, if a flexural wave impinges on the sensor, the piezoelectric elements strain by the same amount but in opposite sense. In this case the difference between the voltages generated by the individual elements gives a measure of flexural motion. If the two elements have independent connections, this simple sensor can be used to decompose longitudinal and flexural motion of the beam. This approach was used by Fuller *et al* [70] when they attempted simultaneous active control of longitudinal and flexural waves.

The sensor has a simple equivalent electrical model consisting of a charge generator in parallel with a capacitor or a voltage source in series with a capacitor as shown in figure 4.8. The relationship between these variables is:

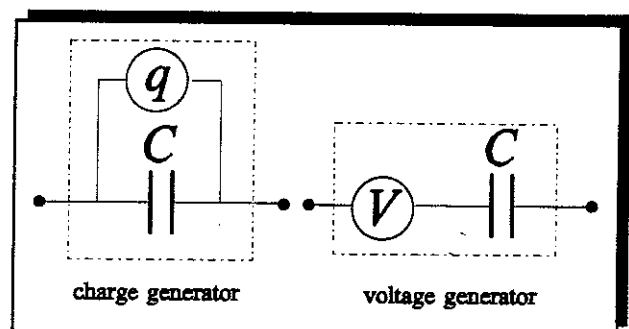


Figure 4.8 Equivalent Electrical Models of a Piezoelectric Sensor

$$q = CV \quad (4.8)$$

where V is the voltage generated, q is the charge generated and C is the capacitance of the sensor. The sensitivity of the sensor depends on the way the piezoelectric elements are connected electrically and various configurations are shown in **figure 4.9** where the +ve and -ve signs denote the polarization of the

elements. The sensitivities of the various configurations are compared with reference to the single element. Let the capacitance of one piezoelectric element be C_1 , the charge generated q_1 and the voltage generated V_1 . If the elements are connected in series, then the voltage generated for a given strain is twice that of a single element. If the elements are connected in parallel then the voltage generated is the same as for a single element for a given strain. This is analogous to connecting batteries in series or in parallel. In configurations (a) and (c) of **figure 4.9**, positive strains in the elements add, and opposite strains subtract. Thus, these configurations are appropriate for the measurement of longitudinal motion. In configurations (b) and (d) of **figure 4.9**, opposite strains in the elements add and strains of the same sense subtract, and therefore these configurations are appropriate for the measurement of flexural motion.

It can be seen that the greatest sensitivity can be achieved by connecting the elements in series, however in this configuration *only one wave motion can be detected*, either longitudinal *or* flexural, but not both simultaneously. The simultaneous detection of the two wave types involves independently connecting the piezoelectric elements with the resulting sensitivity of a single element.

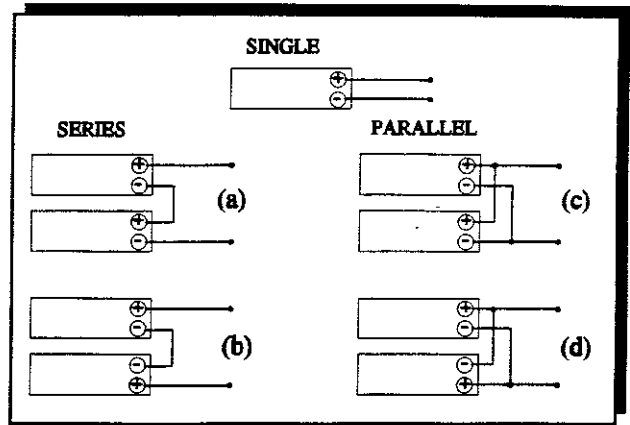


Figure 4.9 Different Ways of Electrically Connecting Piezoelectric Elements to Measure Flexural and Longitudinal Motion of a Beam.

4.4.2 Sensor Sensitivity - Measurement of Flexural Vibration

In this section, the sensitivity of the sensor when the beam is subject to flexural vibration is determined. It is assumed that this strain is due to pure bending and that the strain is constant across the width of the beam and the sensor. It is further assumed that the piezoelectric elements are perfectly bonded to

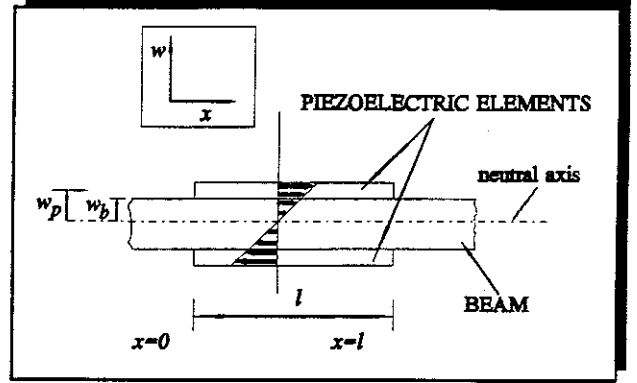


Figure 4.10 Strain Distribution of a Flexural Sensor

the beam and, initially, that they have negligible mass and stiffness. This latter assumption is re-visited later in this chapter. The bending about the neutral axis causes the strain to vary linearly along the w axis as shown in **figure 4.10**. The average strain at a section along the w axis in the piezoelectric material is at the point w_p , where w_p is the perpendicular distance from the beam's neutral axis to the middle of the piezoelectric elements. For such a beam, the stress at a point (x, w_p) , which is also the average stress in the piezoelectric material at that section is:

$$\sigma = \frac{w_p E_p}{R} \quad (4.9)$$

where R is the radius of curvature of the beam. For small deflections, the radius of curvature is related to the displacement as:

$$\frac{1}{R} = \frac{\partial^2 w}{\partial x^2} \quad (4.10)$$

Combining these equations with equation (4.2) and setting E_3 , the applied field, to zero, an expression for the dielectric displacement, i.e., charge per unit area, D_3 , of a single element bonded to the beam is obtained:

$$D_3 = d_{31} w_p E_p \frac{\partial^2 w}{\partial x^2} \quad (4.11)$$

The charge developed on the element can be found by integrating equation (4.11) over the electrode area. This is equivalent to multiplying by the width of the piezoelectric element, b , and integrating over the length, l to give:

$$q = \int_0^l d_{31} w_p E_p b \frac{\partial^2 w}{\partial x^2} dx \quad (4.12)$$

which integrates to give the generated charge on the sensor:

$$q = d_{31} w_p E_p b \{ w'(l) - w'(0) \} \quad (4.13)$$

where the prime denotes the spatial derivative with respect to x . This means that *the charge generated is proportional to the difference in slope at the end of the piezoelectric elements*. At low frequencies, when the length of a flexural wave is much greater than the length of the sensor, the strain of the surface of the beam underneath the piezoelectric strip, ϵ_b , is approximately constant along the length of the sensor, and is related to the radius of curvature by:

$$\frac{1}{R} = \frac{\partial^2 w}{\partial x^2} = \frac{\epsilon_b}{w_b} \quad (4.14)$$

where w_b is the distance from the neutral axis to the surface of the beam. Equation (4.12) then becomes:

$$q \approx \frac{w_p}{w_b} E_p d_{31} b l \epsilon_b \quad (4.15)$$

The voltage generated by the sensor can be found by dividing the charge developed by the sensor's capacitance (equation (4.8)). Equations (4.13) and (4.15) give the charge developed on one element of the two element sensor. However, the sensor's output voltage depends on how the elements are connected electrically as discussed above. The exact and approximate low frequency voltage sensitivities of a *single element* of this two element sensor are:

$$\frac{V}{\{w'(l) - w'(0)\}} = \frac{d_{31} w_p E_p b}{C_1} \quad (4.16)$$

and

$$\frac{V}{\epsilon_b} \approx \frac{d_{31} w_p E_p b l}{w_b C_1} \quad (4.17)$$

As mentioned above, the sensitivity of a parallel connected sensor is the same as for a single element, and the sensitivity of a series connected sensor is double that of the a single element. Because a PVDF sensor is very thin ($\approx 50 \mu\text{m}$) then $w_p \approx w_b$, and equation (4.17), the low frequency sensitivity equation, reduces to:

$$\frac{V}{\epsilon_b} \approx \frac{d_{31} E_p b l}{C_1} \quad (4.18)$$

It should be noted that the sensitivity equations derived above, are in terms of open circuit voltage and that the overall sensitivity of a measurement system depends on the electrical input impedance of the measurement circuit.

4.4.2.1 Stiffening Effect of the Sensor

The piezoelectric elements have a local stiffening effect on the beam, and at very high frequencies a mass loading effect. As the piezoelectric elements are placed some distance from the neutral axis, they can substantially increase the local flexural rigidity (EI) of the beam and thus modify the motion of the beam at the sensor's position. However, if the thickness of the piezoelectric elements are small compared to the beam thickness they will not add an appreciable stiffness or mass. Therefore an appropriate piezoelectric material for a sensor to measure flexural motion is one made from a thin film of PVDF and not a ceramic. However in this study it was intended to use the piezoelectric elements as actuators as well and therefore a piezoceramic material was used which had an appreciable local stiffening effect. To calculate this stiffening effect, the section of beam and the piezoceramic elements are considered as a composite beam as shown in **figure 4.11**. As the PZT and the beam

have different Young's Moduli, the dimension b , the width of the piezoelectric element has to be multiplied by a factor E_p/E_b and then the composite beam can be taken to be made completely of the beam material for the purpose of calculating the flexural rigidity. Now, the second moment of area of the beam alone I_b , is given by:

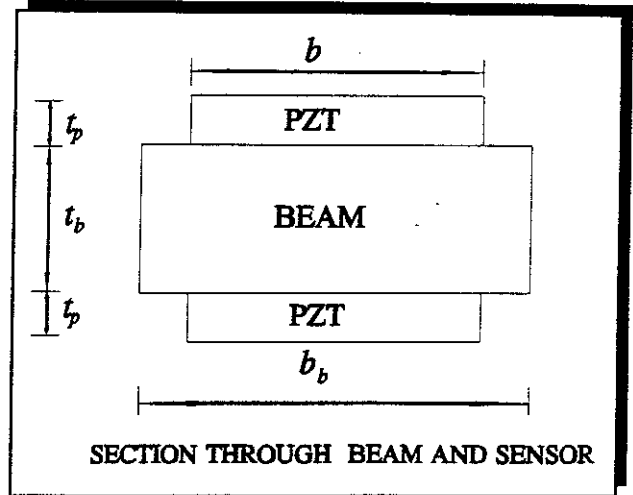


Figure 4.11 Section through Beam and Sensor

$$I_b = \frac{b_b t_b^3}{12} \quad (4.19)$$

and the second moment of area of the composite section I_c , is given by:

$$I_c = \frac{1}{12} \left\{ \frac{E_p}{E_b} b \{ (t_b + 2t_p)^3 - t_b^3 \} + b_b t_b^3 \right\} \quad (4.20)$$

The percentage increase in stiffness due to the sensor is given by $100I_c/I_b$. Using the data for the beam and piezoceramic elements used in the experiments given in Appendix 4, and repeated here for convenience,

$t_b = 6.12$ mm, $b_b = 30$ mm, $t_p = 1.54$ mm (including 0.02 mm bonding layer) and $b = 20$ mm. $E_b = 68.9$ GNm⁻² and $E_p = 59.5$ GNm⁻².

the calculated values of the second moments of area are:

Bare Beam, $I_b = 5.7305 \times 10^{-10}$ m⁴

Composite Beam, $I_c = 1.3639 \times 10^{-9}$ m⁴

Therefore the **local stiffness is increased by 138%, i.e., by a factor of 2.38, due to the sensor.**

Considering the additional stiffness effect only (not the mass), the surface strain of the beam directly beneath the piezoelectric elements is reduced to 42 %, i.e., $1/(2.38)$, of the surface strain of the beam either side of the sensor. This means that the measured strain by the sensor has to be multiplied by 2.38 to refer it to the strain of the beam that is unaffected by the sensor. This result is verified experimentally in the next section.

4.4.2.2 Calibration of the Sensor

The sensitivity of a parallel connected flexural vibration sensor was checked with that of strain gauges fitted either side of the sensor and connected to measure bending. Firstly, however, the sensitivity of strain gauges were checked using a four point static

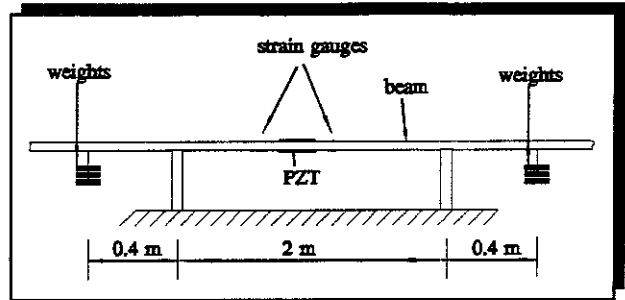


Figure 4.12 Four Point Bending Test to check the Calibration of the Strain Gauges

bending test which was set up as shown in **figure 4.12**. The predicted bending strain can be determined using the simple bending relationship:

$$\frac{M}{I} = \frac{\sigma}{w} \quad (4.21)$$

where M is the bending moment, I is the second moment of area of the cross-section about the neutral axis (equation (4.19)), σ is the bending stress and w is the distance from the neutral axis. Noting that $M = fl$, where f is the force (weight applied) and l is the distance between the position of the weights and the supports, that $\sigma = \epsilon E$, where ϵ is strain, E is the modulus of elasticity, and $w = d/2$ where d is the thickness of the beam. Equation (4.21) can thus be rearranged to give the relationship between the surface microstrain on the beam and the weight applied:

$$\frac{\mu\epsilon}{f} = \frac{6l}{Ebd^2} \times 10^6 \quad (4.22)$$

The theoretical microstrain for different weights applied was calculated using this formula and is tabulated in **Table 4.2**.

The strain gauges were positioned either side of the PZT sensor and connected to measure bending only. The 30 mm x 6.12 mm aluminium beam was positioned on two supports spaced two metres apart. Up to three 2 N (0.204 kg) weights were placed 0.4 m from the supports and the resulting bending strain measured using two Measurements Group P-3500 Strain Indicators.

WEIGHT (N)	STRAIN GAUGE (LEFT)		STRAIN GAUGE (RIGHT)		THEORY
	DIGITAL READOUT ($\mu\epsilon$)	DIGITAL VOLT- METER (mV)	DIGITAL READOUT ($\mu\epsilon$)	DIGITAL VOLT- METER (mV)	STRAIN ($\mu\epsilon$)
0	0	1.2	0	0.35	0
2	112	47.9	112	49.7	62
4	223	94.7	224	98.8	124
6	339	142.8	340	148.8	186

Table 4.2 Strain Gauge Calibration Test

It is clear from **Table 4.2** that the digital readout gives a strain reading that is twice the surface strain (due to two strain gauges being used). The experimental readings were within 10% of the theoretical values, and the sensitivities of the two strain gauges in terms of digital voltmeter output per input strain were (on average):

strain gauge (left) = 0.849 mV/ $\mu\epsilon$

strain gauge (right) = 0.888 mV/ $\mu\epsilon$

The low frequency sensitivity of the PZT sensors can be calculated using equation (4.17), where:

d_{31}	=	$-212 \times 10^{-12} \text{ CN}^{-1}$	(manufacturers data sheet)
E_p	=	$59.5 \times 10^9 \text{ Nm}^{-2}$	(manufacturers data sheet)
w_p	=	3.83 mm	(measured)
b	=	20 mm	(measured)
l	=	100 mm	(measured)
w_b	=	3.06 mm	(measured)
C_1	=	$0.037 \mu\text{F}$	(measured off the beam)

which gives a **PZT sensitivity of $0.8534 \text{ V}/\mu\epsilon$** .

The ratio of the sensitivity of the left-hand strain gauge to the sensitivity of the PZT sensor is thus 1005, and the right-hand strain gauge to the PZT sensor is 960. This, however, does not take into account the effect that the PZT element has in reducing the strain of the beam under the element (in this case by a factor of 2.38). Nonetheless, it is clear that these "active" sensors have a much greater sensitivity than the conventional passive strain gauges. Even if PVDF elements were used (which would have less of a local stiffening effect than PZT), having a typical piezoelectric constant, d_{31} , of $22 \times 10^{-12} \text{ CN}^{-1}$, they would have a sensitivity of about 100 times that of a conventional strain gauge.

An experiment was conducted to validate the model of the PZT sensor as shown in figure 4.13. A suspended aluminium beam with an anechoic termination at one end, that had a measure reflection coefficient of about 0.1 [45], was fitted with two strain gauges

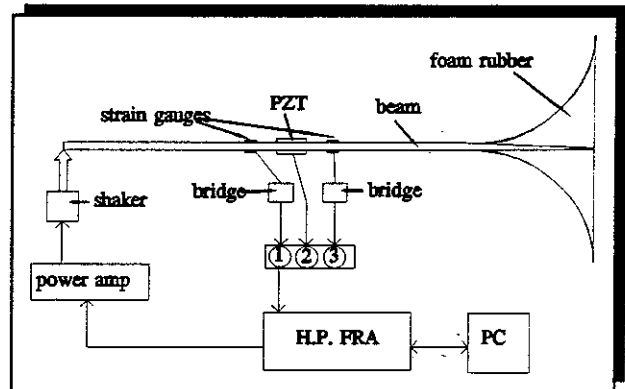


Figure 4.13 Experimental Set Up to Measure the Sensitivity of a PZT Sensor - Plan View

sensors and one PZT sensor. It was excited by the shaker over the frequency range

100 Hz to 1 kHz using stepped sine with 5 Hz intervals. Two measurements were taken at each frequency; the frequency response function of the output from the right-hand strain gauge divided by the output from the left-hand strain gauge, and the frequency response function of the PZT sensor divided by the output from the left-hand strain gauge. These are shown in figures 4.14 and 4.15.

Figure 4.14 shows that above about 200 Hz the beam is reasonably non-resonant and the anechoic termination is reasonably effective. It can also be seen that the flexural wave that impinges on the two pairs of strain gauges is approximately the same. As the strain gauges are placed at either end of the PZT sensor, this means that the strain underneath the PZT sensor is fairly constant over the length of the sensor over the frequency range 100 Hz to 1000 Hz, and thus the low frequency approximation of the sensitivity equation (equation (4.17)) can be

used. The frequency averaged output of the ratio of the PZT sensor to the output of the left-hand strain gauge is 397 as shown in figure 4.15. If the sensitivity of the PZT sensor is divided by the sensitivity of the strain gauges and the results are multiplied by 0.42 to compensate for the local stiffening effect of the PZT sensor we get 422 and 404 which are within 7% of the measured value of 397. It is thus considered that the sensitivity equation for a piezoceramic actuator is valid for the slender aluminium beam and PZT sensor.

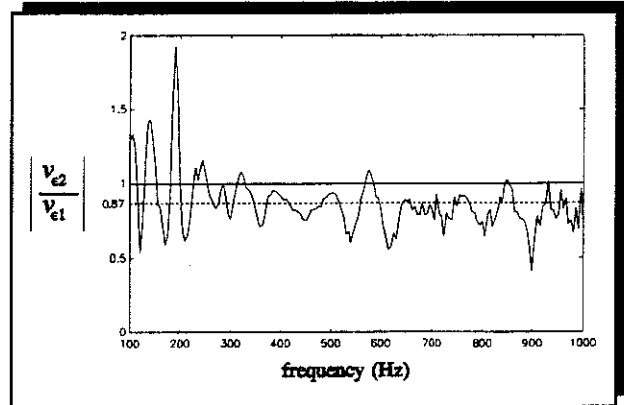


Figure 4.14 Output from the Right-Hand Strain Gauge divided by the Output from the Left-Hand Strain Gauge

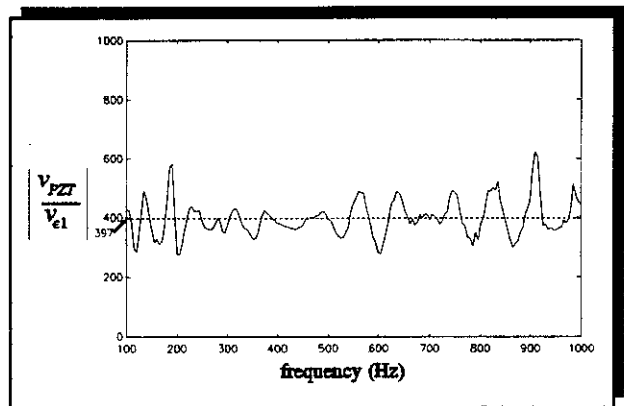


Figure 4.15 Output from PZT Sensor divided by the Output from the Left-Hand Strain Gauge

4.4.3 Sensor Sensitivity - Measurement of Longitudinal Vibration

The aim of this section is to develop an expression for the sensitivity of a surface bonded PZT sensor to measure longitudinal vibration. The derivation is similar to that of a flexural sensor, but in this section no experimental results are presented. Consider the longitudinal strain sensor as shown in figure 4.16.

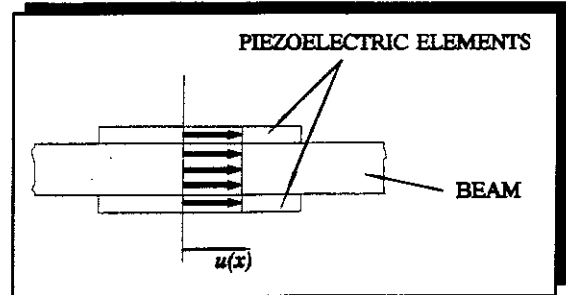


Figure 4.16 Strain Distribution of a Longitudinal Sensor

The strain in the sensor in this case is constant across the section and does not vary as with the flexural sensor. The stress at a point x in the piezoelectric elements is given by:

$$\sigma = E_p \frac{\partial u}{\partial x} \quad (4.23)$$

where u is the displacement in the x direction. Substituting this into equation (4.2) and setting the electric field, E_3 , to zero, an expression for the dielectric displacement, D , of a single element bonded to the beam is obtained:

$$D_3 = d_{31} E_p \frac{\partial u}{\partial x} \quad (4.24)$$

Integrating this over the area, gives the charge developed on one element:

$$q = \int_0^l d_{31} E_p b \frac{\partial u}{\partial x} dx \quad (4.25)$$

which integrates to give:

$$q = d_{31} E_p b \{u(l) - u(0)\} \quad (4.26)$$

At low frequencies, when the length of the sensor is much less than a longitudinal

wavelength, then the strain is approximately constant across the length of the actuator and thus the expression for the charge developed is:

$$q \approx d_{31} E_p b l \epsilon_b \quad (4.27)$$

The voltage generated by the sensor can be found by dividing the charge developed in the sensor by the sensor's capacitance (equation (4.8)). Equations (4.26) and (4.27) give the charge developed on one element of the two element sensor. However, the sensor's output voltage depends on how the elements are connected electrically as with the flexural vibration sensor. The exact and approximate low frequency sensitivities of a *single element* of this two element sensor are:

$$\frac{V}{\{u(l) - u(0)\}} = \frac{d_{31} E_p b}{C_1} \quad (4.28)$$

and

$$\frac{V}{\epsilon_b} \approx \frac{d_{31} E_p b l}{C_1} \quad (4.29)$$

which gives a sensitivity of 0.6818 V/ $\mu\epsilon_{100}$ for the beam and PZT elements discussed in this chapter. As discussed with the flexural vibration sensor, the sensitivity of a parallel connected sensor is the same as for a single element, and the sensitivity of a series connected sensor is double that of a single element.

It is interesting to note that the flexural sensor measures the change in slope at the ends of the sensor, but the longitudinal sensor measures the change in axial displacement at the ends of the sensor. If, however, low frequency approximations are used, the sensitivities of both sensors are in terms of volts generated per strain on the surface of the beam. Generally, the low frequency approximations are valid up to much higher frequencies for longitudinal vibration, as a longitudinal wavelength is generally much larger than a flexural wavelength at a given frequency on most practical structures. (for a 6 mm thick aluminium beam one flexural wavelength = 0.1 m (the length of the PZT elements) at a frequency of 5.48 kHz, and one longitudinal wavelength = 0.1 m at a frequency of 50 kHz).

4.4.3.1 Stiffening Effect of the Sensor

As with the flexural sensor, the longitudinal sensor causes local stiffening. However in this case the longitudinal stiffness (proportional to product of the Young's modulus and cross-sectional area of the beam) of the sensor is the important quantity to be considered. Referring to **figure 4.11**, the cross-section of the beam and sensor, the relevant areas are:

Area of Beam without sensor = $1.836 \times 10^{-4} \text{ m}^2$.

Effective Area of Beam and Sensor = $2.366 \times 10^{-4} \text{ m}^2$

The longitudinal stiffness is thus increased by 29% and the measured strain has to be multiplied by 1.29 to give the strain of the beam adjacent to the sensor. This is much less than with the flexural vibration sensor and if PVDF film was used would be negligible.

4.4.4 Simultaneous Measurement of Longitudinal and Flexural Vibration.

By configuring the PZT elements as shown in **figure 4.17**, it is possible to measure both longitudinal and flexural wave motion. Provided the polarization of the elements is symmetric about the neutral axis of the beam, the sum of the voltages generated by the two elements is proportional to the longitudinal motion and the difference between the voltages generated by the elements is proportional to flexural motion. This can be written in matrix form as:

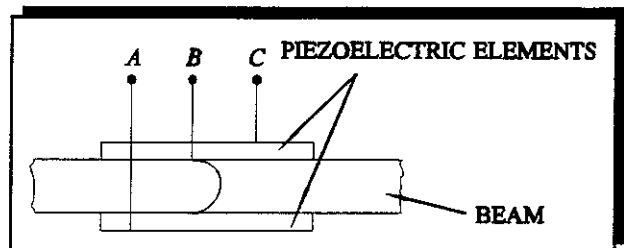


Figure 4.17 Electrical Connections for Simultaneous Longitudinal and Flexural Wave Measurement

$$\begin{bmatrix} V_{long} \\ V_{flex} \end{bmatrix} = 0.5 \begin{bmatrix} 1 & 1 \\ 1 & -1 \end{bmatrix} \begin{bmatrix} V_{AB} \\ V_{CB} \end{bmatrix} \quad (4.30)$$

The voltages V_{AB} and V_{CB} are related to the surface strain of the beam (low frequency approximation) under the sensor according to equations for a single element, i.e., equations (4.17) and (4.29):

$$\text{longitudinal} = 0.6818 \text{ V}/\mu\epsilon_{lon} \quad \text{flexural} = 0.8534 \text{ V}/\mu\epsilon_{lat}$$

The measured strains have to be multiplied by constants due to local stiffening to give the strain of the beam adjacent to the sensor i.e., the strains on the bare beam. These constants are:

$$\text{longitudinal} = 1.29 \quad \text{flexural} = 2.38$$

4.4.4.1 Experimental Verification

An experiment was conducted to see if the PZT sensor can decompose longitudinal and flexural motion on a thin aluminium beam. The experiment was set up as shown in figure 4.18. The beam was the same as that used in previous experiments but in these tests it was excited first laterally and then longitudinally. This was

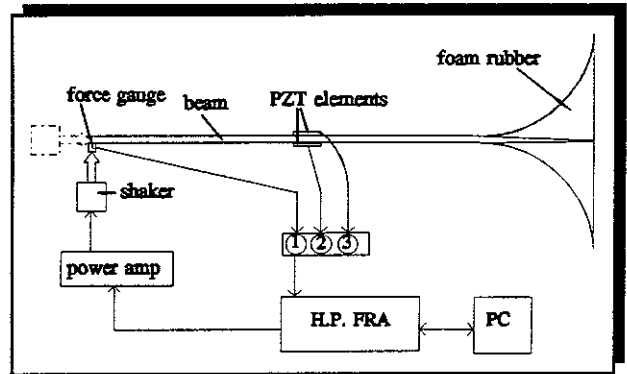


Figure 4.18 Experimental Set Up to Measure Longitudinal and Flexural Motion Simultaneously

done to excite both longitudinal waves and flexural waves, but as the beam was slender and much stiffer in the axial direction than the lateral direction, relatively large amplitude flexural waves were excited in both cases. One other aspect of the beam's configuration should be noted. One end of the beam had an anechoic

termination fitted (the beam was tapered and an exponentially shaped piece of foam rubber fitted). The anechoic termination was effective for flexural waves but not for longitudinal motion, and the beam behaved as a free-free rod in the longitudinal direction with an effective length of 3.56 m.

The results are plotted for lateral excitation in **figure 4.19** and for longitudinal excitation in **figure 4.20**. Overlaid on these graphs are theoretical plots which were derived assuming a semi-infinite beam flexurally, and a free beam longitudinally. When the beam was excited laterally there should have been no longitudinal motion, and when the beam was excited longitudinally there should have been no lateral motion. Clearly this was not the case as can be seen by examining the figures. Notwithstanding this, the theoretical curves which show surface microstrain per unit input force for lateral excitation in **figure 4.19** and longitudinal excitation in

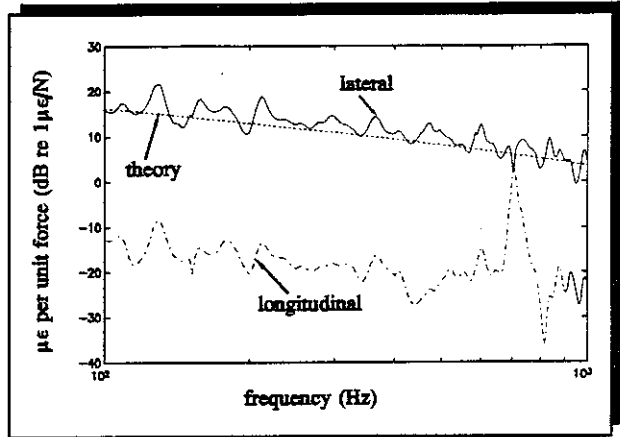


Figure 4.19 Surface Strain per Unit Input Lateral Force Measured using a PZT Sensor

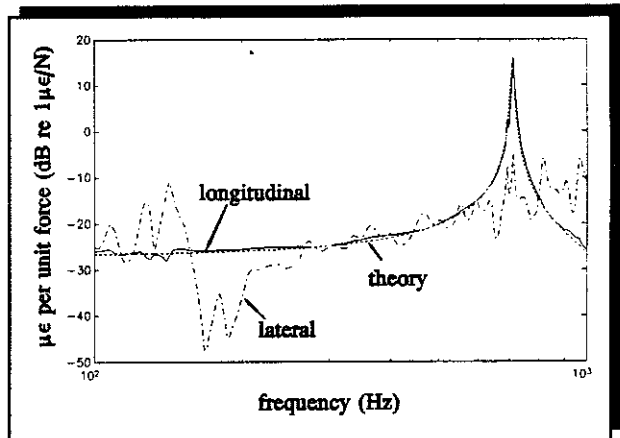


Figure 4.20 Surface Strain per Unit Input Axial Force Measured using a PZT Sensor

figure 4.20 are considered to correlate well with the theory and demonstrate the use of PZT sensors to decompose longitudinal and flexural motion on a beam. The effectiveness of the anechoic termination on flexural wave motion and its ineffectiveness on longitudinal wave motion is also clearly demonstrated.

4.4.5 Conclusions

In this section, theoretical models of flexural and longitudinal vibration PZT sensors for a beam have been derived. Different methods of electrically connecting the elements of the sensor to measure lateral or longitudinal motion exclusively or simultaneously have been described, and the ways in which this affects the sensitivity of the sensor have been discussed. The sensitivity equations are general, and are applicable to both PZT or PVDF sensors, but only PZT sensors were experimentally investigated. PZT sensors however, cause local stiffening of the host structure, and this had to be taken into account in the experimental investigation.

4.5 Piezoelectric Actuators

4.5.1 Introduction

In this section, two types of piezoelectric actuator are discussed, namely flexural and longitudinal vibration actuators. The models are general, and are applicable to PZT and PVDF actuators, but the discussion and experimental work are concerned with PZT actuators only, as these are considered to be of most practical importance. PZT actuators are an attractive way of applying secondary forces and moments to a structure as they are compact and react off the host structure, which removes the need for inertial masses. In certain configurations they can also be used to generate flexural and longitudinal waves simultaneously [70], which means they can be used to control both out-of-plane and in-plane vibration. Since the early work by Crawley and de Luis [32], which related the induced surface strain on a beam to the voltage applied to the PZT elements, there has been a significant amount of research into the use of these actuators for active vibration control, for example [72][73][74]. However, the models for the actuator generally seen in the literature ignore the dynamic effects of the mass and stiffness of the actuators. The gain of an actuator in these cases is the static strain induced in the structure per unit input volts. This can also be written in terms of bending moment per unit per unit input volts for a

flexural vibration actuator, and in-plane force per unit input volts for a longitudinal vibration actuator. Wang and Rogers [74] presented a summary of several different static models for PZT actuators which had the same width as the beam, derived using two different methods; the strain-energy method and the pin-force method and are shown in Table 4.3.

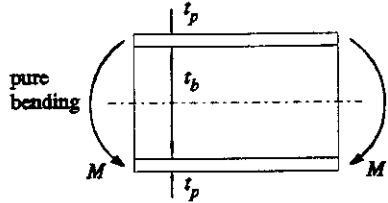
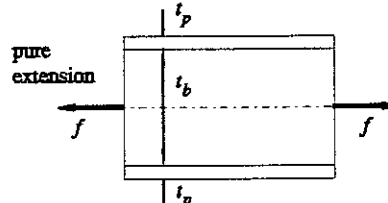
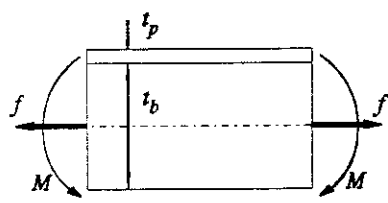
CASE	STRAIN-ENERGY	PIN-FORCE
 <p>pure bending</p>	$M = \frac{t_b^2 E_b}{6 + \Psi} b \Delta$	same
 <p>pure extension</p>	$f = \frac{2 t_b E_b}{6 + \Psi} b \Delta$	$f = \frac{2 t_b E_b}{2 + \Psi} b \Delta$
	$M = \frac{t_b^2 E_b}{2(6 + \Psi)} b \Delta$ $f = \frac{t_b E_b}{6 + \Psi} b \Delta$	$M = \frac{t_b^2 E_b}{2(1 + \Psi)} b \Delta$ $f = \frac{t_b E_b}{1 + \Psi} b \Delta$

Table 4.3 Comparison Between Strain-Energy and Pin-Force Static Models of PZT Actuators [74]

M is the moment generated, f is the force generated and the constant Ψ is given by

the relationship:

$$\psi = \frac{t_b E_b}{t_p E_p}$$

t_b is the thickness of the beam, t_p is the thickness of a PZT element, b is the width of the beam, E_b is the Young's modulus of the beam, E_p is the Young's modulus of the PZT elements and $\Lambda = d_{31}E$, is the piezoelectric strain. The difference between the strain-energy and pin-force models are due to the assumed strain across the beam's cross-section and is discussed later. Referring to **Table 4.3**, it can be seen that if PZT elements are fitted to opposite sides of a beam, and they are driven so that they strain in the opposite sense, then they apply a moment to the beam at each end of the actuator. If the elements are driven so that they strain in the same sense, then they apply an in-plane force to the beam at each end of the actuator. When only one element is fitted to the surface of a beam, both a force and a moment are generated, and thus flexural and longitudinal motion of the beam is induced.

An analysis of these static models is not conducted in this thesis, however they are discussed, and a simple way of coupling the actuators to the dynamics of a beam is presented. A comprehensive (complete) model of an actuator, based on a framework developed by Pines and Von Flotow [22], is developed and compared with a static (simple) model. The complete model includes the mass and stiffness of the PZT elements, and the analysis shows when this is important. To validate the models of the flexural and longitudinal actuators, simple experiments were conducted using the PZT elements and beam discussed in the previous section on piezoelectric sensors. PZT elements, when fitted to a beam, present a discontinuity, which causes wave scattering. This cannot be investigated using the simple model, but can (and is) investigated using the complete model.

4.5.2 A flexural Vibration Actuator

4.5.2.1 Static Model of the Actuator

The flexural vibration actuator considered, consists of two PZT elements glued to opposite sides of a beam, in the same way as the flexural vibration sensor discussed in section 4.4. These are driven in anti-phase and generate moments at the ends of the actuator, provided the PZT elements are perfectly bonded to the beam (infinitely thin bonding layer) [32], as shown in **figure 4.21**. There have been two models postulated for the PZT actuator [32][73]; one assumes that there is uniform strain in the PZT elements and the other, a more complicated model, assumed a linear strain distribution in the PZT elements. Both of these models allow for the width of the PZT elements to be different to the beam unlike the cases considered in **Table 4.3**. These two models are pictured in **figure 4.22**, and the equations relating the applied voltage to the moments generated are given by:

(1) Uniform Strain Model

$$M = \frac{t_b^2 E_b b_b}{6 + \psi} \Lambda \quad (4.31)$$

where:

$$\psi = \frac{E_b b_b t_b}{E_p b_p t_p}$$

and

$$\Lambda = \frac{d_{31} V}{t_p}$$

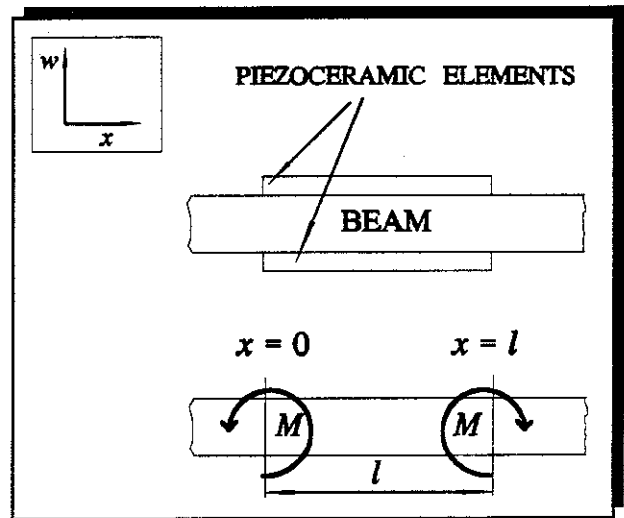


Figure 4.21 A Flexural Vibration Actuator

(2) Euler-Bernoulli Model

$$M = \frac{t_b^2 E_b b_b (1 + T)}{6 + \psi + 12T + 8T^2} \Lambda \quad (4.32)$$

where

$$T = \frac{t_p}{t_b}$$

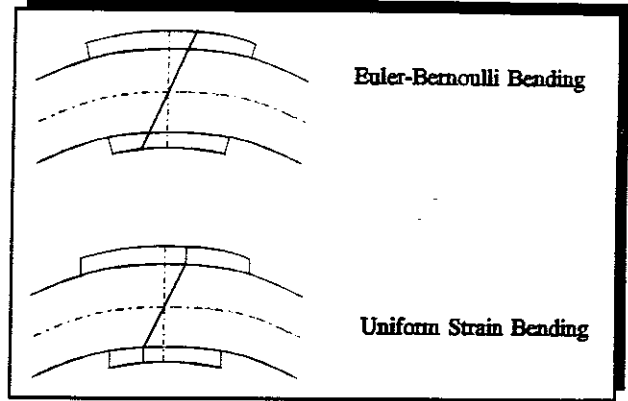


Figure 4.22 Different Models Of Flexural Vibration Actuators

It can be seen that when T , the ratio of the thickness of a PZT element to the thickness of the beam is small, then equation (4.32) reduces to equation (4.31). In fact the difference between the two models is less than 3% for thickness ratios greater than five [73]. However, for thickness ratios less than this, the more complex Euler-Bernoulli strain model should be used, as the applied moment differs by an increasing amount. Crawley and Anderson [73] have checked the Euler-Bernoulli model with a finite element model and showed that the difference between the two models was less than 0.1% for all thickness ratios.

For a 6.12 mm x 30 mm aluminium beam with an actuator made up of two 1.52 mm x 20 mm x 100 mm PZT elements, the relationship between the moment generated and the voltage applied is:

$$V/M = 1203 \text{ V/Nm (Uniform-Strain Model)}$$

$$V/M = 1221 \text{ V/Nm (Euler-Bernoulli Model)}$$

These are useful relationships as they relate the magnitude of a moment applied to a beam by a PZT actuator (connected electrically in parallel) to the voltage applied.

PZT actuators are, in fact, induced strain actuators rather than moment actuators. The moment actuator models described by equations (4.31) and (4.32) are just convenient ways of coupling the actuator into the beam dynamics. It is interesting to examine the strain induced by a PZT flexural vibration actuator to see whether there is an optimum thickness of PZT element. The ratio of the strain at the surface

of the beam ϵ_b , induced by a PZT actuator with the same width as the beam, to the free strain Λ , of a PZT element (which results in the model described by equation (4.32)) is given by the equation [73]:

$$\text{strain ratio} = \frac{\epsilon_b}{\Lambda} = \frac{6(1 + T)}{\left(6 + \frac{E_p}{E_b T}\right) + 12T + 8T^2} \quad (4.33)$$

where T is the thickness ratio (the ratio of actuator thickness to beam thickness) It can be seen that the strain ratio given by equation (4.33) is dependent only on the Young's moduli of the beam and PZT elements and ratio of the actuator thickness to the beam thickness. Equation (4.33) is plotted in **figure 4.23** for steel and aluminium beams with PC5H PZT actuator elements (see Appendix 4). This figure shows that there is an optimum thickness for PZT elements that is about 0.3 of the beam thickness for an aluminium beam and about 0.6 of the beam thickness for a steel beam. The original PZT actuator model developed by de Luis and Crawley [32] (uniform strain model) does not give an optimum thickness and suggests that the thicker the actuator the better.

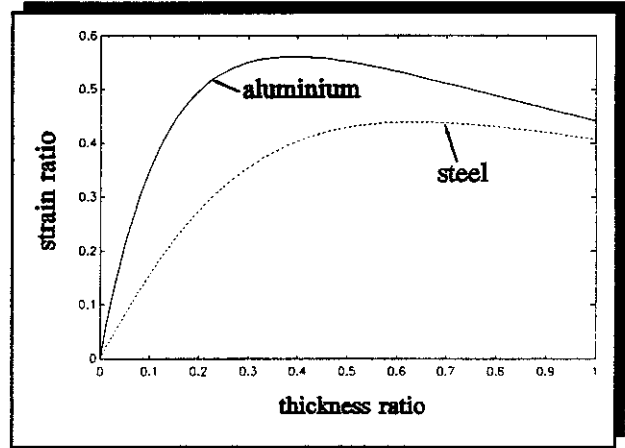


Figure 4.23 Strain Ratio against Thickness Ratio for A PZT Flexural Vibration Actuator Fitted to an Aluminium and a Steel Beam

Clearly this is not the case, but with practical beam-like structures it is unlikely that thick enough actuators will be commercially available to achieve the optimum thickness ratio. On thin plates and shells, however, it is conceivable that actuators of comparable thickness to the plates would be available, in which case an actuator of optimum thickness should be chosen.

The important parameters of induced strain flexural vibration actuators can be seen by examining equation (4.33). It is clear that if the actuator is too thin or too thick it will be ineffective as discussed above. It is also clear that if the actuator has a very

small Young's modulus compared with the beam then it will also be ineffective. In the case of an aluminium beam and PZT actuator the Young's moduli are comparable but in the case of a steel beam and a PVDF actuator there is considerable difference.

4.5.2.2 Coupling the Actuator into the Beam Dynamics

The model of the actuator discussed in the previous section describes how the actuator couples into the structure statically, however as the actuator is designed to dynamically excite the beam, a further model is required to couple the generated moments into the beam dynamics. Actuator arrays, and how they couple into beam dynamics using the wave approach is discussed in Appendix 2 and this approach is adopted here. Consider the flexural actuator fitted to an infinite beam shown in figure 4.24. The actuator is of length l and thus anti-phase moments are a distance l apart are applied to the beam. The wave amplitudes either side of the actuator are the superposition of the waves generated by both of the moments, and are given by:

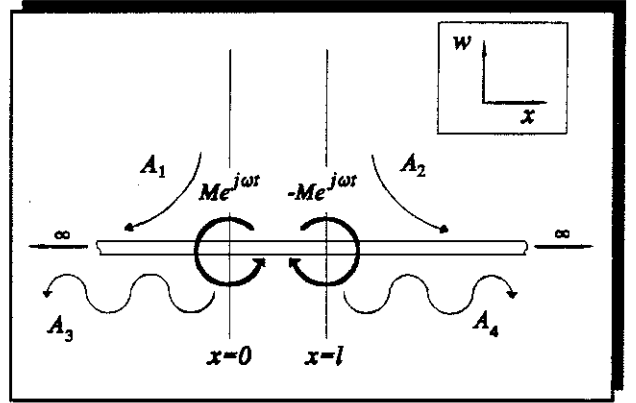


Figure 4.24 Flexural Waves Generated by a PZT Actuator on a Beam

$$\begin{bmatrix} A_1 \\ A_2 \\ A_3 \\ A_4 \end{bmatrix} = \frac{1}{4EI k_b^2} \begin{bmatrix} 1 & e^{-k_b l} \\ -1 & -e^{k_b l} \\ -1 & -e^{-jk_b l} \\ 1 & e^{jk_b l} \end{bmatrix} \begin{bmatrix} M \\ -M \end{bmatrix} \quad (4.34)$$

The generated waves can only propagate away or decay away from the actuator and thus for an infinite beam the displacement of the beam to the right of the actuator ($x \geq l$) is given by:

$$w(x) = A_2 e^{-k_b x} + A_4 e^{-jk_b x} \quad (4.35)$$

and the displacement of the beam to the left of the actuator ($x \leq 0$) is given by:

$$w(x) = A_1 e^{k_b x} + A_3 e^{jk_b x} \quad (4.36)$$

If the beam is finite, then the boundaries on the beam can be modelled by reflection matrices as discussed in Appendix 2, and the total displacement of the beam determined by superposition of direct and reflected waves. Damping in the beam can be modelled by using a complex modulus of elasticity. Equation (4.32) can be used with equations (4.35) and (4.36) to determine the relationship between the flexural waves generated and voltage applied to the actuator.

4.5.2.3 Complete Model of a PZT Flexural Vibration Actuator

The mass and stiffness of the PZT elements will have an effect on the amplitudes of the waves generated by the actuator and will also have a passive effect on the beam in the absence of any voltage being applied to the actuator. Before these effects can be investigated a suitable model of the actuator must be developed. The model is similar to that used by Pines and Von Flotow [22] and involves transforming wave coordinates to the state vector of displacement w , rotation θ , bending moment M , and shear force f , at the ends of the actuator so that it can be coupled to the beam. The relationship between the state vector and the wave-mode coordinates is given by the equation:

$$\begin{bmatrix} w \\ \theta \\ M \\ f \end{bmatrix} = \begin{bmatrix} w \\ w' \\ EIw'' \\ EIw''' \end{bmatrix} = \begin{bmatrix} 1 & 1 & 1 & 1 \\ k_b & -k_b & jk_b & -jk_b \\ EI k_b^2 & EI k_b^2 & -EI k_b^2 & -EI k_b^2 \\ EI k_b^3 & -EI k_b^3 & -jEI k_b^3 & jEI k_b^3 \end{bmatrix} \begin{bmatrix} A_1 \\ A_2 \\ A_3 \\ A_4 \end{bmatrix} \quad (4.37)$$

where the sign convention is shown in figure 4.25 and ' denotes the spatial derivative. The relationship can be written in terms of:

$$\underline{h} = \underline{H} \underline{a} \quad (4.38)$$

where \underline{h} is the state vector, \underline{H} is the transformation matrix and \underline{a} is the vector of waves. A schematic diagram of the PZT actuator, is shown in **figure 4.26**. The section of beam to which the actuators are fitted is known as the active section and the sections of beam either side are denoted passive sections. The left-hand junction between the active and passive sections is junction L and the right-hand junction is labelled R. Force

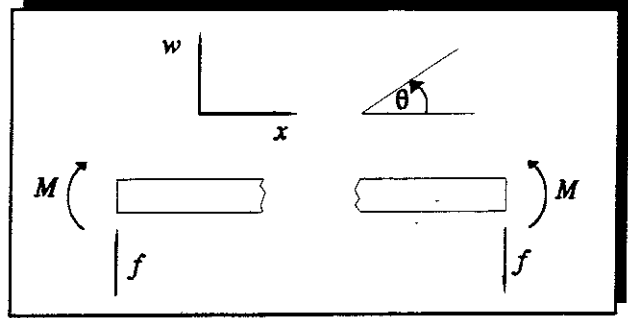


Figure 4.25 Sign Convention used with State Vector

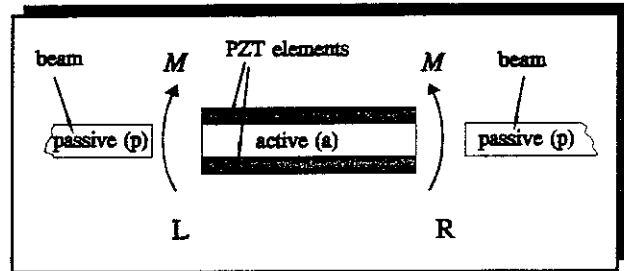


Figure 4.26 Schematic Diagram of the PZT Flexural Actuator

balance and continuity of displacement at these junctions can be applied to give the relationships between the state vectors at the junctions and the applied moments. These are given by:

$$\underline{h}_{Lp} = \underline{h}_{La} + \begin{bmatrix} 0 \\ 0 \\ 1 \\ 0 \end{bmatrix} M \quad (4.39)$$

and

$$\underline{h}_{Rp} = \underline{h}_{Ra} + \begin{bmatrix} 0 \\ 0 \\ 1 \\ 0 \end{bmatrix} M \quad (4.40)$$

where the subscripts a and p denote the active and passive sections of the beam, and L and R are the left and right-hand junctions. These equations show that the state vector on the passive side of a junction is equal to the state vector on the active side of the junction plus the moment applied at the end of the actuator. Equations (4.39)

and (4.40) can be transformed into wave-mode coordinates using equation (4.38) to give:

$$\underline{H}_p \underline{a}_{Lp} = \underline{H}_a \underline{a}_{La} + \begin{bmatrix} 0 \\ 0 \\ 1 \\ 0 \end{bmatrix} M \quad (4.41)$$

and

$$\underline{H}_p \underline{a}_{Rp} = \underline{H}_a \underline{a}_{Ra} + \begin{bmatrix} 0 \\ 0 \\ 1 \\ 0 \end{bmatrix} M \quad (4.42)$$

where \underline{H}_a includes the mass and stiffness of the beam and the PZT elements and \underline{H}_p includes the mass and stiffness of the beam only. The relationship between the wave vectors \underline{a}_{Ra} and \underline{a}_{La} is given by:

$$\underline{a}_{Ra} = \underline{T}_a \underline{a}_{La} \quad (4.43)$$

where \underline{T}_a is the spatial transformation matrix and is given by:

$$\underline{T}_a = \begin{bmatrix} e^{k_{ba}l} & 0 & 0 & 0 \\ 0 & e^{-k_{ba}l} & 0 & 0 \\ 0 & 0 & e^{jk_{ba}l} & 0 \\ 0 & 0 & 0 & e^{-jk_{ba}l} \end{bmatrix} \quad (4.44)$$

substituting equations (4.41) and (4.42) into equation (4.43) gives, after rearranging:

$$\underline{H}_p \underline{a}_{Rp} = \underline{H}_a \underline{T}_a \underline{H}_a^{-1} \underline{H}_p \underline{a}_{Lp} + \underline{Q}M \quad (4.45)$$

where

$$Q = \underline{H}_a \underline{T}_a \underline{H}_a^{-1} \begin{bmatrix} 0 \\ 0 \\ -1 \\ 0 \end{bmatrix} + \begin{bmatrix} 0 \\ 0 \\ 1 \\ 0 \end{bmatrix} \quad (4.46)$$

Equation (4.45) can be rearranged into a partitioned matrix to give the waves at junctions L and R in terms of the moment applied:

$$\begin{bmatrix} \underline{H}_p & | & -\underline{H}_a \underline{T}_a \underline{H}_a^{-1} \underline{H}_p \end{bmatrix} \begin{bmatrix} a_{Rp} \\ a_{Lp} \end{bmatrix} = QM \quad (4.47)$$

This equation can be further rearranged to group the waves into incoming and outgoing waves. This actuator can therefore be represented by the simple block diagram shown in figure 4.27. The resulting expression is:

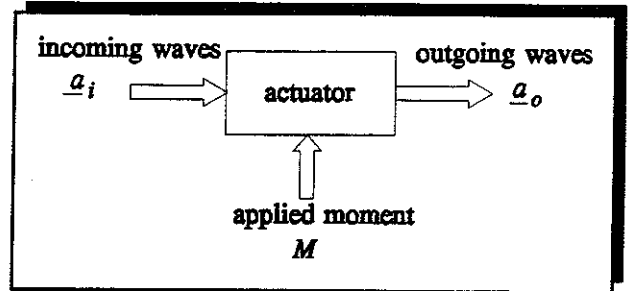


Figure 4.27 Simple Block Diagram of the PZT Actuator

$$\underline{\alpha} a_i + \underline{\beta} a_o = QM \quad (4.48)$$

where the wave vectors are given by:

$$a_i = \begin{bmatrix} A_{R1} \\ A_{R3} \\ A_{L2} \\ A_{L4} \end{bmatrix} \quad \text{and} \quad a_o = \begin{bmatrix} A_{L1} \\ A_{L3} \\ A_{R2} \\ A_{R4} \end{bmatrix} \quad (4.49a \text{ \& } b)$$

and the matrices are given by:

$$\underline{\alpha} = \left[(\underline{H}_p)_1 \mid (\underline{H}_p)_3 \mid (-\underline{H}_a \underline{T}_a \underline{H}_a^{-1} \underline{H}_p)_2 \mid (-\underline{H}_a \underline{T}_a \underline{H}_a^{-1} \underline{H}_p)_4 \right] \quad (4.50)$$

and

$$\underline{\beta} = \left[(-\underline{H}_a \underline{T}_a \underline{H}_a^{-1} \underline{H}_p)_1 \mid (-\underline{H}_a \underline{T}_a \underline{H}_a^{-1} \underline{H}_p)_3 \mid (-\underline{H}_p)_2 \mid (-\underline{H}_p)_4 \right] \quad (4.51)$$

where the subscripts 1 - 4 denote the columns of the respective matrices. Equation (4.48) gives a complete description of the active and passive effects of the actuator. The waves generated by the actuator can be determined by setting the incoming wave vector \underline{a}_i to zero. The passive effects of the actuator can be determined by setting the moment M to zero and the outgoing waves can then be determined in terms of the incoming waves.

4.5.2.4 Comparison Between the Simple and Complete Models of the PZT Flexural Vibration Actuator

To compare the two models of the PZT actuator described above, the propagating waves generated are compared for a given applied moment. As mentioned previously, the actuators induce strain in the beam. To model the coupling between the actuator and the beam, the moment required to induce this strain is calculated and applied to the beam at the each end of the actuator. It is clear that if the mass and stiffness of the actuator elements are included in the model, then a greater static moment is required to induce the same strain as that on a model of the beam that does not have the PZT elements included. Thus, in the model that includes the PZT elements, the static moment applied is greater than the moment applied to the simple model. The relationship between these moments is:

$$M_{complete} = \tilde{I} M_{simple} \quad (4.52)$$

where:

$$\tilde{I} = \frac{I_{complete}}{I_{simple}} = 1 + \frac{E_p}{E_b} \{ (1 + 2T)^3 - 1 \}$$

For simplicity, the actuator is assumed to be the same width as the beam. The magnitude of the generated propagating wave per unit input moment is calculated by rearranging equation (4.48) to give:

$$a_o = \beta^{-1} Q M_{complete} \quad (4.53)$$

The amplitudes of the propagating waves are plotted for thickness ratios ranging from 0 to 0.5 as a function of the length of the PZT actuator divided by a flexural wavelength in the 6.12 mm x 30 mm aluminium beam. These are shown in **figure 4.28**. The simple model described by equation (4.34) is equivalent to the complete model with a thickness ratio of zero. It should be noted that this analysis does not include the relationship between the voltage applied and the moment generated (equation (4.32)). It is only intended to examine the effects of neglecting the mass and stiffness of the actuator. Graphs are also plotted of the ratios of the complex propagating wave amplitudes, calculated using the simple model, to the wave amplitudes calculated using the complete model, for different thickness ratios. These are shown in **figures 4.29** (magnitude) and **4.30** (phase). These figures show that the mass and stiffness of the PZT elements

have an effect on the amplitude and phase of the generated propagating waves.

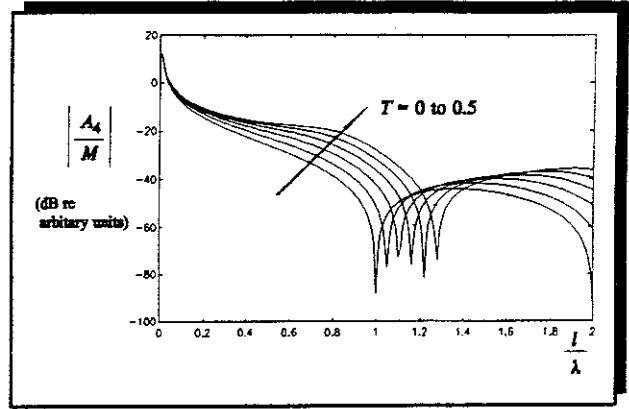


Figure 4.28 Propagating Wave Amplitude per unit Moment Applied

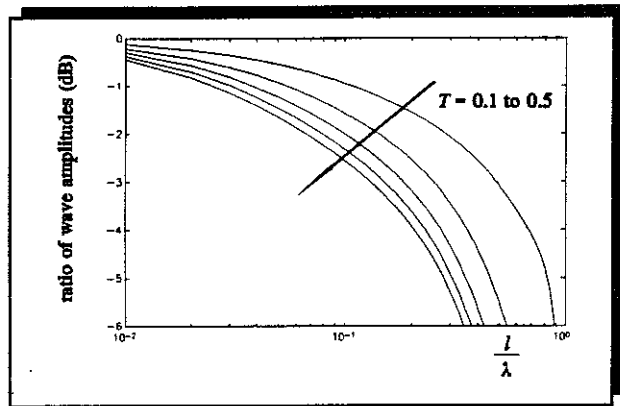


Figure 4.29 Ratios of Propagating Wave Amplitudes Calculated using the Simple and Complete Models

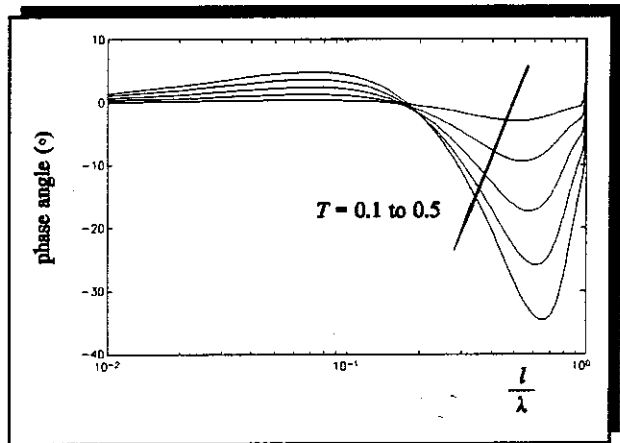


Figure 4.30 Phase Between Propagating Waves Calculated using the Simple and Complete Models

Figures 4.29 and 4.30 show that the simple model is a reasonable representation of a PZT actuator with a low thickness ratio fitted to a beam and operated at low frequencies. However, it underestimates the amplitude of propagating waves generated by an actuator that is relatively thick compared to the beam and is operated at higher frequencies. **Figure 4.30** shows that there is also an effect on the phase relationship between the applied moment and the generated wave. This could be important in the modelling of an active vibration control system, as accurate phasing of a secondary source is vital.

A possible reason for the differences between the simple and the complete model is because the moment at each end of the actuator is driving into a passive section of beam and the thicker actuator section. The actuator section is seen as a stiffness rather than a beam by the applied moment at low frequencies. As the impedance of a stiffness is proportional to $1/\text{frequency}$ and the impedance of a beam is proportional to $1/\text{frequency}^2$, the proportion of the applied moment driving the beam rather than the actuator stiffness increases with frequency.

4.5.2.5 Passive Effects of the PZT Flexural Vibration Actuator

The actuator has a passive effect on the beam dynamics. It is equivalent to a mass and stiffness being added to the beam resulting in a discontinuity with consequential wave conversion. However, because of the symmetry of the arrangement, there is no scattering from flexural to longitudinal motion and vice versa, but with a single element actuator as shown in **Table 4.3**, then there is scattering between these motions. The scattering of flexural waves is investigated in this section by considering a propagating wave incident on the actuator as shown in **figure 4.31**. Using the terminology of the previous section, the incident wave A_i is the incoming wave and near-field waves A_1 and A_2 and the propagating waves A_3 and A_4 are the outgoing waves. Equation (4.48) is used to determine the outgoing wave amplitudes in terms of the incident wave with no applied moment. The applied moment can be

set to zero in this equation which can then be arranged to give:

$$a_o = -\beta^{-1} \alpha a_i \quad (4.54)$$

The magnitude of the outgoing waves for different thickness ratio are plotted in **figures 4.32 - 4.34**. A check was made on the calculations; the amplitudes of the positive and negative-going outgoing propagating waves were squared and summed and divided by the square of the incident propagating wave to check that this was unity. This is a necessary condition for any conservative junction as the power flow into the junction must equal the power flow out of the junction. Examination of **figures 4.32 - 4.34** shows that a thicker actuator has a greater passive effect than a thinner actuator, as expected. It can also be seen that the amplitudes of the waves are dependent not only on the thickness ratio but also frequency. The amplitude of the A_4 wave is at most attenuated by about 20% for a thickness ratio of 0.5, which means that the incident propagating wave generally passes through the actuator without a large

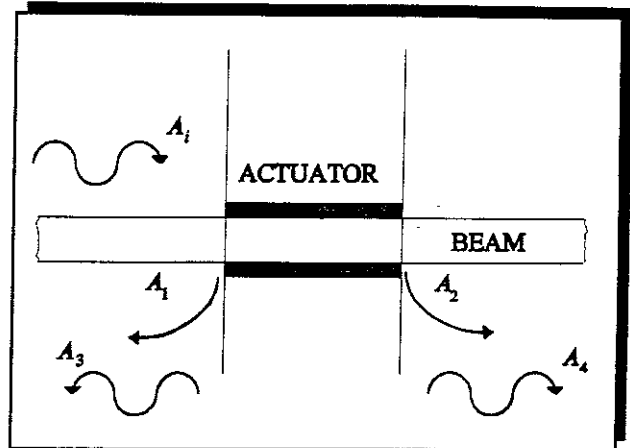


Figure 4.31 Wave Conversion by the PZT Actuator

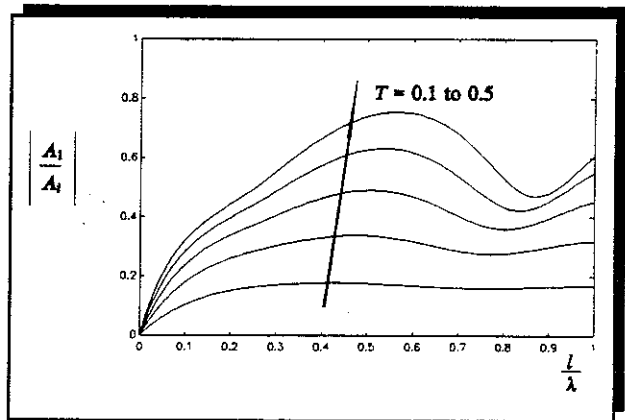


Figure 4.32 Normalised Magnitude of the Reflected Evanescent A_1 Wave.

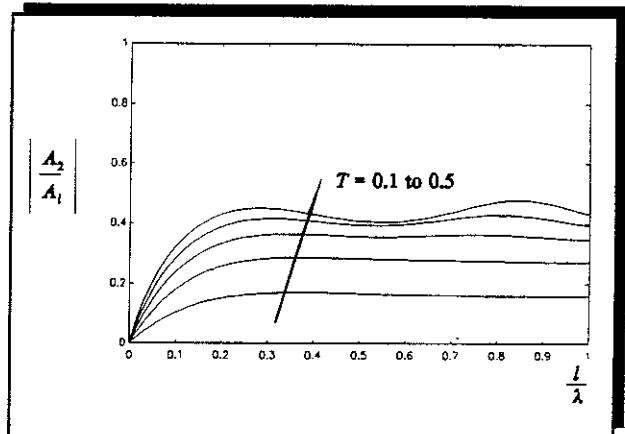


Figure 4.33 Normalised Magnitude of the Transmitted Evanescent A_2 Wave.

degree of attenuation. However a nearfield A_2 wave is generated and this amplitude increases to up to about 50% of the amplitude of the incident propagating wave for the same thickness ratio. The reflected negative-going waves have surprisingly large amplitudes. The A_1 wave has a magnitude approaching about 80% of the incident propagating wave for a

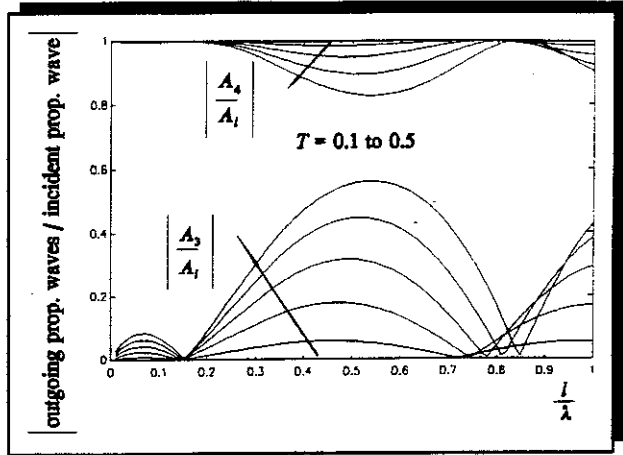


Figure 4.34 Normalised Magnitude of the Reflected Propagating A_3 Wave and the Transmitted A_4 Wave.

thickness ratio of 0.5 and the A_3 wave has an amplitude of almost 60% of the incident wave for the same thickness ratio, but this varies considerably with frequency. This frequency dependent behaviour is similar to that of a spatially periodic structure as discussed by Cremer *et al* [13] where there are frequency bands at which waves are transmitted readily and other frequency bands where they are not.

4.5.2.6 Vibrational Power Supplied by a PZT Flexural Vibration Actuator

To compare a PZT flexural actuator with other generic actuators such as force or moment actuators fitted to an infinite beam, the power supplied by a pair of moments a distance l apart (the simple model of a PZT actuator) is considered. This is derived in Appendix 3 and is given by:

$$P_{\text{PZT}} = \frac{\omega |M|^2}{4EI k_b} (1 - \cos k_b l) \quad (4.55)$$

The power supplied by a *force* and a *moment* actuator to an infinite beam are derived in Appendix 3 and is given by:

$$P_{\text{force}} = \frac{\omega |f|^2}{8EI k_b^3} \quad \text{and} \quad P_{\text{moment}} = \frac{\omega |M|^2}{8EI k_b} \quad (4.56a, b)$$

The power supplied to an infinite beam by force, moment and moment-pair (PZT) actuators as a function of the length of the PZT actuator divided by a flexural wavelength are plotted in Appendix 3. To place this into context for the 6.12 mm aluminium beam discussed in this chapter, the power supplied by a point force of 1 N, a point moment of 0.1 Nm and a pair of 0.1 Nm moments at a distance of 10 cm apart (this is the magnitude of the moments generated by a pair of PZT actuators driven out of phase at about 120 V) are plotted in figure 4.35. It is interesting to note that the graphs for the force and the PZT actuator cross over at about 150 Hz and that the frequency at which one flexural wavelength equals the length of the actuator is about 5.5 kHz. A

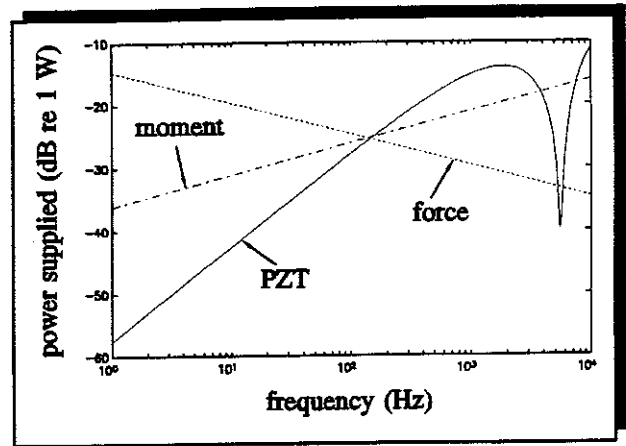


Figure 4.35 Power Supplied to an 6.12 mm Thick Infinite Aluminium Beam by Different Actuators (Theoretical)

flexural wavelength is dependent upon the flexural rigidity, and the aluminium beam has a relatively low flexural rigidity in comparison with many real engineering structures. Hence, on most practical structures the PZT actuator would be used at frequencies well below the frequency where the length of the actuator equals one flexural wavelength. As it is preferable to operate the actuator at frequencies close to the frequency where the length of the actuator equals half a flexural wavelength it will be necessary to tailor the length of the actuator accordingly.

4.5.2.7 Experimental Validation

In order to measure power supplied by an actuator it is generally necessary to measure the force (or moment/pair) applied and the response of the beam at the point

of application of the force or moment/pair. This requires a co-located actuator and sensor, and in the case of a point force is relatively easy to measure with a force gauge and accelerometer. It is more difficult with a PZT actuator as the moment applied has to be determined from the applied voltage and the response from a sensor with identical shape to the actuator. It could also be achieved with a self-sensing actuator [71], which is discussed later in this chapter. However, flexural vibrational power is proportional to the square of the amplitude of a flexural travelling wave and thus if this quantity could be measured this would give an indication of the power supplied to a beam.

An experiment was set up to measure the response of a beam to excitation by a PZT flexural vibration actuator and is shown in figure 4.36. Two 1.5 mm x 20 mm x 100 mm PZT elements were fitted to a 6 mm x 30 mm x 4 m aluminium beam that had an anechoic termination fitted to one end. The beam was thus "semi-infinite". The difference between the transverse acceleration of 6 mm x 30 mm infinite beam and a semi-infinite beam of similar dimensions, when excited by a PZT flexural vibration actuator of the dimensions quoted above, calculated using the complete model is shown in figure

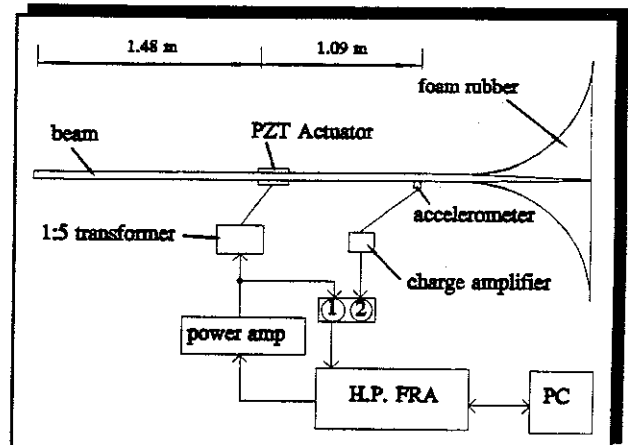


Figure 4.36 Experimental Set Up to Determine the Power Supplied to a Beam by a PZT Flexural Actuator

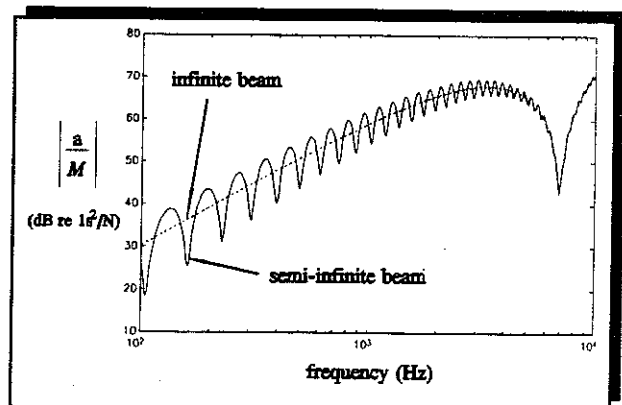


Figure 4.37 Theoretical Response of an Infinite and Semi-infinite Beam to Excitation by A PZT Flexural Vibration Actuator. Loss factor of 1%

4.37. It can be seen that the trends for both infinite and semi-infinite beams are similar. The effect of the boundary can be seen as reflections that either

constructively or destructively interfere with the direct waves generated by the actuator, resulting in the rippled response. The responses plotted in **figure 4.37** are calculated using the complete model of the actuator described previously. The response of the experimental beam calculated using the simple and complete models of the beam are plotted together in **figure 4.38** for comparison. It can be seen that at low frequencies there is little difference between the two models, but at higher frequencies there are considerable differences, as predicted previously. The simple model underestimates the response of the beam, and the predicted frequency at which the dip in the response occurs is over 100 Hz less than with the complete model.

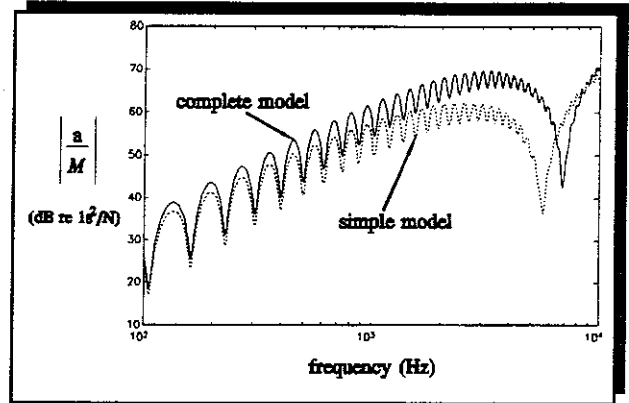


Figure 4.38 Comparison of the Theoretically Calculated Response of the Experimental Beam using the Complete and Simple Models of the Actuator

The beam was excited over a frequency range of 100 Hz to 1 kHz using the stepped sine technique with 5 Hz intervals. The moment applied was measured by sensing the voltage applied to the 1:5 step-up transformer and the response the response downstream of the actuator using an accelerometer B&K type 4638 and charge amplifier B&K type 2626. The analyser used was an HP 3566A HP Frequency Response Analyser. The measurement (in volts) had to be converted to acceleration per unit moment applied ($1/\text{Ns}^2$) which was achieved by the following multiplication:

$$\frac{\text{accel}}{M} = \frac{1221 \cdot 100}{5} * \frac{V_a}{V_m}$$

where the number 1221 is the relationship between the voltage applied and the moment generated, 100 is the attenuation on the accelerometer charge amplifier and 5 is the transformer ratio. V represents voltage and the subscripts a and m represent acceleration and moment respectively. The theoretical and experimental results are plotted in **figure 4.39**. The loss factor in the beam was taken to be 1%.

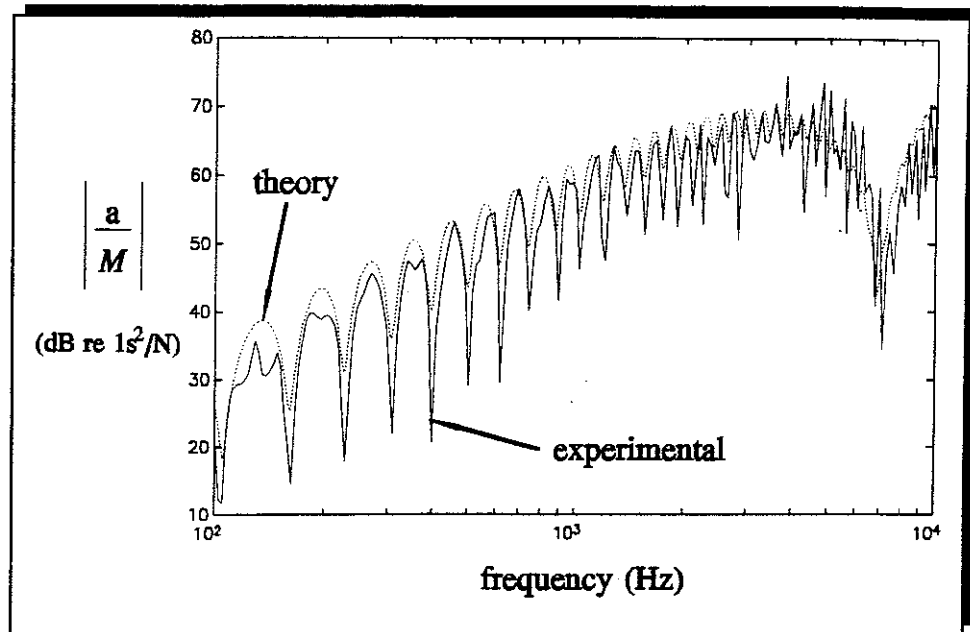


Figure 4.39 Response of the Experimental Beam to Excitation by a PZT Flexural Vibration Actuator - Theoretical and Experimental Results

It can be seen that the experimental and theoretical results compare favourably, and that even with an actuator and beam with a thickness ratio of 0.25, the complete model is required to accurately predict the response of the beam at high frequencies. **Figure 4.38**, however, shows that the simple model is adequate up to about 1 kHz.

It was shown previously by Brennan *et al* [88] that the effect of the actuator on the beam response could be modelled by using the simple model and reducing the effective length of the actuator by an amount proportional to the added stiffness of the actuator. However, whilst this will predict the frequency at which the dip in the response occurs it does not predict the response as accurately as the complete model at high frequencies.

4.5.2.8 Uni-Directional Wave Generators

It was shown in Chapter 2, that in the active control of waves on a beam-like structure, it is advantageous to be able to generate uni-directional propagating waves. This can be achieved by correctly phasing two actuators, but the question addressed

in this section is whether this can be achieved with one actuator shaped to give the required response. The PZT flexural vibration actuator discussed previously consisted of two rectangular elements and generated a moment at each end of the actuator when the PZT elements were driven anti-phase. Bailey and Hubbard [83] showed that by using a triangular PVDF actuator, a force can be generated at one end and a moment and a force at the other end, as shown in figure 4.40. The following analysis investigates whether a combination of forces and moments can be applied to a beam to generate a uni-directional wave. Consider a hypothetical actuator that could generate both forces and moments at each end of the elements as shown in figure

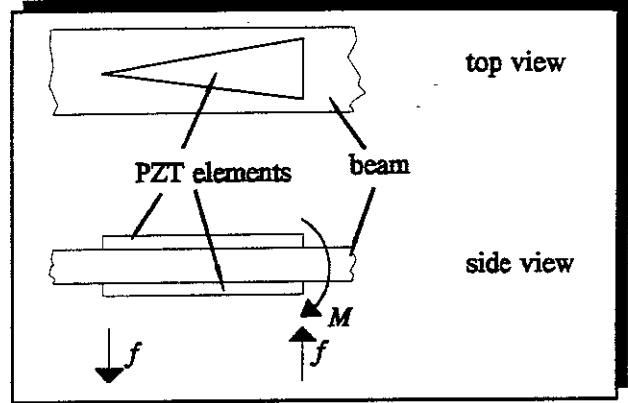


Figure 4.40 A PZT Actuator Comprising Triangular PZT Elements

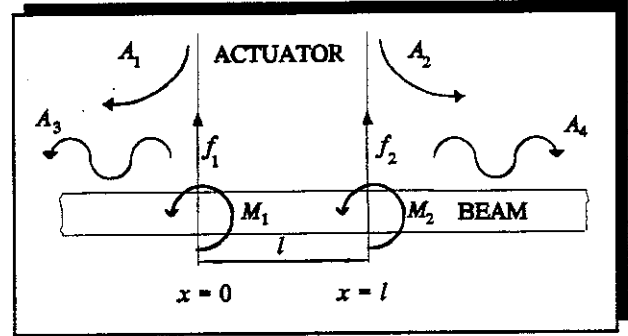


Figure 4.41 A Model of a General Distributed Flexural Actuator

4.41. As we are only interested in propagating waves, the evanescent A_1 and A_2 waves can be ignored. The magnitude of the propagating waves can be described by the matrix equation:

$$\begin{bmatrix} A_3 \\ A_4 \end{bmatrix} = \frac{-1}{4EI k_b^3} \begin{bmatrix} j & j e^{-jk_b l} & k_b & k_b e^{-jk_b l} \\ j & j e^{jk_b l} & -k_b & -k_b e^{jk_b l} \end{bmatrix} \begin{bmatrix} f_1 \\ f_2 \\ M_1 \\ M_2 \end{bmatrix} \quad (4.57)$$

For a positive-going unidirectional wave A_4 , we require $A_3 = 0$, which gives:

$$j f_1 + k_b M_1 = -(j f_2 + k_b M_2) e^{-jk_b l} \quad (4.58)$$

If $f_2 = M_2 = 0$, there is a co-located point force and moment and we get:

$$f_1 = j k_b M_1 \quad (4.59)$$

Thus, a unidirectional wave can be generated using a co-located point force and moment. This, however, is clearly not achievable with a PZT actuator of finite length in which the forces and moments must balance and so there must be at least an f_2 or M_2 . Equation (4.58) shows that in order to generate a unidirectional wave there must be a phase shift of $k_b l$ between the force and moment generated at one end of the actuator and the force and moment generated at the other. The static requirements of the actuator give:

$$\sum f = 0, \quad \therefore f_1 = -f_2 \quad (4.60)$$

and

$$\sum M_{x=0} = 0, \quad \therefore M_1 + M_2 + f_2 l = 0 \quad (4.61)$$

Thus, with a single actuator the forces and moments at each end of the actuator are in anti-phase as they are applied at the same time, and they react against one another. This suggests that an actuator of any shape that applies forces and moments at the ends cannot generate a unidirectional wave. The question which remains to be answered, however, is whether shaping an actuator can cause a change in phase of the generated left-going and right-going propagating waves. To study this the actuator shown in **figure 4.41** is considered. The shape of the actuator can be allowed for by letting M_2 be a fraction of M_1 , which can be written as:

$$M_2 = -\alpha M_1 \quad 0 \leq \alpha \leq 1 \quad (4.62)$$

When $\alpha = 1$ this is equivalent to the rectangular actuator with a moment being applied at each end but no forces are applied. When $\alpha = 0$ this is equivalent to a triangular actuator as shown in **figure 4.40**. Combining equations (4.60 - 4.62), we get the following relationships for the forces.

$$f_1 = \frac{(1 - \alpha)M_1}{l}, \quad f_2 = \frac{(\alpha - 1)M_1}{l} \quad (4.63a, b)$$

Thus the expressions for the propagating waves become:

$$A_3 = \frac{-M_1}{4EI k_b^3 l} \left\{ j((1 - \alpha) + (\alpha - 1)e^{-jk_b l}) + k_b l(1 - \alpha e^{-jk_b l}) \right\} \quad (4.64)$$

and

$$A_4 = \frac{-M_1}{4EI k_b^3 l} \left\{ j((1 - \alpha) + (\alpha - 1)e^{jk_b l}) - k_b l(1 - \alpha e^{jk_b l}) \right\} \quad (4.65)$$

The amplitudes of the A_3 and A_4 waves are equal and are plotted for values of α between 0 and 1 and for values of l/λ between 0 and 2 in **figure 4.42**. It can be seen that the amplitudes of the waves are dependent on both frequency and actuator shape. The phase relationship between the A_3 and A_4 waves for values of α between 0 and 1 and for values of l/λ between 0 and 2 are shown in **figure 4.43**. It is clear from this figure that the shape of the actuator and the frequency affects the relative phase between the positive and negative-going propagating waves even though the amplitudes of the two waves are always the same.

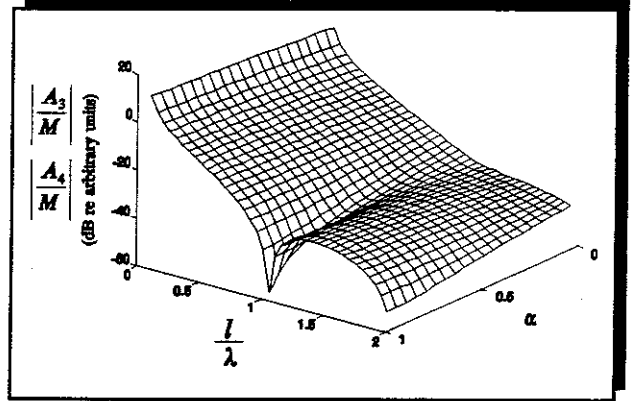


Figure 4.42 Propagating Wave Amplitudes for Different Actuator Shapes

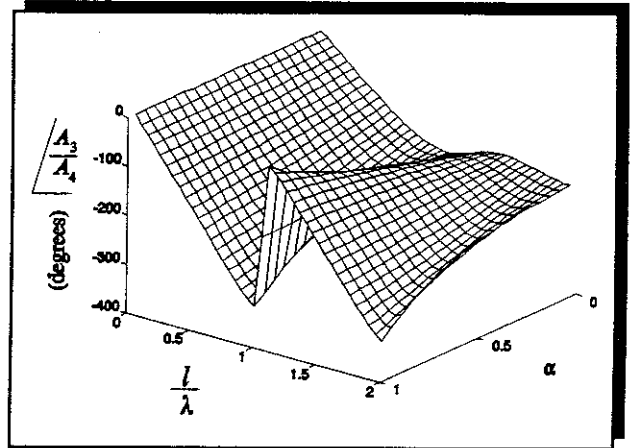


Figure 4.43 Phase Relationship between the Propagating Waves

4.5.2.9 Spacing of Flexural PZT Actuators

When more than one point actuator is used to suppress flexural waves on a beam the secondary effort required is dependent upon the spacing of the actuators as discussed in Chapter 2. It was also shown previously in this chapter that the length of an actuator compared to a flexural wavelength is an important parameter when considering power supplied by the actuator to the beam. Thus, when PZT actuators are used to suppress flexural waves on a beam, two parameters need to be considered from the point of view of secondary effort required; these are actuator length and distance between the actuators. The arrangement discussed in this section consists of

two rectangular PZT elements fixed to a slender beam as shown in **figure 4.44**. This can be represented in terms of the simple models as moments being applied to the beam as shown in **figure 4.45**. A_i is the incident propagating flexural wave to be suppressed by the two actuators. The actuators are configured to suppress the incident propagating wave and at the same time not to generate a negative-going propagating wave (i.e. they have to generate a unidirectional wave). This can be expressed by the equation:

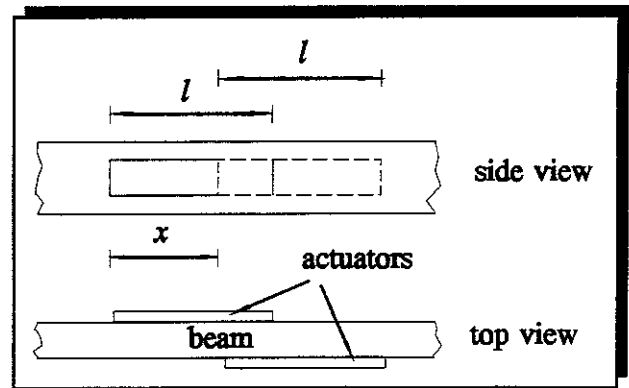


Figure 4.44 Spacing of PZT Flexural Vibration Actuators

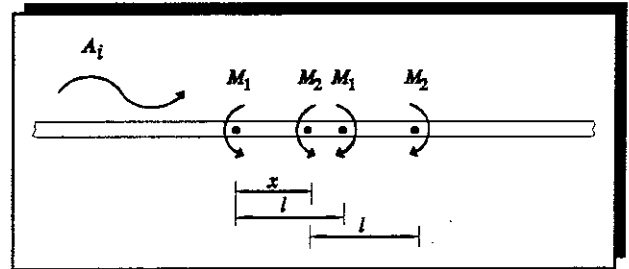


Figure 4.45 Simple Representation of Two Rectangular PZT Actuators Fitted to a Beam

$$\frac{-1}{4EI k_b^2} \begin{bmatrix} 1 - e^{-jk_b l} & e^{-jk_b x} (1 - e^{-jk_b l}) \\ -1 + e^{jk_b l} & -e^{jk_b x} (1 - e^{jk_b l}) \end{bmatrix} \begin{bmatrix} M_1 \\ M_2 \end{bmatrix} + \begin{bmatrix} 0 \\ -A_i \end{bmatrix} = 0 \quad (4.66)$$

This can be solved to determine the magnitude and phase of the moments, M_1 and M_2

required. The algebra is rather tedious so the solutions presented below are from a numerical solution to this matrix equation. If we assume that the incident wave is generated by a moment M_p such that:

$$A_i = \frac{-M_p}{4EI k_b^2} \quad (4.67)$$

The non-dimensional secondary effort required to set the incident and reflected propagating waves to zero can be defined as:

$$Effort = \frac{|M_1|^2 + |M_2|^2}{|M_p|^2} \quad (4.68)$$

with M_1 and M_2 given by the solution to equation (4.66). This is dependent upon the length of the

actuators compared to a wavelength (l/λ) and the distance between the leading edge of the actuators compared to a wavelength (x/λ), and is plotted in **figure 4.46**. It can be seen that the effort required becomes very large when the spacing between the actuators is an integer number of half wavelengths, and when the length of an actuator equals an integer number of whole wavelengths. The minimum effort is required when the distance between the actuators is an odd-integer number of quarter-wavelengths, and the length of the actuator equals an odd-integer number of half-wavelengths. One problem with the arrangement shown in **figure 4.44** is that longitudinal waves will be generated as well as flexural waves, as each actuator generates both a moment and a force. The forces applied by each element are not in anti-phase and thus there is a resultant force that generates a longitudinal wave. Therefore the actuators should be fitted in pairs with two elements on opposite sides of the beam such that they can generate flexural or longitudinal waves independently.

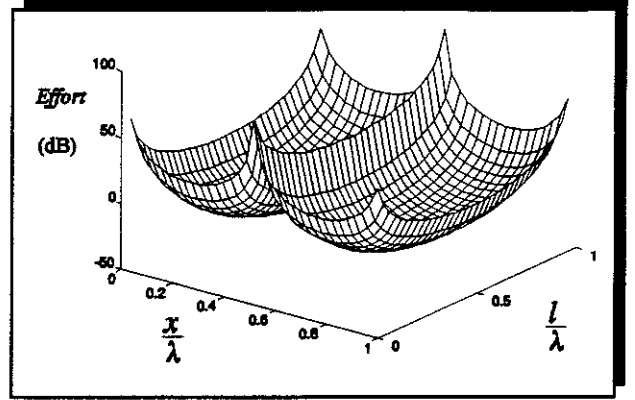


Figure 4.46 Secondary Effort Required to Suppress the Incident and reflected Propagating Flexural Waves

4.5.3 A Longitudinal Vibration Actuator

This section describes how piezoelectric elements such as those discussed in the previous section can be used to generate longitudinal wave motion on a beam. The static model is first discussed and a suitable model then developed to couple the actuator into the beam dynamics. As with the flexural PZT actuator, a complete model is developed that includes the mass and stiffness of the PZT elements and the simple and complete models are then compared. A simple experiment is then conducted to validate the model of the actuator.

4.5.3.1 Static Model of the Actuator

Consider the longitudinal actuator shown in **figure 4.47**. This is the same arrangement as the flexural vibration actuator shown in **figure 4.21** but the PZT elements are driven in phase and generate forces at the ends of the elements. In **Table 4.3** two models of a PZT longitudinal induced strain actuator are shown, one based on a strain-energy model and one based on a pin-force model. The difference between these models is demonstrated in **figure 4.48**; the pin-force model assumes a uniform strain across the beam's cross-section and the strain-energy model assumes that each element induces a linearly varying strain in the beam's cross-section. The equations for both models relating force applied to the beam per unit input voltage are:

(1) Strain-Energy Model

$$f = \frac{2t_b E_b b_b}{6 + \psi} \Lambda \quad (4.69)$$

where:

$$\psi = \frac{E_b b_b t_b}{E_p b_p t_p}$$

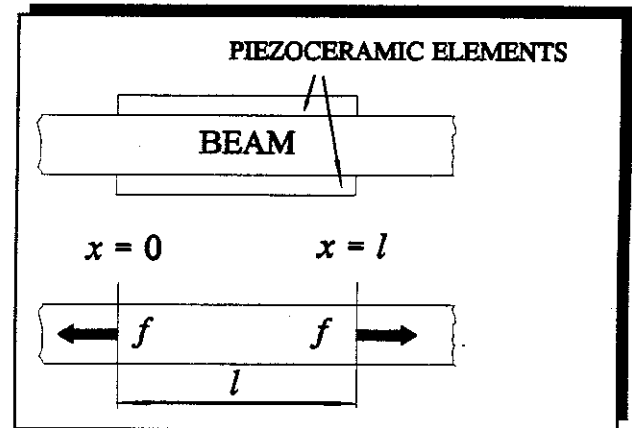


Figure 4.47 A Longitudinal Vibration Actuator

and

$$\Lambda = \frac{d_{31} V}{t_p}$$

(2) Pin-Force Model

$$f = \frac{2t_b E_b b_b}{2 + \psi} \Lambda \quad (4.70)$$

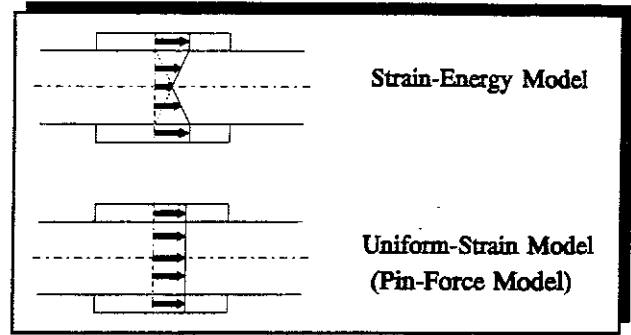


Figure 4.48 Strain Distribution of Different Models of Longitudinal Vibration Actuators

where the subscript b and p stand for beam and PZT respectively. It

can be seen that two static models are similar, and that the pin-force model has a higher gain than the strain-energy model. Wang and Rogers [74], showed that the more accurate model is the strain-energy model, and that the pin-force model overestimates the equivalent force applied by the actuator, especially if the thickness of the beam is large compared with the actuator thickness. For a 6.12 mm x 30 mm aluminium beam with an actuator made up of two 1.52 mm x 20 mm x 100 mm PZT elements, the relationship between the force generated and the voltage applied is:

$$V/f = 3.68 \text{ V/N (Strain-Energy Model)}$$

$$V/f = 2.55 \text{ V/N (Pin-Force Model)}$$

It can be seen that for a relatively small voltage quite large forces can be applied to the beam and that the difference in gain predicted by the two models is quite large.

4.5.3.2 Coupling the Actuator into the Beam Dynamics

As with the flexural vibration actuator, the longitudinal vibration actuator can be coupled into the beam dynamics using a wave model of the beam. This simple model of the actuator is shown in **figure 4.49** where it should be noted that the passive PZT elements are not included. The in-plane forces f , applied by the PZT actuator generate the longitudinal in-plane waves A_i , and A_r . The amplitudes of these waves

on either side of the actuator are the superposition of the waves generated both of the forces and are given by:

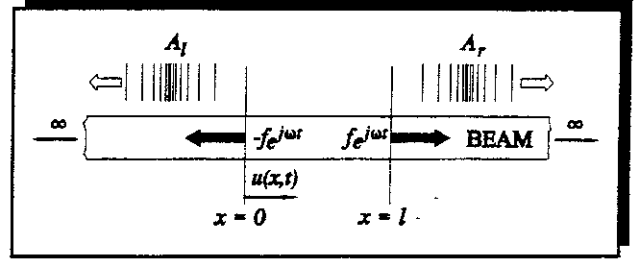


Figure 4.49 Longitudinal Waves Generated by a PZT Actuator on a Beam

$$\begin{bmatrix} A_l \\ A_r \end{bmatrix} = \frac{-j}{2k_l ES} \begin{bmatrix} 1 & e^{-jk_l l} \\ 1 & e^{jk_l l} \end{bmatrix} \begin{bmatrix} -f \\ f \end{bmatrix} \quad (4.71)$$

where k_l is the longitudinal wave number and S is the cross-sectional area of the beam. The longitudinal displacement amplitudes to the left and right of the actuator are also equal to the wave amplitudes A_l and A_r respectively as there are no nearfield longitudinal waves. The amplitudes of the longitudinal waves generated by a point in-plane force are derived in Appendix 2. Boundaries can be modelled as a simple reflection coefficient and examples of these are also shown in Appendix 2.

4.5.3.3 Complete Model of a PZT Longitudinal Vibration Actuator

As with the flexural vibration actuator, the mass and stiffness of the PZT elements will have an effect on the amplitudes of the longitudinal waves generated by the actuator. They will also have a passive effect on the beam in the absence of any voltage being applied to the actuator. Before these effects are investigated, a suitable model of the actuator has to be developed. This model is similar to that used by Pines and Von Flotow [22] and that discussed for the flexural vibration actuator. It involves transforming wave coordinates to the state vector of longitudinal displacement u and force f . The relationship between the state vector and the wave coordinates is given by the equation:

$$\begin{bmatrix} u \\ f \end{bmatrix} = \begin{bmatrix} u \\ ESu' \end{bmatrix} = \begin{bmatrix} 1 & 1 \\ jk_l ES & -jk_l ES \end{bmatrix} \begin{bmatrix} A_l \\ A_r \end{bmatrix} \quad (4.72a)$$

where the sign convention is shown in **figure 4.49** and ' denotes the spatial derivative. This wave coordinate transformation can be used in a similar way to discussed for the flexural vibration actuator to couple the actuator to the beam. Equation (4.72a) can be written as:

$$\underline{y} = \underline{V} \underline{a} \quad (4.72b)$$

where \underline{y} is the state vector, \underline{V} is the transformation matrix and \underline{a} is the wave vector. A schematic of the

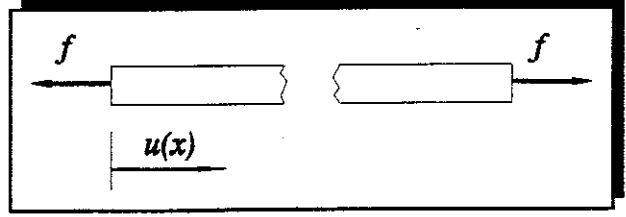


Figure 4.49 Sign Convention used with State Vector

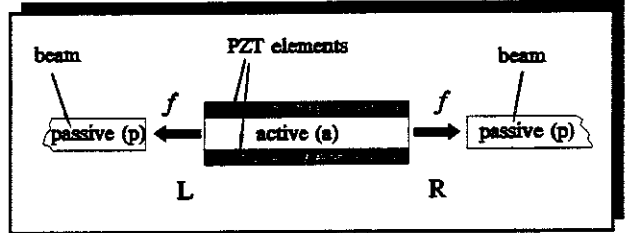


Figure 4.50 Schematic Diagram of the PZT Longitudinal Actuator

PZT longitudinal vibration actuator is shown in **figure 4.50**. As before, the section of beam to which the actuator is fitted is known as the active section and the sections of beam either side are denoted passive sections. The junctions are denoted L and R. The relationships between the state vectors at these junctions and the applied forces are given by:

$$\underline{y}_{Lp} = \underline{y}_{La} + \begin{bmatrix} 0 \\ 1 \end{bmatrix} f \quad (4.73)$$

and

$$\underline{y}_{Rp} = \underline{y}_{Ra} + \begin{bmatrix} 0 \\ 1 \end{bmatrix} f \quad (4.74)$$

where the subscripts a and p denote the active and passive sections of the beam, and L and R are the left and right hand junctions. These equations show that the state vector on the passive side of a junction is equal to the state vector on the active side

of the junction plus the force applied at the end of the actuator. Equations (4.73) and (4.74) can be transformed into wave-mode coordinates using equation (4.72b) to give:

$$\underline{V}_p \underline{a}_{Lp} = \underline{V}_a \underline{a}_{La} + \begin{bmatrix} 0 \\ 1 \end{bmatrix} f \quad (4.75)$$

and

$$\underline{V}_p \underline{a}_{Rp} = \underline{V}_a \underline{a}_{Ra} + \begin{bmatrix} 0 \\ 1 \end{bmatrix} f \quad (4.76)$$

where \underline{V}_a includes the mass and stiffness of the beam and the PZT elements, and \underline{V}_p includes the mass and stiffness of the beam only. The relationship between the wave vectors \underline{a}_{Ba} and \underline{a}_{Aa} is given by:

$$\underline{a}_{Ra} = \underline{T}_a \underline{a}_{La} \quad (4.77)$$

where \underline{T}_a is the spatial longitudinal transformation matrix and is given by:

$$\underline{T}_a = \begin{bmatrix} e^{jk_a l} & 0 \\ 0 & e^{-jk_a l} \end{bmatrix} \quad (4.78)$$

Substituting equations (4.75) and (4.76) into equation (4.77) gives, after rearranging:

$$\underline{V}_p \underline{a}_{Rp} = \underline{V}_a \underline{T}_a \underline{V}_a^{-1} \underline{V}_p \underline{a}_{Lp} + \underline{Q} f \quad (4.79)$$

where

$$\underline{Q} = \underline{V}_a \underline{T}_a \underline{V}_a^{-1} \begin{bmatrix} 0 \\ -1 \end{bmatrix} + \begin{bmatrix} 0 \\ 1 \end{bmatrix} \quad (4.80)$$

Equation (4.79) can be rearranged into a partitioned matrix, as in the flexural case, to give the waves at junctions L and R in terms of the forces applied:

$$\left[\underline{V}_p \mid -\underline{V}_a \underline{T}_a \underline{V}_a^{-1} \underline{V}_p \right] \begin{bmatrix} \underline{a}_{Rp} \\ \underline{a}_{Lp} \end{bmatrix} = \underline{Q} f \quad (4.81)$$

As in the flexural case, this equation can be further rearranged to group the waves into incoming and outgoing waves. This actuator can therefore also be represented

by the simple block diagram shown in **figure 4.27**. The resulting expression is similar to equation (4.48) but with a force applied rather than a moment:

$$\underline{\alpha} \underline{a}_i + \underline{\beta} \underline{a}_o = Qf \quad (4.82)$$

where the wave vectors in this case are given by:

$$\underline{a}_i = \begin{bmatrix} A_{iR} \\ A_{iL} \end{bmatrix} \quad \text{and} \quad \underline{a}_o = \begin{bmatrix} A_{oL} \\ A_{oR} \end{bmatrix} \quad (4.83a \text{ \& } b)$$

and the matrices are given by:

$$\underline{\alpha} = \left[(V_p)_1 \mid (-V_a T_a V_a^{-1} V_p)_2 \right] \quad (4.84)$$

and

$$\underline{\beta} = \left[(-V_a T_a V_a^{-1} V_p)_1 \mid (-V_p)_2 \right] \quad (4.85)$$

where the subscripts 1 and 2 denote the columns of the respective matrices. Equation (4.82) gives a complete description of the active and passive effects of the actuator. As with the flexural actuator, the waves generated can be determined by setting the incoming wave vector \underline{a}_i to zero. The passive effects of the actuator can be determined by setting the force f to zero and the outgoing waves can then be determined in terms of the incoming waves.

4.5.3.4 Comparison Between the Simple and Complete Models of the PZT Longitudinal Vibration Actuator

To compare the two models of the Longitudinal PZT actuator described above, the waves generated are compared for a given applied force. As mentioned previously, the actuators induce strain in the beam. To model the coupling between the actuator and the beam, the force required to induce this strain is calculated and applied to the beam at the each end of the actuator. It is clear that if the mass and stiffness of the

actuator elements are included in the model, then a greater static force is required to induce the same strain as that on a model that does not include the PZT elements. The relationship between these forces is:

$$f_{complete} = A^* f_{simple} \quad (4.86)$$

where:

$$A^* = \frac{A_{complete}}{A_{simple}} = 1 + \frac{E_p}{E_b} 2T \quad (4.87)$$

and $T = t_p/t_b$, is the thickness ratio between one of the PZT elements and the beam. For simplicity, the actuator is assumed to be the same width as the beam. The amplitudes of the generated waves per unit input force are calculated by rearranging equation (4.82) which gives:

$$a_o = \beta^{-1} Q f_{complete} \quad (4.88)$$

The amplitudes of the generated waves are plotted for thickness ratios T , ranging from 0 to 0.5 as a function of the length of the actuator divided by a longitudinal wavelength in the 6.12 mm x 30 mm aluminium beam. These are shown in **figure 4.51**. The simple model described by equation (4.71) is equivalent to the complete model with a thickness ratio of zero. It should be noted that this analysis does not include the relationship between the voltage applied and the force generated as it is only intended to examine the dynamic effects of including the mass and stiffness of the actuator. Graphs are also plotted of the ratio of the complex wave amplitudes calculated using the simple model to the wave amplitudes calculated using the complete model for different thickness ratios. These are shown in **figures 4.52** (magnitude) and **4.53** (phase). Examining these figures, it can be seen that at low

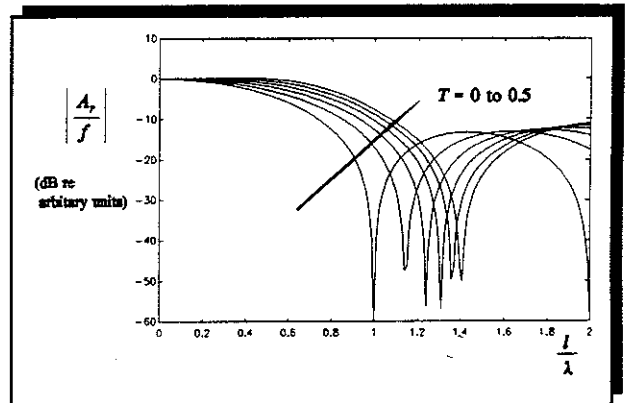


Figure 4.51 Longitudinal Wave Amplitudes per unit Input Force

frequencies there is very little difference between the amplitudes of the waves

frequencies there is very little difference between the amplitudes of the waves generated by the simple and complete models. The loading effects of the actuator only become important at higher frequencies when a longitudinal wavelength approaches the length of the actuator. In most practical situations, the frequencies of interest are such that the length of an actuator is less than one tenth of a longitudinal wavelength and therefore the *simple model is an adequate model of the longitudinal coupling between the actuator and the beam dynamics.*

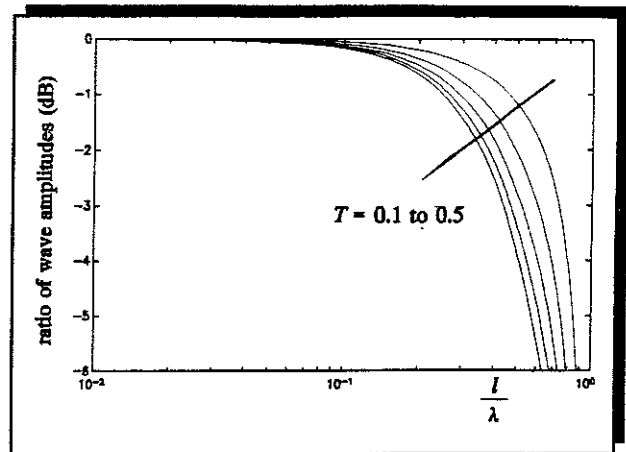


Figure 4.52 Ratio Longitudinal Wave Amplitude Calculated using the Simple and Complete Models

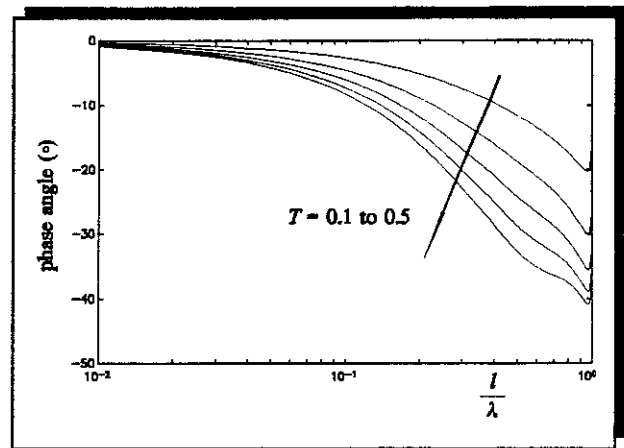


Figure 4.53 Phase Between Longitudinal Waves Calculated using the Simple and Complete Models

4.5.3.5 Passive Effects of the PZT Longitudinal Vibration Actuator

As with the flexural vibration actuator, the mass and stiffness of the longitudinal vibration actuator will have an effect on the beam dynamics. This is investigated by examining the amplitudes of the outgoing waves A_l and A_r from the actuator as a ratio of the incident wave A_i . It should be noted that because the configuration is symmetric there is no scattering from longitudinal to flexural wave motion. The

scattering of the longitudinal waves is investigated by considering a longitudinal wave incident on the actuator as shown in **figure 4.54**. The amplitudes of the A_i and A_r waves can be determined using equation (4.82), where f is set to zero, which can be rearranged to give:

$$a_o = -\beta^{-1} \alpha a_i \quad (4.89)$$

The normalised amplitudes of these waves are plotted in **figure 4.55**. which shows that there is a passive effect on the beam dynamics due to the actuator that depends on frequency and thickness ratio. However, as mentioned before, the actuator will generally be operating at frequencies where the length of the actuator is less than one tenth of a wavelength and thus in practice the actuator has only a minimal effect on the beam dynamics.

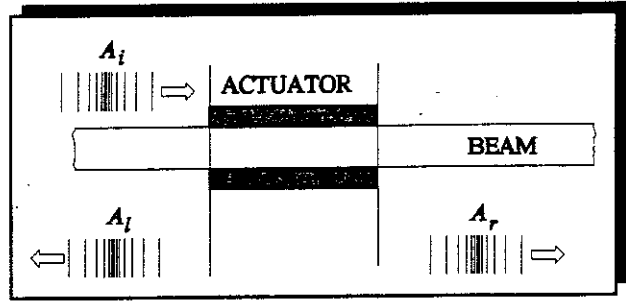


Figure 4.54 Wave Conversion by the PZT Actuator

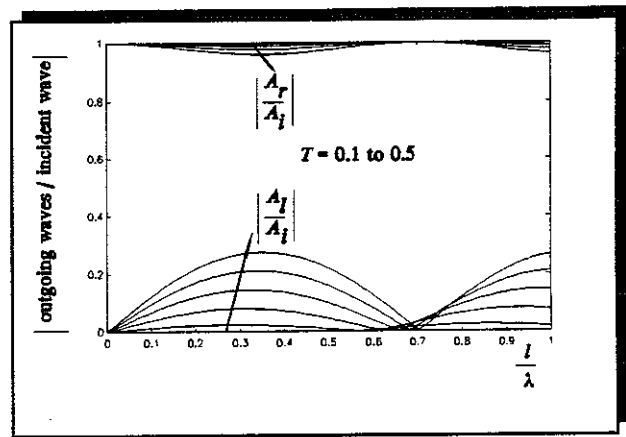


Figure 4.55 Normalised Amplitudes of the Outgoing Waves from the Inactive PZT Longitudinal Actuator

4.5.3.6 Vibrational Power Supplied by a PZT Longitudinal Vibration Actuator

As with the PZT flexural vibration actuator, the effectiveness of the PZT longitudinal actuator of length l , can be assessed by calculating the power it supplies to a beam. The simple model of a pair of forces applied at each end of the actuator is an appropriate model, and the power that this supplies is derived in Appendix 3, and is given by:

$$P = \frac{\omega |f|^2}{2k_l ES} (1 - \cos k_l l) \quad (4.90)$$

The power supplied to a beam as a function of the length of the PZT actuator divided by a longitudinal wavelength is plotted in Appendix 3. To place this into context for the aluminium beam discussed in this chapter, the power supplied by an actuator of length 100 mm

generating a force of 1 N is shown in **figure 4.56** together with the power supplied by a 1 N point force on an infinite beam. It is clear that in the frequency range of interest the power supplied by the actuator increases linearly with log frequency (c.f **figure A3.7**). On most real engineering structures this would also be the case, as the actuator will generally be small compared to a longitudinal wavelength. One longitudinal wavelength on an aluminium or steel beam equals the length of a 0.1 m PZT actuator at a frequency of 50 kHz.

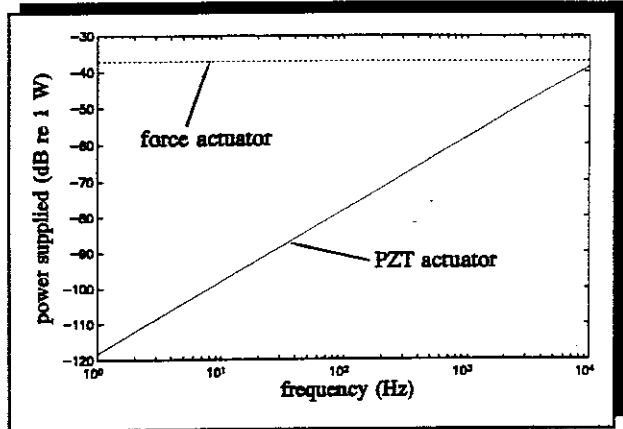


Figure 4.56 Power Supplied to an 6.12 mm Thick Infinite Beam by a Longitudinal PZT Actuator

4.5.3.7 Experimental Validation

The model of the actuator was validated by a simple experiment using the aluminium beam described previously. As the PZT elements were glued to the beam with conducting epoxy and configured as a parallel flexural vibration actuator, they could only be connected as a series longitudinal vibration actuator (see

figure 4.9). The beam was excited with the actuator over a frequency range 100 Hz

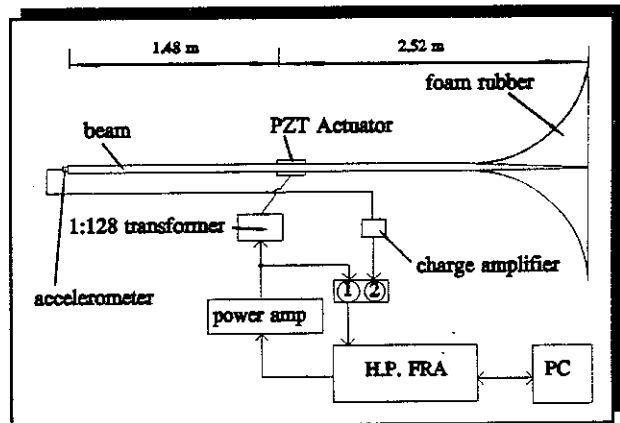


Figure 4.57 Experimental Set Up to Validate the Model of the Longitudinal PZT Actuator

to 1 kHz and the response measured using a B&K accelerometer type 4370 positioned at the end of the beam. **Figure 4.57** shows the experimental set up. The experimental results are plotted in **figure 4.58** with a theoretical plot of the acceleration at the end of the beam per unit input force calculated using the theory outlined in Appendix 2 in which the beam is assumed to be free-free. The loss factor in the beam was taken to be 1%.

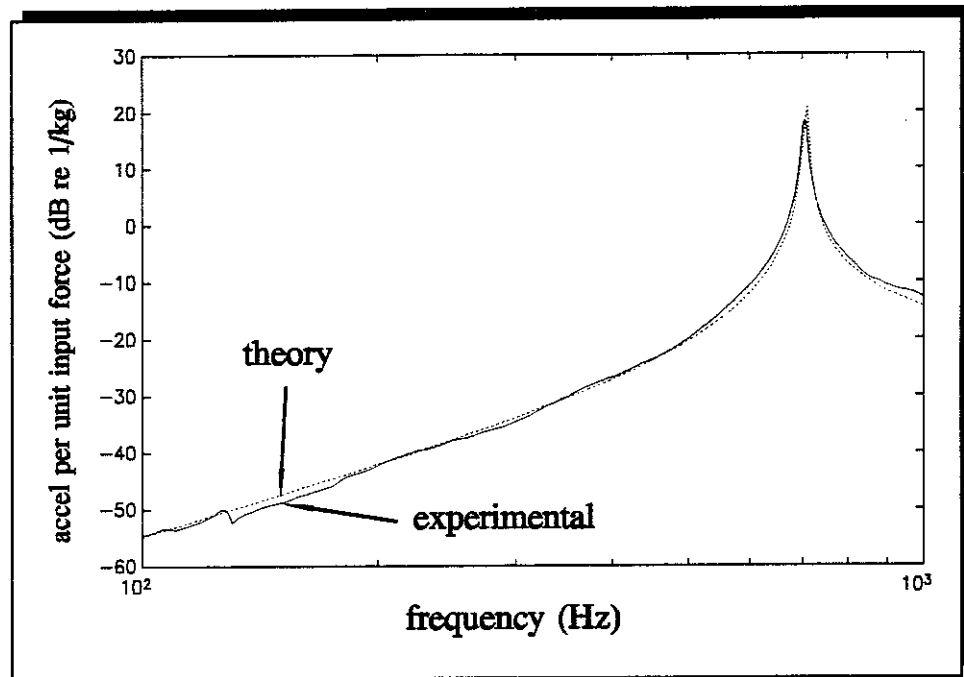


Figure 4.58 Response of the Experimental Beam to Excitation by a PZT Longitudinal Vibration Actuator - Theoretical and Experimental Results

The measured frequency response function (volts/volts) had to be converted to acceleration per unit input force using the following multiplication:

$$\frac{\text{accel}}{f} = \frac{10 * 3.68 * 2}{128} * \frac{V_a}{V_f}$$

The number 10 is to compensate for the attenuation of acceleration by a factor of 10 on the charge amplifier; 3.68 is the sensitivity of the actuator; 2 is the factor required because the actuator is connected in series and the applied voltage is split between the two elements and 128 is the transformer turns ratio. V represents voltage and the

subscripts a and f represent acceleration and force respectively.

It is clear from equation (4.90) that these actuators increase in effectiveness with frequency, but at frequencies when the length of the actuator is an integer number of wavelengths no waves are generated. However, as discussed above, this occurs at about 50 kHz, so it is clearly not a concern in this case. Examining figure 4.58, it can be seen that the foam rubber fitted to one end of the beam is not effective in attenuating reflections from that end. The beam is clearly resonant and has an effective length of 3.56 m. The physical length of the beam was 4 m and the reduction in apparent length may be attributed to the taper and the foam rubber. Notwithstanding this, the agreement between the theoretical model and the experimental results is considered to be good.

4.5.4 Conclusions

In this section, static models of PZT flexural and longitudinal vibration actuators have been discussed, and simple models that couple the actuators into the beam dynamics have been proposed. These simple models do not account for the mass and stiffness of the PZT elements, and so more complicated models which account for the additional mass and stiffness of the actuators were developed. The validity of the simple models were assessed for different actuator sizes and for different frequencies and simple experiments were carried out to validate the models. Expressions quantifying the power supplied by both types of actuators have been derived and the flexural PZT vibration actuator has been compared with other types of generic actuators. The use of actuators to generate unidirectional waves has been discussed. An investigation was carried out to see if changing the shape of a flexural vibration actuator results in the generation of a unidirectional wave. However, it was shown that changing the shape only affected the phase relationship between the generated waves, and that at least two independently driven actuators are required to generate a unidirectional wave. It was also shown that the length of the actuator and the spacing of the actuators affected the effort required to generate such a wave. The

simple models presented in this section are considered to be reasonable representations of how PZT actuators couple into and generate flexural and longitudinal waves on a beam at low frequencies, and for actuators that are relatively thin compared to the beam

4.6 A Self Sensing Actuator

4.6.1 Introduction

The previous sections in this chapter have described the reciprocal property of a piezoceramic material and demonstrated its use both as a vibration sensor and an actuator. The purpose of this section is to investigate a technique whereby the actuator and sensor are combined into a single element which can act as a sensor and an actuator. This type of transducer has been investigated before [71], where it was used in the modal control of a cantilever beam. The analysis conducted here shows that there are inherent difficulties in using such a device if it is to be operated over a wide frequency range, and that its operation is dependent upon tolerances of the electronic components in the "self sensing" circuit.

4.6.2 Electrically Equivalent Model of the Self Sensing Actuator

In section 4.3 it was shown that a piezoelectric sensor could be modelled either as a charge generator in parallel with a capacitor, or a voltage generator in series with a capacitor. When a piezoceramic element is used as a sensor and an actuator there is an additional charge in parallel or voltage in series which represents the voltage applied across the actuator. The equivalent electrical models of the actuator and sensor are shown in **figure 4.59**. The voltage measured across the transducer is given by [71]:

$$V = \frac{q_c}{C} - \frac{q_p}{C} \quad (4.91)$$

or

$$V = V_c - V_p \quad (4.92)$$

where q_c is the applied charge, q_p is the charge generated by the strain of the PZT element, V_c is the applied voltage and V_p is the voltage generated by the PZT element as it strains. $C = \xi S/t_p$, where ξ is the permittivity of the PZT material, S is the area of the PZT element and t_p is the thickness of the element (a capacitor). The self sensing device uses an electrical bridge circuit to measure the charge generated by the PZT actuator due to strain. Such a

bridge circuit is shown in **figure 4.60**. In this circuit, z_p is the electrical impedance of the PZT actuator/sensor, which is characterised as a capacitor as discussed above, and z_2 and z_3 are electrical impedances. The voltage V_1 is related to the applied voltage V_c and the generated voltage V_p by:

$$V_1 = \frac{z_2}{z_p + z_2} (V_p + V_c) \quad (4.93)$$

and the voltage V_2 is related only to the applied voltage V_c by:

$$V_2 = \frac{z_2}{z_2 + z_3} V_c \quad (4.94)$$

If the difference between these voltage is taken we get:

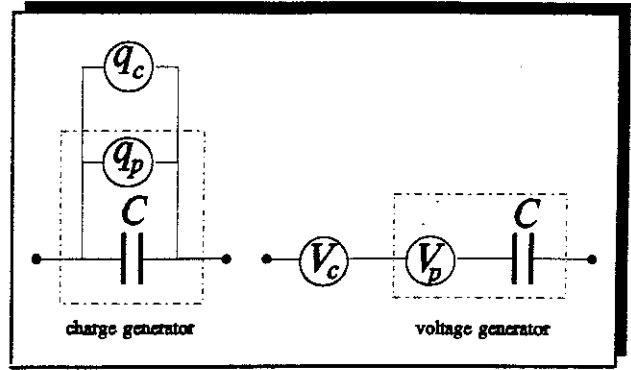


Figure 4.59 Electrical Equivalent Models of a Piezoelectric Actuator and Sensor

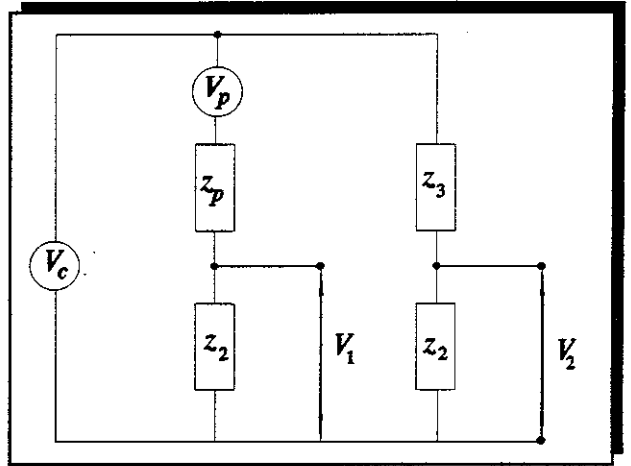


Figure 4.60 Electrical Bridge Circuit of the Self Sensing Actuator

$$V_1 - V_2 = \frac{z_2(z_3 - z_p)}{(z_2 + z_p)(z_2 + z_3)} V_c + \frac{z_2}{(z_2 + z_3)} V_p \quad (4.95)$$

It can be seen that if $z_3 = z_p$, that is, an electrical impedance placed in the bridge with the same impedance as the actuator, the output $V_1 - V_2$ is unrelated to the applied voltage V_c and is given by:

$$V_1 - V_2 = \frac{z_2}{(z_2 + z_3)} V_p \quad (4.96)$$

The output from the device V_p , is proportional to the generated voltage due to strain. It is important to note, however, that should z_3 not equal z_p then the output from the device will be "contaminated" with a proportion of the applied voltage V_c . The capacitance of a PZT element was measured in isolation using a capacitance meter. It was then glued to the 6.12 mm x 30 mm aluminium beam and re-measured using the same meter and the results were:

PZT element in isolation 0.037 μF

PZT element fitted to the beam 0.029 μF

The calculated value of a single element in isolation, using data from the manufactures data sheet, was 0.035 μF . The reduction in measured capacitance, when the element was fitted to the beam, can be attributed to the mechanical impedance of the beam reflecting into the electrical circuit. Another PZT element was fitted to the beam and the two elements connected in parallel to form a flexural vibration actuator as discussed in section 4.5. The capacitance of the actuator was measured using the capacitance meter and found to be 0.058 μF , exactly twice the value of the single element.

A simple experiment was conducted to measure the impedance of the flexural vibration actuator over the frequency range 100 Hz to 1 kHz. This involved the measurement of the voltage applied to the actuator and the current flowing through the device. The current was measured by monitoring the voltage across a 10 Ω resistor in series with the actuator. The experimental set up is shown in **figure 4.61**. A 10 Ω resistor was used so that a reasonably large signal could be measured across

the resistor, as a 10 V limit was imposed on the applied voltage to the PZT actuator due to the upper voltage limit of the frequency response analyzer. The actuator was not driven through a transformer in this experiment so that the characteristic of the actuator alone could be measured. By dividing the voltage applied to the actuator by the current flowing in the circuit, the electrical impedance of the actuator can be approximated, provided the impedance of the actuator is much greater than the series resistance. The experimental results are plotted with predicted results in figures 4.62 and 4.63. The combined electrical impedance of the actuator and the series resistor was determined by dividing the voltage applied across the two elements by the current induced. This current was calculated from the resistor value ($10\ \Omega$) and the measured voltage drop across it. A capacitance of $0.058\ \mu\text{F}$ was used to calculate the theoretical impedance.

The results show that the measured

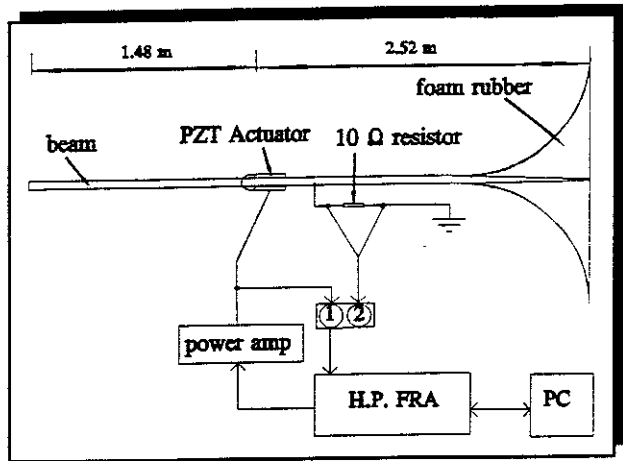


Figure 4.61 Experimental Set Up to Measure the Electrical Impedance of the PZT Actuator

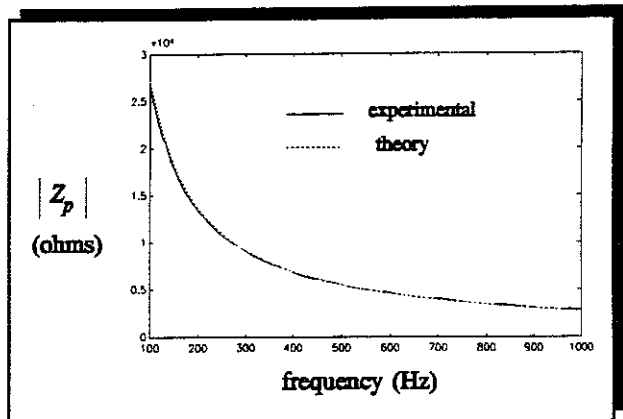


Figure 4.62 Experimental Results Showing the Magnitude of the Actuator Impedance

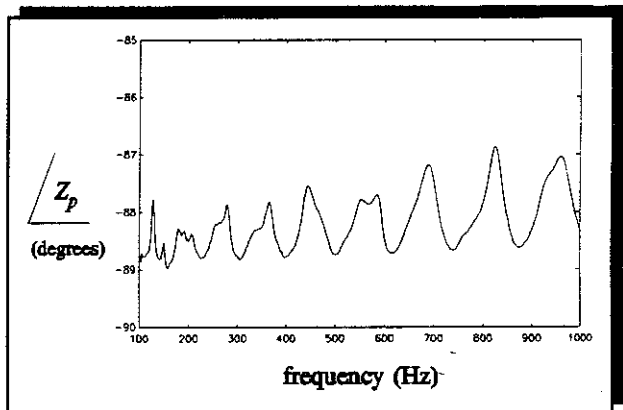


Figure 4.63 Experimental Results Showing the Phase of the Actuator Impedance

magnitude of the impedance agrees very well with calculated impedance. The phase, however does differ from the theoretical value of -90° and varies with frequency. This could possibly be due to the mechanical loading of the PZT elements by the beam.

4.6.3 Sensitivity of the Self Sensing Actuator

Equation (4.95) shows that the self sensing circuit *relies on the electrical impedance z_3 being exactly the same as the impedance of the actuator*, and if the circuit is to be operated over a broadband of frequencies this must be true over the entire frequency range of interest. It was shown in figures 4.62 and 4.63, that although the magnitude of electrical impedance of the actuator is capacitor-like, the phase varies with frequency. This will have an effect on the measured motion of the structure by a self sensing actuator. Additionally, in practice there will always be a small difference between z_3 and the electrical impedance of the actuator due to tolerances in electrical components and this will also affect the output. It is clear, therefore, that there will be "crosstalk" between the applied voltage and the measured voltage in a self sensing actuator and the question is how sensitive is the device to this? A simple analysis was carried out to see what effect a small difference between z_3 and z_p has on the output from a self sensing PZT actuator. Letting

$$\Gamma = \frac{z_2}{z_2 + z_p} \quad (4.97)$$

equation (4.95) becomes:

$$v_1 - v_2 = \Gamma \left\{ \frac{(z_3 - z_p)}{(z_2 + z_3)} v_c + v_p \right\} \quad (4.98)$$

Noting that $V_p = \alpha V_c$, where α is proportional to the mechanical receptance of the beam, equation (4.98) can be rearranged to give:

$$\frac{V_1 - V_2}{V_c} = \Gamma \left\{ \frac{(\Omega - 1)}{\left(\frac{z_2}{z_p} + \Omega \right)} + \alpha \right\} \quad (4.99)$$

where $\Omega = z_3/z_p$. This equation can be plotted for different values of α for varying Ω . Setting the following constants; $z_2 = 1/2\pi f C_3$ where $C_3 = 0.5 \mu F$; $z_p = 1/2\pi f C_p$, where $C_p = 0.058 \mu F$; α has values 0, $0.01(1+j)$ and $0.1(1+j)$, equation (4.99) is plotted for $0 \leq \Omega \leq 2$ in figures 4.64 (magnitude) and 4.65 (phase). It can be seen that when the receptance of the beam is very small, the self-sensing actuator is very sensitive to differences between z_3 and z_p . Even a small difference causes a large change in both the magnitude and phase of the output with respect to the input. Over any frequency range, the mechanical receptance of the structure α , will generally change so any difference between z_3 and z_p , even if constant with frequency, will have a variable effect on the output over a range of frequencies.

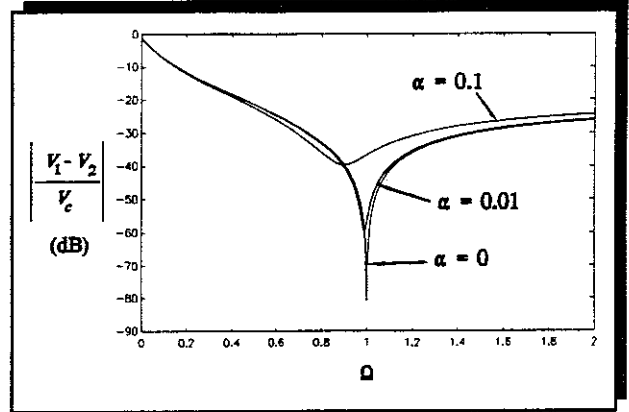


Figure 4.64 Magnitude of Input/Output Characteristic of a Self Sensing Actuator as a function of z_3/z_p

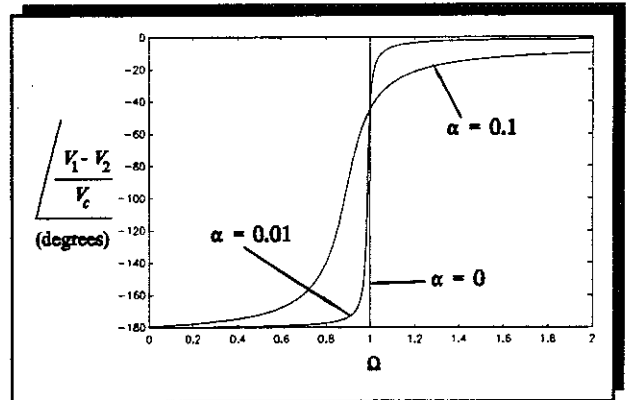


Figure 4.65 Phase of Input/Output Characteristic of a Self Sensing Actuator as a function of z_3/z_p .

In Chapter 3, active control strategies that use power as a controlling parameter were discussed, and this requires the measurement of the power supplied by the secondary control sources. Initially, it was thought that the self sensing actuator would be an ideal secondary source for use with these control strategies, as the power supplied

(absorbed) could be measured with the actuator, dispensing with the requirement for force and motion transducers. However, it is now clear that such a device is unsuitable for measuring power supplied to a structure by the PZT actuator, as the accuracy of magnitude and phase of the structure's response measured by the device cannot be guaranteed.

4.6.4 Experimental Investigation

A self sensing circuit was constructed, and a diagram of this is shown in figure 4.66.

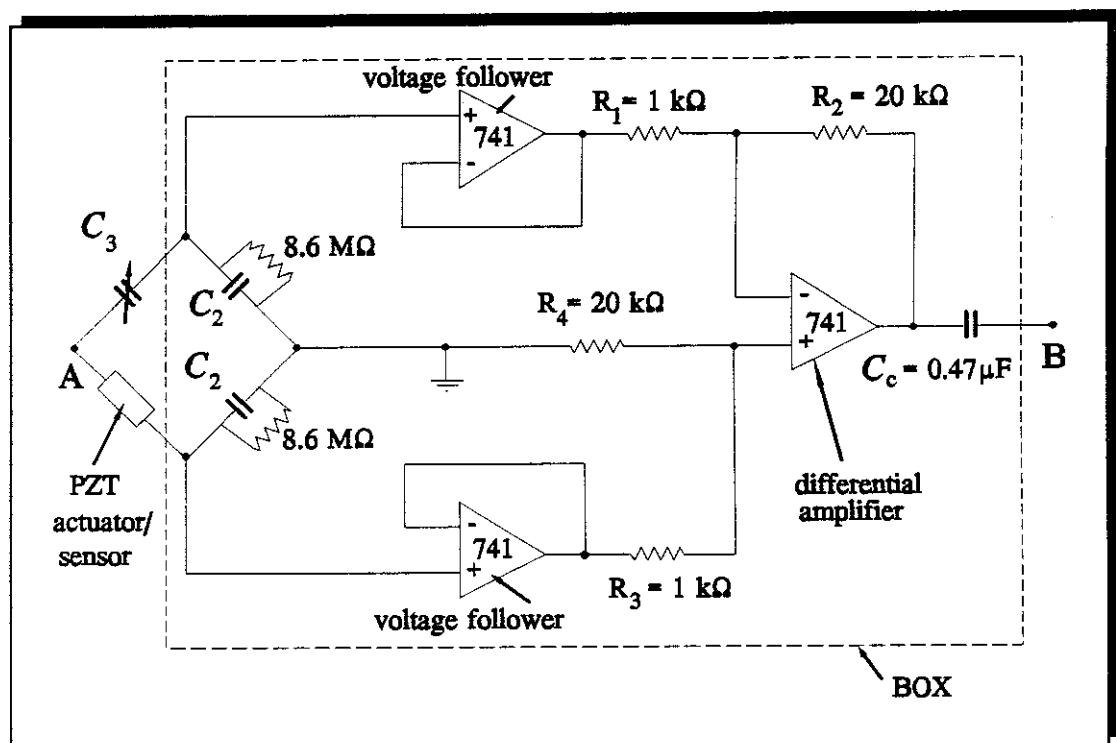


Figure 4.66 Diagram of the Self Sensing Circuit

The actuator excitation voltage is applied between *A* and earth and the response of the structure is measured between *B* and earth. The capacitors C_2 have values of $0.5 \mu\text{F}$ which attenuates the measured voltages at the voltage followers by a factor of about ten. This voltage is amplified by the differential amplifier which has a gain set at about ten, so the nominal gain of the device is about one. The voltage followers (741 Op amps) were placed in the circuit to present a high electrical impedance to the capacitance bridge to ensure there is very little current flow in the circuit and hence

the voltage measured is effectively the open circuit voltage. The gain of the differential amplifier is given by the expression:

$$G = \frac{R_2}{R_1 + (R_1 || R_2)} = \frac{R_4}{R_3 + (R_3 || R_4)} \approx 10 \quad (4.100)$$

where $||$ denotes in parallel with. The $8.6 \text{ M}\Omega$ resistors across the capacitors are to avoid DC drift and the capacitance C_3 is a variable capacitor. The function of capacitor C_c is to act as a decoupling capacitor so that the DC voltage does not appear at the output.

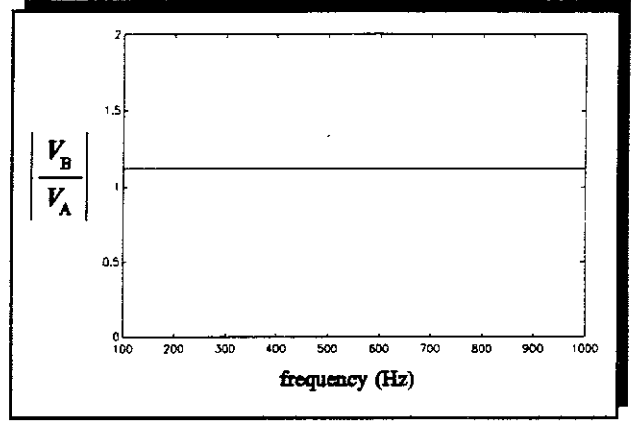


Figure 4.67 Frequency Response (Magnitude) of the Self Sensing Circuit

Before attaching the circuit to the actuator it was tested in isolation. A $0.058 \text{ }\mu\text{F}$ capacitor was connected in place of the PZT and the frequency response function V_B/V_A was measured over the frequency range 100 Hz to 1 kHz. This characteristic (magnitude and phase) is shown in **figures 4.67** and **4.68**. The gain of the device is about 1.12 and is fairly constant over the frequency range with the phase accuracy within $\pm 1^\circ$.

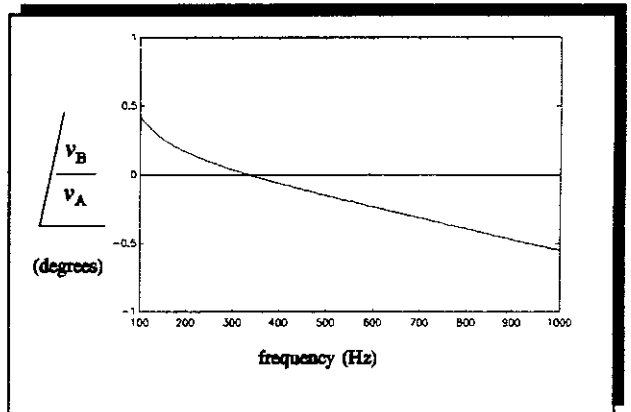


Figure 4.68 Frequency Response (Phase) of the Self Sensing Circuit

The self sensing circuit was then connected to the PZT actuator/sensor fitted to the aluminium beam as shown in **figure 4.69**. The beam was excited over the frequency range 100 Hz to 1 kHz and the response measured with the self sensing device. The moment applied to the beam was measured by monitoring the voltage applied to the

transformer that was used to drive the actuator. The measured frequency response function (response/moment applied in volts) had to be converted to response/moment applied in rad Nm^{-1} using the following multiplication:

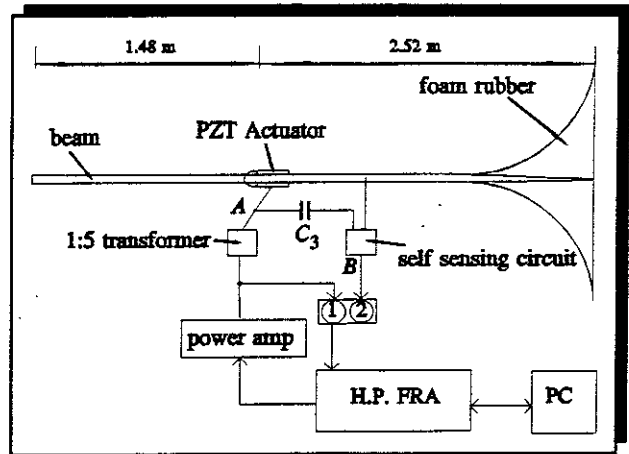


Figure 4.69 Experimental Set Up to Test the Self Sensing Circuit

$$\frac{w'(l) - w'(0)}{M} = \frac{1221}{2.61 * 10^4 * 5 * 1.12} * \frac{V_{resp}}{V_m}$$

where V_{resp} is the voltage measured by the self sensing circuit and V_m is the voltage applied to the transformer driving the actuator. $2.61 * 10^4$ is the sensitivity of the sensor obtained from equation (4.16), 5 is the gain of the transformer, 1.12 is the gain of the self sensing circuit and 1221 is the reciprocal of the gain of the actuator (equation (4.32)). The experimental results are plotted together with the theoretical predictions in figures 4.70 and 4.71.

These experimental results appear to be reasonable and suggest that the impedance z_3 is very similar to

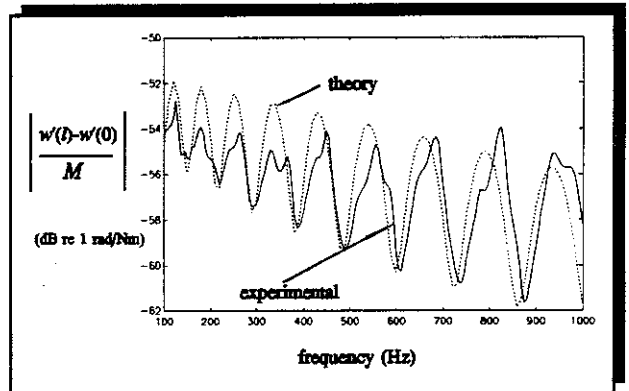


Figure 4.70 Response (Magnitude) of Beam per unit Moment Applied by the PZT Actuator and Measured with the Self Sensing Circuit

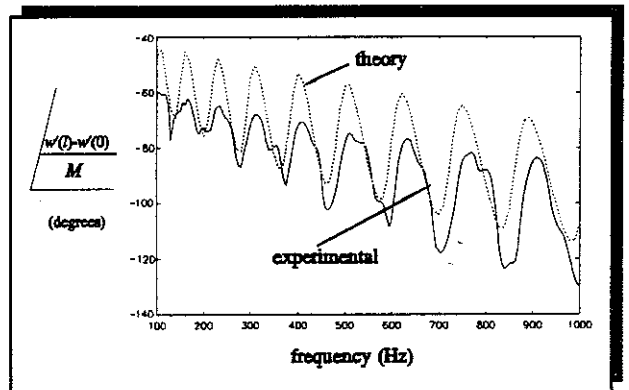


Figure 4.71 Response (Phase) of Beam per unit Moment Applied by the PZT Actuator and Measured with the Self Sensing Circuit

the impedance of the actuator/sensor. However, although the experimental results follow the general trend predicted, there is a phase difference between the predicted results and the actual results, which varies over the frequency range. The capacitor C_3 could only be adjusted to an accuracy of $0.001 \mu\text{F}$ and it is not known whether this accuracy was sufficient.

It was decided to conduct a further experiment to see how the results would vary if the capacitance is changed so that it does not equal that of the PZT. The analysis conducted previously suggested that it would have a profound effect. The capacitance C_3 was changed in $0.02 \mu\text{F}$ steps from $0.054 \mu\text{F}$ to $0.062 \mu\text{F}$ and a frequency sweep was carried out for each value from 100 Hz to 1 kHz. The results are plotted in figures 4.72 and 4.73. It can be seen that the effect of changing the capacitance C_3 by $0.002 \mu\text{F}$ (3% of the PZT capacitance) has a marked effect on both the magnitude and phase of the measured beam receptance as predicted. The magnitude changes by about 10 dB, but the phase changes by tens of degrees.

Clearly this is not acceptable for a broadband vibration sensor, as the accuracy of the output cannot be guaranteed.

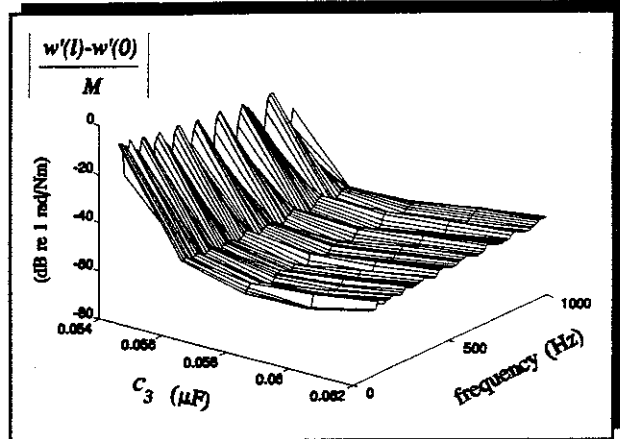


Figure 4.72 Receptance (Magnitude) of the beam Measured with the Self Sensing Actuator, Showing the Effect of Changing C_3

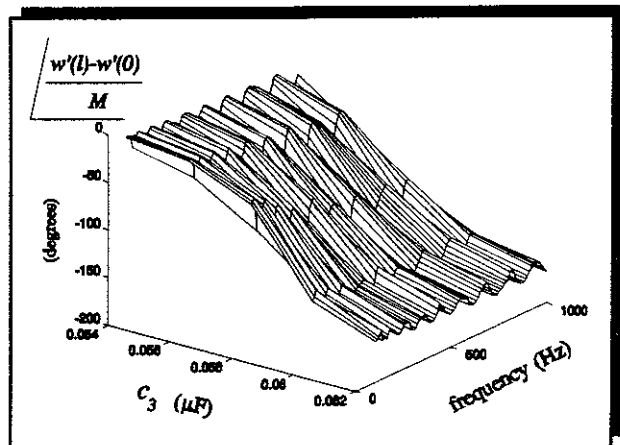


Figure 4.73 Receptance (Phase) of the beam Measured with the Self Sensing Actuator, Showing the Effect of Changing C_3

4.6.5 Conclusions

This section has discussed the theory behind a self sensing PZT actuator and has shown why it is unsuitable as a practical secondary source in an active vibration control system employing power control strategies over a broadband of frequencies. A self sensing circuit has been built and tested using a flexural PZT vibration actuator fitted to a slender aluminium beam, and the sensitivity of the device to tolerances in electrical components has been demonstrated.

4.7 Discussion and Conclusions

This chapter has discussed the use of PZT elements as vibration sensors and actuators on a beam. After reviewing the research into piezoelectric actuators in section 4.2, section 4.3 discussed the electromechanical properties of piezoelectric devices and the results of simple experiments on a PZT element have been presented.

Section 4.4 described the use of PZT elements as sensors to measure longitudinal and lateral motion. An electro-mechanical model which coupled the sensor to the motion of the beam was derived for both types of motion and validated with simple experiments. It was shown that the sensitivity of the sensor depended on how the PZT elements were connected electrically, and that if the elements are connected independently then both types of wave motion can be sensed simultaneously. A substantial local stiffening effect of the PZT sensor was observed and quantified which allowed accurate measurements of the beam over a frequency range 100 Hz to 1 kHz. The sensitivity of the PZT sensor was shown to be about 400 times that of a foil strain gauge and ten times that of a PVDF sensor. The PVDF sensor has the advantage over an ordinary foil strain gauge of (a) being much more sensitive and (b) not requiring a power supply. Although it is not as sensitive as PZT, PVDF does not cause an appreciable local stiffness and it is much cheaper; it was thus used to measure radial motion of a pipe wall discussed in Chapter 6 of this thesis. At the present time, these sensors are probably the cheapest and the best to use as error

sensors in the active control of vibrations of slender structures, such as plates and beams.

Section 4.5 contained a discussion on the use of PZT elements as longitudinal and flexural vibration actuators on a beam. These elements are particularly attractive for use as secondary sources in active vibration control systems, as they react off the structure that they are controlling, and do not require an additional inertial mass. Different actuator models proposed by other researchers were compared and contrasted, and simple electromechanical models which couple the actuators to the motion of the beam were described. These actuators were also investigated experimentally, and the validity of the simple models were examined using complete models that account for the mass and stiffness of the PZT elements. PZT flexural actuators were compared with other actuators (force and moment) and it was shown that it is better to operate the PZT actuators at high frequencies, close to those where the length of the actuator equals half a wavelength. This is true for both the longitudinal and flexural actuators, but for a given length of actuator, the ideal operating frequency for a longitudinal actuator is much higher than for a flexural actuator. The spacing of two flexural vibration actuators (four elements) as a unidirectional wave generator was discussed but not verified experimentally. This section adequately demonstrated the use of PZT actuators as secondary sources in active vibration control and highlighted their strengths and weaknesses.

An arrangement whereby a set of PZT elements can be used as both a vibration actuator and a sensor was the subject of discussion in section 4.6. This "self sensing actuator" had been used previously for single frequency modal control and the purpose of the investigation in this thesis was to see whether the device could be used over a wide frequency range. A theoretical analysis and some simple experimental work showed that the self sensing actuator is a finely balanced ill-conditioned device, that requires electrical components with tolerances that cannot be achieved in practice. The ability to measure the response of a structure at the point of application of a secondary source is useful in the active control of vibrations, and it appears that this device is not suitable for this purpose over a range of frequencies.

Overall, this Chapter has demonstrated that piezoelectric devices have properties which make them particularly attractive as secondary sources and error sensors in active vibration control systems, especially at high frequencies.

CHAPTER 5

5 FEEDBACK CONTROL OF FLEXURAL AND LONGITUDINAL WAVES ON A BEAM

5.1 Introduction

In this chapter, feedback control of flexural and longitudinal waves on a beam is discussed. This is the second of the two control strategies used in the active control of sound and vibration, the other being feedforward control. Both of these strategies can be used for either single frequency or broadband control, but there are some fundamental limitations in the application of broadband control that are not applicable to single frequency control. Feedforward control has been used extensively in the active control of sound [12], where it has been employed in systems to control discrete frequencies (tones) in aircraft cabins, and controlling tones and broadband noise in cars and ducts. The principle of controlling waves on a beam is similar to that of controlling sound waves propagating in a duct.

In a feedforward control system, a reference signal is required at the frequency of the sound or vibration to be controlled. If the sound or vibration is tonal and is generated by a machine, then this signal can be obtained using a tachometer fitted to the offending machine. This technique has been found to be appropriate for fans fitted in ducts [12], or the reduction of structure-borne noise through gearbox supporting struts fitted to helicopters [89]. If the sound or vibration to be controlled is broadband, this reference signal has to be measured using a suitable transducer. This signal is then fed forward to the secondary source as in the single frequency case, but there is the constraint of causality imposed. In the case of a beam or a duct, the sensor has to be fitted upstream of the secondary source, i.e., between the primary and secondary sources. The time taken to process the reference signal and to generate an appropriate response by the secondary source must be less than the

propagation delay between the sensor and the secondary source. This was demonstrated by Elliott and Billet [29], who showed that the high frequency limit of this control strategy, when used to control flexural waves on a beam, was determined by the processing delay in the controller. With flexural waves, the propagation delay becomes smaller as frequency increases as the phase speed of flexural waves is proportional to the square root of frequency. They also showed there was a low frequency limit that was caused by the presence of nearfield waves at the error sensor position, and this was discussed in Chapter 2. In a practical system, there may be more than one primary source, and it can be difficult to obtain the required reference signals.

If longitudinal waves instead of flexural waves are to be controlled, there is no high frequency limit for control, as the phase speed of longitudinal waves is constant with frequency. There is, however, a minimum distance between the sensor and the secondary source, which is again governed by the processing delay. This distance is generally quite large due to the relatively high phase speed of longitudinal waves. There thus appears to be some merit in investigating whether feedback control could be used as an alternative to feedforward control as this might overcome this difficulty, as a reference signal is not required.

The active control of sound using feedback has been implemented in ducts [12] and more recently in commercially available active head sets [90]. In the active control of vibration, it has been generally used in modal control systems to control low frequency structural modes, for example [77][91] or used for rate feedback with collocated actuators and sensors on larger structures to give local damping [17]. There has, however, been little work carried out in the control of structural waves using feedback. It is this area that is addressed in this chapter, which itself follows on from some previous work reported in [92].

In this chapter, feedback control of both flexural and longitudinal waves on a beam is discussed, and a theoretical analysis and experimental investigation is carried out for the two wave types. A sensor and actuator pair which results in an optimal

feedback gain that is constant, real and independent of frequency and thus causal, is sought for each wave type. The analytical models suggest suitable combinations of transducers and experiments are carried out to validate the theoretical predictions. Significant practical problems associated with the transducers were found in practice, and these are discussed.

5.2 Feedback Control of Flexural Waves

The aim of this section is to investigate the feedback gains required to suppress an incident propagating flexural wave for various types of secondary sources and using various types of sensors. In the first instance, the actuators and sensors considered are all idealised. The actuators can apply a point force, a moment or a moment-pair as discussed in Appendix 2, and the sensors can detect displacement, rotation or curvature of the beam. This enables a simple theoretical analysis to be conducted which demonstrates what potentially can and cannot be achieved with feedback control. Practical actuators and sensors are then discussed and the limitations of the simple models highlighted. Finally, a simple feedback system was constructed using the beam and PZT actuators discussed in Chapter 4, and experiments were then conducted to validate the theory covered in this section.

5.2.1 Force Actuator as a Secondary Source

Consider the system shown in figure 5.1. The secondary source in this case is a force actuator and the sensor can measure either displacement, rotation or curvature. The aim of the feedback system is to suppress the incident propagating wave A_i , and the aim of the analysis in this section is to

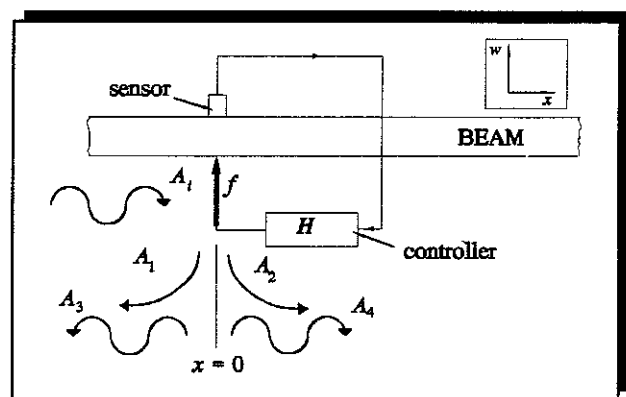


Figure 5.1 Feedback Control using a Force Actuator

discover the gain of the controller H , required to achieve this aim, for each of the sensor types.

Referring to **Figure 5.1**, we initially assume that displacement is measured and fed back to a force through a controller with a frequency response function H . The displacement to the right of the actuator is made up the incident propagating wave A_i , and the A_2 and A_4 waves generated by the actuator. This can be written as:

$$w(x) = A_i e^{-jk_b x} - \frac{f}{4EI k_b^3} (e^{-k_b x} + j e^{-jk_b x}) \quad (5.1)$$

where E is the Young's modulus of the beam, I is the second moment of area about the neutral axis and k_b is the flexural wavenumber given in Appendix 1. The $e^{j\omega t}$ time dependence has been suppressed for clarity. In the far-field, downstream of the actuator, the nearfield wave A_2 has a very small amplitude and the displacement is predominantly the sum of the incident propagating wave and the propagating wave generated by the secondary force, that is:

$$\text{for } x > 0, \quad w(x) = A_i e^{-jk_b x} - \frac{j f e^{-jk_b x}}{4EI k_b^3} \quad (5.2)$$

If this is set to zero, then at the sensor position the only contribution to the displacement is from a residual nearfield wave, so that for control:

$$w(0) = -\frac{f}{4EI k_b^3} \quad (5.3)$$

Therefore the required gain of the controller to suppress the incident propagating wave must be:

$$H = \frac{f}{w(0)} = -4EI k_b^3 \quad (5.4)$$

The optimal feedback controller provides a force proportional to the transverse displacement of the beam and thus acts in the same way as a conventional passive spring. The use of such a passive spring for wave control has been discussed by Mead [15], where it was shown that a spring could be used to suppress a propagating

flexural wave at a single frequency. Although a feedback controller could be designed to work in this configuration at a single frequency, *it cannot be physically realised over a range of frequencies*, as the optimal controller would be non-causal. This is because equation (5.4) represents a frequency response with no phase shift, so the impulse response must be symmetrical about the origin of time. However, the impulse response cannot be a delta function as the modulus of the frequency response is not flat and so the impulse response must have non-causal components [92].

Alternatively, the slope of the beam $\partial w(0)/\partial x = w'(0)$, can be measured and fed back to a force f . The required frequency response function of the controller H , to bring the beam to rest in the far-field downstream of the secondary force can be calculated using a similar method to that outlined above, and is given by:

$$H = \frac{f}{w'(0)} = 4EI k_b^2 \quad (5.5)$$

As the controller gain is dependent on frequency ($k_b^2 \propto \omega$) the optimal controller is again non-causal and cannot be physically realised over a range of frequencies.

Finally, if the curvature of the beam $\partial^2 w(0)/\partial x^2 = w''(0)$, is measured and fed back to a force f , then the required frequency response function of the controller H , to bring the beam to rest in the far-field downstream of the secondary force is given by:

$$H = \frac{f}{w''(0)} = -4EI k_b \quad (5.6)$$

Again this is dependent on frequency, and the optimal controller is non-causal and cannot be physically realised over a range of frequencies.

5.2.2 Moment Actuator as a Secondary Source

Consider the system shown in figure 5.2. The secondary source in this case is a moment actuator and the sensor is again assumed to be one that can measure either displacement, rotation or curvature. The aim of the feedback system is again to

suppress the incident propagating wave A_i , and the aim of the analysis in this section is again to discover the required gain of the controller H , for each of the sensor types.

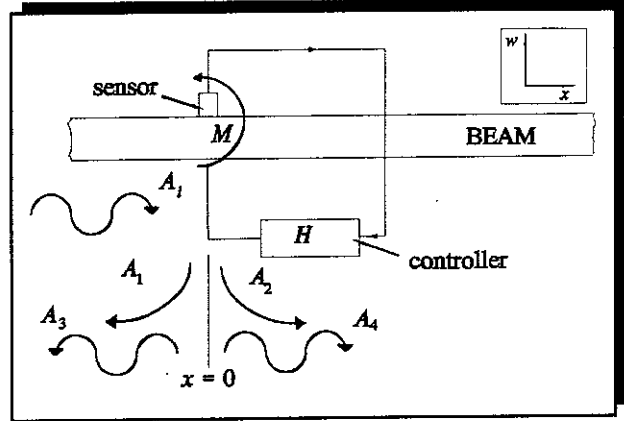


Figure 5.2 Feedback Control using a Moment Actuator

Referring to **figure 5.2**, if displacement is measured and fed back to a moment actuator through

a controller with a frequency response function H , the displacement to the right of the actuator is made up the incident propagating wave A_i , and the A_2 and A_4 waves generated by the actuator. This can be written as:

$$w(x) = A_i e^{-jk_b x} + \frac{M}{4EI k_b^2} (e^{-k_b x} - e^{-jk_b x}) \quad (5.7)$$

In the far-field, downstream of the actuator, the nearfield wave has a very small amplitude and the displacement is predominantly the sum of the incident propagating wave and the propagating wave generated by the secondary force, that is:

$$\text{for } x > 0, \quad w(x) = A_i e^{-jk_b x} - \frac{M e^{-jk_b x}}{4EI k_b^2} \quad (5.8)$$

If this is set to zero, then there is only a residual nearfield wave at the actuator position, thus:

$$w(0) = \frac{M}{4EI k_b^2} \quad (5.9)$$

Therefore the required gain of the controller is:

$$H = \frac{M}{w(0)} = 4EI k_b^2 \quad (5.10)$$

Again this is dependent on frequency and the optimal controller is non-causal and cannot be physically realised over a range of frequencies.

If the slope of the beam $w'(0)$, is measured and fed back to a moment M , then the required frequency response function of the controller H , to bring the beam to rest in the far-field downstream of the secondary force is given by:

$$H = \frac{M}{w'(0)} = -4EI k_b \quad (5.11)$$

Again this is dependent on frequency and the optimal controller is non-causal and cannot be physically realised over a range of frequencies.

If the curvature of the beam $w''(0)$, is measured and fed back to a moment M , then the required frequency response function of the controller H , to bring the beam to rest in the far-field downstream of the secondary force is given by:

$$H = \frac{M}{w''(0)} = 4EI \quad (5.12)$$

This is *not dependent on frequency and thus the frequency response of the controller is causal and an optimal controller can be physically realised over a range of frequencies.*

5.2.3 Moment-Pair Actuator as a Secondary Source

Consider the system shown in **figure 5.3**. The secondary source in this case is a moment-pair actuator and the sensor is one that can measure either displacement, rotation or curvature. The aim of the feedback system is again to suppress the incident propagating wave A_i and the aim of the analysis in this section is again to discover

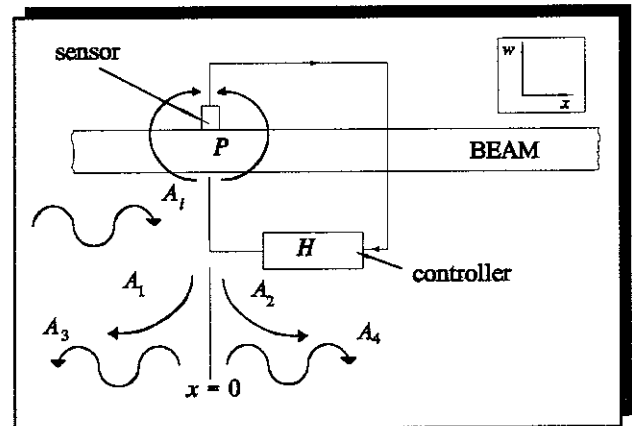


Figure 5.3 Feedback Control using a Moment-Pair Actuator

the required gain of the controller H , for each of the sensor types.

Referring to **figure 5.3**, if displacement is measured and fed back to a moment-pair actuator through a controller with a frequency response function, H , the displacement to the right of the actuator is made up the incident propagating wave A_i and the A_2 and A_4 waves generated by the actuator. This can be written as:

$$w(x) = A_i e^{-jk_b x} - \frac{P}{4EI k_b} (e^{-k_b x} - j e^{-jk_b x}) \quad (5.13)$$

In the far-field, downstream of the actuator, the nearfield wave has a very small amplitude and the displacement is predominantly the sum of the incident propagating wave and the propagating wave generated by the secondary force, that is:

$$\text{for } x > 0, \quad w(x) = A_i e^{-jk_b x} + \frac{j P e^{-jk_b x}}{4EI k_b} \quad (5.14)$$

If this is set to zero, then there is only a residual nearfield wave at the actuator position, thus:

$$w(0) = -\frac{P}{4EI k_b} \quad (5.15)$$

Therefore the required gain of the controller is:

$$H = \frac{P}{w(0)} = -4EI k_b \quad (5.16)$$

Again this is dependent on frequency and the optimal controller is non-causal and cannot be physically realised over a range of frequencies.

If the slope of the beam $w'(0)$, is measured and fed back to a moment-pair P , then the required frequency response function of the controller, H to bring the beam to rest in the far-field downstream of the secondary force is given by:

$$H = \frac{P}{w'(0)} = 4EI \quad (5.17)$$

This is not dependent on frequency and thus the frequency response of the controller is causal and an optimal controller can be physically realised over a range of frequencies.

If the curvature of the beam $w''(0)$, is measured and fed back to a moment-pair P , then the required frequency response function of the controller H , to bring the beam to rest in the far-field downstream of the secondary force is given by:

$$H = \frac{P}{w''(0)} = \frac{-4EI}{k_b} \quad (5.18)$$

Again this is dependent on frequency and the optimal controller is non-causal and cannot be physically realised over a broadband range of frequencies.

5.2.4 Comparison of Feedback Controllers

The feedback controller gains discussed for the actuator sensor pairs discussed above are summarised in **Table 5.1** [92]. Examination of this table reveals a pattern. The power dependence of the optimal frequency responses of feedback controllers on the wavenumber k_b , decreases as one moves to the right, or down the table. The two particularly interesting entries are the ones in the shaded cells. They predict that there are two combinations of sensors and actuators that require a feedback gain that is independent of frequency. These are where the output from a curvature sensor is fed back to a moment actuator or the output from a rotation sensor is fed back to a moment-pair actuator. There are, however, practical difficulties associated with these idealised actuators and sensors, and these are discussed in the next section.

SENSOR	ACTUATOR		
	Point Force $f(0)$	Moment $M(0)$	Moment-Pair $P(0)$
Displacement $w(0)$	$-4EI k_b^3$	$4EI k_b^2$	$-4EI k_b$
Rotation $w'(0)$	$4EI k_b^2$	$-4EI k_b$	$4EI$
Curvature $w''(0)$	$-4EI k_b b$	$4EI$	$-4EI/k_b$

Table 5.1 Transfer Functions of the Feedback Controllers for Various Collocated Sensor and Actuator Combinations which Suppress Propagating Flexural Waves

5.2.5 Practical Considerations

5.2.5.1 Practical Actuators and Sensors

As mentioned above, there are practical problems associated with both of the configurations that have an optimal frequency independent feedback gain. Although the curvature of a beam is readily measured with a strain measuring sensor such as a conventional strain gauge or a PVDF film sensor, a pure moment is difficult to apply in practice. Commercial moment actuators that can fit to a slender beam are not known to be available, but a moment can be generated by using two force actuators positioned a certain distance apart on the beam and driven in anti-phase. However, as there are small differences in the characteristics of practical force actuators it is difficult to generate a moment with no resultant force using this arrangement. A line moment-pair actuator is not known to exist, but an actuator that generates a pair of moments some distance apart, is a PZT actuator such as that discussed in Chapter 4.

One way of measuring the rotation (slope) of a beam is to measure displacement at two points and use finite difference techniques to calculate the slope. However, with this technique, there is an error between the calculated and the actual slope of the beam. This error increases with frequency and thus imposes an upper frequency limit

on the control system. As it is possible to measure the displacement of the beam at two points (and hence calculate slope) and also to generate a pair of moments using a PZT actuator, it was decided to investigate this arrangement further with a view to conducting a laboratory experiment.

If a pair of moments is applied a distance l apart and the rotation of the beam is sensed using a finite difference technique, then the situation different in two respects from the ideal arrangement shown in **figure 5.3**. Thus the ideal feedback gain will be different to that given in equation (5.17). To examine these two effects separately, two different configurations are analysed. The first is the effect of applying a pair of moments rather than a line moment-pair, and this arrangement is shown in **figure 5.4**. In this configuration a pair of moments are applied to the beam a distance l apart and the rotation at $x = 0$ is sensed.

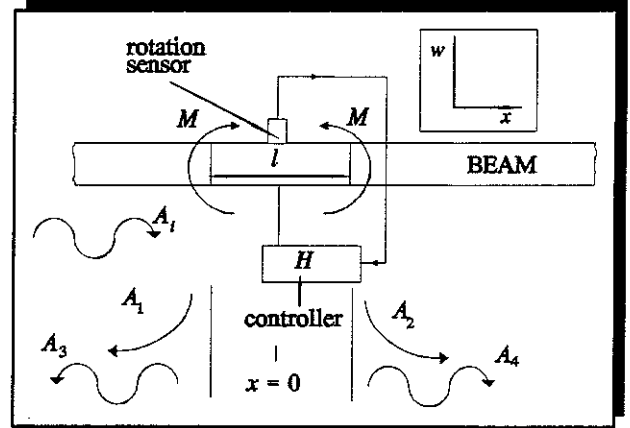


Figure 5.4 Feedback Control using a PZT Actuator

The displacement of the beam to the right of the actuator, where $x \geq l/2$ is given by:

$$w(x) = A_i e^{-jk_b x} - \frac{M}{4EI k_b^2} \left\{ \left(e^{-k_b \frac{l}{2}} - e^{k_b \frac{l}{2}} \right) e^{-k_b x} - \left(e^{-jk_b \frac{l}{2}} - e^{jk_b \frac{l}{2}} \right) e^{-jk_b x} \right\} \quad (5.19)$$

If the far-field displacement of the beam downstream of the actuator is set to zero, then the required (optimum) moment M_o to achieve this is given by:

$$M_o = \frac{-j2EI k_b^2}{\sin(k_b \frac{l}{2})} A_i \quad (5.20)$$

Now, the application of the secondary moment-pair has no effect on the slope of the beam at $x = 0$. Thus, the relationship between the slope of the beam at this position and the incident wave, with or without control is given by:

$$w'(0) = -jk_b A_i \quad (5.21)$$

equation (5.20) can therefore be written as:

$$M_o = \frac{2EI k_b}{\sin(k_b \frac{l}{2})} w'(0) \quad (5.22)$$

Thus, if rotation is measured and fed back to a PZT actuator, the required (optimum) feedback gain to suppress an incident propagating wave is given by:

$$H_o = \frac{2EI k_b}{\sin(k_b \frac{l}{2})} \quad (5.23)$$

This has a low frequency approximation when $k_b l/2 \ll 1$, and is given by:

$$H_o = H_1 = \frac{4EI}{l} \quad (5.24)$$

The feedback gain H_1 , should be compared with equation (5.17) which describes the optimal feedback gain for a control system that has a rotation sensor and a line moment-pair actuator. It can be seen that a pair of moments is equivalent to a line moment-pair at low frequencies, where $P = Ml$. If this constant feedback gain is used (which is possible to do in practice using a power amplifier) then the moment applied is given by:

$$M_1 = H_1 w'(0) \quad (5.25)$$

which in terms of the incident wave is:

$$M_1 = \frac{-j4EI k_b}{l} A_i \quad (5.26)$$

As mentioned previously, in order to implement a feedback controller that is capable of control over a broad band of frequencies, the feedback gain should be real and independent of frequency. Clearly equation (5.23) does not fulfil this condition, but the low frequency approximation (5.24) does.

Consider now the configuration shown in **figure 5.5**. As in the previous case a pair of moments is applied to the beam using a PZT actuator, but the rotation of the beam is calculated by measuring displacement at two positions and using the relationship:

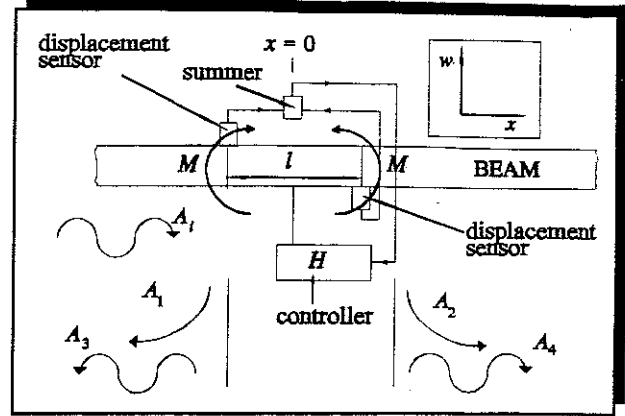


Figure 5.5 Feedback Control using a PZT Actuator and Measuring Slope with Displacement Transducers

$$\hat{w}'(0) = \frac{w(\frac{l}{2}) - w(-\frac{l}{2})}{l} \quad (5.27)$$

This can be written in terms of the incident wave as:

$$\hat{w}'(0) = \frac{-j2\sin(k_b \frac{l}{2})}{l} A_i \quad (5.28)$$

Equations (5.20) and (5.28) can be combined to give the optimum feedback for a PZT actuator when the slope is measured using a finite difference approximation:

$$H_2 = \frac{EI k_b^2 l}{\sin^2(k_b \frac{l}{2})} \quad (5.29)$$

This controller cannot be achieved in practice, so if the measured slope is fed back using the *constant feedback gain* of equation (5.24), then the moment applied is:

$$M_2 = \frac{4EI}{l} \hat{w}'(0) \quad (5.30)$$

This can be written in terms of the incident propagating wave as:

$$M_2 = \frac{-j8EI}{l^2} \sin(k_b \frac{l}{2}) A_i \quad (5.31)$$

Plots of the moments M_1 and M_2 (equations (5.26) and (5.31)) normalised by the optimal moment M_o required to suppress an incident propagating wave (equation (5.20)) are shown in **figure 5.6**. It can be seen that in both cases the actual moment applied is far from ideal when the length of the actuator is a significant fraction of a flexural wavelength. At low frequencies, when the length of the actuator is small compared to a flexural wavelength, moments M_1 and M_2 are similar to the moment required to suppress the incident propagating wave. However, as frequency increases the optimal feedback gain changes and the applied moments progressively deviate from the optimum. Also, there is an

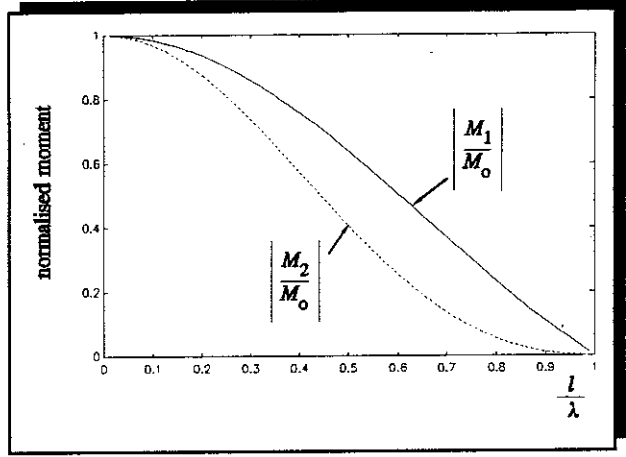


Figure 5.6 Normalised Moments Applied by the PZT Actuator

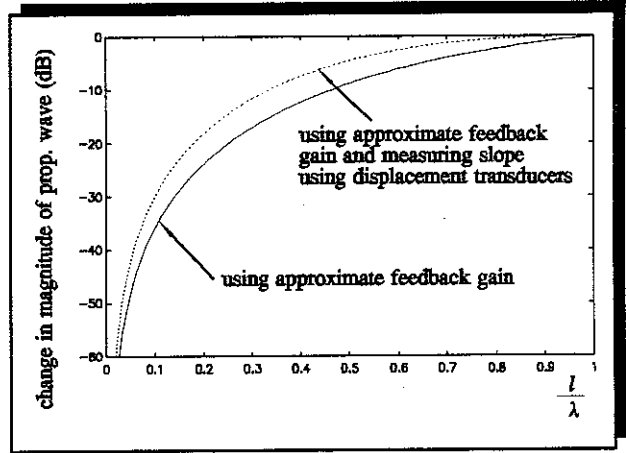


Figure 5.7 Change in Amplitude of the Propagating Wave when Moments M_1 and M_2 are Applied

additional error introduced by measuring the slope using two displacement transducers (M_2). The effectiveness of applying these control strategies to a beam can be seen by examining **figure 5.7**. This graph shows the *change* in the amplitude of a propagating wave on an infinite beam when the moments M_1 and M_2 are applied. Obviously if the optimum moment M_o , is applied then the change is infinite.

It can be seen that when the slope of the beam is measured with two displacement transducers positioned at each end of a PZT actuator, the feedback control system is

only effective at low frequencies, when a flexural wavelength is much greater than the length of the actuator. PZT actuators, however, are not very effective at these frequencies, as they require large voltages to drive them as discussed in Chapter 4. They are more effective at higher frequencies when the length of the actuator is about half a flexural wavelength. However, with a constant feedback gain, the potential reduction in the amplitude of the propagating wave at this frequency is much diminished (to about 10 dB). There are other problems associated with this control strategy such as stability and reflections of waves that occur at terminations on a finite beam, and these are discussed in the next section.

5.2.5.2 Effects of Wave Reflections from Beam Terminations

The aluminium beam used in the experiments to validate the theory was not infinite in length and therefore there were frequencies at which the PZT actuator was positioned at a node and could only excite the beam with considerable effort. There were thus frequencies when active control of flexural

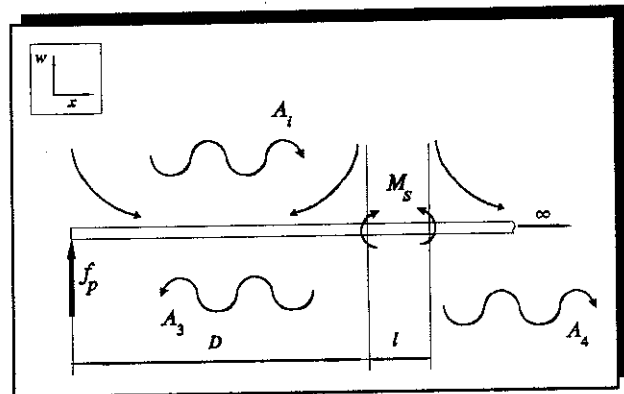


Figure 5.8 Semi-Infinite Aluminium Beam with a Primary Force and a PZT Secondary Source

motion was difficult. Consider the semi-infinite beam shown in **figure 5.8**. The wave to be suppressed using the secondary source M_s , is the incident wave A_i , which is generated by the primary force f_p . According to equation (5.31), the moment required is proportional to the magnitude of the incident propagating wave, but the feedback gain is not affected by the termination. If the feedback arrangement for this set up is the same as that in **figure 5.5**, where *the slope of the beam is detected by displacement transducers at each end of the actuator* and this is fed back through a *constant feedback gain* to the PZT actuator, the change in the propagating wave amplitude generated by the primary force in these circumstances is shown in **figure**

5.9 for a 6 mm x 30 mm aluminium beam, where the length of the actuator d , is 100 mm, the distance between the primary and secondary sources l , is 1.48 m and the loss factor is set at 1%. Examining figure 5.9, the difference between the infinite and semi-infinite beam is evident. There are frequencies where there is a greater reduction in the

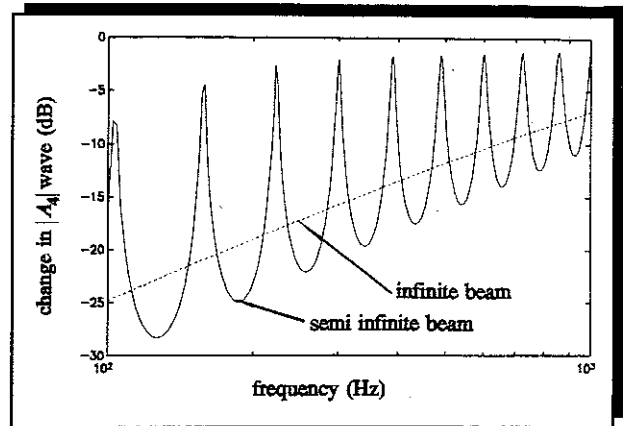


Figure 5.9 Change in the Magnitude of the Flexural Propagating Wave on a Semi-Infinite Beam with a Constant Feedback Gain

amplitude of the propagating wave and there are frequencies where the reduction is less. These latter frequencies coincide with those at which a large effort is required to attenuate the wave, because the A_3 wave generated by the secondary actuator is reflected from the left-hand boundary and destructively interferes with the A_4 wave generated by the secondary actuator, leaving only a small residual wave to destructively interfere with the incident wave. Thus, the reduction in the amplitude of the incident wave ranges between about 5 and 25 dB in the frequency range 100-1000 Hz. This is considerably less than the infinite reduction predicted on an infinite beam using a moment-pair.

If the beam is finite rather than semi-infinite, then the residual propagating wave downstream of the actuator will be reflected from the right-hand boundary and superimpose with positive-going propagating flexural wave. The contribution of this wave to the overall motion at the sensor positions is dependent upon:

1. The effectiveness of the control strategy in attenuating the incident propagating wave.
2. The amount by which the flexural wave downstream of the actuator is attenuated by damping in the beam and the reflection coefficient of the right-hand boundary.

At low frequencies the control strategy is most effective and thus the residual downstream wave will be small and therefore will not contribute greatly to the displacement of the beam at the measurement positions. At higher frequencies the control strategy is less effective, and thus the residual downstream propagating wave is relatively large. This has a greater "corrupting" effect at the sensor positions, but as the control strategy has minimal effect at higher frequencies this is of little consequence.

5.2.5.3 Closed Loop Stability

With any feedback system there is a chance that it may become unstable and thus the stability of the control system has to be checked before implementation. **Figure 5.10** shows a block diagram of the control system for the physical system that is shown in **figure 5.5**. The error e is the motion of the beam that is sensed by the transducers, which is the displacement at one end of the actuator subtracted from the displacement at the other end of the actuator. It should be noted that when the feedback system is operating with optimum gain to suppress the propagating wave, the "error" has a finite value and is not driven to zero in this application. d is the primary disturbance measured at the sensors, and y is the motion of the beam due to the action of the secondary source measured at the sensors. u is the moment applied to the beam by the PZT actuator and the net response of the feedback loop is $H(j\omega)$, which includes K , the gain control on the power amplifier. The relationship between these variables is given by:

$$e = \frac{d}{1 - GH} \quad (5.32)$$

This is a classic closed loop transfer function that will only be stable provided the open loop frequency response function $G(j\omega)H(j\omega)$ has a net phase shift of less than 360° and a gain of less

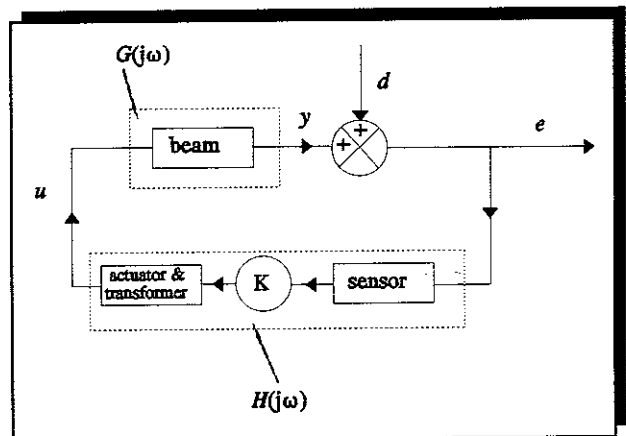


Figure 5.10 Block Diagram of the Feedback Control System

than unity [12]. Now the required feedback gain H , is given by equation (5.29). G is the response of the beam measured by the sensors to excitation by the secondary source. This is *zero* for a beam anechoically terminated at each end, because a symmetrical moment-pair will generate no slope on an infinite beam. Therefore, the feedback loop, GH , for an infinite beam has zero gain, and the control system has an infinite gain and phase margin. Thus, in principle, the loop is stable for any value of controller H . If, however, the beam is terminated upstream of the incident wave then this is not the case. For the system shown in **figure 5.8**, for example, the beam transfer function is given by:

$$G = \frac{\hat{w}'(0)}{M} = -\frac{(1 - e^{-jk_b l})^2 e^{-j2k_b D}}{4EI k_b^2 l} \quad (5.33)$$

Thus the open loop transfer function is given by:

$$GH = -\frac{(1 - e^{-jk_b l})^2 e^{-j2k_b D}}{k_b^2 l^2} \quad (5.34)$$

which has a magnitude of less than unity for all k_b . The phase, however, increases monotonically with frequency. The stability of the system is thus more sensitive to mistakes in the feedback gain setting at higher frequencies.

5.2.6 Experimental Validation

An experiment was set up using a PZT actuator as a secondary source on a semi-infinite beam to see if broadband control of flexural waves could be achieved using the simple feedback control system described above. The experimental set up is shown in **figure 5.11** and the experimental apparatus is listed in Appendix 4.

The primary force was provided by a shaker fitted to the end of the beam and the secondary source was a PZT actuator glued to the beam. The slope of the beam was sensed using two capacitance probes fitted to opposite sides of the beam at each end of the actuator and their outputs summed. Initial experiments with accelerometers

gave problems due to phase shifts in the integrator, as discussed later. The output from the summer was then fed to a manual phase controller [46], before being amplified using a power amplifier and transformer and then being fed to the PZT actuator to complete the loop. Before the feedback control experiments were carried out on the beam, the effectiveness of the PZT actuator in suppressing a propagating wave was first tested by using a feedforward control system. To do this the experimental equipment was set up as shown in figure 5.12. At discrete frequencies in the frequency range 100 Hz to 1 kHz ($l/\lambda = 0.14$ to 0.43), the magnitude and phase of the secondary source was manually adjusted with reference to the primary force, to suppress the propagating wave generated by the primary force. The displacement downstream of the secondary source was measured using an accelerometer and the amplitude was minimised as measured by monitoring the signal on an oscilloscope. The measured

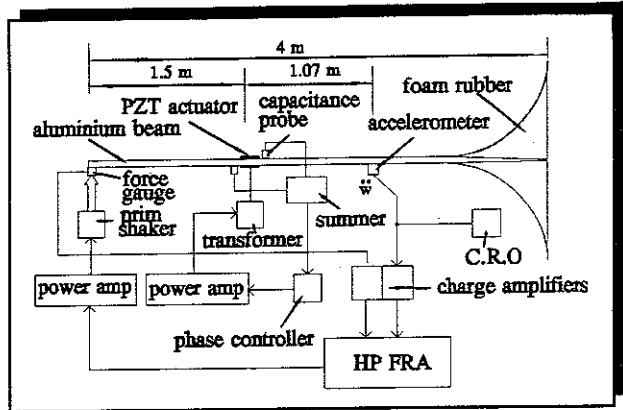


Figure 5.11 Experimental Set Up to Test the Effectiveness of the Feedback Control System in the Suppression of Flexural Propagating Waves

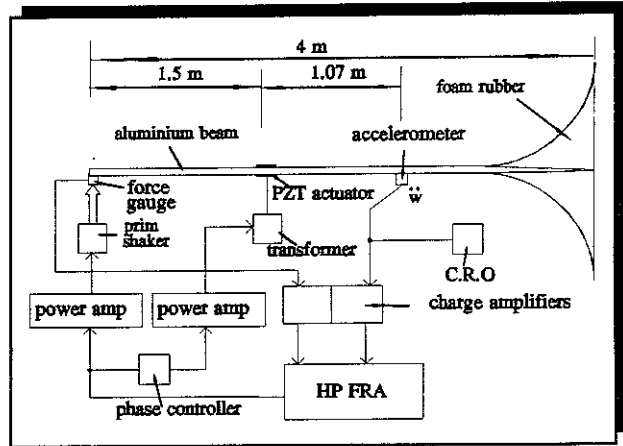


Figure 5.12 Experimental Set Up to Test the Effectiveness of a PZT Actuator in the Suppression of Flexural Propagating Waves

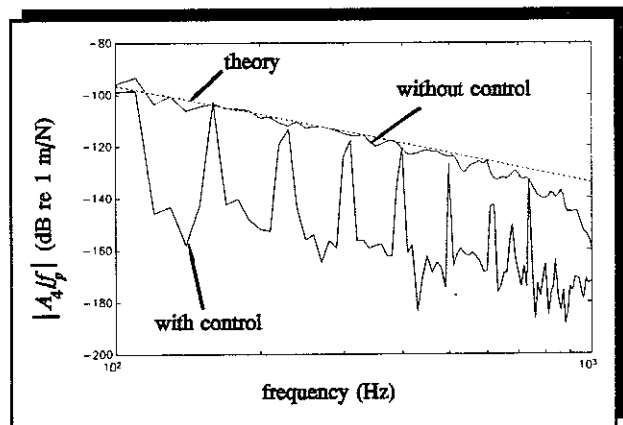


Figure 5.13 Measured Displacement of the Beam Downstream of the PZT Actuator

displacement with and without control is plotted in **figure 5.13** and the reduction in the displacement is plotted in **figure 5.14**.

Once it had been demonstrated that the actuator was capable of attenuating a propagating wave, feedback control was implemented. However, before broadband feedback control was implemented an initial series of pure tone tests were undertaken. The beam was excited at 280 Hz by the primary force and the magnitude and phase of the secondary source, which was connected as shown in **figure 5.11**, was adjusted until the displacement downstream was a minimum without the control system becoming unstable. Although the phase should have theoretically been zero, it was found necessary to adjust the phase to suppress the propagating wave. This is discussed later. The primary force shaker was then driven with random noise over the frequency range 200 Hz to 500 Hz and the feedback control system was used to attenuate the incident

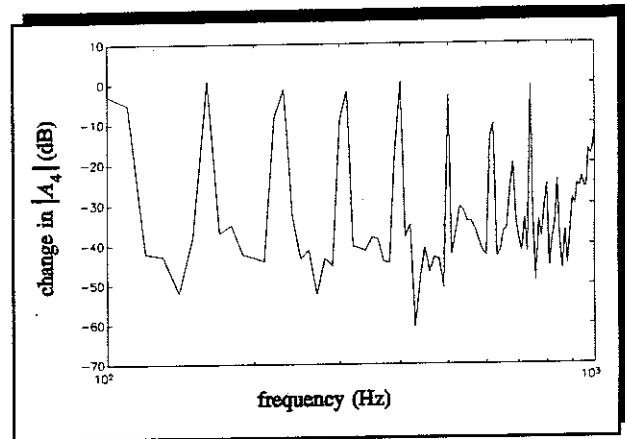


Figure 5.14 Reduction in Measured Downstream Displacement. Phase Reference Taken from the Primary Force

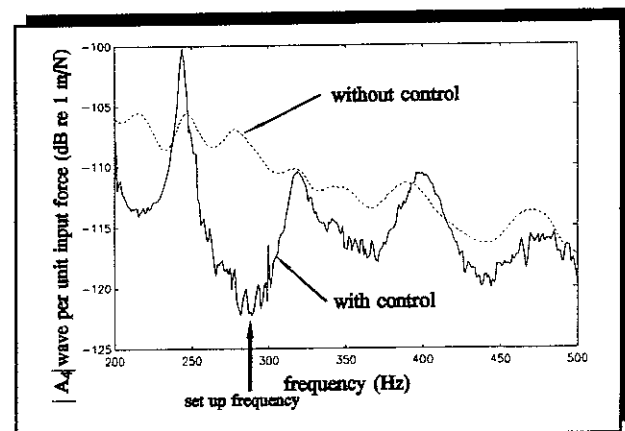


Figure 5.15 Measured Lateral Displacement of the Beam Downstream of the Secondary Source. Broadband Excitation and Feedback Control

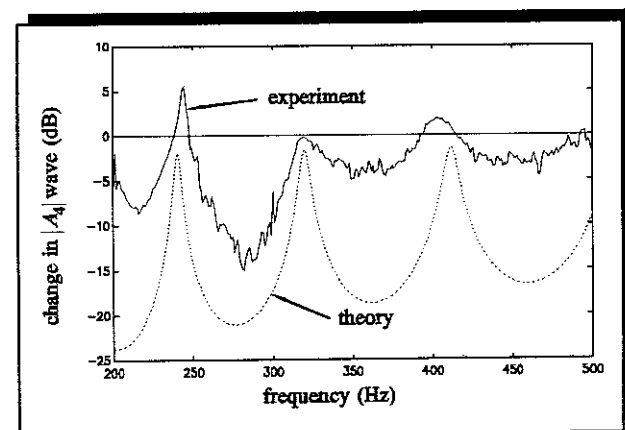


Figure 5.16 Reduction in Measured Lateral Displacement of the Beam Downstream of the Secondary Source. Broadband Excitation and Feedback Control

propagating wave. The measured displacement downstream of the secondary source with and without control is plotted in **figure 5.15** and the measured and the predicted reduction in the displacement is plotted in **figure 5.16**. The open loop transfer function was also measured and is shown in **figure 5.17**. Additionally, the frequency

responses of two of the components in the feedback loop whose behaviour may have caused the instability of the system at high gain were also measured. These were the transformer and the phase controller and their frequency responses are shown in **figures 5.18** and **5.19**.

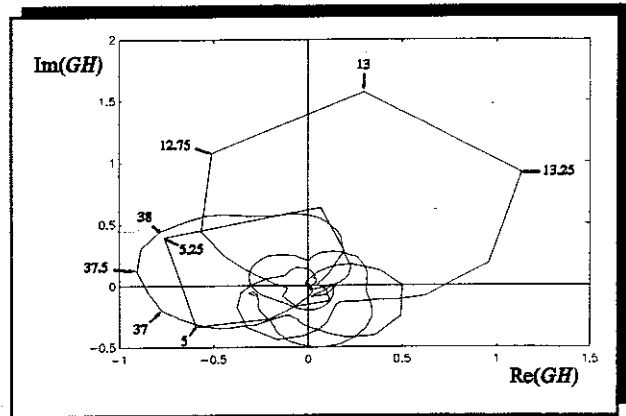
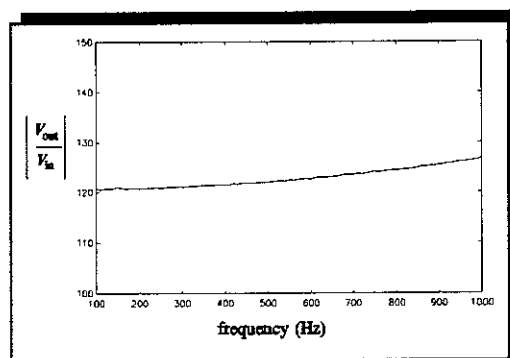
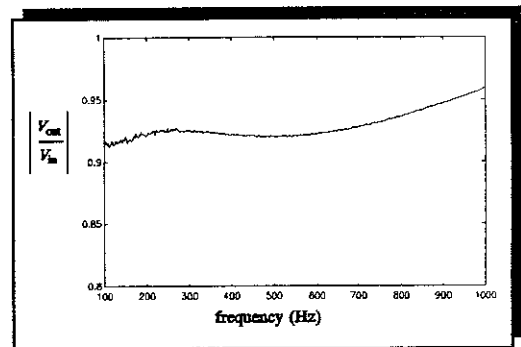


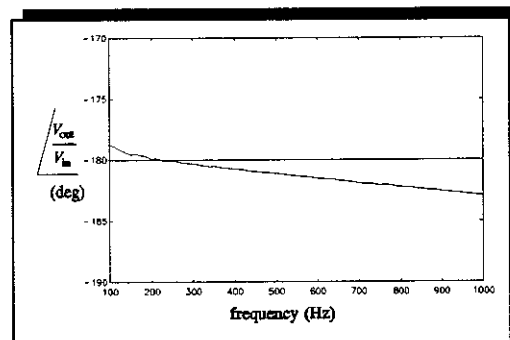
Figure 5.17 Open Loop Transfer Function. The Numbers are Frequencies in Hz



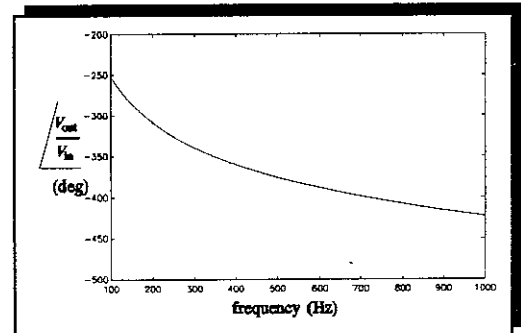
(a) Magnitude of Output/Input



(a) Magnitude of Output/Input



(b) Phase of Output/Input



(b) Phase of the Output/Input

Figure 5.18 Gain of the Transformer

Figure 5.19 Gain of the Phase Controller

5.2.7 Discussion

The theory discussed in the first part of this section indicated that the two combinations of (a) a rotation sensor and moment-pair and (b) a curvature sensor and a moment actuator result in an optimal feedback controller gain that is real and independent of frequency. All the other transducer combinations of displacement, rotation and curvature sensors and force, moment and moment-pair actuators result optimal feedback gains that *are* frequency dependent and also non-causal.

Further investigation of the configuration using the rotation sensor and moment-pair actuator implemented with practical transducers revealed that there are several shortcomings with this feedback control strategy in practice. Firstly, the moment-pair was applied to the beam using a PZT actuator that actually applies moments at each end of the actuator. Therefore, this actuator only approximates to a moment-pair at low frequencies when the length of the actuator is small compared to a flexural wavelength. There is a degradation of performance with increasing frequency when such an actuator is used with a constant feedback gain. Secondly, rotation of the beam was measured using two transducers, one at each end of the actuator rather than measuring rotation at the centre, and this causes an additional degradation of performance. These effects can be seen in **figure 5.7**. Finally, when the system was implemented on a finite rather than an infinite beam there was a further predicted degradation of performance as was shown in **figure 5.9**, and discussed in section 5.2.5.2.

A major problem in the stability of the feedback system was highlighted when the experiments were undertaken. Initially, accelerometers were used instead of displacement transducers at the ends of the actuator to measure the rotation of the beam. However, angular displacement not angular acceleration was the quantity required to be fed back to the pair of moments, so the output from the summer, which added together the outputs from the accelerometers, had to be integrated twice. This was achieved by passing the signal through a low pass filter, and using the roll-

off characteristic above the cut-off frequency, to integrate the signal. There were two problems in using the low pass filter. The first was that it attenuated the signals at a rate of 40 dB per decade, and thus the high frequency signals were very small indeed. Although the filter cut-off frequency could be set to any frequency, if this was set too high, then there was significant phase variation through the filter with increasing frequency. The second problem with the filter was that it caused the feedback system to go unstable at the filter's resonant frequency. It was found that even a small gain set on the power amplifier caused the system to go unstable immediately. Thus it was decided to abandon the use of accelerometers and to use capacitance probes, which measure displacement, instead. This removed the need for the low pass filter, but these transducers are not as versatile as accelerometers and it is questionable whether they could be used on a real system outside the laboratory. However, in this case they enabled the concept of a constant gain frequency independent feedback controller to be studied experimentally. There was a very low frequency problem, however, even when these transducers were used, which was caused by the beam moving laterally. This was overcome by supporting beam in the vicinity of the secondary source on some soft foam rubber.

Notwithstanding all of the problems discussed above, broadband control of flexural vibrations on a beam was only partially achieved as shown by the results in **figures 5.15 and 5.16**. The largest attenuation (10 - 15 dB) in the frequency region 250 - 300 Hz was achieved because the magnitude and phase of the secondary force was set using the power amplifier and phase controller to minimise the displacement of the beam at a frequency of 280 Hz. It is believed that the bandwidth over which control was most effective (about 250 Hz to 300 Hz) was limited by the unmodelled phase changes around the feedback loop. **Figures 5.18 and 5.19** shows that there was very little phase variation through the transformer, but there was a substantial phase variation in the phase controller over the frequency range of interest. There would also be a frequency dependent phase change associated with the actuator, which behaves as a capacitor as shown in Chapter 4. It is believed that these additional phase shifts in the feedback loop resulted in a much smaller phase margin and hence the optimum gain setting on the power amplifier could not be reached. Examination

of the open loop response plot in figure 5.17 shows that the system was conditionally stable and that it would become unstable at around 37 Hz if the gain setting was increased (the -1, 0 point would become encircled at this frequency).

5.3 Feedback Control of Longitudinal Waves

The partial success of the feedback control system for the control of flexural waves prompted an investigation to see whether there are combinations of actuators and sensors that can be configured to control longitudinal waves such that the optimal feedback gain is also independent of frequency. However, the choice of transducers is more restricted in this case, and only force actuators and translational motion sensors are considered. This section investigates whether there is such an appropriate combination of transducers. A theoretical study is first carried out, and this is followed by a simple experiment to check the predictions. The practical issues that make the implementation of such a feedback system difficult are then discussed.

5.3.1 Feedback Control Applied at the End of a Beam

Consider the system shown in figure 5.20, where a secondary force f , is applied at the end of a beam. A_i is an incident wave which is reflected at the free end into the negative-going propagating (reflected) wave A_r . The object of the control strategy is to suppress

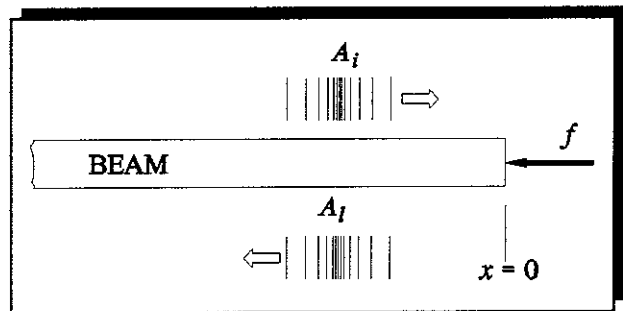


Figure 5.20 Force Applied at the End of a Beam

this reflected wave. Effectively the secondary force acts as an active wave absorber at the end of the beam and emulates an impedance equal to that of an infinite rod. The longitudinal displacement of the beam is given by:

$$u(x) = A_i e^{-jk_l x} + A_l e^{jk_l x} - \frac{jf e^{jk_l x}}{k_l ES} \quad (5.35)$$

where E is the Young's modulus of the beam, k_l is the longitudinal wave number and S is the cross-sectional area. The $e^{j\omega t}$ time dependence has been suppressed for clarity. If the negative-going wave A_l , is to be suppressed, then the secondary force f , has to generate a wave that is in anti-phase with it. Thus:

$$A_l = -\frac{jf}{k_l ES} \quad (5.36)$$

and therefore $u(0) = A_i$. But in the absence of control $A_l = A_i$ since the boundary condition is free, and therefore the required relationship between the displacement and the force is:

$$u(0) = -\frac{jf}{k_l ES} \quad (5.37)$$

Noting that $k_l = \omega/c_l$, where $c_l = \sqrt{E/\rho}$, equation (5.37) can be differentiated with respect to time, and rearranged to give the required gain of an optimal feedback controller, where velocity of the end of the beam is fed back to a force. This feedback gain is:

$$H = \frac{f}{\dot{u}(0)} = -S\sqrt{E\rho} \quad (5.38)$$

This shows that if velocity is sensed at the end of the beam and fed back to a force through a frequency independent gain, the incident wave is suppressed. The optimal feedback gain H , is just the characteristic longitudinal impedance of the beam, which is independent of frequency.

5.3.2 Feedback Control Using an Actuator Integrated into the Beam

5.3.2.1 Theory

Consider the model of an actuator of length l , fitted to a beam shown in **figure 5.21**. This model is appropriate for a PZT actuator made up of two elements joined to the surface of the beam and driven in phase as discussed in Chapter 4, or a magnetostrictive actuator fitted inside a strut as described by

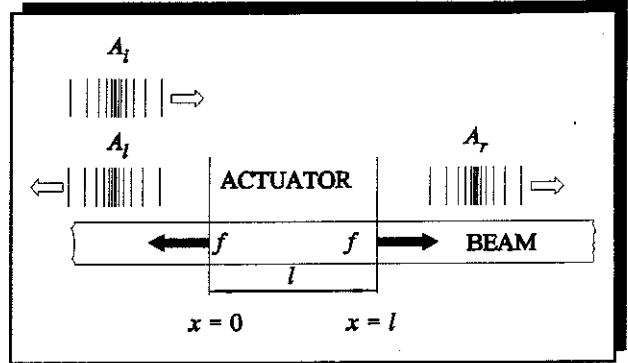


Figure 5.21 Integrated Longitudinal Vibration Actuator

Brennan *et al* [89]. The actuator is required to suppress the incident compressional wave A_i . The longitudinal displacement of the beam for $x \leq 0$ is given by:

$$u(x) = A_i e^{-jk_i x} + A_r e^{jk_i x} \quad (5.39)$$

and for $x \geq l$ the displacement is given by:

$$u(x) = A_i e^{-jk_i x} + A_r e^{-jk_i x} \quad (5.40)$$

where A_i and A_r are waves in the left and right directions generated by the actuator. If the incident wave is to be suppressed we require $A_r = -A_i$, therefore $u(x) = 0$ for $x \geq l$, and:

$$u(x) = -A_i e^{-jk_i x} + A_i e^{jk_i x} \quad \text{for } x \leq 0 \quad (5.41)$$

which gives:

$$u(0) = -A_i + A_i \quad (5.42)$$

Now, referring to Appendix 2, A_i and A_r are related to the actuator force by:

$$A_l = \frac{jf}{2k_l ES} (1 - e^{-jk_l l}) \quad (5.43)$$

and

$$A_r = \frac{jf}{2k_l ES} (1 - e^{jk_l l}) \quad (5.44)$$

Combining equations (5.42), (5.43) and (5.44) gives the required feedback gain for an optimal controller, provided the longitudinal displacement at $x = 0$ is fed back to an integrated force actuator. This feedback gain is given by:

$$H = \frac{f}{u(0)} = -\frac{k_l ES}{\sin k_l l} \quad (5.45)$$

It should be noted that this is not independent of frequency and is not causal. However, the low frequency approximation of H , when $k_l l \ll 1$ is given by:

$$H_1 = \frac{f}{u(0)} = -\frac{ES}{l} \quad (5.46)$$

which is independent of frequency. This low frequency approximation is valid provided that the length of the actuator is much less than a longitudinal wavelength, which is dependent only upon the density and Young's modulus of the beam and frequency. For steel or aluminium, a wavelength of 100 mm (a typical length of PZT actuator) occurs at a frequency of about 50 kHz. Thus, in most practical situations, there is little difference between the frequency independent low frequency approximation of the optimal feedback gain and the actual feedback gain. Rather than measure axial displacement, a better quantity to measure in practice is axial strain. If a strain sensing transducer of the same length of the actuator is placed alongside the actuator such that it measures $\epsilon_{lat} = \{u(0) - u(l)\}/l$, then this should have the same effect as sensing $u(0)$ provided that the axial displacement at $x = l$ is zero. This feedback gain is given by:

$$H_2 = \frac{f}{\epsilon_{lat}} = -ES \quad (5.47)$$

5.3.2.2 Practical Considerations

As with the feedback control system for flexural waves, the optimal feedback controller required to completely attenuate the incident longitudinal wave at all frequencies *is frequency dependent*. It is only at relatively low frequencies, when the length of the actuator is small compared to a longitudinal wavelength, that the feedback gain is almost independent of frequency. It is also apparent that if the longitudinal wave incident on the actuator is not completely suppressed, then the strategies of measuring axial displacement and strain over the length of the actuator are different. To examine this difference, the effects are considered of applying the feedback gains (H_1 and H_2) to a control system with either a point sensor or a strain sensor 100 mm long, and an actuator 100 mm long, fitted to an infinite aluminium beam of 6 mm x 30 mm cross-section. The changes in the axial displacement downstream of the actuator as a function of frequency are plotted in **figure 5.22**, where the frequency range shown (100 Hz to 1 kHz) corresponds to $l/\lambda = 0.002$ to 0.02. It can be seen that the strategies of measuring displacement and strain are indeed different. Reductions in the longitudinal wave amplitude of between about 48 dB and 28 dB in the frequency range 100 Hz - 1 kHz. are achieved when strain is measured. When axial displacement is measured at the left-hand end (that closest to the primary source) of the actuator, the wave is almost completely suppressed over the same frequency range.

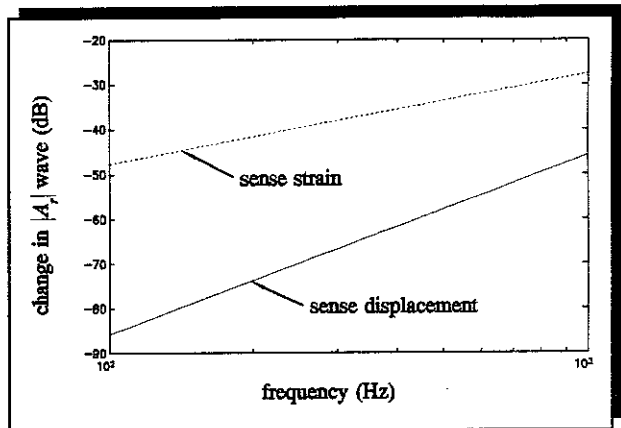


Figure 5.22 Changes in Axial Displacement when Axial Displacement and Axial Strain are Measured and fed back to an In-Plane Force

As discussed in the previous section on flexural waves, if acceleration is measured and integrated twice to give displacement, then there are problems with closed loop stability due to the dynamic behaviour of the integrator. Thus, axial displacement,

or axial strain over the length of the actuator, has to be measured. Axial displacement can be measured using a capacitance probe, and this involves attaching a small angled section to the beam to provide a surface normal to the edge of the beam whose motion can be sensed with a capacitance probe. Axial strain can be measured using strain sensing devices which are discussed more fully in the next section.

In the section on flexural waves, it was shown that the reflections from the boundaries of the beam influence the effectiveness of the feedback control strategy in suppressing a wave incident on the actuator. Boundaries also have an effect on the control strategy to control longitudinal waves, and this can be seen in **figure 5.23**. This shows the predicted reduction in axial displacement downstream of a 100 mm actuator fitted to an aluminium beam of 6 mm x 30 mm cross-section, when the displacement measured and fed back via the feedback gain H_1 , for three cases:

- a. an infinite beam
- b. a semi-infinite beam (left-hand boundary)
- c. a finite beam

The behaviour of the infinite and semi-infinite beams follow similar patterns to the flexural case, except that the frequency range 100 Hz to 1 kHz is relatively low in this case as the length of the 100 mm actuator is small compared to a longitudinal wavelength. The behaviour of the finite beam, however, is different and the predicted reduction in downstream

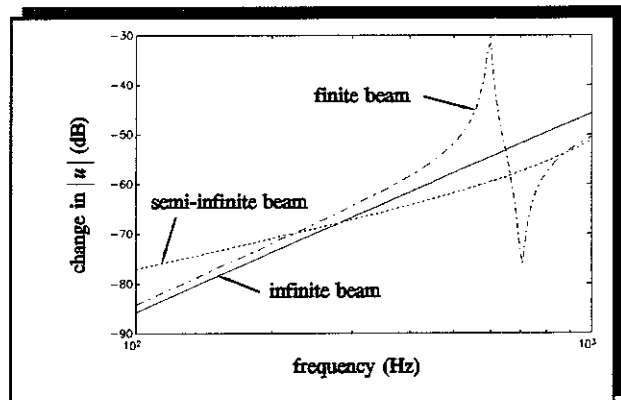


Figure 5.23 Change in Axial Displacement Downstream of the Actuator when Axial Displacement is Sensed and a Constant Feedback Gain H_1 is Used.

displacement is not as great. This can be explained by considering the reflection of the residual wave from the right-hand boundary which contributes to the axial motion

of the beam at the sensor position. Recall that the theoretical model assumed that there were only positive-going waves present on the beam without control. However, reductions in displacement downstream of the actuator are predicted to be at least 30 dB over the frequency range of interest, even on the finite beam.

The closed loop stability considerations are similar to the flexural case, and the system should be stable provided that the feedback gain does not exceed the optimum given in equations (5.46) and (5.47).

5.3.2.3 Experimental Validation

To test the theoretical predictions, an experiment was set up using the same beam that was used for the feedback control of flexural waves. Before conducting the main experiments, tests were conducted on various sensor arrangements to determine which sensor was best to use in the feedback experiments. Three alternative methods of measuring axial strain and one method of measuring axial displacement were investigated. The three methods of measuring axial strain are discussed below.

a. *Measurement of axial strain using a PVDF Sensor.*

A PVDF (piezopolymer) element was placed alongside the PZT (piezoceramic) actuator and a simple experiment was conducted to see whether there was any electrostatic interference between the actuator and the sensor. The PVDF sensor was screened using aluminium tape and held a few millimetres away from the beam so that there was no mechanical coupling between the sensor and the beam. The PZT actuator was used to excite the beam and the output from the sensor monitored. A large signal output was evident from the transducer which indicated substantial electrostatic crosstalk between the actuator and the sensor of about -20 dB. Thus, it would be difficult to use this combination of actuator and sensor in a feedback control system.

b. *Measurement of axial strain using the PZT elements as a self-sensing actuator*

Previous work [71] had demonstrated that PZT elements could be configured to act as both actuator and sensor simultaneously in a feedback control system on a beam. However, it was shown in Chapter 4 that this arrangement was unlikely to work over a range of frequencies because of tolerances within the electrical bridge circuit required for its operation. In particular, the phase accuracy of the device was extremely sensitive to the tolerances. It was thought, however, that this arrangement might be able to work at a single frequency, but all attempts at using the circuit to measure axial strain and feeding the signal back to the actuator failed, as the system immediately became unstable as soon as any feedback gain was introduced.

c. *Measurement of axial strain using a composite PZT actuator and sensor*

Work by Harris *et al* [93] suggested that a single PZT element could be used as both an actuator and a sensor by etching a channel in the electrode such that there are two distinct electrode areas, one associated with the actuator and the other with the sensor. It was decided to try this technique using the PZT elements fitted to the beam and longitudinal channels were etched on the PZT elements fitted to each side of the beam. One of these elements is shown in figure 5.24. This resulted

in a sensor electrode width of 5 mm and actuator electrode width of 15 mm.

This composite actuator and sensor device was used in the feedback system, but

again the instability occurred as soon as any feedback gain was introduced.

It is believed that this was again due to crosstalk between the actuator and

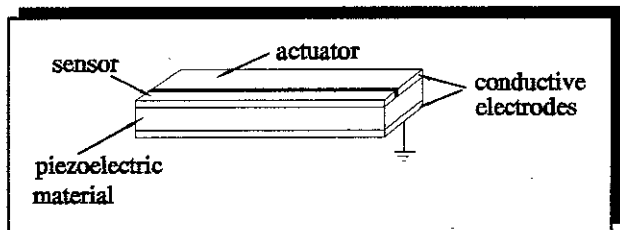


Figure 5.24 Single PZT Element used as a Sensor and Actuator

sensor, though it was not possible to determine this absolutely with the element fitted to the beam. This crosstalk could be measured, however, if the actuator was fitted to a solid block that could not strain when voltage was applied to the actuator.

As the implementation of feedback control using strain sensors was unsuccessful, it was decided to measure axial displacement using a capacitance probe. This was fitted at the left-hand end of the actuator and measured the axial motion of the beam by sensing the motion of the angle section fitted to the beam as discussed previously. The secondary actuators were the same PZT elements used in the experiment to control flexural waves, but in this case they were driven in phase to generate longitudinal waves. Prior to conducting the experiment control longitudinal waves using feedback, an experiment was set up as shown in **figure 5.25** to minimise the axial displacement downstream of the actuator using feedforward control at discrete frequencies between 100 Hz and 1 kHz. This was done to independently test the capabilities of the PZT actuator configured to suppress longitudinal motion. The equipment used is listed in Appendix 4.

At discrete frequencies (10 Hz intervals) the magnitude and phase of the secondary source was adjusted by hand until the axial displacement downstream of the PZT actuator was at a minimum as measured by eye using an oscilloscope connected to the output from an accelerometer. The measured displacements with and without control are plotted in **figure 5.26** and the reduction in the displacement is plotted in **figure 5.27**. The ratio of the secondary force to the primary force was calculated from the measured results and is plotted in **figure 5.28**. The measured quantity was the voltage supplied to the transformer per unit primary force. The secondary force applied

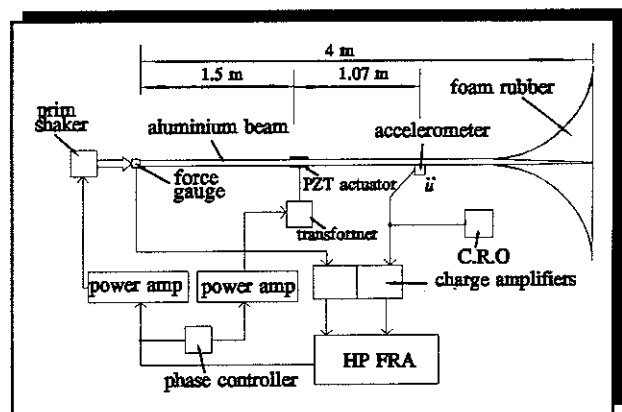


Figure 5.25 Experimental Set Up to Test the Effectiveness of the PZT Actuator in the Suppression of Longitudinal Waves

to the beam was calculated using the transformer gain and the actuator gain calculated in Chapter 4 (equation (4.69)). Figures 5.26 and 5.27 show that above about 300 Hz the PZT actuator is capable of significantly attenuating the incident propagating wave. Reduction in the displacement downstream of the secondary actuator of between 10 and 50 dB was possible. The reason why the secondary force actuator was ineffective below 300 Hz can be seen by examining figure 5.28. This shows the theoretical normalised magnitude of secondary force required to suppress a wave incident on the PZT actuator, and the ratio of the secondary force applied to the primary force. Above 300 Hz there is good agreement between the theoretical force required and the actual force applied. However, below this frequency the applied force was significantly less than that required, as the actuator was not capable of generating a force of appropriate magnitude. This was expected and the inability of PZT actuators to generate large longitudinal forces at

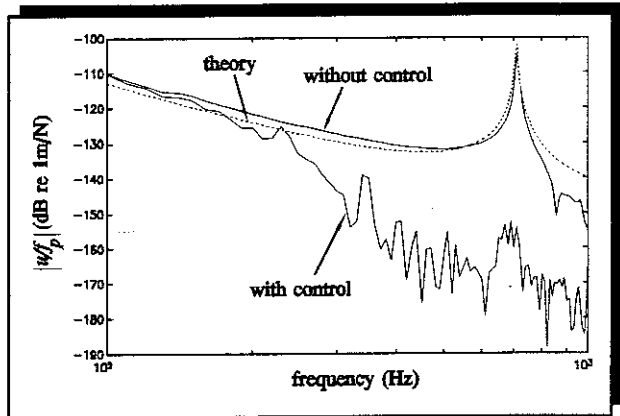


Figure 5.26 Measured Displacement of the Beam Downstream of the Secondary Force Actuator

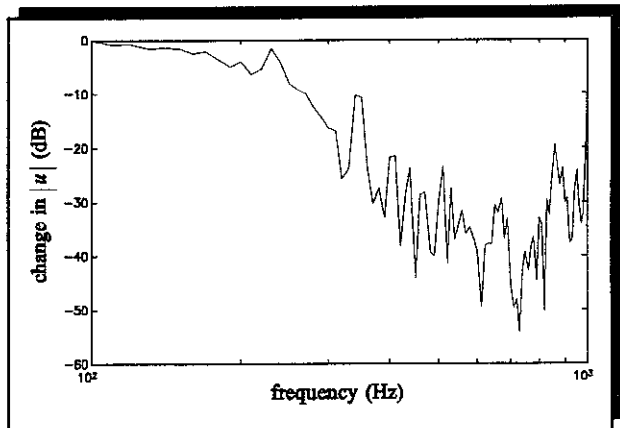


Figure 5.27 Reduction in the Measured Downstream Axial Displacement. Phase Reference Taken from the Primary Force

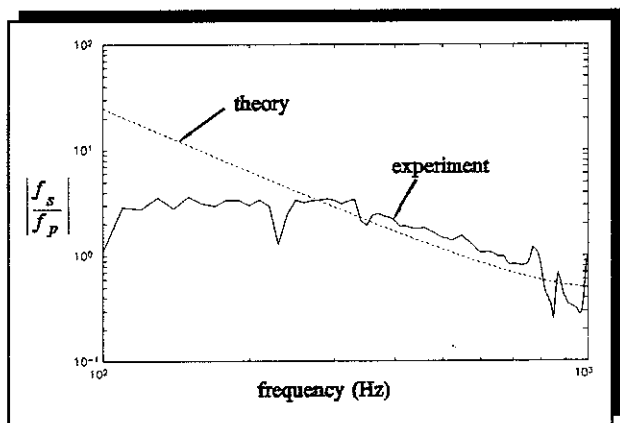


Figure 5.28 Ratio of the Secondary Force to Primary Force Applied to Suppress the Downstream Axial Displacement of the Beam

low frequencies has been shown in Chapter 4.

Once the limitations of the PZT actuator had been determined, feedback control of longitudinal waves was implemented. An experiment was set up as shown in figure 5.29, and the details of the positioning of the capacitance probe can be seen in figure 5.30. The output from a capacitance probe positioned at the left-hand edge of the PZT actuator was fed back through a phase controller, power amplifier and transformer to the PZT actuator. The beam was initially excited at 700 Hz and the magnitude and phase of the secondary source adjusted until the axial displacement downstream of the secondary actuator was at a minimum without the control system becoming unstable. The primary force shaker was then driven with a random signal over the frequency range 200 Hz to 1

kHz and the feedback control system was used to attenuate the incident propagating wave. The measured displacement downstream of the secondary source with and without control is plotted in figure 5.31 and the reduction in the displacement at this position is shown in figure 5.32. As with the flexural case, the open loop transfer function was measured and this is shown in figure 5.33.

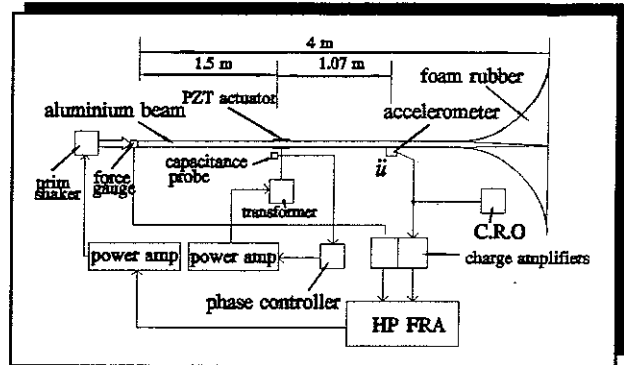


Figure 5.29 Experimental Set Up to Check the Effectiveness of the Feedback Control System to Suppress Longitudinal Waves

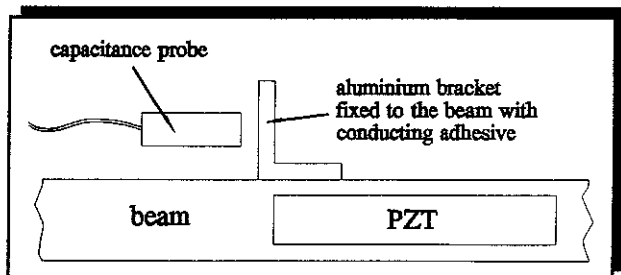


Figure 5.30 Positioning of the Capacitance Probe

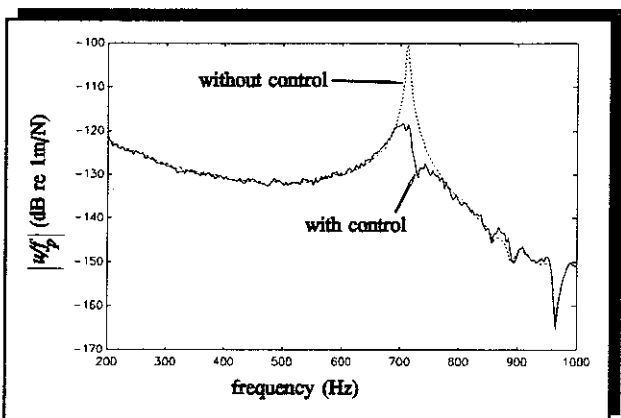


Figure 5.31 Measured Axial Displacement of the Beam per Unit Input Force Downstream of the Secondary Source. Broadband Excitation and Feedback Control

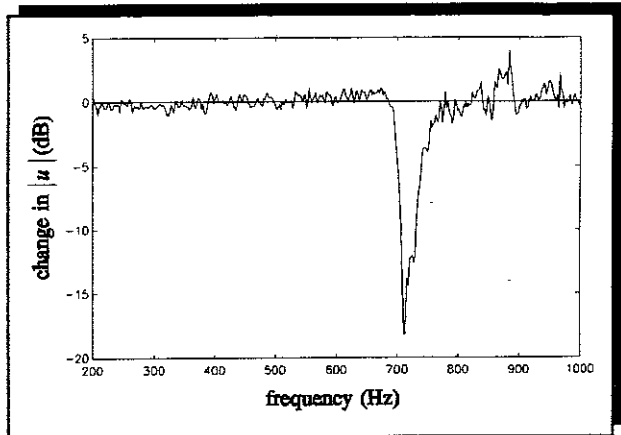


Figure 5.32 Reduction in Measured Axial Displacement of the Beam Downstream of the Secondary Source. Broadband Excitation and Feedback Control

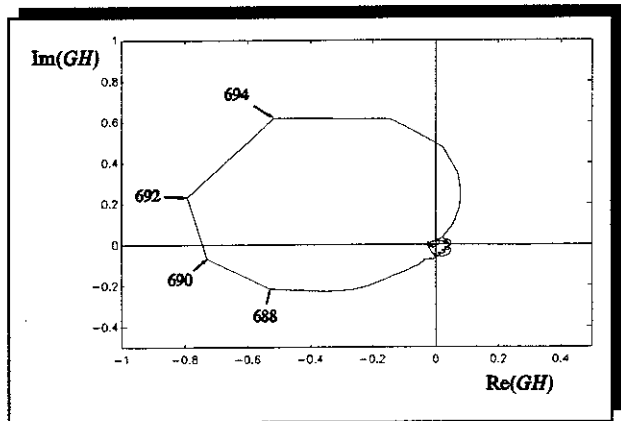


Figure 5.33 Open Loop Transfer Function. The Numbers are Frequencies in Hz

5.3.2.4 Discussion

It can be seen from **figures 5.26, 5.27, 5.31 and 5.32** that although the actuator was capable of suppressing a longitudinal wave above about 300 Hz, the feedback control of longitudinal waves was not particularly successful. If the gain was increased, the system became unstable at around 690 Hz, close to the fundamental natural frequency of the beam as can be seen by the open loop response plot in **figure 5.33**. In the experiments the gain was increased until the system was just stable. A high gain through the power amplifier was required as the output from the capacitance probe

was very small at all frequencies except at those close to the fundamental longitudinal resonant frequency of the beam at around 700 Hz. This small signal was as a result of very small beam displacement at all frequencies except those close to the resonant frequency. A transducer with greater gain would have been more suitable, for example a transducer that measures axial strain as discussed in section 5.3.2.2. However, there proved to be significant practical problems in using a piezoelectric sensor of this type in conjunction with a PZT actuator due to electrostatic interference. An alternative sensor would have been a conventional strain gauge, but this was not used as it was thought that the output voltage from this sensor would have been very small and there was limited space on the beam to fit such a sensor. A sensor that could possibly overcome these problems is a fibre optic strain sensing sensor [94][95]. This sensor could be fitted adjacent to the actuator in place of the PVDF sensor and is insensitive to electrostatic interference. However, these sensors are the subject of current research and are not commercially available at present.

The experimental validation of feedback control of longitudinal waves over a range of frequencies was only marginally successful. This was because a suitable sensor that was insensitive to electrostatic field generated by the actuator could not be found. However, the use of a PZT actuator as a secondary source to control longitudinal motion of a beam has been demonstrated, and its ineffectiveness at low frequencies highlighted.

5.4 Conclusions

The control strategy investigated in this chapter was the feedback control of flexural and longitudinal waves. A theoretical framework for the control of both wave types has been developed which showed that at low frequencies, and with a suitable choice of actuators and sensors, the optimal feedback gain is real and independent of frequency. This means that the control system is causal and thus capable of broadband control using a simple analogue amplifier as a controller. In practice, however, the characteristics of real actuators and sensors do not exactly match the ideal, and this

introduces a requirement for a controller that is frequency dependent. If a feedback controller with constant gain is used in conjunction with these practical transducers, there is then a degradation of performance that becomes more pronounced as frequency increases. This degradation of performance has been investigated theoretically and demonstrated by way of some simple experiments.

In the control of flexural waves, the practical actuator-sensor combination consisted of a PZT actuator which applied a pair of moments and a pair of displacement transducers used to sense the lateral slope of the beam. In the control of longitudinal waves the practical actuator-sensor combination consisted of a PZT actuator generating an in-plane force and either a displacement sensor or a sensor that measures axial strain across the actuator.

During the experiment on the feedback control of flexural waves it was found that it was essential to measure displacement rather than a double integrated signal from an accelerometer. This was because the filter used for the integration had a resonant frequency that caused the instability of the feedback system. The main disadvantage of using displacement transducers, however, is that they cannot be attached to the structure whose motion they are sensing, and they have to be fixed to a relatively rigid mounting adjacent to the structure. It is thus difficult to see how this arrangement would be useful in a practical active vibration control system. However, the use of the capacitance probes to sense displacement enabled the basic theory to be validated.

In the experiments on the feedback control of longitudinal waves the practical issues of sensing motion also proved to be a major issue. Displacement was again the physical quantity to be measured and so the above comments are also applicable. The main problem in using a displacement transducer in this case, however, was that the axial motion of the beam was very small resulting in signals that were too small for effective feedback control. Alternative piezoelectric strain sensors were investigated but the problem of electrostatic interference between the actuator and the sensor was encountered, making feedback control using these sensors impractical.

It is thought that the implementation of feedback control of longitudinal waves shows more promise than the feedback control of flexural waves, provided that the interaction between the actuator and the sensor can be overcome. Computer simulations show that constant gain feedback control should be effective over a much wider frequency range and the disadvantages of the displacement sensors can be avoided by using an appropriate strain sensing transducer.

CHAPTER 6

6 ACTIVE CONTROL OF FLUID WAVES IN A PIPE

6.1 Introduction

The propagation of vibration in fluid-filled pipes is an important problem in many industrial and defence applications, particularly in submarines where acoustic stealth is vital for operational efficiency. Piping systems can be excited by a large number of sources such as pumps and compressors, and vibration can propagate along the pipes to excite other structures or equipment. This vibrational energy is transmitted in both the fluid and the structure, and it is the active control of the fluid-borne vibrations that is the subject of this chapter. There has only been a limited amount of work carried out to date in the active control of fluid waves in a pipe. Brévert and Fuller [96] carried out an analytical study into the active control of total power propagating along an infinite fluid-filled pipe using radial line forces. Harper and Leung [86] carried out an experimental study, embedding helical PVDF wires in a rubber section of pipe to control structural waves and using a hydrosounder to control the axisymmetric fluid wave.

Before attempting to control fluid-borne vibrations in a pipe, a thorough understanding of the dynamic behaviour of a fluid-filled pipe is required, and the first part of this chapter reviews the work carried out by other investigators in this area and summarises a previous study carried out by the author [97]. Following this review, the design of a fluid wave actuator is discussed and a theoretical framework is developed to couple such an actuator to a propagating fluid wave in the pipe. A non-intrusive actuator and sensor combination were designed and fitted to a perspex pipe filled with water, and a set of experiments were carried out to see if the control of fluid waves is a practical proposition.

6.2 Dynamic Behaviour of Fluid-Filled Pipes

The dynamic behaviour of a pipe, whether it be *in vacuo* or fluid-filled, falls into two distinct frequency regions which are separated by the ring frequency, ω_o . This is the frequency at which the pipe shell vibrates in a breathing mode and occurs when one wavelength of a longitudinal plate wave (see Appendix 1) equals the circumference of the pipe (shell), i.e., when:

$$\omega_o = \frac{\left(\frac{E_s}{\rho_s(1 - \nu^2)} \right)^{\frac{1}{2}}}{a} \quad (6.1)$$

where E_s is the Young's modulus, ρ_s is the density of the shell, ν is Poisson's ratio and a is the radius of the shell. It is normal convention when considering shell vibrations to normalise frequency ω , to the ring frequency ω_o , so that:

$$\Omega = \frac{\omega}{\omega_o} \quad (6.2)$$

Below the ring frequency in a fluid-filled pipe there are four wave types that propagate energy [98][99]. Three of these wave types are axisymmetric ($n = 0$), the others being flexural wave types ($n = 1, 2, 3, \dots$) in the pipe shell. The mode shapes and coordinate system for a fluid-filled pipe can be seen in **figure 6.1**.

The first two axisymmetric waves involve both structural and fluid motion, and the strength of coupling between these motions is governed by the physical properties and dimensions of the pipe. The

first of these waves is termed $s = 1$ and is predominantly a fluid-based wave with some radial shell motion associated with the shell compliance. The second wave is

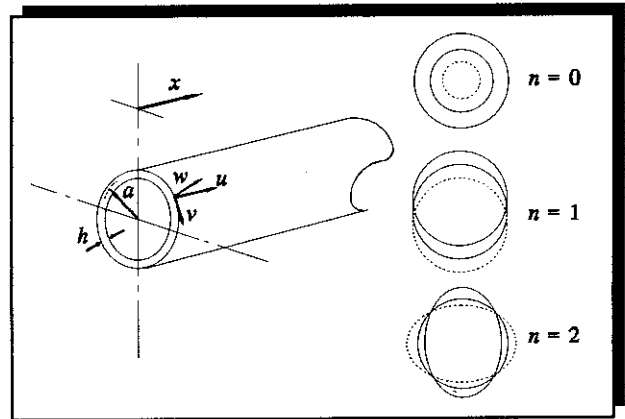


Figure 6.1 Fluid-Filled Pipe Co-ordinate System and Mode Shapes

the $s = 2$ wave and is predominantly a compressional wave in the shell with some associated radial wall motion influenced by Poisson's ratio and fluid loading. The third axisymmetric wave is a torsional shell wave which is uncoupled from the fluid and does not have significant radial motion. The flexural $n = 1$ wave is a beam-like flexural wave as discussed in Appendix 1 and consists of nearfield and dispersive propagating waves. With this wave type, the cross-section of the pipe remains largely undeformed. As the pipe behaves as a Timoshenko beam, at higher frequencies rotary inertia and shear effects become important, and the out-of-plane motion is made up shear waves and non-dispersive bending waves.

The higher order flexural wave-modes ($n \geq 2$) have a helical path with circumferential and axial components. A pipe exhibits wave-guide behaviour and these waves have cut-off frequencies below which they cannot propagate and are discussed in some detail by Fahy [100].

Above the ring frequency, the dynamic behaviour of a fluid-filled pipe is much more complicated and this has been explored at some length by Fuller and Fahy [20]. The $n = 0$ flexural wave can propagate axially, which means that the curvature assumes less structural significance and the dynamic behaviour is similar to that of a flat plate with propagating and nearfield flexural plate waves. Increasing the frequency further leads to more complications such as higher order acoustic modes in the fluid, and shear effects in thick walled shells. In practical pipe-work systems these phenomena occur at relatively high frequencies and it is the low frequency region, well below the ring frequency ($\Omega \ll 1$), that is of concern in this work. At these frequencies the motion of the fluid and the pipe is relatively simple.

Fuller and Fahy [20] showed that at these low frequencies energy is carried in both the axisymmetric and the flexural waves. Low frequency flexural waves ($n = 1$) can be controlled actively, possibly using the control strategies and actuators discussed previously in connection with beams, or by using conventional passive vibration control measures. The majority of energy in the $n = 0$ mode is propagated in the shell or the fluid, depending on whether the excitation is structural or located in the

fluid. There is thus a need to control fluid-borne waves. In a pipe system where the shell is relatively stiff, then this problem is similar to controlling acoustic waves in a duct, and acoustic filters such as a Helmholtz resonator [101], can be used to suppress the propagation of fluid-borne waves. In a soft-walled pipe, where there is strong coupling between the shell and the fluid, active control of the fluid waves by exciting the pipe wall may be more appropriate, and it is this that is discussed in this chapter.

Before considering how fluid waves can be controlled using an actuator, a model of the low frequency behaviour of a fluid-filled pipe is required. Such a model is not developed in this thesis as this has been accomplished by other researchers. However, these models are compared to see if there is general agreement in the understanding of the low frequency dynamic behaviour of fluid-filled pipes. Lin and Morgan [102] developed a model which includes fluid loading, shell bending, transverse shear and rotary inertia. This model is inevitably complicated, but they made approximations to describe the behaviour at low frequencies. They presented four low frequency models catering for various combinations of structure and fluid types. One of these, which is appropriate for a soft-walled pipe filled with fluid, is shown below. The assumption is that $\alpha \psi > 1$ and $\psi < 1$ where:

$$\alpha = \frac{\rho_f a}{\rho_s h} \quad \text{and} \quad \psi = \frac{c_f^2}{c_l^2}$$

and ρ_f and ρ_s are the densities of the fluid and the shell respectively, a is the mean radius of the pipe and h is the pipe thickness. c_f is the speed of sound in the fluid and c_l is the longitudinal wave speed in a slender beam. The wavenumbers of the first two axisymmetric waves are given by:

$$k_1 = \frac{\Omega}{a \left(\frac{1 - \nu^2}{2\alpha} \left\{ 1 - \frac{1 - \nu^2}{2\alpha\psi} \right\} \right)^{\frac{1}{2}}} \quad (6.3)$$

and

$$k_2 = \frac{\Omega}{a \left(1 - \frac{v^2}{2\alpha\psi} \right)^{\frac{1}{2}}} \quad (6.4)$$

where k_1 is the wavenumber of a predominantly fluid based wave and k_2 is the wavenumber of a predominantly shell based wave. More recent work by Pavic [99] resulted in alternative expressions for the low frequency approximations to these wavenumbers. He used Flügge's equations [103] which incorporate fluid loading and shell bending stresses, but neglect transverse shear and rotary inertia. His formulae include fluid loading terms as a power series of Ω , and the derivation of the low frequency wavenumbers involve taking first order approximations to give:

$$k_1 = \left(\frac{1}{\psi} + \frac{(2\alpha + v^2)}{1 - v^2} \right)^{\frac{1}{2}} \frac{\Omega}{a} \quad (6.5)$$

and

$$k_2 = \left(1 + \frac{v^2 \left(\frac{1}{\psi} - 1 \right)}{\left(\frac{1}{\psi} - 1 \right) (1 - v^2) + 2\alpha + v^2} \right)^{\frac{1}{2}} \frac{\Omega}{a} \quad (6.6)$$

Pinnington and Briscoe [98] adopted a different approach than previous investigators. They used simplified Kennard's equations [104] which neglect shell bending, transverse shear and rotary inertia and are thus *only valid below the ring frequency*. The wavenumbers they derived are:

$$k_1 = k_f \left(\frac{1 + \beta - v^2 - \Omega^2}{1 - v^2 - \Omega^2} \right)^{\frac{1}{2}} \quad (6.7)$$

and

$$k_2 = k_{pl} \left(\frac{1 - \Omega^2 + \beta}{1 + \beta - \Omega^2 - v^2} \right)^{\frac{1}{2}} \quad (6.8)$$

where k_f is the fluid wavenumber, k_{pl} is the longitudinal wavenumber in a plate, v is Poisson's ratio and β is the fluid loading term which is given by:

$$\beta = \frac{2Ba}{E_s h} (1 - \nu^2) \quad (6.9)$$

where E_s is the Young's modulus of the pipe and B is the bulk modulus of the fluid. The two wavenumbers derived in the three pieces of work are plotted in **figure 6.2** for a perspex pipe filled with water with the material properties and dimensions given in **Table 6.1** ($\beta = 9.48$ and $\Omega = 5.17$ kHz). a is from [102], b is from [99] and $[c]$ is from [98].

Perspex Pipe

mean radius, a	72.5 mm
pipe thickness, h	5 mm
density, ρ_s	$1.2 \times 10^3 \text{ kg m}^{-3}$
Young's modulus, E_s	$5.6 \times 10^9 \text{ N m}^{-2}$
Poisson's ratio, ν	0.4

Water

Bulk modulus, B	$2.18 \times 10^9 \text{ N m}^{-2}$
Density, ρ_f	$1 \times 10^3 \text{ kg m}^{-3}$

Table 6.1 Material Properties of the Perspex Pipe and Water

It can be seen that there are no discernable differences between models a and b for both wave numbers and there is only a slight deviation in k_1 (a predominantly fluid based wave) in model c derived by Pinnington and Briscoe. This discrepancy is to be expected as only membrane stresses were included in this model and bending stresses were neglected, which limits the bandwidth over which the

model is applicable. The advantage of this model, however, is that it enables

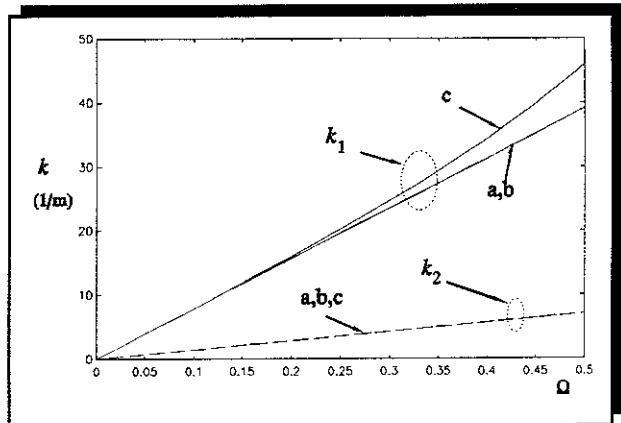


Figure 6.2 Wavenumbers derived by (a) Pavic [99], (b) Lin and Morgan [102] and (c) Pinnington and Briscoe [98] for a water filled perspex pipe, $a = 72.5$ mm and $h = 5$ mm

physical insight into the behaviour of the pipe, which is essential for the design of a non-intrusive fluid wave actuator. Model c is therefore used as the representative model of a fluid-filled pipe for the remainder of this work; it is considered accurate enough for our purposes since only frequencies $< 0.2\Omega$ are of interest. Examining equations (6.7) and (6.8) and figure 6.2 the following observations can be made:

1. The predominantly fluid wave in the pipe is always slower than in an infinite medium as $k_1 > k_f$. The fluid wave decreases in speed with increasing fluid loading, which occurs when the bulk modulus of the fluid is increased or the wall stiffness is decreased.
2. At low frequencies ($\Omega \ll 1$) *and* if the fluid loading is very small ($\beta \ll 1$), then $k_2 \approx k_l$ and the pipe behaves as a simple rod. The radial wall motion is then only controlled by the Poisson's ratio.
3. As the frequency increases such that $\Omega \gg \nu$, *and* if the fluid loading remains very small ($\beta \ll 1$), then the radial wall motion is constrained by inertia effects and the wavenumber becomes slightly lower, i.e., that of a plate (see Appendix 1).
4. The predominantly structural wavenumber k_2 is smaller than the predominantly fluid wavenumber k_1 . The velocities of these two waves for the experimental water-filled perspex pipe, with the properties and dimensions listed in Table 6.1, are predicted to be about 420 ms^{-1} for the fluid wave and about 2400 ms^{-1} for the structural wave. This means that a wavelength in the pipe wall is much larger than in the fluid, and the effect of the fluid is to act a stiffness (controlled by the bulk modulus) and restrict radial wall motion of the pipe. *Thus the $s = 2$ wave will not have large radial motion.*

Four equations describe the axisymmetric motion of a fluid-filled *semi-infinite* pipe, such as that shown in figure 6.1, where wave propagation is in the positive x direction only. Suppressing the $e^{j\omega t}$ time dependence for clarity, the axial motion of

the pipe is given by:

$$u(x) = U_1 e^{-jk_1 x} + U_2 e^{-jk_2 x} \quad (6.10a)$$

The radial motion of the pipe is given by:

$$w(x) = W_1 e^{-jk_1 x} + W_2 e^{-jk_2 x} \quad (6.10b)$$

and the axial motion and pressure of the fluid are given by:

$$u_f(x) = U_{f1} e^{-jk_1 x} + U_{f2} e^{-jk_2 x} \quad (6.10c)$$

and

$$p(x) = P_1 e^{-jk_1 x} + P_2 e^{-jk_2 x} \quad (6.10d)$$

Pinnington and Briscoe [98] derived some basic expressions relating pressure and radial and axial wall motion for the $s = 1$ and 2 waves, and these are given below without proof. The reader is referred to the reference for further details. The relationship between fluid pressure and radial wall motion are given by:

$$W_1 = \frac{P_1 a^2}{h E_s} \left(\frac{1}{1 - \frac{\Omega^2}{1 - \nu^2}} \right) \quad s = 1 \quad (6.11)$$

$$W_2 = \frac{-P_2 a}{2B} \quad s = 2 \quad (6.12)$$

These can be combined to give the ratio of the radial wall motions in terms of the pressure waves for the two wave types:

$$\frac{W_1}{W_2} = -\mu \frac{P_1}{P_2} \quad (6.13)$$

where

$$\mu = \frac{\beta}{1 - \nu^2 - \Omega^2}$$

μ ranges from about 11 to 12 for the experimental water-filled perspex pipe used in this thesis, over the frequency range 0 to 1 kHz. The axial motions are related to the

radial motion by:

$$U_1 = \frac{-j\nu W_1}{k_1 a} \quad s = 1 \quad (6.14)$$

and

$$U_2 = \frac{-jW_2(1 + \beta - \Omega^2)}{\nu k_2 a} \quad s = 2 \quad (6.15)$$

These can be combined to give the ratio of the radial wall motions in terms of the axial motions for the two wave types:

$$\frac{W_1}{W_2} = \frac{1}{\chi} \frac{U_1}{U_2} \quad (6.16)$$

where

$$\chi = \left(\frac{\nu^2}{1 + \beta - \Omega^2} \right) \frac{k_2}{k_1}$$

χ is approximately equal to 0.003 for the experimental water-filled perspex pipe over the frequency range 0 to 1 kHz. If the shell is excited and there is no separate excitation of the fluid, which has a free surface, then the pressure at the end of the pipe is zero and $P_1 = -P_2$. Thus equation (6.13) reduces to:

$$\left[\frac{W_1}{W_2} \right]_s = \frac{\beta}{1 - \nu^2 - \Omega^2} \quad (6.17)$$

where the s denotes excitation of the shell. It should be noted that for structural excitation of the experimental pipe, the ratio of the radial wall motions ranges from about 11 to 12. If the fluid is excited instead of the pipe at the free end, then there is no axial stress in the pipe wall at the free end. Now the axial stress at any point in the shell is given by [98]:

$$\sigma(x) = -j\rho\omega^2 \left(\frac{U_1 e^{-jk_1 x}}{k_1} + \frac{U_2 e^{-jk_2 x}}{k_2} \right) \quad (6.18)$$

If this is set to zero, then

$$\left[\frac{U_2}{U_1} \right]_f = -\frac{k_2}{k_1} \quad (6.19)$$

where f denotes excitation of the fluid. This can be combined with equation (6.16) to give the ratio of the radial wall motions in terms of the pressure waves for the two wave types when the fluid is excited alone:

$$\left[\frac{W_1}{W_2} \right]_f = -\left(\frac{k_1}{k_2} \right)^2 \left(\frac{1 + \beta - \Omega^2}{\nu^2} \right) \quad (6.20)$$

The energy e_1 of the $s = 1$ wave per unit length of the pipe is given by [98]:

$$e_1 \approx \bar{P}_1^2 \frac{\pi a^2}{\rho_f c_1^2} \quad (6.21)$$

where \bar{P}_1^2 is the spatially averaged mean square pressure along the length of the pipe. The energy e_2 of the $s = 2$ wave per unit length of the pipe is given by [98]:

$$e_2 \approx \bar{U}_2^2 \omega^2 2\pi a h \rho \quad (6.22)$$

where \bar{U}_2^2 is the spatially averaged mean square axial displacement. Equations (6.11), (6.15), (6.21) and (6.22) can be combined to give the ratio of the energies in the two waves:

$$\frac{e_1}{e_2} \approx \left| \frac{W_1}{W_2} \right|^2 \frac{\nu^2(1 - \nu^2)}{\beta(1 + \beta)^2} \quad (6.23)$$

The ratio of the energy in the two waves can be calculated for (a) the case when the pipe is structurally excited or (b) when the fluid is excited by substituting for the ratios of the radial displacements in each case given in equations (6.17) and (6.20). A typical value of the energy ratio for the water-filled perspex pipe with the properties depicted in **Table 6.1** can be seen along with other variables in **Table 6.2**.



			$\left \frac{W_1}{W_2} \right $	$\left \frac{U_1}{U_2} \right $	$\left \frac{P_1}{P_2} \right $	$\frac{e_1}{e_2}$
	structural	(a)	11	0.03	1	0.016
	excitation	(b)	12	0.03	1	0.018
	fluid	(a)	2020	5.6	178	526
	excitation	(b)	2060	5.6	178	551

Table 6.2 Ratios of Variables due to the "Fluid" Wave to those due to the "Structural" Wave for Different Excitations of the Experimental Water-Filled Perspex Pipe at a Frequency of (a) 10 Hz and (b) 1 kHz

Equations (6.11), (6.17) and (6.20) are the important equations in the design of a non-intrusive fluid actuator and sensor. *The key to the design is that the dynamic radial wall motion of a pipe is strongly coupled to the dynamic pressure of the fluid in the pipe.* Equation (6.11) shows that the pressure in a pipe is related to the radial wall motion. It can be further seen that for an actuator that squeezes a pipe and hence induces radial wall motion, it is better to have a large value of W_1 and hence to use a soft-walled pipe (small E_s) and a large pipe radius to wall thickness ratio (large a/h). For this type of actuator, it is desirable not to excite the structural $s = 2$ wave and equations (6.17) and (6.20) show that a high fluid loading ensures that the radial motion of the shell is predominantly due to the $s = 1$ wave alone. Thus a large diameter thin-walled perspex pipe containing a fluid such as water might be an appropriate pipe system for an fluid wave actuator. For example a water-filled perspex pipe with dimensions and properties as described in **Table 6.1** and excited on the shell, the ratio W_1/W_2 in the frequency range 10 Hz to 1 kHz calculated using equation (6.17), is between 11 and 12, as discussed above. For fluid excitation W_1/W_2 over the same frequency range calculated using equation (6.20) is between 2020 and 2060 as shown in **Table 6.2**. Examination of this table shows that if the fluid is excited then the energy carried in the predominantly fluid wave is significantly more than the energy carried in the predominantly structural wave. Thus there is

much to be gained by actively controlling the fluid wave.

6.3 Design of a Fluid Wave Actuator

6.3.1 Theory

One design of non-intrusive fluid wave actuator involves the application of an external pressure to a section of the pipe to induce motion of the pipe wall and hence generate a pressure inside the pipe. Before considering the relatively complicated situation of a fluid filled pipe, the static radial motion of an *in vacuo* pipe by an external

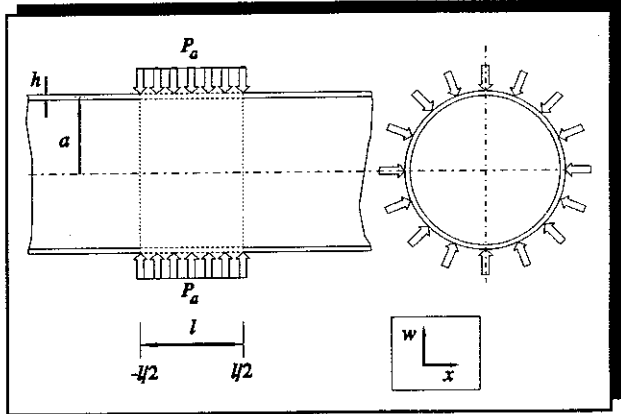


Figure 6.3 Application of an External Pressure to an infinite *In Vacuo* Pipe

pressure is examined. This situation is depicted in **figure 6.3** and has been discussed by Flügge [103]. **Figure 6.3** shows an infinite pipe with a uniform pressure applied to a section of length l . Flügge [103] derived expressions relating the radial displacement w , of an infinite pipe to the applied pressure P_a . There are two expressions; one for the section of pipe where the pressure is applied and one for the sections of pipe either side of this. These are:

for $-l/2 \leq x \leq l/2$

$$\frac{w}{P_a} = \frac{-a^2}{E_s h} \left(1 - e^{\frac{-lv}{2a}} \left(\cos \frac{vl}{2a} \cosh \frac{vx}{a} \cos \frac{vx}{a} + \sin \frac{vl}{2a} \sinh \frac{vx}{a} \sin \frac{vx}{a} \right) \right) \quad (6.24)$$

for $x < -l/2$ and $x > l/2$

$$\frac{w}{P_a} = \frac{-a^2}{2E_s h} e^{\frac{-v x}{a}} \left(e^{\frac{v l}{2a}} \cos \frac{v \left(x - \frac{l}{2} \right)}{a} - e^{\frac{-v l}{2a}} \cos \frac{v \left(x + \frac{l}{2} \right)}{a} \right) \quad (6.25)$$

where

$$v = \left(3(1 - \nu^2) \frac{a^2}{h^2} \right)^{\frac{1}{4}}$$

v is approximately 4.8 for the experimental pipe used in this work. Thus if $l \approx 2a$, then $e^{-lv/2a} \approx 0.008$. It is clear that equations (6.24) and (6.25) are complicated and it is worth considering whether any approximations can be made before proceeding to an analysis of the dynamic behaviour of a fluid-filled pipe. If only the first term of equation (6.24) is used (which is a reasonable approximation if $l = 2a$, since $e^{-lv/2a} \approx 0.008$), then the resulting expression is for a simple ring [103], and it can be seen from equation (6.25) that the radial displacement of the pipe away from the pressure region decays away exponentially, falling to about 0.00007 of its initial value over a distance equal to one pipe diameter, and can thus be set to zero. This approximation results in:

for $-l/2 \leq x \leq l/2$

$$\frac{w}{P_a} = \frac{-a^2}{E_s h} \quad (6.26)$$

for $x < -l/2$ and $x > l/2$,

$$\frac{w}{P_a} = 0 \quad (6.27)$$

and correspond to a simple ring fitted to a pipe that responds to an

external pressure. To compare the approximation with the complete solution, equations (6.24) - (6.27) are plotted in figure 6.4 for which $l = 60$ mm and the pipe having the properties shown in Table 6.1. It can be seen from figure 6.4 that although there are differences between the complete model and the approximate

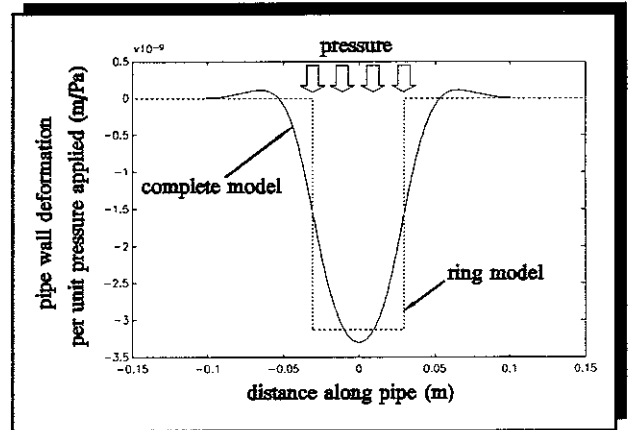


Figure 6.4 Comparison Between the Actual Radial Displacement and Approximate Radial Displacement of a Pipe due to External Pressure Loading

"ring" model, in terms of the *average* radial displacement of the pipe wall there is little difference between the two models. As the ring model is very simple and can thus be easily incorporated into a dynamic model of a fluid-filled pipe it was decided to proceed with the analysis using this model.

The receptance approach was used in the modelling of the fluid wave actuator, as this enabled the ring and the fluid contained in the ring to be modelled in isolation and then coupled to the pipe through the state vector of pressure and axial displacement of the fluid. In effect this is an active ring coupled to two

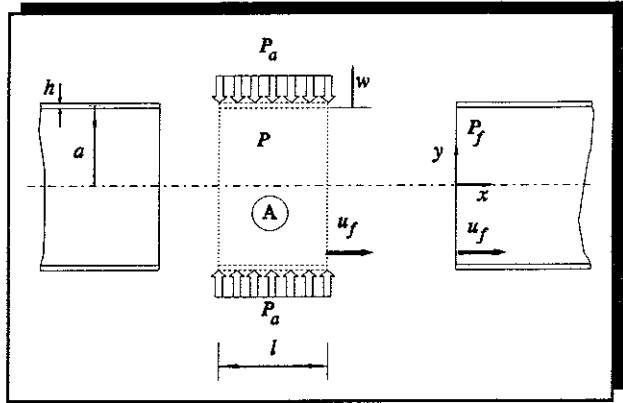


Figure 6.5 Fluid wave Actuator

semi-infinite pipes. The system can be seen in **figure 6.5**. The applied pressure P_a causes radial wall motion of the pipe, w which in turn induces a pressure P in the section of pipe labelled A. This pressure is assumed to be uniformly distributed at any given frequency and causes the fluid to displace u_f at the interface between the active and passive sections of pipe. These variables can be related using the matrix equation:

$$\begin{bmatrix} w \\ u_f \end{bmatrix} = \begin{bmatrix} \alpha_{11} & \alpha_{12} \\ \alpha_{21} & \alpha_{22} \end{bmatrix} \begin{bmatrix} P_a \\ P_f \end{bmatrix} \quad (6.28)$$

where the α 's are complex frequency dependent receptance functions. The relationship between the pressure and the displacement of the fluid at the interface is given by:

$$u_f = \alpha_f P_f \quad (6.29)$$

where α_f is the compliance of the fluid. Noting that at the interface between the actuator and the pipe, $P_f = P$, equations (6.28) and (6.29) can be combined to give the relationship between the generated pressure in the pipe P_f and the applied pressure P_a :

$$\frac{P_f}{P_a} = \frac{\alpha_{21}}{\alpha_f - \alpha_{22}} \quad (6.30)$$

The relationship between the radial shell motion w and the axial displacement of the fluid u_f , at the interface between the active and passive sections of pipe can be determined as follows. Assuming that the volume of fluid in the active section is incompressible and that $a/h \gg 1$, the swept volume of the ring section is given by:

$$V = \pi l(a^2 - (a + w)^2) \quad (6.31)$$

and this displaces a volume of fluid:

$$V = 2\pi a^2 u_f \quad (6.32)$$

assuming that $w \ll a$ then equations (6.31) and (6.32) combine to give the relationship between radial pipe wall motion and axial displacement of the fluid:

$$w = \frac{-a}{l} u_f \quad (6.33)$$

To determine the relationship between the generated pressure in the pipe and the applied pressure, the α 's in equation (6.30) need to be found. Referring to equation (6.28), the function α_{21} is defined as:

$$\alpha_{21} = \left. \frac{u_f}{P_a} \right|_{P_f=0} \quad (6.34)$$

There are three components of the receptance, namely the mass of the ring, the stiffness of the ring and the inertia of the fluid contained within the ring. It is more

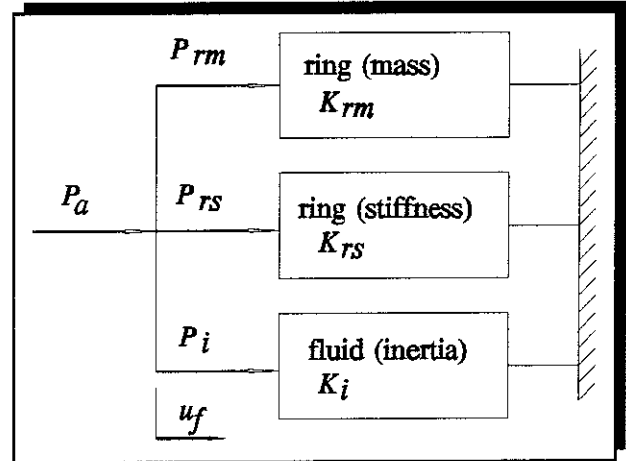


Figure 6.6 Dynamic Stiffness of the Ring and Contained Fluid

convenient to describe these individual effects in terms of dynamic stiffness as shown in **figure 6.6**, and then combine them before inverting to give the receptance. The relationship between the receptance in terms of the axial fluid motion, and the

combination of dynamic stiffnesses is given by:

$$\alpha_{21} = \frac{1}{K_{rm} + K_{rs} + K_i} \quad (6.35)$$

where K_{rm} is the mass component of the dynamic stiffness of the ring, K_{rs} is the stiffness component of the dynamic stiffness of the ring and K_i is the dynamic stiffness of the fluid. These can be determined using Newton's second law, Hooke's law and the relationship between w and u given in equation (6.30). The ring's mass component is given by:

$$K_{rm} = \frac{P_{rm}}{u_f} = \frac{-\omega^2 \rho_s h a}{l} \quad (6.36)$$

The ring's stiffness component is given by:

$$K_{rs} = \frac{P_{rs}}{u_f} = \frac{E_s h}{a l} \quad (6.37)$$

For a perspex pipe filled with water with the properties as described in Table 6.1, the total dynamic stiffness is dominated by the stiffness of the ring over the frequency range 10 Hz to 1 kHz. The mass of the ring and the inertia of the fluid contained in the ring are insignificant over this frequency range and thus the approximate receptance α_{21} is given by:

$$\alpha_{21} \approx \frac{1}{K_{rs}} = \frac{a l}{E_s h} \quad (6.38)$$

The other receptance associated with the ring is defined as:

$$\alpha_{22} = \left. \frac{u_f}{P_f} \right|_{P_a=0} \quad (6.39)$$

Now, the magnitude of the axial motion of the fluid at the interface between the actuator and the pipe is the same whether a pressure is applied at that interface or whether the pressure is applied externally to the pipe. The direction of the motion is, however, opposite in sense, thus:

$$\alpha_{21} = -\alpha_{22} \quad (6.40)$$

It was shown by Pinnington and Briscoe [98] that for a semi-infinite soft-walled pipe such as the one being considered, the dynamic compliance of the fluid is governed by the $s = 1$ wave and is given by:

$$\alpha_f \approx \frac{-jk_1}{\rho_f \omega^2} \quad (6.41)$$

where k_1 is given by equation (6.7). Noting that $k_1 = \omega/c_1$, where c_1 is the phase speed of the $s = 1$ wave, then:

$$\alpha_f \approx \frac{-j}{\omega \rho_f c_1} \quad (6.42)$$

which is the characteristic compliance of the fluid in a soft-walled pipe. Combining equations (6.30), (6.40) and (6.42) gives the relationship between the generated pressure in the pipe and the applied pressure:

$$\frac{P_f}{P_a} = \frac{1}{\frac{\alpha_f}{\alpha_{21}} + 1} = \frac{1}{1 - j \frac{E_s h}{\omega \rho_s c_1 a l}} \quad (6.43)$$

This shows that the generated pressure is dependent primarily upon two factors; the stiffness of the ring and the characteristic compliance of the fluid in the pipe. It should be noted that the compliance of the ring is approximately constant over the frequency range of interest and the compliance of the fluid reduces with frequency. If the ring is comparatively stiff (α_{21} small compared with α_f), then the ratio between the generated pressure and the applied pressure is very small. This will generally

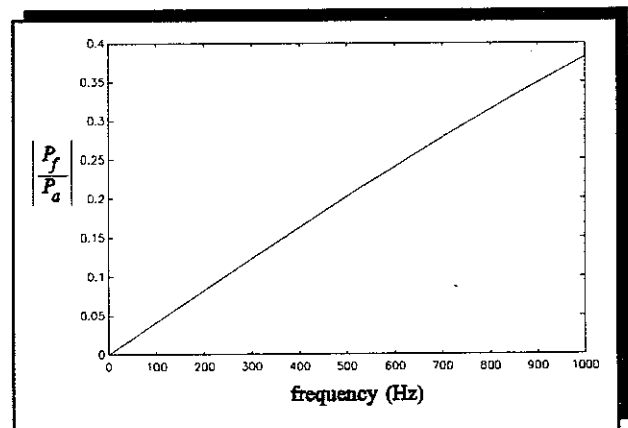


Figure 6.7 Ratio of Internal to Applied Pressure for the Water-Filled Perspex Pipe

occur at low frequencies or if the fluid has low density or bulk modulus. Equation (6.43) is the key equation in the design of a fluid wave actuator, and is plotted in figure 6.7 for the pipe with the properties in Table 6.1 with $l = 60$ mm.

6.3.2 Potential Types of Actuator

Two methods of applying a pressure P_a are examined theoretically. To simplify matters a static analysis is carried out, and the measure by which the two methods are judged is the maximum radial displacement of the ring that can be achieved. The first technique involves attaching several turns of PVDF wire around the pipe which expand and contract in response to an alternating voltage. The displacement of a ring with one turn of PVDF wire, as shown in figure 6.8, is examined and to keep the analysis simple, the width of the ring is

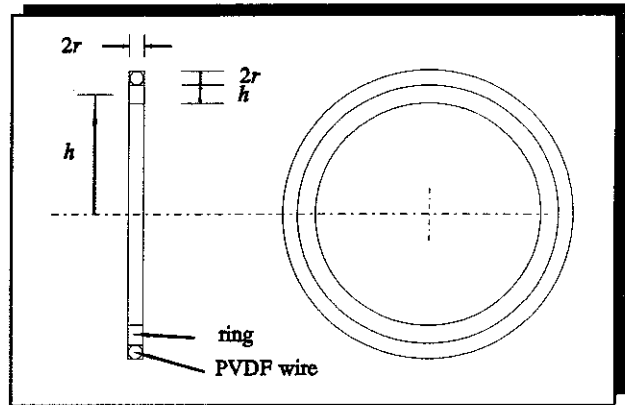


Figure 6.8 PVDF Actuator Fitted to a Ring

assumed to be equal to the diameter of the PVDF wire. The combination of the PVDF wire and the glue used to bond it to the ring is considered to have a square cross-section with a length equal to the radius of the PVDF wire as can be seen in figure 6.8. An equivalent representation of the actuator and the ring is shown in figure 6.9, where K_r is the stiffness of the ring and K_a is the stiffness of the PVDF actuator. P_a , the maximum pressure that can be generated by the actuator, can be found by applying Newton's Third law, and is given by:

$$P_a = -\sigma_a \frac{2r}{a} \quad (6.44)$$

where σ_a is the longitudinal stress in the PVDF wire and is related to the voltage applied, by the piezoelectric equations given in Chapter 4, i.e:

$$\sigma_a = \frac{-d_{31} V}{r} E_p \quad (6.45)$$

where d_{31} is the piezoelectric constant, V is the voltage applied and E_p is the Young's modulus of the PVDF wire. Referring to **figure 6.9**, the relationship between the pressure generated by the PVDF wire P_a and the pressure applied to the ring P_{rs} is given by:

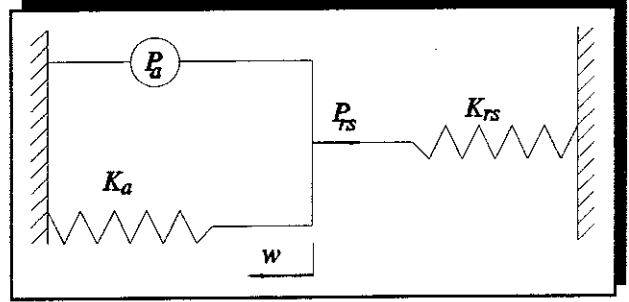


Figure 6.9 Equivalent Representation of a PVDF Wire Actuator Fitted to a Ring

$$P_{rs} = \frac{P_a K_{rs}}{K_{rs} + K_a} \quad (6.46)$$

Assuming that the radius of the ring is much bigger than the thickness of the ring and the diameter of the PVDF wire ($a \gg h$), these stiffnesses are given by:

$$K_{rs} = \frac{E_s h}{a^2}, \quad K_a = \frac{E_a 2r}{a^2} \quad (6.47a, b)$$

Applying Hooke's law and using equation (6.46) gives the radial displacement of the ring:

$$w = \frac{-P_a}{K_{rs} + K_a} \quad (6.48)$$

Substituting for P_a in equation (6.48), using equations (6.45) and (6.46) and noting the expressions for the stiffnesses of the ring and the PVDF actuator given in equation (6.47) gives, after rearranging, the expression relating the radial displacement of the ring as a function of the voltage applied.

$$w = \frac{\frac{-d_{31} V}{r} a}{\frac{K_{rs}}{K_a} + 1} \quad (6.49)$$

This shows that the radial displacement of the ring is dependent upon the relative stiffnesses of the PVDF actuator and the ring. If the ring is very much stiffer than the PVDF wire then a much greater voltage is required to induce radial strain in the ring. It should be noted that equation (6.49) assumes that there is perfect bonding between the PVDF wire and the ring. Typical properties of PVDF wire are given in **Table 6.3**.

PVDF Wire (Kynar Piezo Cable [105])

radius, r	0.325 mm
density, ρ_p	$1.89 \times 10^3 \text{ kg m}^{-3}$
Young's modulus, E_p	$2.3 \times 10^9 \text{ N m}^{-2}$
Piezoelectric Constant, d_{31}	$20 \times 10^{-12} \text{ V m}^{-1}$

Table 6.3 Properties of PVDF Wire

If a PVDF wire actuator is bonded to a perspex ring with properties as described in **Table 6.1**, the relationship between the radial displacement and the voltage applied is **0.23 $\mu\text{m/kV}$** . For the water-filled perspex discussed in this chapter this results in the relationship between the pressure and the applied voltage for an active length of pipe of 60 mm of between 0 and 500 Pa kV^{-1} over the frequency range 0 to 1 kHz. This means that large voltages are required to induce even small radial displacements in the ring and hence pressure in the pipe. A major difficulty encountered in practice is that it is very difficult to achieve a good bond between the PVDF wire and the perspex ring. This is because the PVDF core is covered with a copper braided sheath which in turn is covered with a polyurethane film. Thus it was not considered

practical to use PVDF wire as the active element in a fluid wave actuator on a perspex pipe. It is noted, however, that PVDF wire elements have been used as an actuator fitted to a rubber pipe [86], but voltages of about 8 kV were required in practice.

The second type of actuator considered was a hydraulic device, where a steel shell was fitted to the outside of the pipe forming a small annular cavity that was filled with water. A magnetostrictive actuator was used to drive a piston

that excited the water entrapped in this cavity which in turn applied a dynamic pressure externally to a section of the pipe. A magnetostrictive actuator was chosen as it has a large force capacity and a reasonable displacement capacity (the

specification for the actuator used in this work is given in Appendix 4). The actuator assembly can be represented schematically as shown in **figure 6.10**, where the fluid in the pipe has again been omitted for simplicity. In **figure 6.10** K_{rs} is the stiffness of the shell, S_1 is the area of the piston driven by the magnetostrictive actuator, S_2 is the surface area of the pipe over which the entrapped fluid in the cavity acts. f is the force generated by the actuator and x is the displacement of the actuator. The two limiting factors of an actuator are the force and the displacement capacity and these must be considered when designing an actuator such as that shown in **figure 6.10**. If the inertia effect of the entrapped fluid is neglected, the relationship between the pressure in the fluid and the applied force is given by:

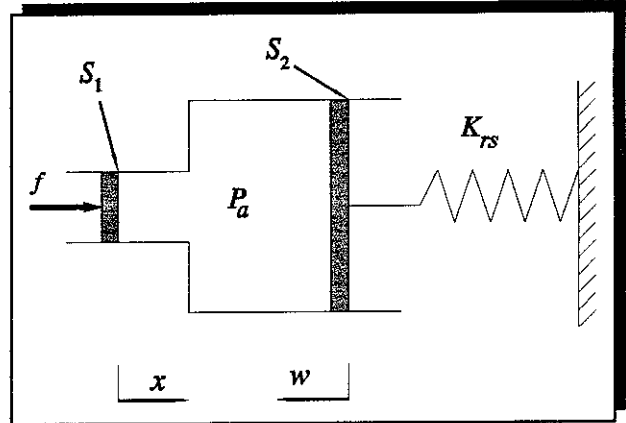


Figure 6.10 Representation of a Hydraulic Actuator Driven by a Magnetostrictive Actuator

$$P_a = \frac{f}{S_1} \quad (6.50)$$

and the application of Hooke's law gives:

$$P_a = -K_{rs} w \quad (6.51)$$

The relationship between the displacement of the actuator and the displacement of the ring is given by:

$$w = -\frac{S_1}{S_2} x \quad (6.52)$$

Combining equations (6.50) - (6.52) gives the ratio of the required actuator force to the required actuator displacement:

$$\frac{f}{x} = \frac{S_1^2}{S_2} K_{rs} \quad (6.53)$$

which relates the "capacity" of the actuator to the stiffness of the ring, the area of the piston and the area over which the pressure is applied to the outside of the pipe. Noting that K_{rs} is given by equation (6.47a) and that $S_2 = 2\pi a l$ where l is the width of the fluid actuator, then an upper bound can be found for the area of the actuator piston S_1 if the full displacement capacity of the actuator is to be used. If it is assumed that the piston has a radius R then this inequality can be written in terms of the piston's radius:

$$R \leq \left(\frac{f}{x} \frac{2a^3}{E_s h \pi} \right)^{\frac{1}{4}} \quad (6.54)$$

For a perspex pipe with the properties described in Table 6.1 and using a magnetostrictive actuator with a force capacity of 490 N and displacement capacity of

20 μm , this results in the upper bound for R of 120 mm. This, however, maybe difficult to achieve in practice and is governed by the detailed design of the actuator assembly which is shown schematically in figure 6.11. The design constraints were as follows:

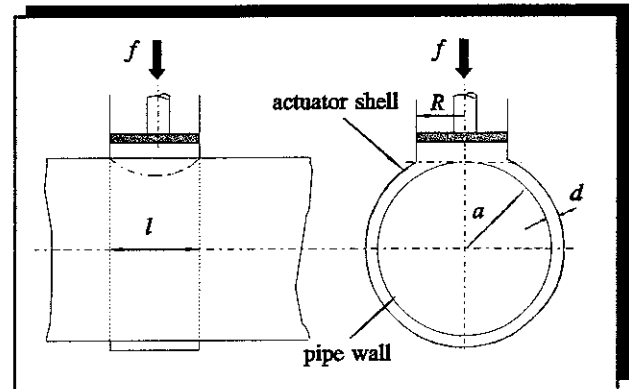


Figure 6.11 Line Diagram of the Fluid Wave Actuator

1. The actuator shell should be much stiffer than the pipe wall.
2. The annular gap between the pipe and the actuator shell should be kept small to minimise the inertia effects of the entrained fluid.

Assuming that the pipe radius is large compared to the thickness of the pipe, the approximate relationship between the piston radius, the pipe radius and the annular gap is given by:

$$R \approx ((a + d)^2 - d^2)^{1/2} \quad (6.55)$$

For a 3 mm gap, an actuator shell thickness of 5 mm and a mean pipe radius of 72.5 mm then $R = 35$ mm. Allowing for a cylinder wall thickness of 5 mm, a piston radius of 30 mm is required which results in a maximum pipe wall displacement of $2 \mu\text{m}$. The length of the actuator is twice the radius of the piston and is therefore 60 mm. A detailed design was undertaken and the engineering drawings can be found in Appendix 4.

6.4 Design of a Fluid Wave Sensor

A non-intrusive transducer to sense axial motion of fluid in a pipe would complement the fluid wave actuator described above. A PVDF wire sensor bonded to the surface of a pipe has been designed by Pinnington and Briscoe [98] and was, in fact, the motivation for the

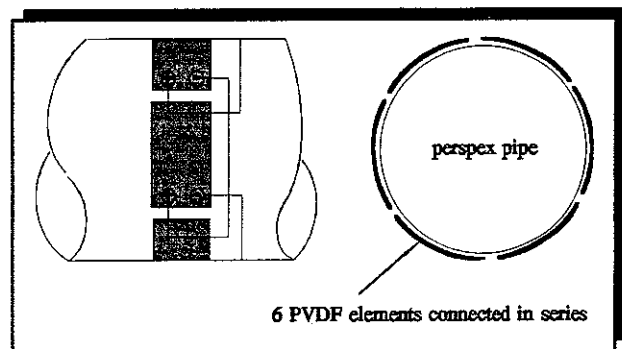


Figure 6.12 A PVDF Fluid Wave Sensor

study of the fluid wave actuator discussed in this chapter. A similar arrangement was considered in this work, but PVDF film rather than wire was used since it was more readily available. Six elements were fitted to a perspex pipe using double sided tape and connected in series as shown in **figure 6.12**. This sensor works on a reciprocal

basis to the actuator. It is based on the principle that the radial wall motion of the pipe is caused predominantly by the fluid wave (equations (6.17) and (6.20)), and not the compressional structural wave. The series connected PVDF elements act as a spatial filter, in that they are sensitive to axisymmetric motion of the pipe, but not the flexural $n = 2, 3, \dots$ modes. Strains of the same sign in each of the elements sum and strains of opposite sign subtract and hence cancel. This means that the sensitivity of the sensor is the sum of the sensitivities of each of the elements. The sensitivity expression of a single PZT element in terms of voltage generated per longitudinal strain was derived in Chapter 4 and is the same for a PVDF element. From the equations derived in Chapter 4, the sensitivity for the sensor in terms of circumferential strain is given by:

$$\frac{V}{\epsilon} = \frac{6 d_{31} E_p b l}{C} \quad (6.56)$$

where d_{31} is the piezoelectric constant, E_p is the Young's modulus of the PVDF film, b and l are the breadth and length of a single PVDF element and C is the capacitance of one element. Noting that equation (6.11) can be written in terms of circumferential strain, assuming that the radial motion of the pipe due to the $s = 2$ wave is negligible and that $\omega \ll \Omega$, then the circumferential strain can be written in terms of the pressure as:

$$\epsilon = \frac{W}{a} = \frac{P a}{h E_s} \quad (6.57)$$

Combining equations (6.56) and (6.57), the sensitivity equation can therefore be written in terms of voltage generated as a function of pressure in the pipe:

$$\frac{V}{P} = \frac{6 d_{31} E_p b l}{C} \frac{a}{h E_s} \quad (6.58)$$

The average capacitance of the elements was measured to be 1.3×10^{-9} F. Using the properties of the PVDF elements listed in Table 6.4 and a perspex pipe with properties listed in Table 6.1, gives a sensitivity of **0.72 mV Pa⁻¹**.

PVDF Film Elements [105]

Young's modulus, E_p	$2.5 \times 10^9 \text{ N m}^{-2}$
density, ρ_p	$1.728 \times 10^3 \text{ kg m}^{-3}$
breadth, b	15 mm
length, l	70 mm
thickness	52 μm
Piezoelectric constant, d_{31}	$23 \times 10^{-12} \text{ V m}^{-1}$

Table 6.4 Material Properties of PVDF Film Elements

6.5 Experimental Design

Having established that the active control of fluid waves could be achieved in principle, it was decided to carry out a series of experiments using a non-intrusive actuator and sensor to control fluid waves in a pipe. The aims of the experiments were:

1. To test the effectiveness of a practical non-intrusive fluid wave actuator.
2. To test the effectiveness of a non-intrusive fluid wave sensor.
3. To see if the combination of an actuator and sensor could be used to actively control fluid waves in a pipe.

The experimental set up is shown in **figure 6.13**. A 2.5 m water-filled perspex pipe of 150 mm outside diameter and 140 mm inside diameter was chosen for the experiments, as its circumferential stiffness was relatively small which resulted in a fairly high fluid loading. The radial pipe-wall motion was thus well coupled to the fluid motion. It was decided to try and make an anechoic termination for the two wave types at the bottom of the pipe to avoid longitudinal resonances in the pipe and

the fluid, and this required two measures; a structural termination and an acoustic termination. Part of the acoustic termination consisted of an exponentially shaped piece of foam rubber placed inside the pipe, and the termination for the pipe *and* the fluid consisted of fitting a resiliently supported damped plate to the bottom of the pipe in a similar manner to that described by Horner [106].

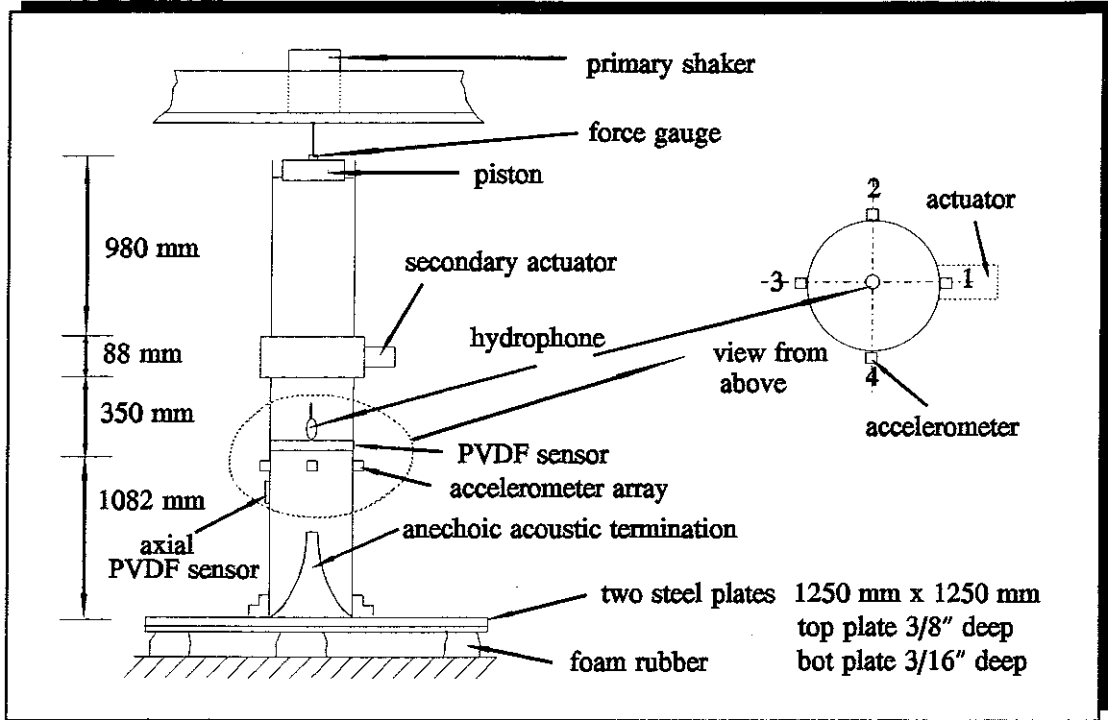


Figure 6.13 Active Control of Fluid waves - Experimental Set Up

The principle behind using a plate as an anechoic termination is one of impedance matching. If the impedance of the termination is similar to that of the pipe and the fluid it contains then energy can be transferred from the pipe to the termination and thus reflections will be minimised. A plate was used as the termination, since it is known that an infinite plate has a frequency independent mechanical input impedance, which, to a first approximation, is the characteristic of a semi-infinite fluid-filled pipe. The impedance of an infinite plate is given by [106]:

$$Z_{pl} = 8 \sqrt{\frac{E_{pl} \rho_{pl} h^4}{12(1 - \nu^2)}} \quad (6.59)$$

where E_{pl} is the Young's modulus of the plate, ρ_{pl} is the density of the plate, h is the

plate thickness and ν is Poisson's ratio. *To a first approximation*, the impedance of a fluid-filled pipe of outside radius r_o and inner radius r_i is the sum of the impedances of the fluid contained in the pipe and the pipe itself, i.e:

$$Z_p = Z_{\text{fluid}} + Z_{\text{pipe}} \quad (6.60)$$

where

$$Z_{\text{fluid}} \approx \rho_f c_1 \pi r_i^2 \quad \text{and} \quad Z_{\text{pipe}} \approx \rho_s c_2 \pi (r_o^2 - r_i^2)$$

and c_1 is the phase speed of the $s = 1$ wave and c_2 is the phase speed of the $s = 2$ wave. The calculated impedances were $Z_{\text{fluid}} = 6895 \text{ N s m}^{-1}$ and $Z_{\text{pipe}} = 6388 \text{ N s m}^{-1}$, so it can be seen that the pipe and the fluid had similar impedances. Equating equations (6.59) and (6.60) results in a plate thickness of about 12 mm. Clearly an infinite plate is not a practical proposition so a damped finite plate was used, with dimensions such that at the lowest frequency of interest (100Hz), the width of the plate (1250 mm) was equal to two flexural wavelengths. The plate was damped using a squeeze film damping method as described by Chow and Pinnington [107]. This involved bolting two plates together, one half the thickness of the other, the thicker plate being attached to the pipe. The damping mechanism is caused by the high velocity pumping of the air between the plates so that energy is dissipated due to the viscosity of the air. The two plates chosen for the experiment did not meet the exact specification, but were cut from available sheet steel and measured 1250 mm square; the top plate was 3/8" thick and the bottom plate 3/16" thick giving a total thickness of 14.3 mm. The pipe was fixed to an aluminium end cap using epoxy resin, and the end cap was attached to the thicker plate with six bolts.

The final part of the experimental rig preparation was to fit PVDF sensors to the pipe to measure radial and axial motion of the pipe-wall. Four small accelerometers were also fitted to give a measure of the pipe vibration, as shown in **figure 6.14**. A photograph of the experimental rig is shown in **Plate 6.1** and photographs of the secondary actuator and sensors are shown in **Plates 6.2** and **6.3**.

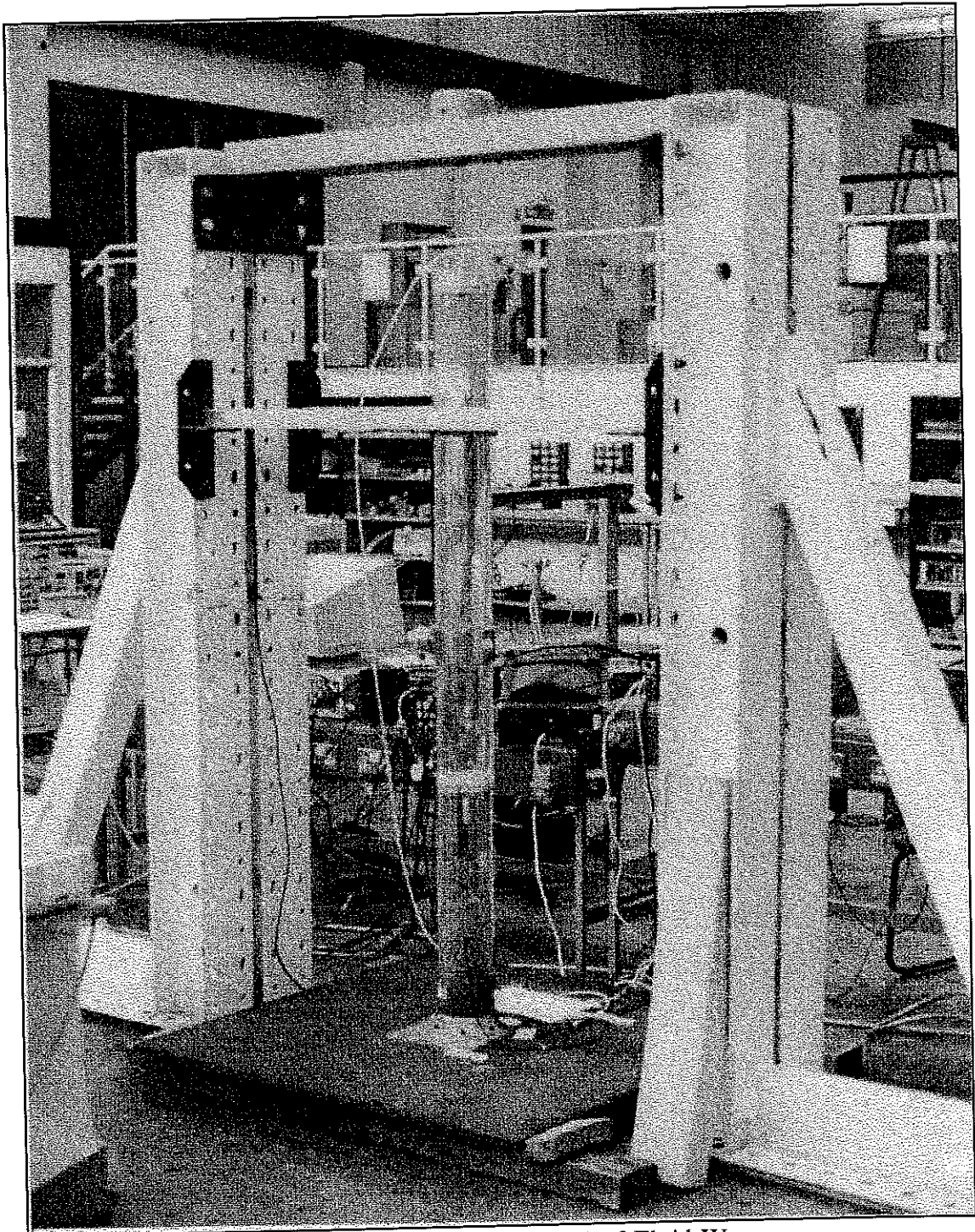


Plate 6.1 Experimental Rig used for the Control of Fluid Waves

The experimental rig was constructed so that a primary shaker fitted at the top of the pipe could excite the pipe and the fluid separately, and the applied force measured. This involved using a thin rod to connect the shaker to a stiff, light piston made from a honeycomb material. The piston used to excite the fluid had a diameter 20 mm less than the inside diameter of the pipe and was made into a sealed unit using waterproof tape. The piston used to excite the pipe was cut larger than the pipe diameter and the connection to the pipe involved placing petroleum jelly between the piston and the pipe. Prior to filling the pipe with water, the secondary actuator was fitted to the pipe using epoxy resin and the annular cavity in the actuator filled with boiled water and a wetting agent. Air bubbles were then carefully expelled from the cavity as this was essential for the correct operation of the actuator.

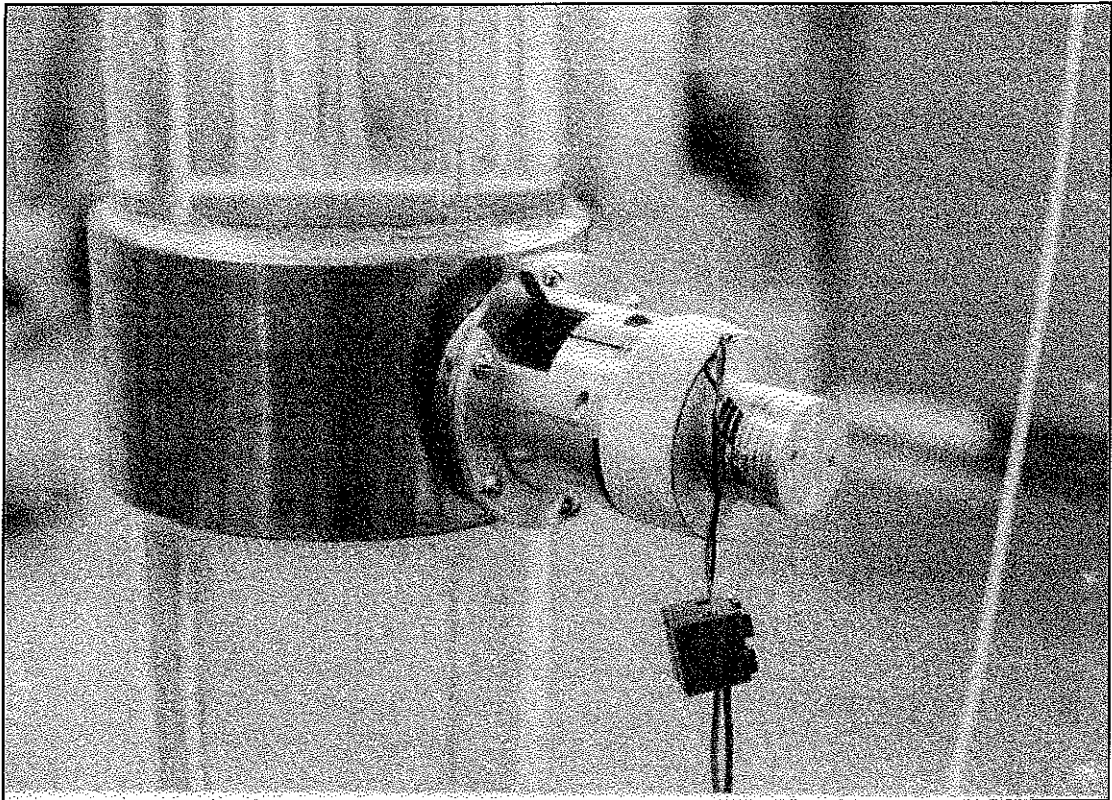


Plate 6.2 The Fluid Wave Actuator

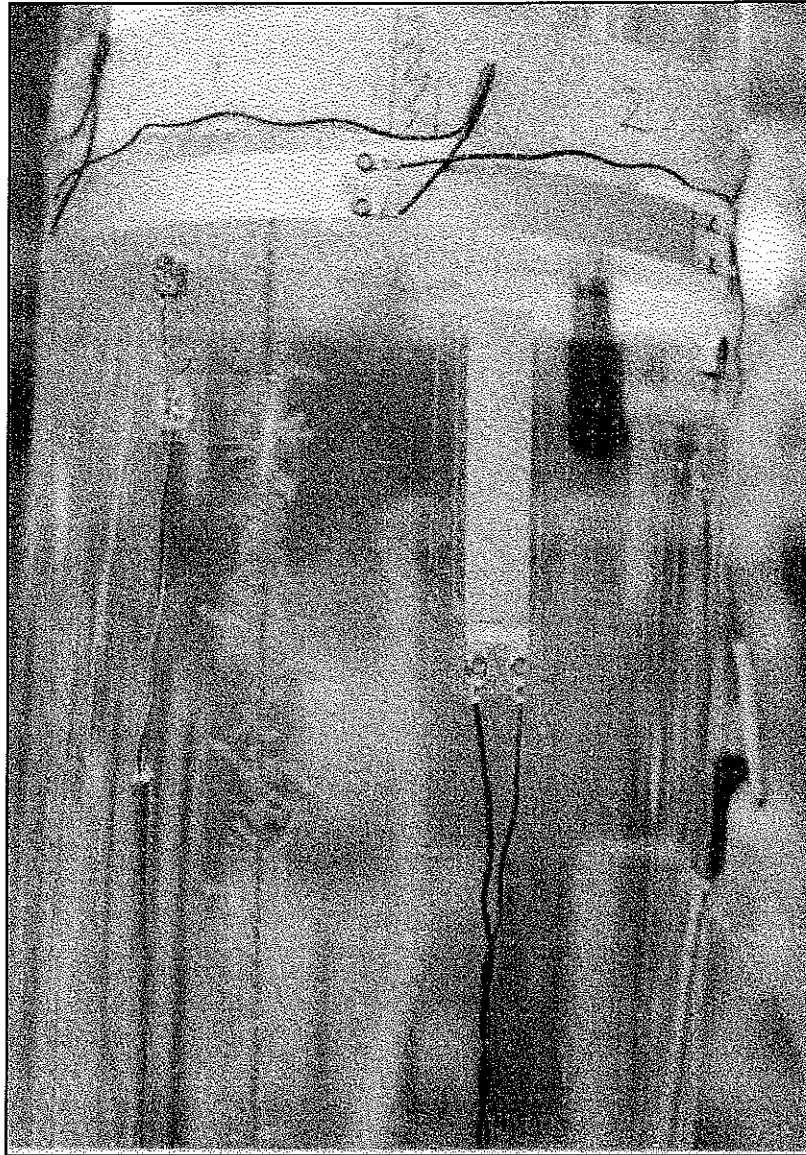


Plate 6.3 Photograph Showing the Hydrophone (inside the pipe), the Radial and Axial PVDF Sensors and the Accelerometers.

6.6 Experimental Procedure

Four experiments were conducted:

- 1 Measurement of the mechanical impedance of the support plates.
2. Measurement of the apparent mass of the piston used to excite the fluid.

3. Measurement of the frequency response functions between the primary and secondary forces excited separately and the PVDF sensors, the accelerometers, and the hydrophone.
4. Active control of a fluid wave at single frequencies between 10 Hz and 1 kHz using the secondary actuator.

6.6.1 Measurement of the Mechanical Impedance of the Support Plates

The plates with the aluminium end cap attached (without the pipe) were placed on foam rubber as can be seen in **plate 6.1**. An instrumented hammer was used to excite the plates over the frequency range 100 Hz to 1.1 kHz at the position where the pipe was to be attached, and the response was measured with a small accelerometer. A Solartron 1200 Signal Processor was used to process the data to give the point mechanical impedance of the plate assembly. Details of the experimental equipment used can be found in Appendix 4 and the frequency response plot is in **figure 6.17**.

6.6.2 Measurement of the Apparent Mass of the Piston used for Excitation of the Fluid

To check whether the piston was behaving as a rigid body, its apparent mass was measured over the frequency range 10 Hz to 1 kHz. A stepped sine technique was used with 2 Hz intervals with a Solartron 1254 Signal Analyser. The piston, which is shown in **figure 6.14**, was suspended from a

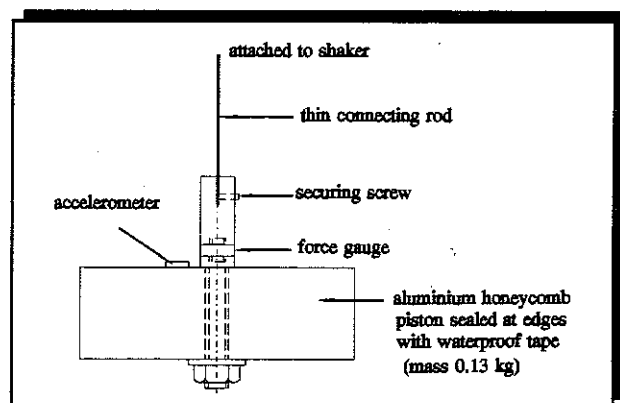


Figure 6.14 The Piston Assembly used to Excite the Fluid

shaker by a thin connecting rod, the end being free. The measured apparent mass is shown in **figure 6.18**.

6.6.3 Measurement of the Frequency Response Functions using the Primary and Secondary Actuators

Once the experimental rig had been assembled and the pipe filled with water, the characteristics of the anechoic termination were investigated. This was done by exciting the fluid to test the effectiveness of the acoustic termination, which consisted of the plates and the foam wedge, and exciting the pipe wall axially to test the effectiveness of the structural termination, which were the plates. In both cases receptance (displacement of the driving piston per unit input force) was measured over the frequency range 10 Hz to 1 kHz using a Solartron 1254 signal Analyser. The test technique used was stepped sine with 2 Hz intervals and the measured receptances are plotted in **figures 6.19** and **6.20**.

The frequency response functions between the primary force and seven measurement transducers, which were four radial accelerometers, two PVDF sensors and the hydrophone, as shown in **figure 6.15**, were then measured. The test technique used was again stepped sine over the frequency range 10 Hz to 1

kHz with 2 Hz intervals, but as eight channels had to be measured simultaneously, the Solartron 1251 twelve channel expansion box had to be used in addition to the

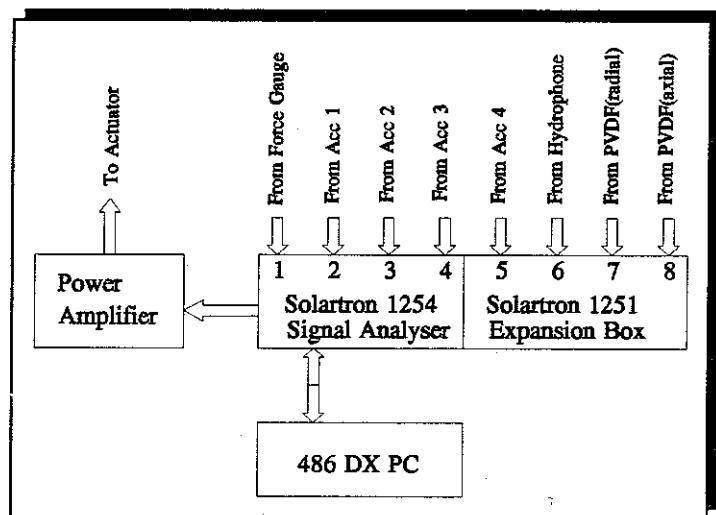


Figure 6.15 Schematic Diagram of the Measurement of the Frequency Response Functions between the Primary Force and the Seven Sensors.

Solartron 1254 Signal Analyser. Some measurements required post processing and these are discussed in Section 6.8.

A similar experiment was carried out using the secondary fluid wave actuator as the exciter. As it was not possible to measure force directly in this case, the current supplied to the magnetostrictive actuator was measured by monitoring the voltage drop across a $0.05\ \Omega$ resistor in the supply cable between the power amplifier and the actuator. This was fed into channel one of the analyser and all measurements were referred to this. Again some post processing of the results was required and this is discussed in Section 6.8.

6.6.4 Active Control of Fluid Waves

Once the relationship between the primary and secondary forces and the pressure of the fluid measured with the hydrophone and the PVDF sensor had been established, active control of fluid waves at discrete frequencies between 10 Hz and 1 kHz was attempted. A

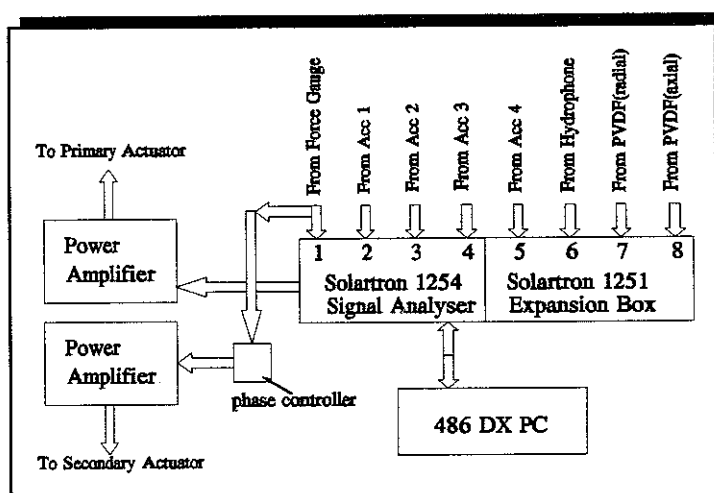


Figure 6.16 Schematic Diagram of the Measurements Taken during the Active Control Experiments

schematic of the experiment is shown in **figure 6.16**. The fluid was excited using the electrodynamic shaker and piston at discrete frequencies between 10 Hz and 1 kHz at intervals of 10 Hz. At a single frequency, when the system had reached a steady state, a secondary pressure was applied using the fluid wave actuator. The amplitude and phase of the electrical power supply to this actuator was adjusted using the gain control on the power amplifier and a locally manufactured phase controller [46], until the fluid pressure measured with the hydrophone and monitored on an oscilloscope

was a minimum. Once this was achieved, all the measurements that were recorded when the fluid was excited under the action of the primary force alone were taken, so that the effects of active control could be assessed.

6.7 Experimental Results

Once the measurements were taken some post processing was required and these results are presented in this section and are listed below:

Figure 6.17 Real and Imaginary Components of the Measured Impedance of the Support Plates

Figure 6.18 Real and Imaginary Components of the Apparent Mass of the Primary Piston used to Excite the Fluid

Figure 6.19 Point Receptance of the Fluid-Filled Pipe with Excitation of the Fluid

Figure 6.20 Point Receptance of the Fluid-Filled Pipe with Excitation of the Pipe Wall

Figure 6.21 Pressure Measured by Hydrophone due to Excitation by Primary Force

Figure 6.22 Phase Angle between the Pressure Measured by Hydrophone and the Primary Force

Figure 6.23 Phase Angle Between Accelerometers due to Excitation by Primary Force

Figure 6.24 Pressure Measured by Hydrophone and PVDF Sensor due to Excitation by Primary Force

Figure 6.25 Ratio between the Output from the PVDF Sensor and the Pressure Measured by Hydrophone due to Excitation by Primary Force

Figure 6.26 Phase Angle between the Output from the PVDF Sensor and the Pressure Measured by Hydrophone due to Excitation by Primary Force

Figure 6.27 Phase Angle between Accelerometers due to Excitation by Secondary Source

Figure 6.28 Pressure Measured by Hydrophone and PVDF Sensor due to Excitation by Secondary Source

- Figure 6.29** Ratio of the Output from the PVDF Sensor and the Pressure measured by Hydrophone due to Excitation by the Secondary Source
- Figure 6.30** Phase Angle between the Output from the PVDF Sensor and the Pressure Measured by Hydrophone due to Excitation by the Secondary Source
- Figure 6.31** Pressure Measured using the Hydrophone with and without Control
- Figure 6.32** Change in Pressure when the Secondary Source was Applied. Measured using the Hydrophone
- Figure 6.33** Pressure Measured using the PVDF Sensor with and without Control
- Figure 6.34** Change in Pressure Measured using PVDF Sensor with Control
- Figure 6.35** Graph Showing How Effective Active Control of the Fluid Waves Could be if the PVDF Sensor was used as the Error Sensor
- Figure 6.36** Magnitude of Secondary Effort Required to Minimise the Downstream Pressure
- Figure 6.37** Phase Angle between the Secondary and Primary Sources when the Downstream Pressure is Minimised
- Figure 6.38** Sum of the Squared Radial Acceleration Levels of the Pipe
- Figure 6.39** Change in the Sum of the Squared Acceleration Levels of the Pipe
- Figure 6.40** Phase Angle between Accelerometers with Control

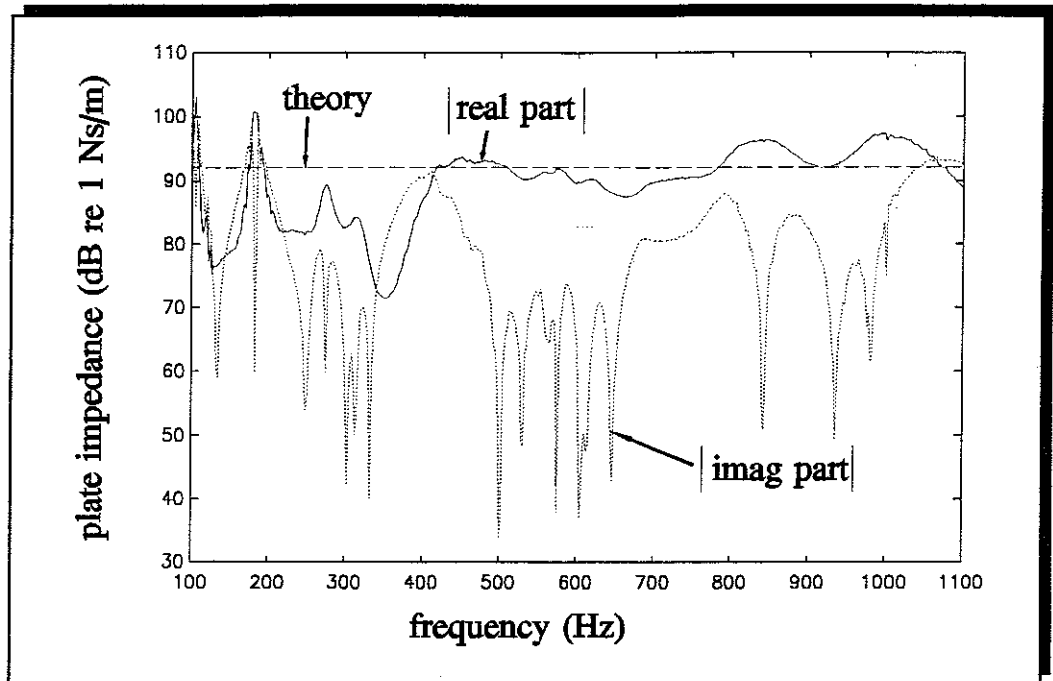


Figure 6.17 Real and Imaginary Components of the Measured Impedance of the Support Plates

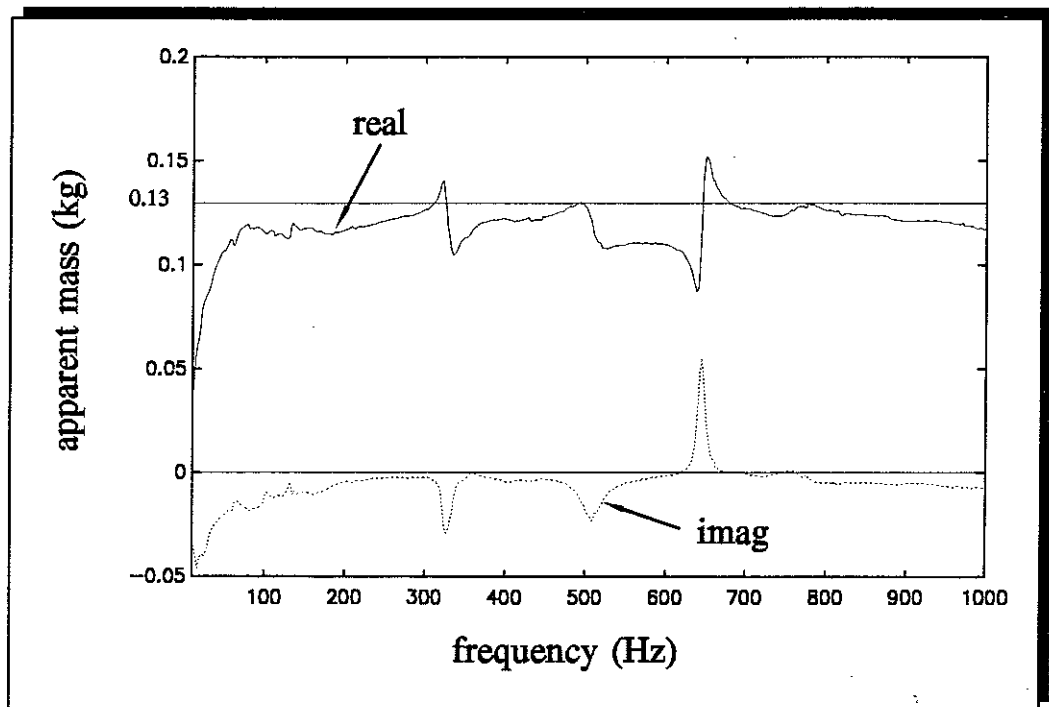


Figure 6.18 Real and Imaginary Components of the Apparent Mass of the Primary Piston used to Excite the Fluid

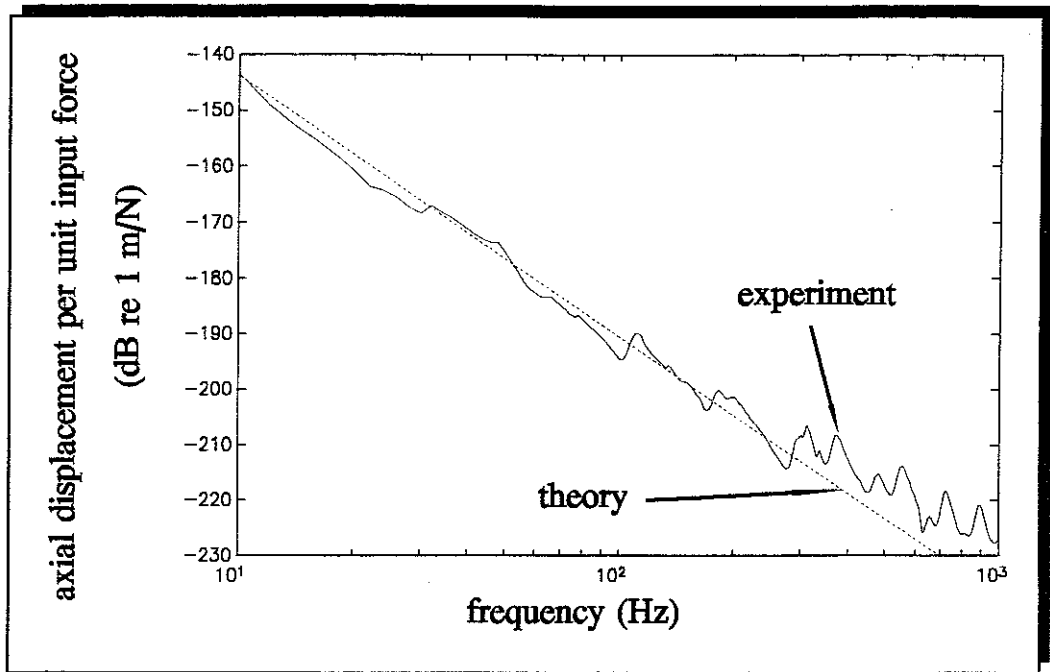


Figure 6.19 Point Receptance of the Fluid-Filled Pipe with Excitation of the Fluid

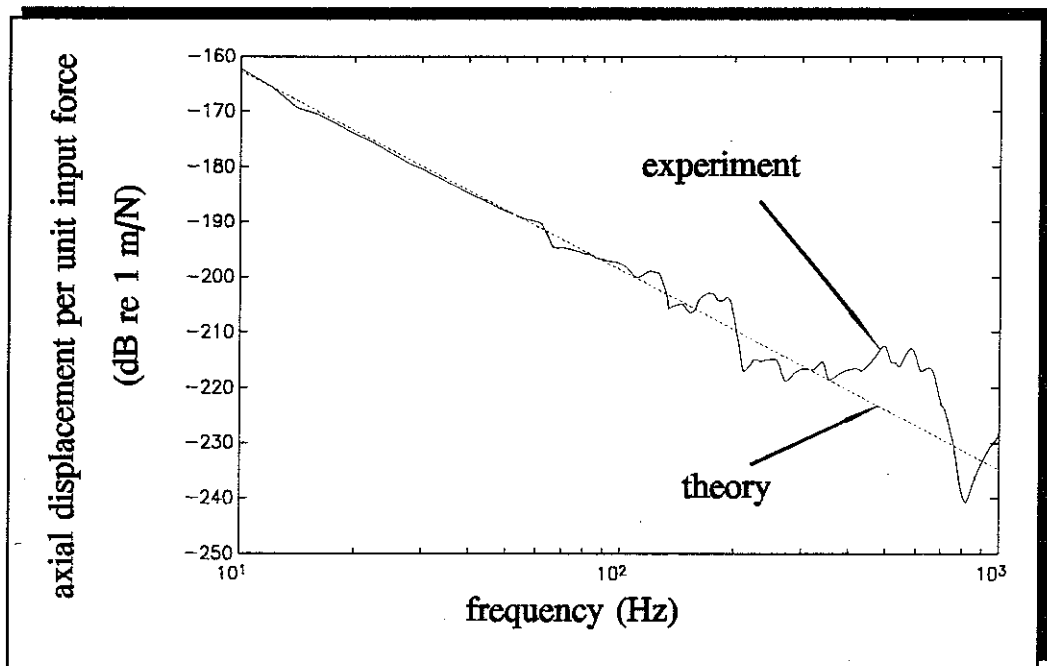


Figure 6.20 Point Receptance of the Fluid-Filled Pipe with Excitation of the Pipe Wall

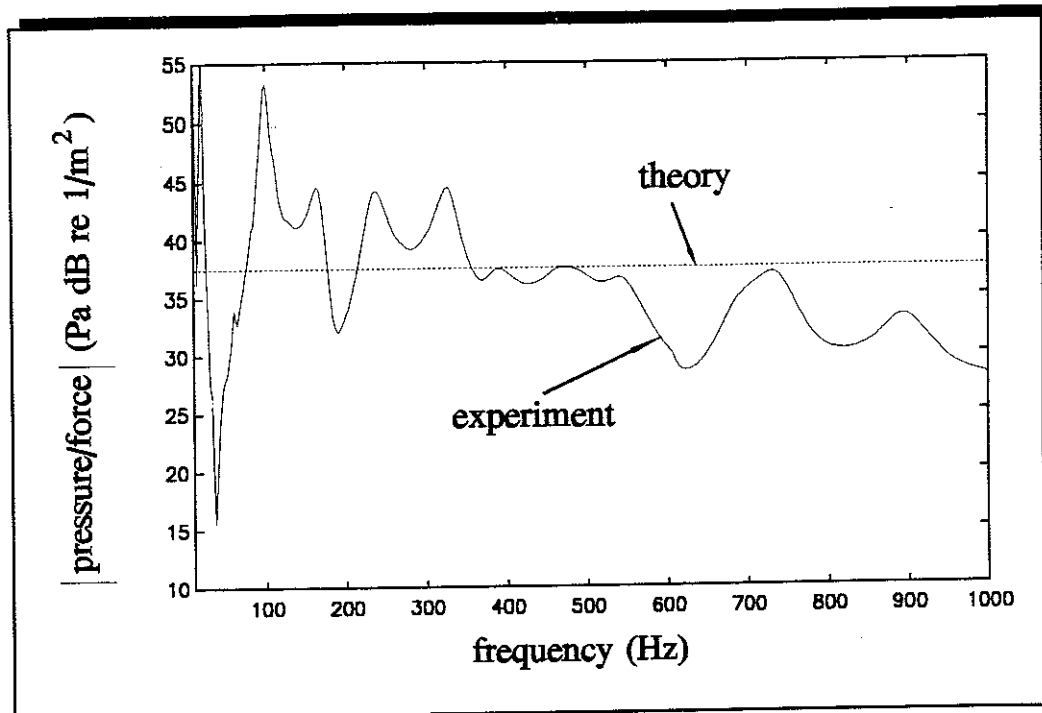


Figure 6.21 Pressure Measured by Hydrophone due to Excitation by Primary Force (Fluid Excitation)

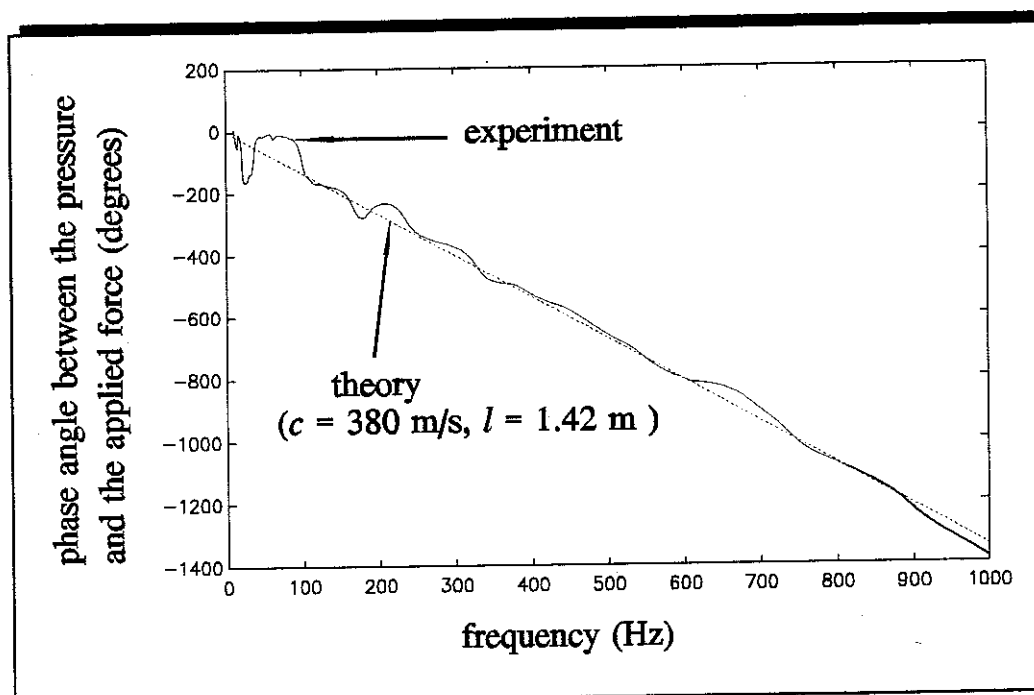


Figure 6.22 Phase Angle between the Pressure Measured by Hydrophone and the Primary Force (Fluid Excitation)

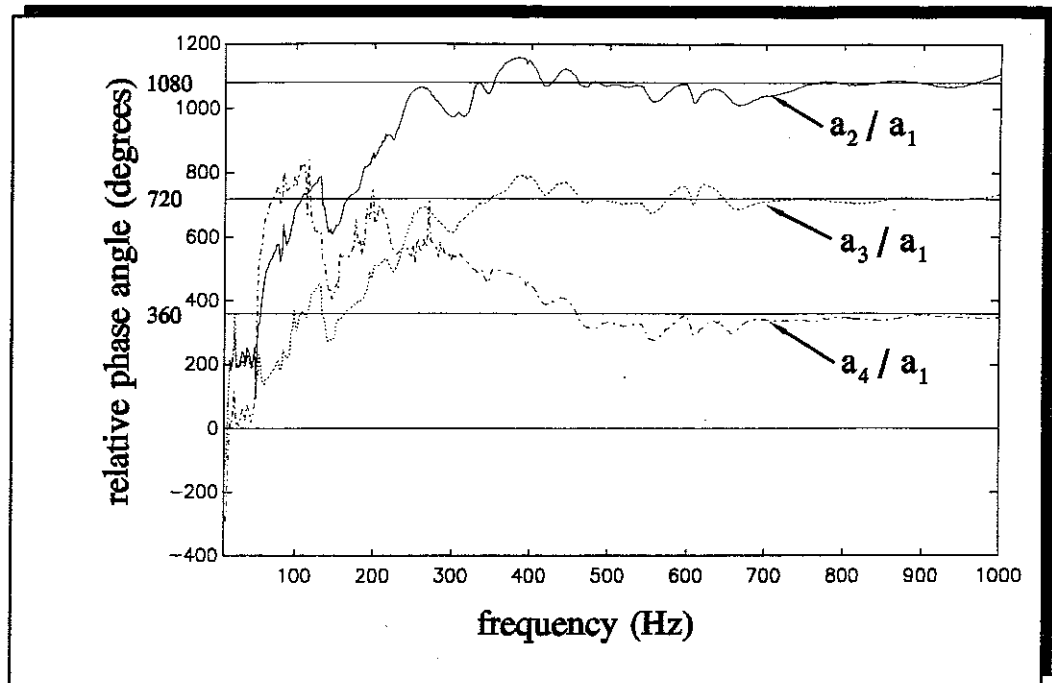


Figure 6.23 Phase Angle Between Accelerometers due to Excitation by Primary Force (Fluid Excitation)

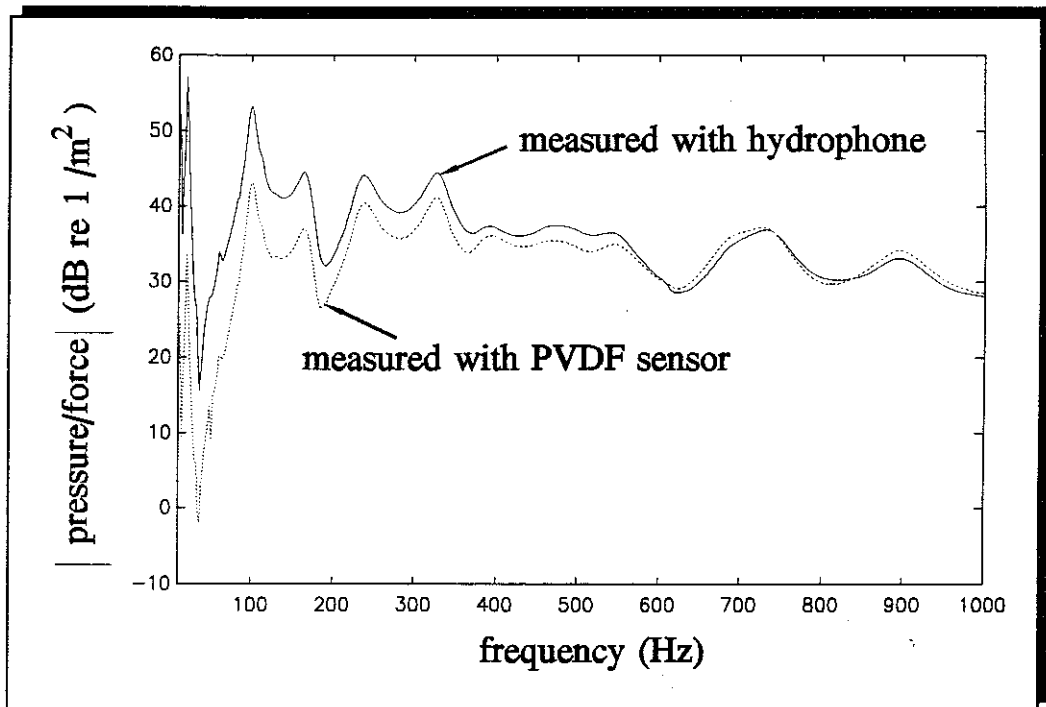


Figure 6.24 Pressure Measured by Hydrophone and PVDF Sensor due to Excitation by Primary Force (Fluid Excitation)

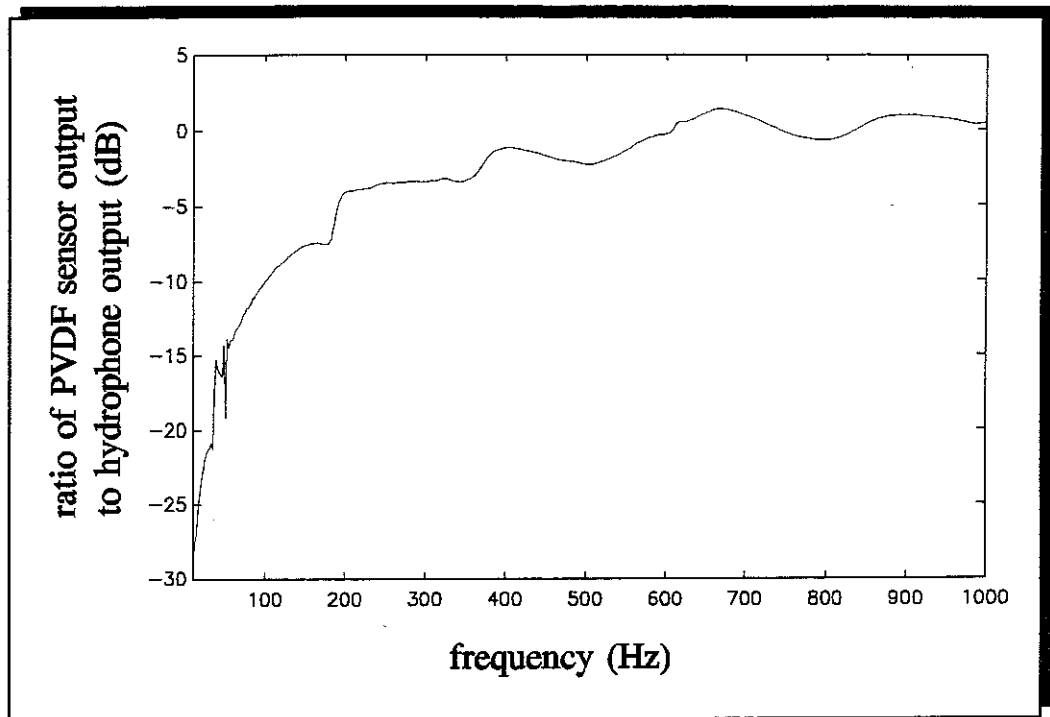


Figure 6.25 Ratio between the Output from the PVDF Sensor and the Pressure Measured by Hydrophone due to Excitation by Primary Force (Fluid Excitation)

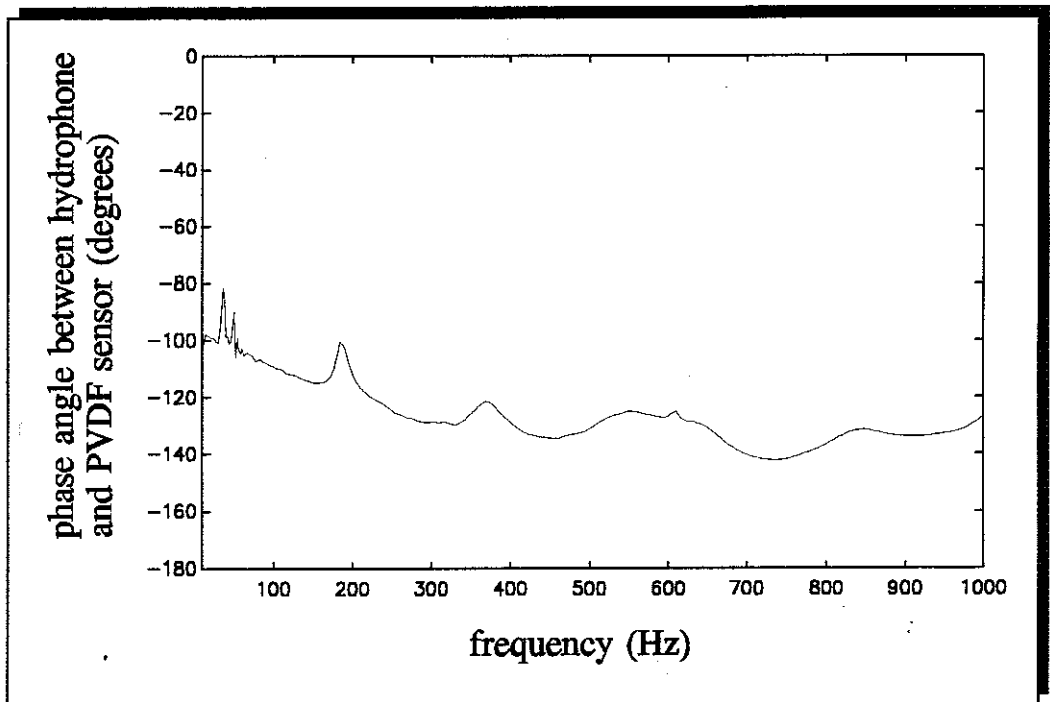


Figure 6.26 Phase Angle between the Output from the PVDF Sensor and the Pressure Measured by Hydrophone due to Excitation by Primary Force (Fluid Excitation)

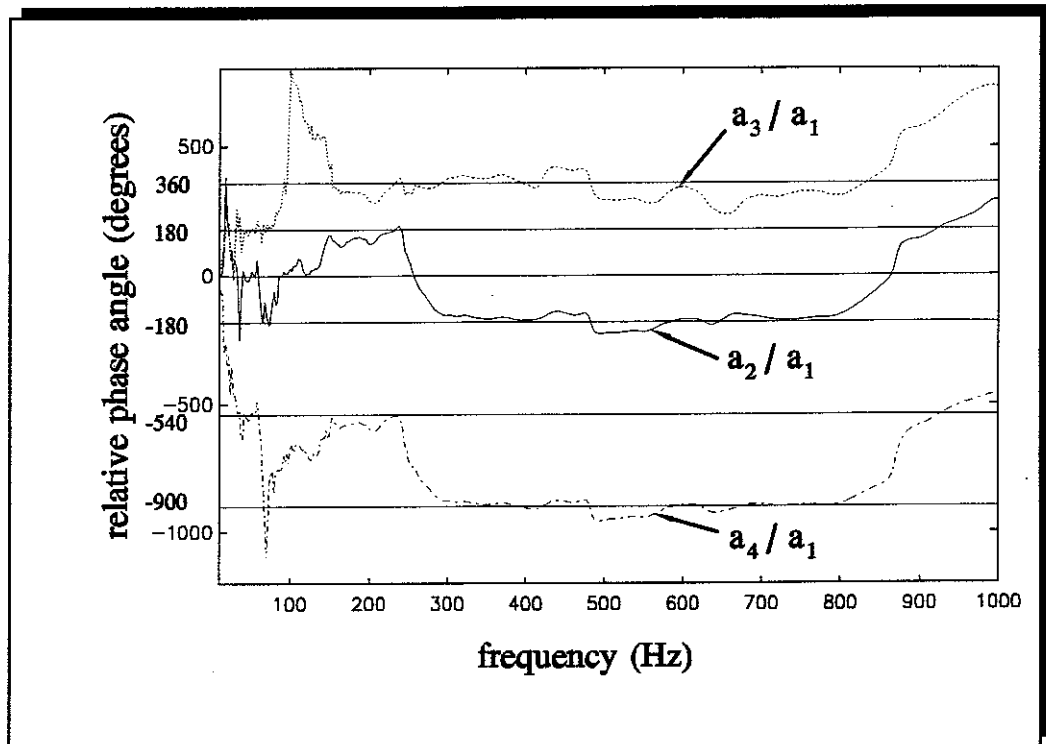


Figure 6.27 Phase Angle between Accelerometers due to Excitation by Secondary Source

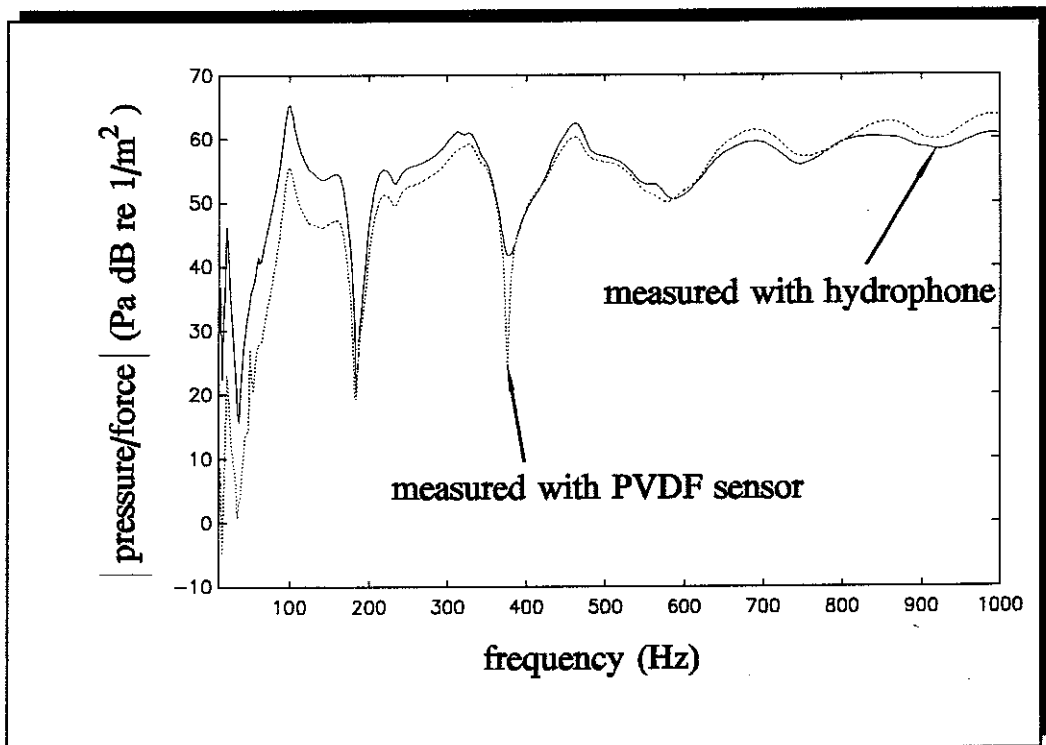


Figure 6.28 Pressure Measured by Hydrophone and PVDF Sensor due to Excitation by Secondary Source

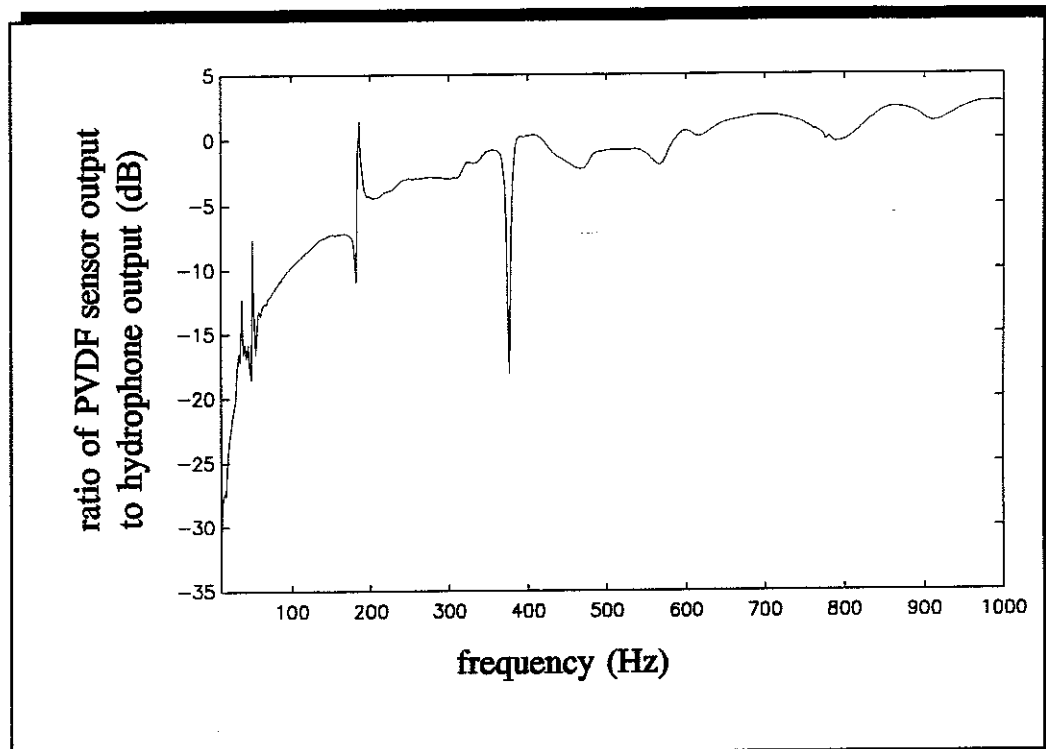


Figure 6.29 Ratio of the Output from the PVDF Sensor and the Pressure measured by Hydrophone due to Excitation by the Secondary Source

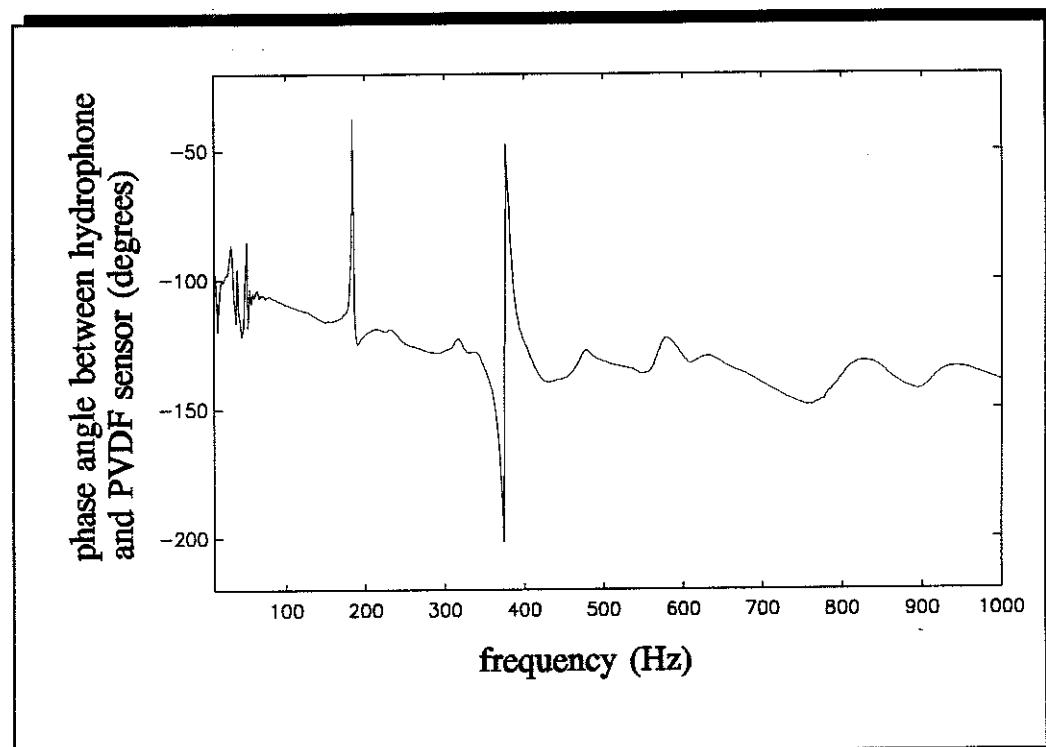


Figure 6.30 Phase Angle between the Output from the PVDF Sensor and the Pressure Measured by Hydrophone due to Excitation by the Secondary Source

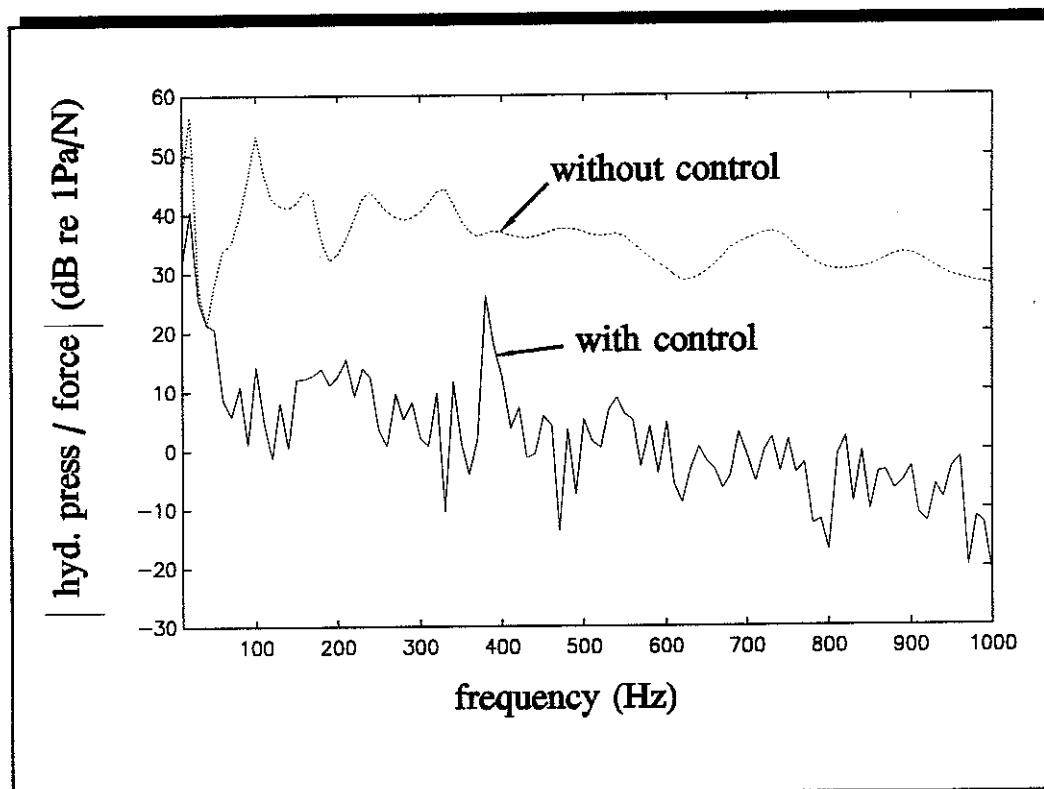


Figure 6.31 Pressure Measured using the Hydrophone with and without Control

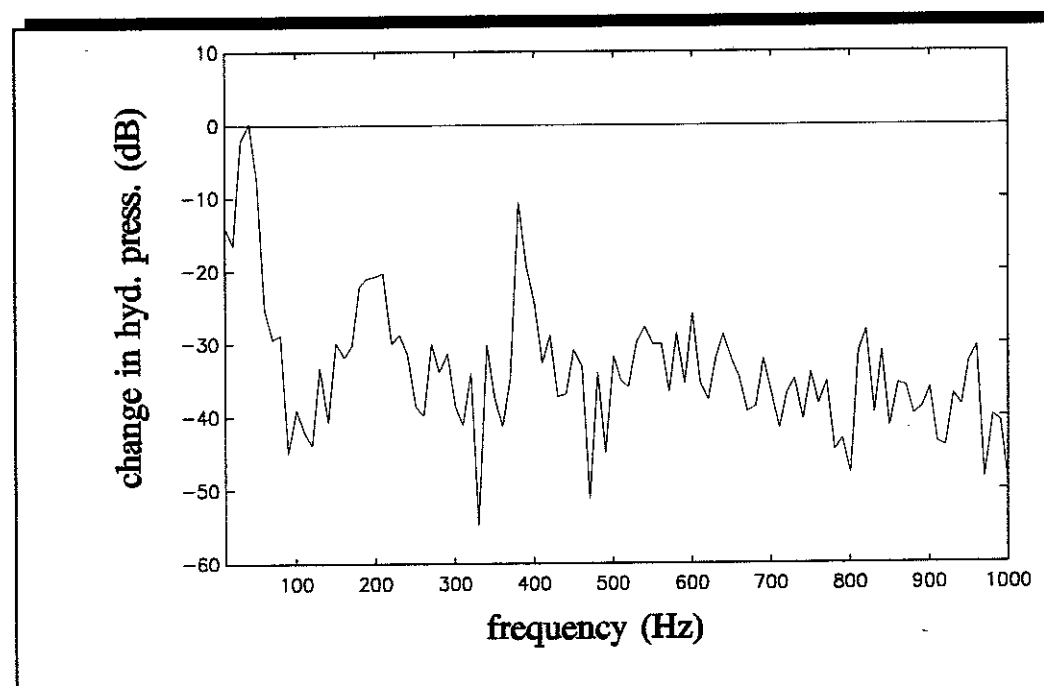


Figure 6.32 Change in Pressure Measured using the Hydrophone with Control

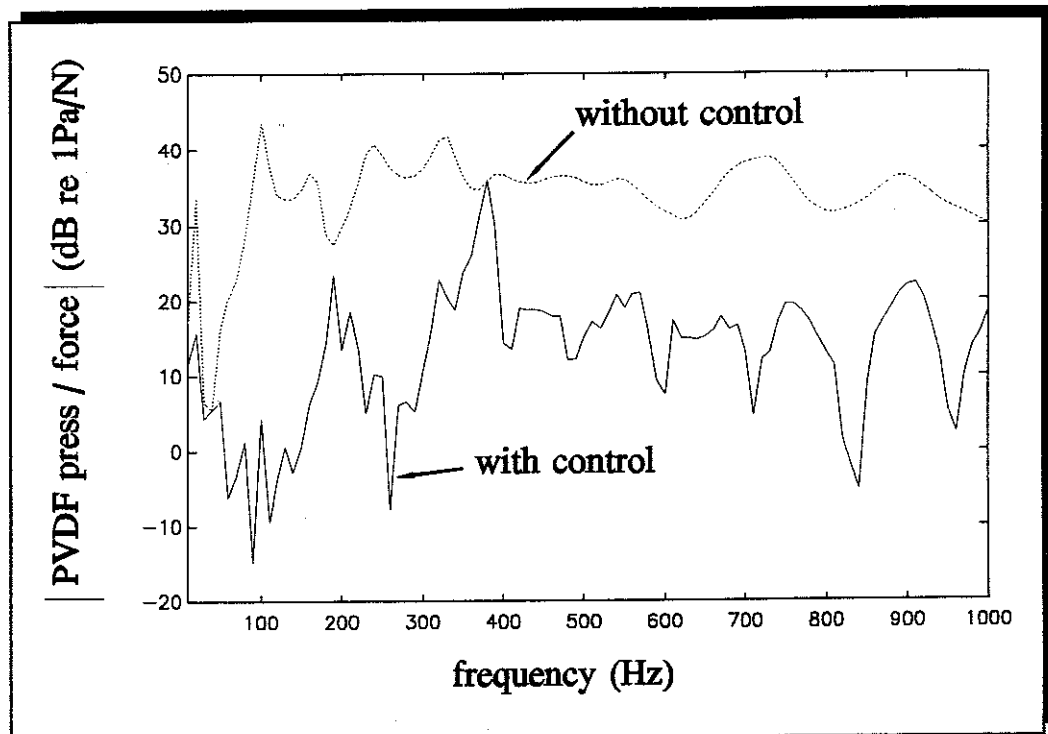


Figure 6.33 Pressure Measured using the PVDF Sensor with and without Control

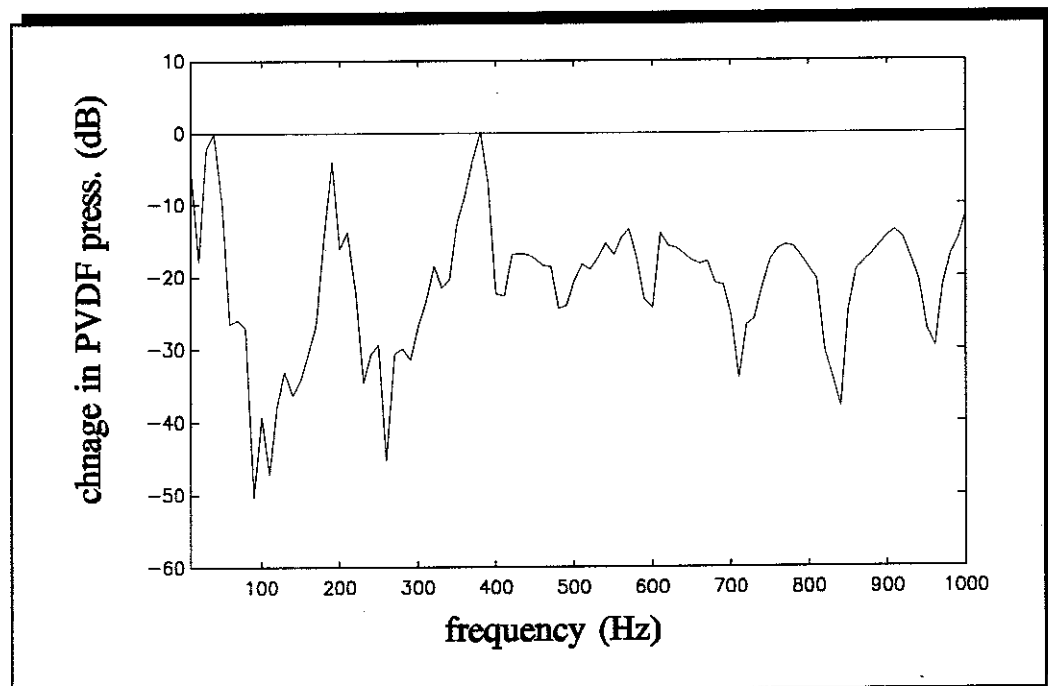


Figure 6.34 Change in Pressure when the Secondary Source was Applied. Measured using the PVDF Sensor

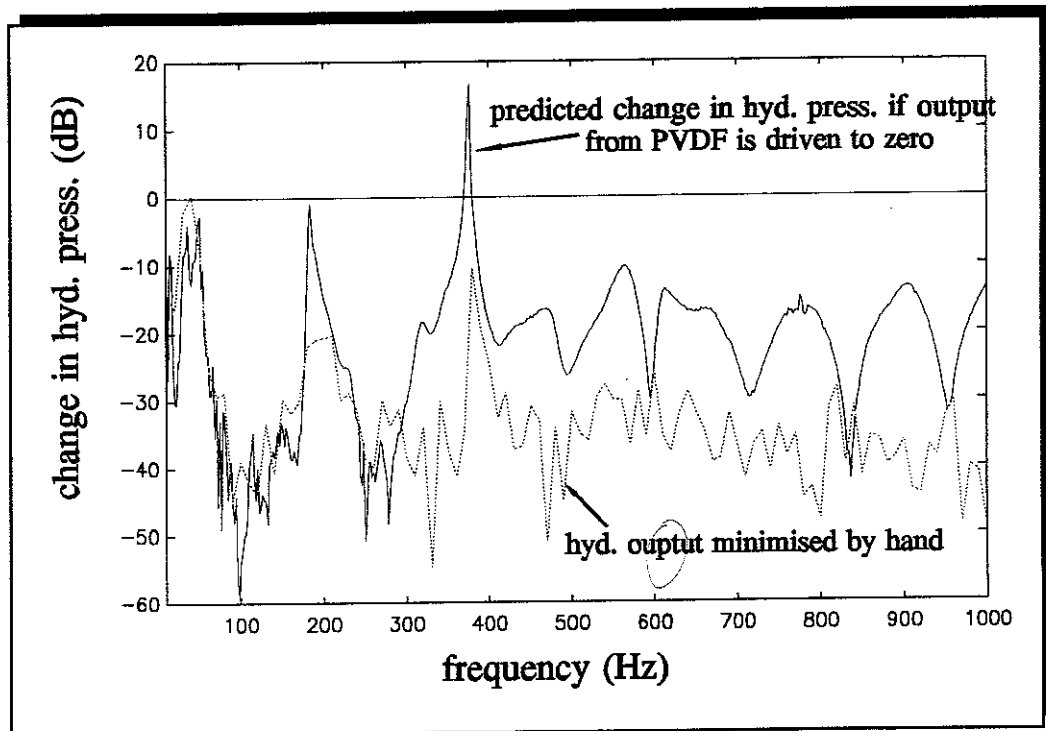


Figure 6.35 Graph Showing How Effective Active Control of the Fluid Waves Could be if the PVDF Sensor was used as the Error Sensor

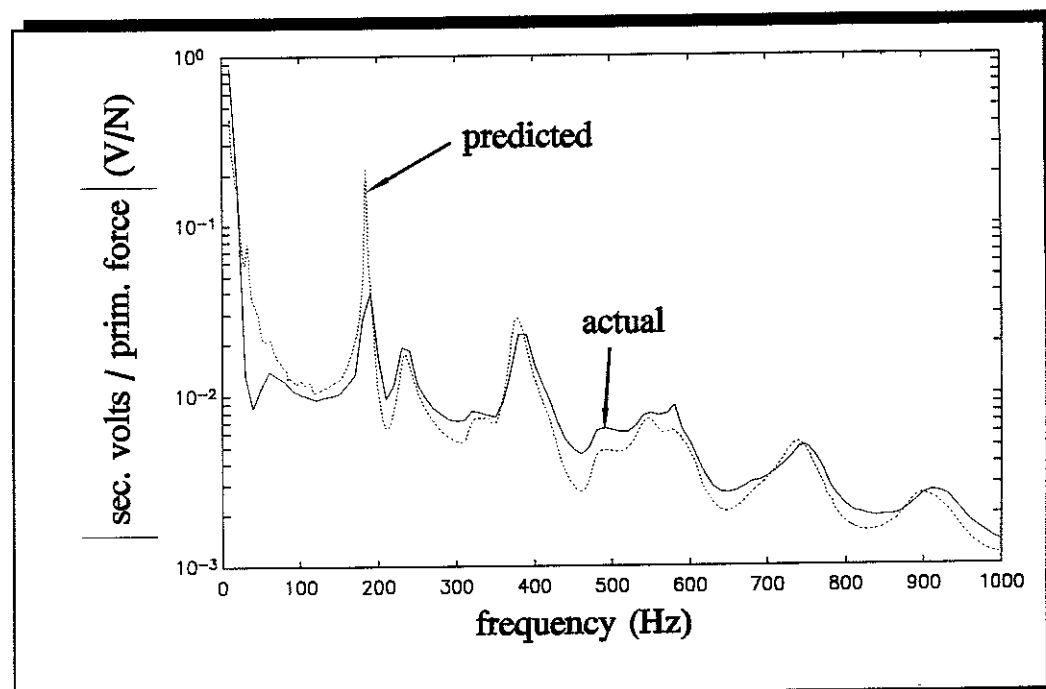


Figure 6.36 Magnitude of Secondary Effort Required to Minimise the Downstream Pressure

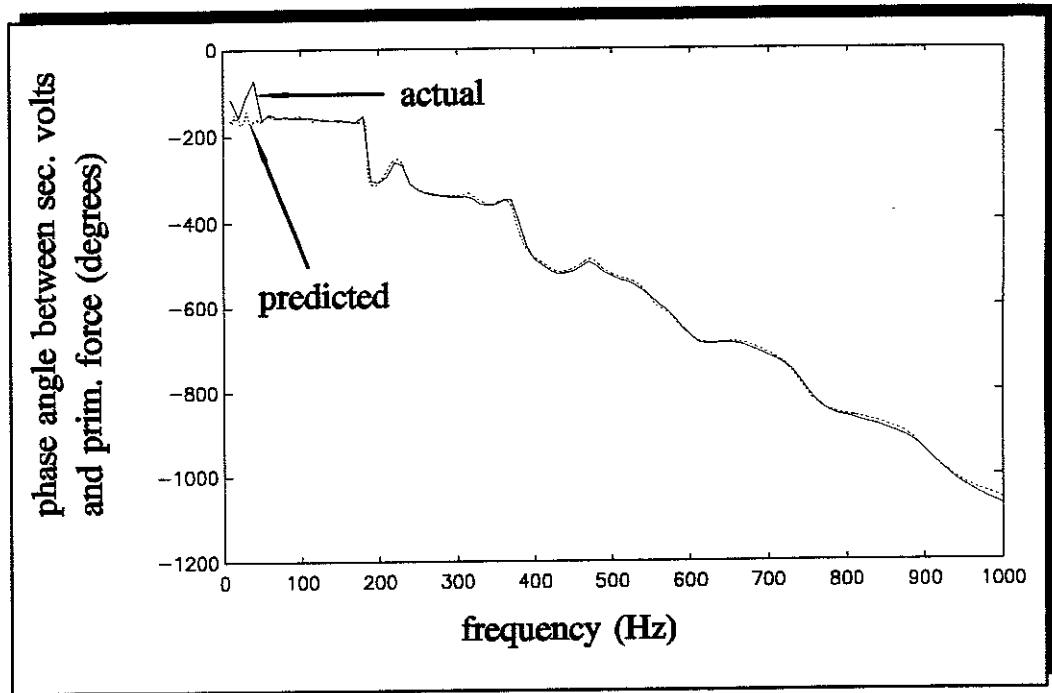


Figure 6.37 Phase Angle between the Secondary and Primary Sources when the Downstream Pressure is Minimised

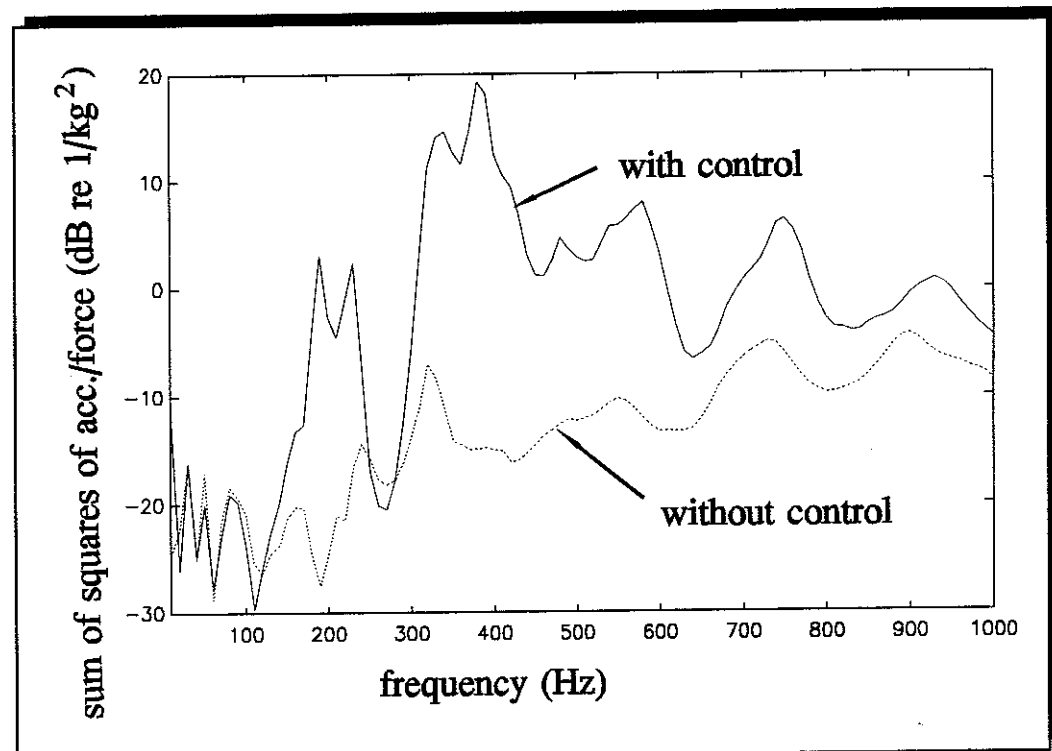


Figure 6.38 Sum of the Squared Radial Acceleration Levels of the Pipe

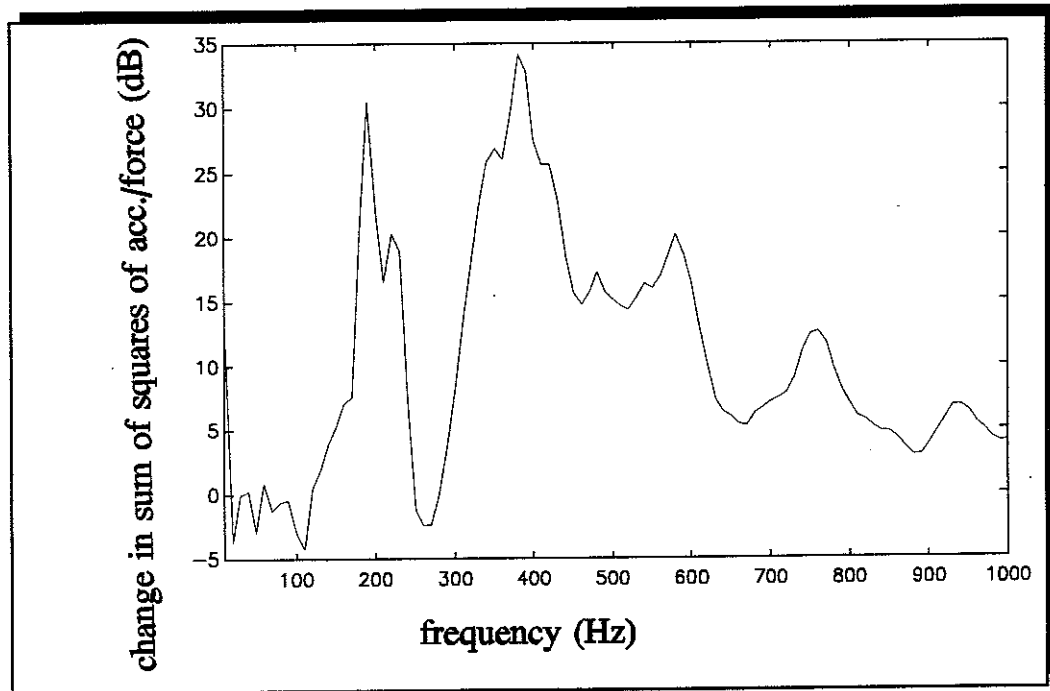


Figure 6.39 Change in the Sum of the Squared Acceleration Levels of the Pipe

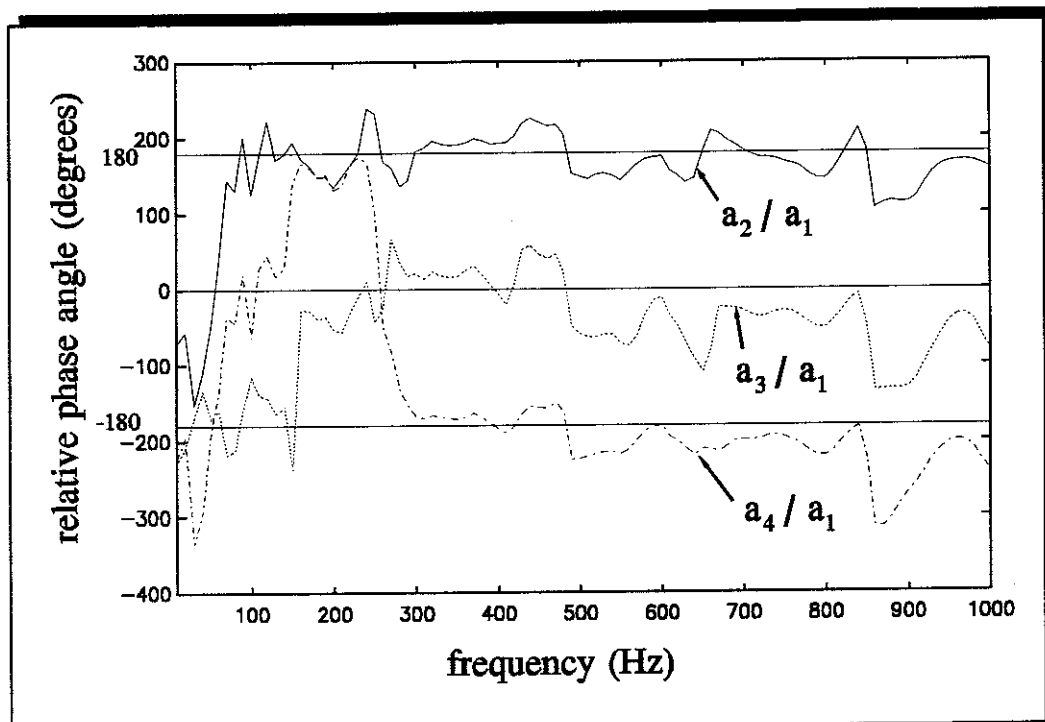


Figure 6.40 Phase Angle between Accelerometers with Control

6.8 Discussion

The first experiment involved the measurement of the mechanical impedance of the supporting plate assembly to see if it would be an appropriate longitudinal anechoic termination for the fluid-filled pipe. The frequency response plot is in **figure 6.17**, where the modulus of the real and imaginary parts of the impedance of the plate assembly are plotted. Referring to equation (6.59) it can be seen that the impedance of an undamped, infinite plate is entirely real and constant with frequency, and this is also plotted in **figure 6.17** for comparison with the experimental results. The imaginary part of the measured impedance is a measure of the damping in the plate assembly. It can be seen that above about 400 Hz the plate behaves largely as an infinite plate with the real part of the impedance being on average 10 to 20 dB greater than the imaginary part. At frequencies up to about 200 Hz there is evidence of modal behaviour and thus the plate assembly is probably not an effective longitudinal anechoic termination below this frequency.

The second experiment concerned the measurement of the dynamic properties of the piston used to excite the fluid in the pipe. This assembly was designed to act as a rigid body below 1 kHz, and was thus made out of an aluminium honeycomb material so that it was light and stiff. However, a bolt had to be fitted to the piston together with a force gauge and connecting rod as can be seen in **figure 6.14**, and there was concern that this assembly might exhibit complex dynamic behaviour at high frequencies. Therefore the apparent mass of the assembly was measured over the frequency range 10 Hz to 1 kHz as this could then be compared with the measured mass of the piston which was 130 g. The results are plotted in **figure 6.18**, and it can be seen that although there is some dynamic behaviour (perhaps due to bending of the connecting rod), the piston assembly behaves by and large as a small mass. This means that the force measurements taken during later experiments when the fluid was excited, indicate to a reasonable first approximation, the force being applied to the fluid.

The next two experiments concerned the measurement of the dynamic properties of the complete experimental rig as shown in **plate 6.1**. The first experiment involved the measurement of the axial point receptance of the rig when the fluid was excited using the piston discussed in the previous paragraph. The frequency response plot is shown in **figure 6.19**, where it can be seen that the system exhibits semi-infinite behaviour over the whole of the frequency range of interest. Although there is some evidence of reflections from the end of the pipe attached to the plate, they are relatively small (< 10 dB). **Figure 6.20** shows the receptance of the rig when it is excited axially on the pipe wall. Again it can be seen that the frequency response is relatively flat, but there is evidence of modal behaviour around 200 Hz and 600 Hz.

It is thought that three factors contributed to the almost semi-infinite behaviour observed in the experimental rig:

1. The acoustic wedge, which was an exponentially shaped, open cell, foam rubber cone, reduces the fluid reflections from the end of the pipe connected to the supporting plates.
2. The plates act as a longitudinal anechoic termination at frequencies greater than about 400 Hz.
3. There is strong coupling between the fluid and the pipe, and the high damping in the pipe dissipates energy in both the structural wave and the fluid wave.

Figures 6.21 and **6.22** show the magnitude and phase of the pressure measured by the hydrophone in response to excitation of the fluid by the primary force actuator. The theoretical pressure (\approx force applied / area of piston) is also plotted in **figure 6.21**. The modal behaviour of the fluid can be seen at low frequencies, and above about 200 Hz the measured response is within ± 8 dB of the predicted response of a semi-infinite pipe. This indicates that the acoustic and structural anechoic terminations are reasonably effective. Superimposed on the phase diagram in **figure**

6.22 is the theoretical phase lag between the hydrophone and point of excitation, assuming a phase velocity of 380 ms^{-1} and a distance between the hydrophone and point of excitation of 1.42 m. The phase was calculated using the formula:

$$\phi = \frac{2\pi lf}{c_1} \quad (6.61)$$

where ϕ is the phase angle l is the distance between the force and the response, f is the frequency of excitation and c_1 is the phase velocity of the $s = 1$ wave. This formula is derived from the fundamental relationship between wavenumber, frequency and phase angle. It is interesting to compare the experimentally estimated wave velocity with that calculated using equation (6.7). It is also of interest to see how the velocities of a fluid wave in a rigid pipe and a structural axial wave in an *in vacuo* pipe change when these waves interact in a soft-walled fluid-filled pipe. The wave velocities are given in Table 6.5 for the water-filled perspex pipe used in the experiments.

Wave Type	Calculated Wave Speed (ms^{-1})	Measured Wave Speed (ms^{-1})
Longitudinal Wave in a Rod, c_l	2160	
Longitudinal Wave in a Plate, c_{pl}	2357	
Fluid Wave in a Rigid Walled Pipe, c_f	1477	
Coupled Wave, c_1 (predominantly fluid)	423	≈ 380
Coupled Wave, c_2 (predominantly structure)	2337	

Table 6.5 Effect of Fluid-Structure Interaction on Wave Speeds

This table shows that the wave speed in the structure (c_2) is predicted to increase slightly due to the effect of the contained fluid, and that it lies between that of a longitudinal wave in a rod and a plate. This is because the fluid in the pipe restricts the radial wall motion and thus axial compressional wave tends towards that of a compressional plate wave. The wave speed in the fluid is dramatically affected by the soft-walled pipe and slows to less than one third of the wave speed in a rigid-walled pipe. This is because in a soft-walled pipe the fluid moves radially as well as axially and this causes a reduction in the axial velocity of the fluid. The measured wave velocity (c_1) of 380 ms^{-1} is within 11% of the calculated wave velocity.

Figure 6.23 shows the relative phase angles between the signals from the accelerometers placed to measure radial wall motion as shown in **figure 6.13** and **plate 6.3**. These graphs have been obtained by post-processing the experimental data, as all the measurements were made with reference to the primary force. This involved division of the frequency response functions, for example $a_2/a_1 = a_2/f_p \div a_1/f_p$, and the "unwrapping" of the phase function. **Figure 6.23** indicates that there is modal behaviour in the structural response of the pipe at low frequencies, which is probably due to wave reflection and conversion at the asymmetric discontinuities in the experimental rig such as the secondary actuator and the support plates. At frequencies greater than about 400 Hz, the pipe is moving in a breathing mode, with all the accelerometers moving in-phase.

Figures 6.24, 6.25 and 6.26 show the outputs of the hydrophone and the PVDF radial sensor. These graphs were again obtained by post-processing experimental data. To obtain **figure 6.24** the manufacturers calibration sensitivity for the hydrophone was applied at the Brüel and Kjær charge amplifier, and the voltage measured from the PVDF sensor was related to the pressure in the pipe using equation (6.58). It is clear from **figure 6.24** that although there are some differences between the measurements from the hydrophone and the PVDF radial sensor, there is considerable agreement between the measurements, particularly considering the indirect calibration methods used here. To see this relationship more clearly, the frequency response functions between the two sensors was computed from the

experimental data and is plotted in the form of magnitude and phase in **figures 6.25** and **6.26**. It can be seen that above about 200 Hz, the difference between the output from the two sensors is less than 5 dB and the phase is within a 20° band. It is thought that the poor low frequency response is due to the sensing circuit of the PVDF film. It acts very much like a high pass filter [105] where the low frequency cut-off point is dependent upon the electrical impedance of the measurement circuit. It is believed that if this was increased then the low frequency behaviour of the PVDF sensor could be improved. However, the experiments show that a PVDF radial sensor gives a reasonably accurate measure of the pressure inside a soft-walled pipe, and therefore it could be used as a non-intrusive error sensor in an active control system.

The next experiment involved measuring the response of the experimental rig when subject to excitation by the secondary actuator. **Figures 6.27 - 6.30** show the results of this experiment. **Figure 6.27** shows the relative phase between the accelerometers positioned to measure the radial wall motion of the pipe. As discussed above, this gives an indication of how the pipe is moving and hence the structural waves that are being excited by the secondary actuator. Comparing this figure with **figure 6.23**, it is clear that the motion of the pipe wall is different when excited by the primary and the secondary actuators. Below about 250 Hz there is modal behaviour in a similar way to when the fluid was excited using the primary actuator, but between about 250 Hz and 850 Hz, the phase shifts between the accelerometers indicate the pipe is ovalling. Accelerometers 1 and 3 are moving in phase and these are moving in anti-phase with accelerometers 2 and 4. This is an indication that the $n = 2$ wave is being excited (see **figure 6.1**). To gain further insight into this behaviour it is worthwhile calculating the approximate natural frequencies of the circumferential modes of an infinite, *in vacuo* pipe. The effect of the fluid is to mass load the pipe [99], and to shift the cut-on frequencies downwards. The ring frequency of the perspex pipe *in vacuo* can be calculated, using the expression [100], as:

$$f_{ring} = \frac{1}{2\pi} \sqrt{\frac{E_s}{\rho(1-\nu^2)}} \frac{1}{a} = 5.17 \text{ kHz}$$

and the number of circumferential modes that cut-on below this frequency are given approximately by the formula [100]:

$$n_r \approx \left(\frac{h}{\sqrt{12}a} \right)^{-1/2} \approx 7$$

The two lowest cut-off frequencies, which are in the frequency range of interest, are approximated by the formulae [100]:

$$n = 2, \quad \frac{h}{\sqrt{12}a} 2.68 f_{ring} = 275 \text{ Hz}$$

$$n = 3, \quad \frac{h}{\sqrt{12}a} 7.65 f_{ring} = 787 \text{ Hz}$$

Referring to **figure 6.27**, it can be seen that there is indication that the $n = 2$ wave is excited at around 250 Hz - 300 Hz and that possibly the $n = 3$ wave is excited at around 800 Hz. It thus appears that the secondary actuator is not only exciting axisymmetric waves, but also unwanted higher order circumferential waves as well. This behaviour is discussed further, later in this section, when the fluid wave control experiments are discussed.

Figure 6.28 shows the pressure measured by the hydrophone and the PVDF radial sensor when the rig is excited using the secondary actuator. This should be compared with **figure 6.24**. One point to note about this graph is that it shows that the PVDF radial sensor is *insensitive to circumferential modes*. This can be seen by the close agreement between the hydrophone and PVDF measurements, even though it is known that higher order structural modes are being excited in this case, as discussed above. In **figure 6.28** it can be seen that there are two frequencies above 100 Hz, when there is poor coupling between the secondary actuator and the pressure sensors

(around 184 Hz and 376 Hz); this means that it will be difficult to obtain significant attenuation of the pressure at the sensor positions at these frequencies. The reason for this poor coupling is probably because the upward-going wave generated by the secondary actuator, when reflected off the primary source, destructively interferes with the downward-going wave generated by the actuator resulting in a very low generated pressure to the right of the actuator. This phenomenon occurs when the distance between the secondary actuator and the free surface of the fluid is an integer number of half-wavelengths. Theoretically, the two lowest frequencies when this occurs are at 177 Hz and 355 Hz, which are reasonably close to the predicted frequencies of 184 Hz and 376 Hz, given the imprecise boundary condition at the free surface and at the secondary actuator. A similar effect to this was seen when the active control of flexural waves on a beam was attempted, which is discussed in Chapter 3. The reason why destructive interference does not occur at higher frequencies in the experimental rig is probably because the wave is damped due to the fluid-structure interaction and thus the amplitude of the reflected upward-going wave returning to the actuator is much diminished. The frequencies at which control will not be successful are because only one secondary actuator was used. This could be avoided if two actuators were used as in the control of flexural waves on a beam discussed in Chapter 3.

Figures 6.29 and 6.30 show the magnitude and phase of the calibrated PVDF sensor output relative to the hydrophone. Apart from the ill-conditioning near 184 Hz and 376 Hz, these graphs are similar to **figures 6.25 and 6.26** indicating that the differences between the hydrophone and PVDF sensor are due to calibration problems.

Once the rig had been characterised in response to excitation by primary and secondary sources, active control of a fluid wave was attempted as explained in section 6.6.4. The dynamic fluid pressure measured using the hydrophone with and without control can be seen in **figure 6.31**, and the change in pressure can be seen in **figure 6.32**. Significant reductions of between 30 to 40 dB were achieved over most of the frequency range of interest. The notable exceptions were at very low

frequencies and around 184 Hz and 376 Hz, the frequencies discussed above. The signal from the PVDF sensor was also measured during the experiments and this is shown in **figures 6.33** (with and without control) and **6.34** (change with control). These figures should be compared with **figures 6.31** and **6.32**. The reductions achieved in the signal from the PVDF sensor were on average between 15 and 30 dB. The question then remains, what would be the reduction in the pressure measured by the hydrophone if the output from the PVDF sensor was minimised? Although this experiment was not conducted, the results to be expected from it can be calculated from the experimentally measured frequency response functions. The required magnitude and phase of the secondary source to bring the PVDF sensor output to zero can be calculated using experimental data and the equation:

$$f_s = \frac{-\alpha_p}{\alpha_s} f_p \quad (6.62)$$

where α_p and α_s are the measured frequency response functions between the primary and secondary sources and the PVDF output respectively. The principle of superposition can then be invoked, and the response of the hydrophone if this force was applied together with the primary force is given by:

$$\frac{p}{f_p} = \beta_p - \frac{\alpha_p}{\alpha_s} \beta_s \quad (6.63)$$

where β_p and β_s are the measured frequency response functions between the primary and secondary sources and the hydrophone output respectively. The calculated reduction in pressure with control at the PVDF sensor is shown in **figure 6.35**, where it is compared with the reduction in pressure that was achieved by manually adjusting the magnitude and phase of the secondary source to minimise the output from the hydrophone. This clearly shows that there is a penalty for using the non intrusive sensor in terms of pressure reduction, but nonetheless significant reductions of around 20 dB can be achieved.

As control was implemented by manually adjusting the magnitude and phase of the secondary source until the output from the hydrophone was at a minimum as measured by eye using an oscilloscope, it is questionable whether the optimum

secondary force was applied. However, this can be checked against the prediction of the secondary force requirement calculated in a similar way to equation (6.62) but in this case the frequency response functions are between the primary and secondary forces and the hydrophone output. The predicted and measured magnitude and phase of the secondary source with respect to the primary force are plotted in figures 6.36 and 6.37. It can be seen that at most frequencies, with the exception of the two frequencies where control was difficult, the magnitude of the applied secondary force was very close to that predicted. The measured and predicted phase correlated very well over the whole frequency range. We can thus conclude that the manual tuning of the secondary source was very close to optimum.

As discussed above, the experimental rig was instrumented with four accelerometers to measure the radial motion of the pipe wall. It was noticed during the control experiment that the pipe wall vibration increased when the secondary source was excited. To quantify this, the outputs from the accelerometers were squared and then summed, to give a single measure of radial vibration of the pipe. This was measured with and without control and are plotted in figure 6.38. The increase in the vibration of the pipe wall is plotted in figure 6.39. It can be seen that at most frequencies the vibration of the pipe wall increases due to the action of the secondary actuator. In particular there are significant increases in vibration at the frequencies where there is poor coupling between the secondary actuator and the hydrophone. This is because the actuator was driving very hard to generate only a small control pressure at these frequencies. The way in which the pipe wall was moving can be seen by examining the relative phases between these accelerometers, which is shown in figure 6.40. It can be seen that the pipe is ovaling at frequencies greater than about 275 Hz which indicates that the $n = 2$ wave is being generated by the secondary actuator. On a closer inspection of the design of the secondary actuator detailed in Appendix 4, it is thought that the actuator applies a lateral force to the pipe as well as the radial pressure intended. This is because the actuator reacts off the steel ring and generates a point lateral force. This lateral force excites the higher order circumferential modes and only if the actuator was made so that it acted against an inertial mass, would the generation of this lateral force be avoided.

As higher order structural modes were excited, it is prudent to consider whether higher order acoustic modes were excited. Higher order acoustic modes are evanescent at low frequencies and it is possible that this evanescent wave may interfere with the sensor array which is designed to measure plane waves. To consider whether this evanescent wave is important, it is necessary to calculate the cut-on frequency of the first higher order mode. The formula for the cut-on frequency f_c , of the first higher order acoustic mode in a rigid-walled pipe given by [100]:

$$f_c = 1.84 \frac{c_f}{c_p} f_{ring} = 5.96 \text{ kHz}$$

As the highest frequency of interest is much lower than this then the evanescent wave decays away to a very small amplitude over a very small distance, and it is considered that this wave had a negligible effect in the experiments. Thus, in this case, and in most practical pipework systems, the non-intrusive pressure sensor could be placed very close to the secondary actuator.

6.9 Conclusions

The work reported in this Chapter has demonstrated the practical viability of a non-intrusive actuator and sensor for the active control of fluid waves in a pipe. A theoretical framework coupling the actuator to the fluid was developed and applied in the design a fluid wave actuator powered by a magnetostrictive element. The theory of a non intrusive sensor developed by Pinnington and Briscoe [98] was successfully applied. The combination of the actuator and sensor were experimentally tested and it was shown that it is possible to incorporate these elements into an "active" section of pipe that can be used to suppress fluid waves. Significant reductions in dynamic pressure of between 30 and 40 dB were achieved over a wide frequency range. However, this must be set against an increase in vibration of the pipe wall. It is believed that this increase in vibration could be either allowed for in the design of the "active" section, or be ameliorated by modifying the actuator so that it acts against an inertial mass. If the current design of actuator is adopted, then the

increase in pipe vibration may be acceptable, provided the "active" section of pipe can be isolated from adjacent sections using either active or passive isolation measures. If an inertial actuator is used it would probably be restricted to a high frequency range.

If only a single actuator is used then there will always be frequencies when fluid waves cannot be suppressed due to poor coupling between the actuator and the fluid pressure as demonstrated by the experimental results. It is thus recommended that two actuators be used so that waves can be controlled over a wide range of frequencies.

CHAPTER 7

7 GENERAL CONCLUSIONS

7.1 Conclusions

This chapter contains the general conclusions of this thesis. Detailed conclusions are included in each chapter, so only the main points are discussed here. The work covered various aspects of the active control of waves on one-dimensional structures, and each chapter addresses a different topic. The main theme throughout, has been the use of waves to model the structures under investigation, which allowed the study of both local and global dynamic behaviour. This was particularly useful for coupling the secondary sources to the structure to be controlled, as it allowed detailed examination of the coupling mechanisms, and also the global effects due to the implementation of various control strategies.

Following the introduction and literature review, Chapter 2 investigated the control of structure-borne noise on a beam by explicitly controlling flexural waves. It was shown that four secondary sources were required to completely suppress a propagating wave, such that no residual propagating or nearfield waves were generated by the secondary source array. Examples of what could be achieved with one, two, three and four secondary sources have been presented. The relationship between the secondary effort required and the distance between the secondary sources was established for all the cases considered. If the positive and negative-going waves propagating away from the secondary array are to be suppressed then very large forces are required at frequencies close to when the distance between the sources is an integer number of half-wavelengths. The least effort is required when the distance between the sources is an odd integer number of half-wavelengths. Three types of secondary sources have been considered; a force, a moment and a moment-pair, and the wave amplitudes and power generated by these sources have been discussed in Appendix 2. The final section of Chapter 2 contains an analysis of the control

strategy where a flexural propagating wave is suppressed using minimum secondary effort. It has been shown that on an infinite beam, the effort required is independent of the distance between the secondary forces, and that the effort decreases as the number of forces increases. This control strategy was also compared with a wave control strategy where the positive and negative-going waves were suppressed on a finite beam. It was shown that the minimum effort control strategy has the significant advantage that smaller secondary sources are required, which is very important in practice, as smaller actuators can be used.

Chapter 3 discussed the active control of vibrations on a beam using power as a controlling parameter. The effects of implementing two control strategies were considered; that of maximising the power absorbed by the secondary sources and the minimisation of the total power supplied to the beam by the primary and secondary sources. These control strategies were analysed on an infinite and a finite beam with up to two secondary forces. Both of these structures were modelled using waves, with the boundaries on the finite structure being modelled using reflection matrices as discussed in Appendix 2. It was already known from previous work that the power absorption control strategy, when implemented on an infinite, undamped beam using two secondary forces, was the same as the wave suppression control strategy in which the positive and negative-going propagating waves away from the array were suppressed. In this thesis it has been demonstrated that on a finite beam the strategies have strikingly different effects. Although the power absorption control strategy results in a large reduction in the displacement of the beam downstream of the secondary source array, the upstream displacement increases dramatically. This is because the strategy causes more power to be supplied by the primary force under the action of control. The most effective global control strategy proved to be minimisation of the total power supplied. A physical interpretation of the ways in which these power based control strategies work has also been presented. Some experimental work was carried out to validate the theoretical predictions, using one secondary force only on a long slender aluminium beam. The results generally correlated well with the theory.

A detailed investigation has been carried out into the use of piezoelectric devices as vibration sensors and actuators for use as error sensors and as secondary sources, and this is reported in Chapter 4. The literature was reviewed, and this revealed that there are several established models which describe the static coupling of the actuators to the structure to be controlled. Sensitivity equations for piezoelectric sensors were developed and it was shown experimentally that two piezoelectric elements fixed to opposite sides of a beam could simultaneously measure longitudinal and flexural motion on a beam. Two models of an actuator that *dynamically* couple the flexural and longitudinal actuators to a beam were then developed. In both of these models the actuators were considered as wave generators. One of these is a simple model that ignores the dynamic effects of the actuator's mass and stiffness, and the other more complicated model includes these effects. These models were then compared with each other and also with some experimental results. It was shown that the simple model adequately represented the longitudinal actuator over most practical frequencies of interest. However, the simple model of the flexural actuator was only representative provided the actuator was relatively thin compared to the host structure, and if the frequencies of interest were such that the length of the actuator was relatively small compared to a flexural wavelength. As a uni-directional actuator could be a useful secondary source, the way in which this type of actuator could be realised was investigated. It was shown that the shaping of a single actuator was an ineffective way of achieving this, and that at least two actuators were required. The actuators have to be driven with appropriately phased signals that are dependent upon the distance between the actuators and the frequency of excitation.

A self-sensing actuator was investigated theoretically and experimentally. It was shown that the fundamental design of the device is ill-conditioned. The tolerances of the electrical components in the bridge circuit required for its operation were shown to be critical, and that any deviation from the design values have a profound effect on the sensitivity of the device, in particular phase. It was thus concluded that a simple bridge circuit was inadequate in the design of a self-sensing actuator that is required to operate over a range of frequencies.

Chapter 5 discussed the control of flexural and longitudinal waves using a feedback strategy. A theoretical framework for the feedback control of both wave types has been developed. This shows that for the suppression of a propagating wave, there are certain combinations of actuator and sensor that result in an optimal feedback gain that is causal and independent of frequency. As with the other control strategies discussed in this thesis, the effects of the strategies were predicted to be different when implemented on a finite rather than an infinite structure. This again shows the importance of analysing active control strategies on finite structures once they have been shown to be effective on infinite structures. The experimental results on the implementation of the feedback control strategies were only partially successful. It is thought that unmodelled phase lags, partly due to practical transducers in the feedback loops, could cause instability if the gain was high, and if the gain was reduced they caused a degradation of performance.

Chapter 6 extended the investigation of the active control of structural waves to fluid waves in a pipe. The aim of this work was to see whether a non-intrusive sensor and actuator could be designed and built for the active control of fluid-borne waves. A theoretical framework based on an impedance model was developed that coupled the actuator to the motion of the fluid. An existing theoretical model was used for the sensor. It was demonstrated that the operation of these two devices depends upon the radial motion of the pipe being well coupled to the fluid motion, which only occurs with a soft-walled pipe. The actuator used a magnetostrictive driving element and the sensor consisted of PVDF elements connected in series around the pipe. The experimental results validated the theory and demonstrated the concept of the excitation and sensing of fluid waves using non-intrusive devices.

Overall, the thesis has demonstrated the value of modelling structures in terms of waves. The coupling of actuators to structures and the effects of a number of active control strategies on one-dimensional structures have been analysed using these models.

7.2 Recommendations for Further Work

The work reported in Chapters 2 and 3 could be extended. Using *two* secondary forces, experiments involving the wave control strategy, the wave suppression strategy using minimum effort, and the power absorption and minimisation control strategies on infinite and finite beams could be conducted. Ways of implementing the power absorption control strategy such that the de-reverberated power is measured and absorbed rather than the total secondary power, requires further investigation.

A logical extension of the research into PZT actuators discussed in Chapter 4 is an investigation into the wave scattering between longitudinal and flexural waves and vice-versa when a single PZT element is fitted to a beam. Experiments on the feedback control of longitudinal waves using actuators and sensors that do not interfere electrostatically could also be carried out. As the concept of a self-sensing actuator is attractive, an investigation should be conducted into alternative designs of a self-sensing actuator that are better conditioned against tolerances in component values.

The active control of fluid waves discussed in Chapter 6 was successful, but the disadvantage with the configuration used in this work was that the vibration of the pipe increased under the action of control. Therefore a redesign of the fluid-wave actuator should be undertaken, such that it does not excite higher order circumferential modes of the pipe when a fluid wave is generated. An investigation should also be conducted into the ways in which the fluid wave actuator and sensor could be incorporated into a practical pipework system.

APPENDIX 1

A1 WAVE MOTION IN SOLIDS AND FLUIDS

This appendix contains a brief description of the most common wave types that propagate in solids and fluids. These waves are generally described by their wavenumbers, k , which are a function of wave (phase) velocity, c , and circular frequency, ω , and the relationship between these variables is:

$$k = \frac{\omega}{c} \quad (\text{A1.1})$$

Structural waves have been described by several authors, for example [13][100], therefore only the main properties of these waves are summarized in this appendix. There are three classes of commonly occurring structural waves, namely longitudinal, shear and flexural. In an infinite medium only longitudinal and shear waves exist. Their equations of motion are:

Longitudinal

$$\frac{\partial^2 u}{\partial x^2} - \frac{1}{c_{\text{inf}}^2} \frac{\partial^2 u}{\partial t^2} = 0 \quad (\text{A1.2})$$

Shear

$$\frac{\partial^2 \theta}{\partial x^2} - \frac{1}{c_s^2} \frac{\partial^2 \theta}{\partial t^2} = 0 \quad (\text{A1.3})$$

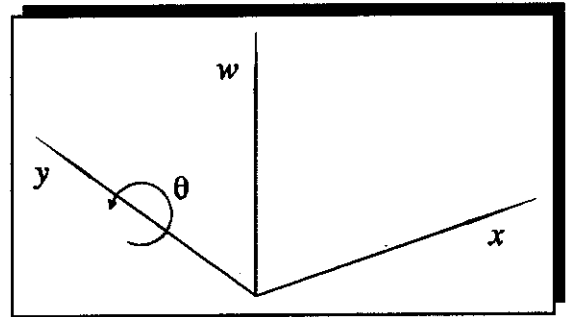


Figure A1.1 Notation for the Equations of Motion

where the notation is defined in figure A1.1 and u is in the x direction.

The wavenumbers are given by [108]:

Longitudinal Wave (infinite medium), wavenumber k_{inf}

$$k_{\text{inf}} = \frac{\omega}{\left(\frac{E(1 - \nu)}{\rho(1 + \nu)(1 - 2\nu)} \right)^{\frac{1}{2}}} \quad (\text{A1.4})$$

Shear Wave, wavenumber k_s

$$k_s = \frac{\omega}{\left(\frac{G}{\rho} \right)^{\frac{1}{2}}} = \frac{\omega}{\left(\frac{E}{2\rho(1 + \nu)} \right)^{\frac{1}{2}}} \quad (\text{A1.5})$$

where E is the Young's modulus G is the shear modulus, ρ is the density and ν is Poisson's ratio. Longitudinal and shear waves can potentially propagate in any solid. The shear wavenumber does not depend upon the shape of the body, but the longitudinal wavenumber does, as it is affected by the strain perpendicular to the wave motion. In an infinite medium all lateral motion is prevented, but in a plate, lateral motion is possible in one plane, and in a slender rod or beam lateral motion is possible in two planes. This lateral motion is governed by Poisson's ratio and its effect is to reduce the wave velocity. Thus, longitudinal waves propagate more slowly in a rod than in a plate and longitudinal waves propagate in a plate more slowly than in an infinite medium. The equations of motion for longitudinal waves in a plate and a slender rod are governed by similar wave equations to (A1.2), but with slightly different wave velocities. The longitudinal wavenumbers for a plate and a rod whose thicknesses are small compared with a longitudinal wavelength are given by:

Longitudinal Wave in a Plate, wavenumber k_{pl}

$$k_{pl} = \frac{\omega}{\left(\frac{E}{\rho(1 - \nu^2)} \right)^{\frac{1}{2}}} \quad (\text{A1.6})$$

Longitudinal Wave in a Rod, wavenumber k_l

$$k_l = \frac{\omega}{\left(\frac{E}{\rho}\right)^{\frac{1}{2}}} \quad (\text{A1.7})$$

It should be noted that the phase velocities of shear waves and all longitudinal waves are constant with frequency. The velocities of shear waves only depend on the material properties of the solids in which they propagate. Longitudinal wave velocities depend on material properties and also on whether dimensions are large or small.

Flexural waves are another class of structural waves that propagate in beams and plates. The dynamic behaviour of a beam has been described by two classic models, namely the Euler-Bernoulli and the Timoshenko model [109]. Euler-Bernoulli theory describes a simple beam model and assumes pure bending, no deformation of the beam cross-section by shear forces, and negligible rotary inertia. It is appropriate for relatively low frequencies when the thickness of the beam is less than one tenth of a flexural wavelength. The governing wave equation is given by [109]:

$$EI \frac{\partial^4 w}{\partial x^4} + \rho S \frac{\partial^2 w}{\partial t^2} = 0 \quad (\text{A1.8})$$

where w is the lateral displacement and is a function of space and time, S is the cross-sectional area of the beam, E is Young's modulus, I is the second moment of area and ρ is the density. This equation has a harmonic solution of the form:

$$w(x, t) = w \cos \omega t \quad (\text{A1.9})$$

Substituting this in to equation (A1.8) leads to the ordinary differential equation:

$$\frac{d^4 w}{dx^4} - k_b^4 w = 0 \quad (\text{A1.10})$$

where k_b is the flexural wavenumber for a beam and is given by:

Flexural (Bending) Wave on an Euler-Bernoulli Beam, wavenumber k_b

$$k_b = \left(\frac{\rho S}{EI} \right)^{\frac{1}{4}} \omega^{\frac{1}{2}} \quad (\text{A1.11})$$

The governing equation for the out-of-plane motion of a plate is similar to that of a beam, but includes the second spatial dimension and is given by [109]:

$$D \nabla^4 w + \rho h \frac{\partial^2 w}{\partial t^2} = 0 \quad (\text{A1.12})$$

where D is the flexural rigidity and is given by $D = Eh^3/12(1-\nu^2)$ and the differential operator ∇ is given by:

$$\nabla^4 = \frac{\partial^4}{\partial x^4} + 2 \frac{\partial^2}{\partial x^2 \partial y^2} + \frac{\partial^4}{\partial y^4}$$

Assuming a harmonic solution $w(x,y,t) = w \cos \omega t$, equation (A1.12) becomes:

$$\nabla^4 w - k_{\text{plate}}^4 w = 0 \quad (\text{A1.13})$$

where k_{plate} is the flexural wavenumber for a plate. As a plate has a slightly larger flexural rigidity than a rectangular beam of similar thickness, h , ($Eh^3/12(1-\nu^2)$ rather than $Eh^3/12$), its wavenumber slightly smaller. These wavenumbers are given by:

$$k_{\text{beam}} = \left(\frac{12 \rho}{Eh^2} \right)^{\frac{1}{4}} \omega^{\frac{1}{2}} \quad \text{and} \quad k_{\text{plate}} = \left(\frac{12 \rho (1 - \nu^2)}{Eh^2} \right)^{\frac{1}{4}} \omega^{\frac{1}{2}} \quad (\text{A1.14a,b})$$

Flexural waves behave in a similar way in both beams and plates and so the discussion in this appendix is confined to the behaviour of these waves in a beam. Comparison of the flexural wavenumber given in equation (A1.11), with the longitudinal and shear wavenumbers given in equations (A1.4)-(A1.7) shows that their dependency on frequency differs. The phase velocities of shear and longitudinal waves are constant and independent of frequency (non-dispersive), whereas the phase velocity of flexural waves increases with the square root of frequency (dispersive). Flexural waves also differ from longitudinal and shear waves in that there are two types of flexural wave; a propagating wave and a nearfield (evanescent) wave. The nearfield wave decays away exponentially from discontinuities, and over a distance

equal to three quarters of a wavelength its amplitude reduces by approximately 40 dB. Thus, this wave is generally only important close to discontinuities or at low frequencies.

As mentioned above the Euler-Bernoulli model is only valid for relatively low frequencies, and the Timoshenko model is required for high frequencies or for deep beams. As the analysis of a Timoshenko beam is not as well documented as the Euler-Bernoulli model, it is included in this appendix. The equation of motion for free vibration of a Timoshenko beam is [109]:

$$EI \frac{\partial^4 w}{\partial x^4} - \left(\rho \frac{EI}{\kappa G} + \rho I \right) \frac{\partial^4 w}{\partial x^2 \partial t^2} + \rho S \frac{\partial^2 w}{\partial t^2} + \frac{\rho^2 I}{\kappa G} \frac{\partial^4 w}{\partial t^4} = 0 \quad (\text{A1.15})$$

κ is the Timoshenko's shear coefficient that depends on the shape of the cross-section of the beam. (For a rectangular section $\kappa = 5/6$, for a circular section $\kappa = 9/10$ [110]), and the beam is assumed to be lossless. If the terms with $1/G$ (shear stiffness) and ρI (rotary inertia) are excluded, i.e. $G \rightarrow \infty$ and $\rho I = 0$, equation (A1.15) reduces to equation (A1.8), the Euler-Bernoulli bending equation. Assuming a harmonic solution to (A1.15) of $w(x,t) = w \cos \omega t$, dividing by EI and substituting for the longitudinal, shear and bending wavenumbers, equation (A1.15) becomes:

$$\frac{d^4 w}{dx^4} - \left(\frac{k_s^2}{\kappa} + k_l^2 \right) \frac{d^2 w}{dx^2} - k_b^4 + \frac{k_s^2 k_l^2}{\kappa} = 0 \quad (\text{A1.16})$$

This is a fourth order equation and hence has four solutions. It leads to the dispersion relation (wave number equation for free waves):

$$k^2 = \frac{\frac{k_s^2}{\kappa} + k_l^2}{2} \pm \sqrt{k_b^4 + \frac{1}{4} \left(\frac{k_s^2}{\kappa} - k_l^2 \right)^2} \quad (\text{A1.17})$$

To gain physical insight into the dynamical behaviour of the beam it is necessary to take low and high frequency limits of this equation. At low frequencies (as $\omega \rightarrow 0$) equation it reduces to:

$$k^2 = \frac{\frac{k_s^2}{\kappa} + k_l^2}{2} \pm k_b^2 \quad (\text{A1.18})$$

Substituting for the longitudinal and shear wavenumbers this becomes:

$$k^2 = k_b^4 \frac{I}{A} \left(1 + \frac{2(1 + \nu)}{\kappa} \right) \pm k_b^2 \quad (\text{A1.19})$$

Taking a rectangular uniform cross-section beam of depth h , this can be written as:

$$k^2 = k_b^2 \left(\pm 1 + Q \frac{h^2}{\lambda_b^2} \right) \quad (\text{A1.20})$$

where:

$$Q = \frac{\pi^2}{6} \left(1 + \frac{12(1 + \nu)}{5} \right) \approx 6 \quad (\text{for } \nu = 0.3)$$

and λ_b is the flexural wavelength. Examining equation (A1.19) it can be seen that if the flexural wavelength is large compared to the depth of the beam then the equation reduces to:

$$k^2 \approx \pm k_b^2 \quad (\text{A1.21})$$

i.e. there are two real and two imaginary roots which correspond to positive and negative-going propagating waves and two nearfield non propagating waves as discussed above. This behaviour is similar to that of an Euler-Bernoulli beam. At high frequencies ($\omega \rightarrow \infty$) equation (A1.17) reduces to:

$$k = \frac{k_s}{\kappa} \quad \text{and} \quad k_l \quad (\text{A1.22})$$

i.e., at high frequencies, there are two non-dispersive propagating waves that have out-of plane motion; one propagates with the velocity of a longitudinal wave, the other is a shear wave and there are no bending waves. Thus, it can be seen that the low and high frequency behaviour of a beam are significantly different. Longitudinal, shear and flexural waves can potentially propagate at low frequencies, but only

longitudinal non-dispersive out-of plane waves can propagate in a beam at high frequencies.

The governing equation for plane acoustic waves is given by [100]:

$$\frac{\partial^2 p}{\partial x^2} - \frac{1}{c_o^2} \frac{\partial^2 p}{\partial t^2} = 0 \quad (\text{A1.23})$$

where c_o is the phase velocity of the acoustic wave. The wavenumbers in air and a liquid are given by:

Sound in Air, wavenumber k_a

$$k_a = \frac{\omega}{\left(\frac{\gamma P_a}{\rho_a} \right)^{\frac{1}{2}}} \quad (\text{A1.24})$$

where γ is the ratio of heat capacities, P_a is air pressure and ρ_a is air density.

Sound in a Fluid, wavenumber k_f

$$k_f = \frac{\omega}{\left(\frac{B}{\rho_f} \right)^{\frac{1}{2}}} \quad (\text{A1.25})$$

where B is the bulk modulus of the fluid and ρ_f is the density of the fluid.

The wavenumbers for solids and fluids can be plotted on a wavenumber diagram as shown in **figure A1.2**. This shows the dispersion curves for structural waves in steel and for acoustic waves in air and water. It can be seen from equation (A1.1) that the phase velocity of a wave is inversely proportional to its wavenumber. Thus, **figure A1.2** shows that the waves with the highest wave velocity are longitudinal waves, and those with the slowest wave velocity are flexural waves (at very low frequencies) and sound waves in air.

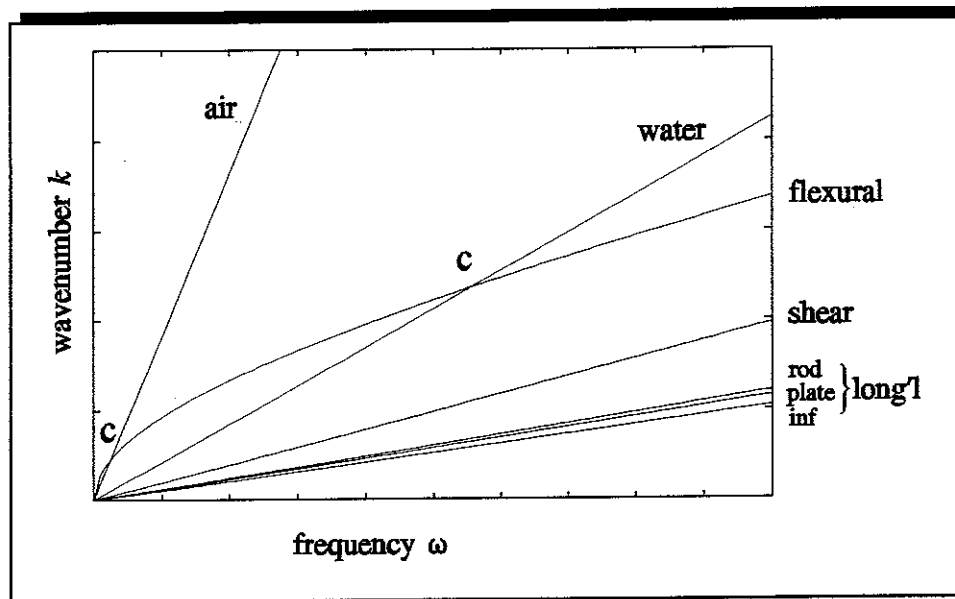


Figure A1.2 Wavenumber Diagram for Sound and Structural Waves

Typical wave velocities are:

Longitudinal waves in a steel bar	≈	5000 ms ⁻¹
Shear waves in steel	≈	3000 ms ⁻¹
Sound waves in water	≈	1500 ms ⁻¹
Sound waves in air (at 20°C)	≈	343 ms ⁻¹

The points C in **figure A1.2** are the frequencies when the flexural wave speed equals the speed of sound in air and water. These frequencies are known as the *critical*, or *lowest coincidence frequencies*, which are the frequencies when sound waves in the fluid and air are well coupled with the structural waves and energy is easily transferred from one medium to the other. The flexural wave in **figure A1.2** is the positive root of equation (A1.17) and at low frequencies its behavior is dispersive, increasing with the square root of frequency. At high frequencies the wave is non-dispersive and behaves as a shear wave. Note that it has the same slope as the shear wave. Generally, most practical vibration problems occur in the low frequency region of **figure A1.2** and thus, as well as longitudinal and shear waves, the dispersive flexural waves are of considerable importance.

APPENDIX 2

A2 A WAVE MODEL FOR A BEAM

A2.1 Introduction

The dynamics of continuous systems, such as beams and plates are described by partial differential equations. These governing equations can be solved in terms of modes or waves. In a modal model a structure is characterised by its natural frequencies, mode shapes and loss factors [14], and is generally appropriate for low frequencies. A suitable model for a structure vibrating at acoustic frequencies is a wave model as described by Mead [15] and Mace [16], and this appendix uses such a model to describe the dynamic response of a beam to the application of forces and moments.

The appendix is split up into four sections. Following the introduction, two sections are devoted to an investigation into flexural and longitudinal waves, where the relationships between the waves, and the forces and moments that generate them are discussed. The final section describes a framework which enables the study of finite beams using a wave approach. Transmission matrices are used to model the beam and reflection matrices are used to model the boundary conditions.

A2.2 Flexural Wave Generation

Lateral motion on a slender uniform beam is governed by the free flexural wave equation for an Euler-Bernoulli beam, which is:

$$EI \frac{\partial^4 w}{\partial x^4} + \rho S \frac{\partial^2 w}{\partial t^2} = 0 \quad (\text{A2.1})$$

where w is the lateral displacement, S is the cross-sectional area of the beam, E is Young's modulus, I is the second moment of area and ρ is the density. This equation

has a harmonic solution of the form:

$$w(x,t) = \text{Re}\{w(x)e^{j\omega t}\} \quad (\text{A2.2})$$

where $w(x)$ is called the complex displacement and Re stands for the real part. Substituting this into equation (A2.1) leads to the ordinary differential equation:

$$\frac{d^4 w}{dx^4} - k_b^4 w = 0 \quad (\text{A2.3})$$

where k_b is the flexural wave number described in Appendix 1. Suppressing the $e^{j\omega t}$ time dependence for clarity, the transverse displacement at any point on the beam is given by the equation:

$$w(x) = A_1 e^{k_b x} + A_2 e^{-k_b x} + A_3 e^{jk_b x} + A_4 e^{-jk_b x} \quad (\text{A2.4})$$

where the A 's are complex wave amplitudes and are dependent upon the way in which the beam is excited. The complex wave amplitudes resulting from the application of a harmonic point force and line moment are described by Mead [15] and are summarized in this Appendix.

A2.2.1 Waves Generated by a Point Force

In the case when a lateral force is applied two structures are considered; a semi-infinite and a finite beam. If a force is applied at the end of a semi-infinite beam as shown in **figure A2.1**, then two waves are generated; a propagating wave, A_4 and an exponentially decaying nearfield (evanescent) wave, A_2 . The complex amplitudes of these waves are given by the equation [15]:

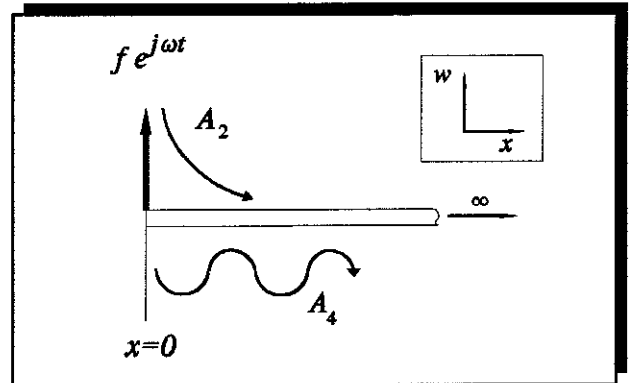


Figure A2.1 Flexural Waves Generated by a Lateral Force on a Semi-infinite Beam

$$\begin{bmatrix} A_2 \\ A_4 \end{bmatrix} = \frac{-f(1+j)}{2EI k_b^3} \begin{bmatrix} 1 \\ 1 \end{bmatrix} \quad (\text{A2.5})$$

If the complex force is applied to an infinite beam instead, as shown in **figure A2.2**, then waves are generated on either side of the force. The amplitudes of these waves are given by [15]:

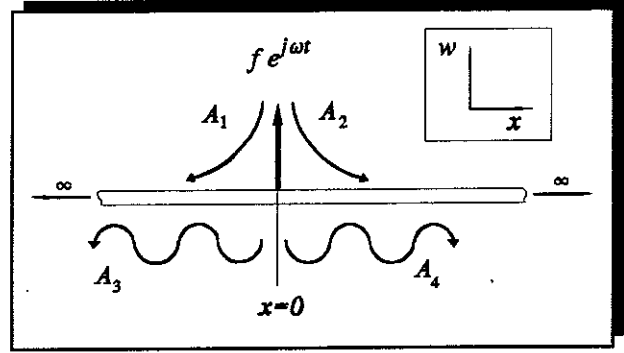


Figure A2.2 Flexural Waves Generated by a Lateral Force on an Infinite Beam

$$\begin{bmatrix} A_1 \\ A_2 \\ A_3 \\ A_4 \end{bmatrix} = \frac{-f}{4EI k_b^3} \begin{bmatrix} 1 \\ 1 \\ j \\ j \end{bmatrix} \quad (\text{A2.6})$$

The generated waves can only propagate away or decay away from the applied force, thus for a semi-infinite and infinite beam the displacement of the beam to the right of the force is given by:

$$w(x) = A_2 e^{-k_b x} + A_4 e^{-jk_b x} \quad (\text{A2.7})$$

and on an infinite beam, the displacement of the beam to the left of the applied force is given by:

$$w(x) = A_1 e^{k_b x} + A_3 e^{jk_b x} \quad (\text{A2.8})$$

where the wave amplitudes are defined in equations (A2.5) and (A2.6). It should be noted that on both a semi-infinite and infinite beam, all of the generated wave amplitudes are the same. However, on a semi-infinite beam the nearfield and propagating waves are in-phase, but on an infinite beam they are in quadrature. Damping can be included in this wave model of a beam by using a complex wave number which is a function of a complex Young's modulus [13], used to represent internal losses within the beam.

A2.2.2 Waves Generated by Line Moments

In this section only an infinite beam is considered, as moment excitation at the end of a semi-infinite beam was not applicable to the work in this thesis. Consider the line harmonic moment applied to an infinite beam as shown in figure A2.3. Four flexural waves are generated as with the point force, and the complex wave amplitudes are given by the equation [15]:

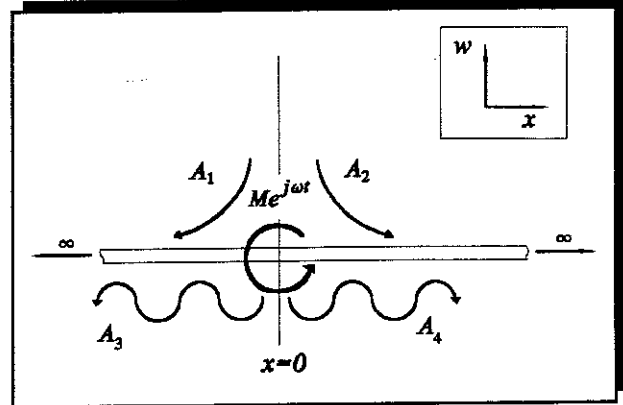


Figure A2.3 Flexural Waves Generated by a Moment on an Infinite Beam

$$\begin{bmatrix} A_1 \\ A_2 \\ A_3 \\ A_4 \end{bmatrix} = \frac{M}{4EI k_b^2} \begin{bmatrix} 1 \\ -1 \\ -1 \\ 1 \end{bmatrix} \quad (\text{A2.9})$$

These wave amplitudes can be substituted into equations (A2.7) and (A2.8) to give the response of the beam to the applied moment. It should be noted that when a moment is applied, the displacement of the beam at the point of application is zero as the propagating and nearfield waves are in anti-phase.

The application of a single line moment is difficult to achieve in practice, because generic moment actuators are not commercially available. Crawley and de Luis [32], however, showed that a piezoceramic actuator generates

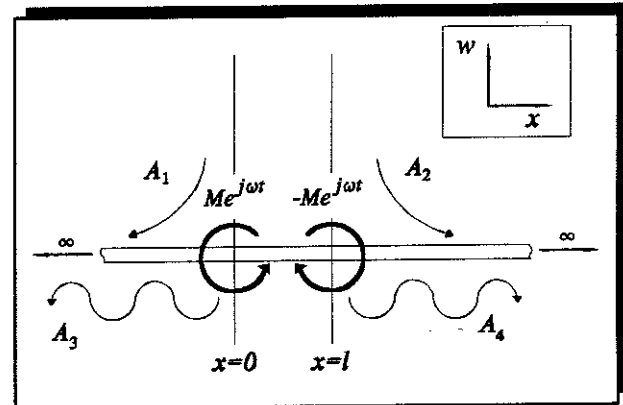


Figure A2.4 Flexural Waves Generated by a Pair of Moments on an Infinite Beam

moments, working in anti-phase, at the each end of the actuator. Consider the pair

of moments a distance l apart applied to an infinite beam as shown in **figure A2.4**. The wave amplitudes either side of the actuator are the superposition of the waves generated by both of the moments, and are given by:

$$\begin{bmatrix} A_1 \\ A_2 \\ A_3 \\ A_4 \end{bmatrix} = \frac{1}{4EI k_b^2} \begin{bmatrix} 1 & e^{-k_b l} \\ -1 & -e^{k_b l} \\ -1 & -e^{-j k_b l} \\ 1 & e^{j k_b l} \end{bmatrix} \begin{bmatrix} M \\ -M \end{bmatrix} \quad (\text{A2.10})$$

At low frequencies, when a flexural wavelength is large compared to the length of the actuator, then $kl \rightarrow 0$ and the approximations $e^{\pm k_b l} \approx 1 \pm k_b l$ and $e^{\pm j k_b l} \approx 1 \pm j k_b l$ can be substituted into equation (A2.10) to give the approximate wave amplitudes:

$$\begin{bmatrix} A_1 \\ A_2 \\ A_3 \\ A_4 \end{bmatrix} \approx \frac{Ml}{4EI k_b} \begin{bmatrix} 1 \\ 1 \\ -j \\ -j \end{bmatrix} \quad (\text{A2.11})$$

These can be substituted into equations (A2.7) and (A2.8) to give the response of a beam to a pair of moments working in anti-phase at low frequencies.

A2.3 Longitudinal Wave Generation

Longitudinal motion on a slender, uniform beam is governed by the free longitudinal wave equation [13], which is:

$$\frac{\partial^2 u}{\partial x^2} - \frac{1}{c_l^2} \frac{\partial^2 u}{\partial t^2} = 0 \quad (\text{A2.12})$$

where c_l is the longitudinal wave speed in a rod discussed in Appendix 1 and u is the axial displacement. This has a harmonic solution of the form:

$$u(x, t) = \text{Re}\{u(x)e^{j\omega t}\} \quad (\text{A2.13})$$

Substituting this into equation (A2.12) leads to the ordinary differential equation:

$$\frac{d^2 u}{dx^2} + k_l^2 u = 0 \quad (\text{A2.14})$$

where k_l is the flexural wave number described in Appendix 1. Suppressing the $e^{j\omega t}$ time dependence for clarity, the axial displacement at any point on the beam is given by the equation:

$$u(x) = A_l e^{jk_l x} + A_r e^{-jk_l x} \quad (\text{A2.15})$$

where the A 's are complex wave amplitudes and are dependent upon the way in which the beam is excited. Comparison of flexural and longitudinal wave motion shows that there are significant differences in their behaviour. In Appendix 1 it was shown that Longitudinal waves have a constant phase speed and inspection of equations (A2.4) and (A2.15) shows that there are no longitudinal nearfield waves.

A2.3.1 Waves Generated by In-Plane Forces

Consider an infinite slender beam with a point harmonic force applied as shown in figure A2.5. Two longitudinal waves are generated by this force; one propagating in a negative direction and the other in a positive direction. The axial displacement of the beam for $x \leq 0$ can be written as:

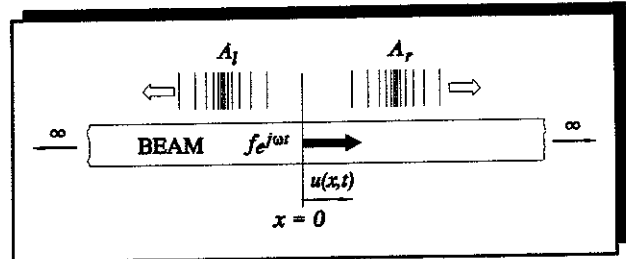


Figure A2.5 Longitudinal Waves Generated by an In-Plane Force on an Infinite Beam

$$u_-(x) = A_l e^{jk_l x} \quad (\text{A2.16})$$

and the displacement when $x \geq 0$, as:

$$u_+(x) = A_r e^{-jk_l x} \quad (\text{A2.17})$$

Continuity of displacement at $x = 0$ means that $u_-(0) = u_+(0)$, therefore:

$$A_l = A_r \quad (\text{A2.18})$$

The stress-strain relationship at $x = 0$, on the right hand section of the beam is:

$$\frac{f}{2} = -ES \frac{\partial u(0)}{\partial x} \quad (\text{A2.19})$$

where S is the cross-sectional area of the beam. Combining equations (A2.17)-(A2.19) gives the complex wave amplitudes:

$$\begin{bmatrix} A_l \\ A_r \end{bmatrix} = \frac{-jf}{2k_l ES} \begin{bmatrix} 1 \\ 1 \end{bmatrix} \quad (\text{A2.20})$$

These can be substituted into equations (A2.16) and (A2.17) to give the axial displacement of the beam in response to an in-plane harmonic force. If a force of similar magnitude is applied at the end of a semi-infinite beam then there is only longitudinal wave generated with twice the amplitude of the waves generated on an infinite beam.

A PZT actuator fitted to a beam and driven to generate longitudinal waves can be modelled as forces applied to the beam at each end of the actuator [32] as shown in **figure A2.6**. The wave amplitudes either side of the actuator are the superposition of the waves

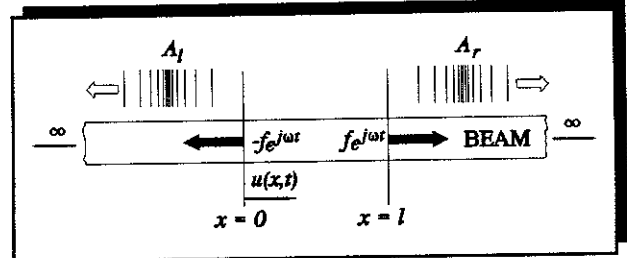


Figure A2.6 Longitudinal Waves Generated by a Pair of In-Plane Forces on an Infinite Beam

generated by each of the forces in a similar way to the pair of moments in the flexural case. The wave amplitudes are given by the equation:

$$\begin{bmatrix} A_l \\ A_r \end{bmatrix} = \frac{-j}{2k_l ES} \begin{bmatrix} 1 & e^{-jk_l l} \\ 1 & e^{jk_l l} \end{bmatrix} \begin{bmatrix} -f \\ f \end{bmatrix} \quad (\text{A2.21})$$

These can be substituted into equations (A2.16) and (A2.17) to give the axial displacement of the beam in response to a pair of in-plane forces a distance of l apart

working in anti-phase. Approximations can be made in a similar way to the flexural case when a longitudinal wavelength is large compared to the length of the actuator. The resulting approximate wave amplitudes at low frequencies are given by:

$$\begin{bmatrix} A_l \\ A_r \end{bmatrix} \approx \frac{fl}{2ES} \begin{bmatrix} -1 \\ 1 \end{bmatrix} \quad (\text{A2.22})$$

which are independent of frequency.

A2.4 Modelling of Finite Beams

The analysis conducted in this appendix so far gives the relationships between generated wave amplitudes and applied forces and moments on *infinite* beams and *semi-infinite* beams excited at the end. The lateral and axial displacements of a beam are the superposition of these generated (direct) waves. However, on a *finite* beam the situation is more complex, as waves are reflected from boundaries and combine with the direct waves resulting in a complicated wave-field. The general framework for a finite beam is similar for both flexural and longitudinal waves, but the lateral model is more complicated as there are nearfield as well as propagating waves. These flexural waves interact at a boundary, and so a 2 x 2 matrix is required to describe a lateral boundary condition, but only a single coefficient is necessary to describe a longitudinal boundary condition. In this section a wave-model is developed for a finite beam with flexural wave motion and this model is then modified for longitudinal motion.

Consider first an infinite beam excited by a lateral point harmonic force as shown in **figure A2.2**. The four wave components can be conveniently grouped in two vectors, one of positive-going waves, \underline{a}^+ and one of negative-going waves \underline{a}^- , i.e.,

$$\underline{a}^+ = \begin{Bmatrix} A_2 \\ A_4 \end{Bmatrix} ; \quad \underline{a}^- = \begin{Bmatrix} A_1 \\ A_3 \end{Bmatrix}$$

The wave amplitudes along a uniform length of beam are related by [16]:

$$\underline{a}^+(x_o + x) = \underline{T}_f \underline{a}^+(x_o)$$

$$\underline{a}^-(x_o + x) = \underline{T}_f^{-1} \underline{a}^-(x_o)$$

where the flexural transmission matrix \underline{T}_f is given by:

$$\underline{T}_f = \begin{bmatrix} e^{-k_b x} & 0 \\ 0 & e^{-jk_b x} \end{bmatrix} \quad (\text{A2.23})$$

This model enables the amplitudes and phase of the waves to be determined at any point on the beam. Consider now a finite beam with arbitrary boundary conditions as shown in **figure A2.7**. The displacement of the beam will now not only be the superposition of the waves generated directly by the force, f , but will comprise the waves that are reflected from the boundaries as well, i.e:

$$\text{Beam Displacement} = \text{Direct Waves} + \text{Reflected Waves}$$

It is first necessary to determine an expression for the displacement of the beam due to the reflected waves. Referring to **figure A2.7**, the vectors \underline{a}_d^+ and \underline{a}_d^- are the direct waves generated by the application of the force f and are defined as:

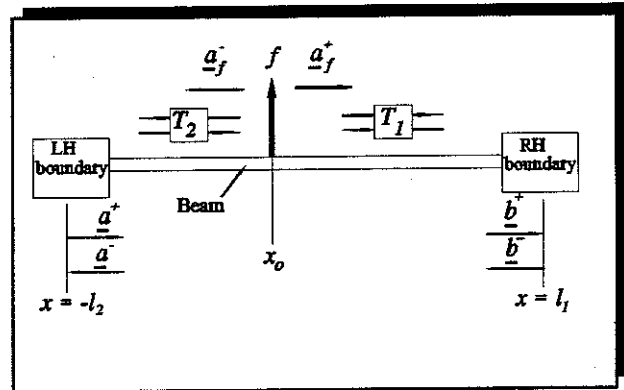


Figure A2.7 Forced Vibration of a Finite Beam

$$\underline{a}_d^+ = \begin{Bmatrix} A_{2d} \\ A_{4d} \end{Bmatrix} ; \quad \underline{a}_d^- = \begin{Bmatrix} A_{1d} \\ A_{3d} \end{Bmatrix}$$

where the superscript d denotes that the waves are *direct* waves generated by the force, f , i.e., those generated on an infinite beam. \underline{T}_1 and \underline{T}_2 are the transfer matrices as defined in equation (A2.23) but with $x = l_1$ and $x = -l_2$ respectively, and the

vectors \underline{a}^+ , \underline{a}^- , \underline{b}^+ and \underline{b}^- contain the wave amplitudes at the boundaries. The incident waves at the boundaries are reflected, and the phase shifts associated with these reflections depend on the particular boundary conditions [16]; wave conversion between propagating and evanescent components also occurs at these boundaries. The relationship between the incoming and outgoing waves at a boundary are related by reflection matrices, \underline{R}_L and \underline{R}_R , where the suffices L and R denote left and right. Hence:

$$\underline{a}^+ = \underline{R}_L \underline{a}^- \quad \text{and} \quad \underline{b}^- = \underline{R}_R \underline{b}^+$$

Three common boundaries are simply supported, clamped and free, and the associated matrices with these conditions are [16]:

$$\underline{R}_S = \begin{bmatrix} -1 & 0 \\ 0 & -1 \end{bmatrix} \quad \underline{R}_C = \begin{bmatrix} j & -(1-j) \\ -(1+j) & -j \end{bmatrix} \quad \underline{R}_F = \begin{bmatrix} j & (1-j) \\ (1+j) & -j \end{bmatrix}$$

where \underline{R}_S is the reflection matrix for the simply supported condition, \underline{R}_C is the reflection matrix associated with the clamped or fixed condition and \underline{R}_F the reflection matrix associated with the free condition. Now the wave vectors can be related thus:

$$\begin{aligned} \underline{a}^+ &= \underline{R}_L \underline{a}^- \\ &= \underline{R}_L (\underline{T}_2 \underline{a}_d^- + \underline{T}_2 \underline{T}_1 \underline{b}^-) \\ &= \underline{R}_L \underline{T}_2 (\underline{a}_d^- + \underline{T}_1 \underline{R}_R (\underline{T}_1 \underline{a}_d^+ + \underline{T}_1 \underline{T}_2 \underline{a}^+)) \end{aligned}$$

Noting that $\underline{a}_{x_0}^+ = \underline{T}_2 \underline{a}^+$, this can be re-arranged to give the amplitudes and phase

of the *reflected positive-going waves* at the position on the beam where the force is applied:

$$\underline{a}_{x_0}^+ = \left[[I] - (\underline{T}_2 \underline{R}_L \underline{T}_2) (\underline{T}_1 \underline{R}_R \underline{T}_1) \right]^{-1} \underline{T}_2 \underline{R}_L \underline{T}_2 (\underline{a}_d^- + (\underline{T}_1 \underline{R}_R \underline{T}_1) \underline{a}_d^+) \quad (\text{A2.24})$$

Similarly the *reflected negative-going waves* are given by:

$$\underline{a}_{x_0}^- = \left[[I] - (\underline{T}_1 \underline{R}_R \underline{T}_1) (\underline{T}_2 \underline{R}_L \underline{T}_2) \right]^{-1} \underline{T}_1 \underline{R}_R \underline{T}_1 (\underline{a}_d^+ - (\underline{T}_2 \underline{R}_L \underline{T}_2) \underline{a}_d^-) \quad (\text{A2.25})$$

It should be noted that if there are no boundaries, i.e. R_L and R_R are equal to zero then both the vectors are identically zero. If $R_L = 0$ there are no positive-going reflections (equation (A2.24)) and if $R_R = 0$ there are no negative-going reflections (equation (A2.25)). Now, in terms of their wave components, the vectors are:

$$\underline{a}_{x_0}^+ = \begin{Bmatrix} A_{2r} \\ A_{4r} \end{Bmatrix}; \quad \underline{a}_{x_0}^- = \begin{Bmatrix} A_{1r} \\ A_{3r} \end{Bmatrix}$$

where the subscript r denotes reflection. Equations (A2.24) and (A2.25) are shown pictorially in figures A2.8 and A2.9 respectively. As mentioned above the total displacement of the beam will be made up of reflected waves and direct waves generated by the force, f . The lateral displacement of the beam is given by equation (A2.4) and if $x_0 = 0$, the wave amplitudes are given by:

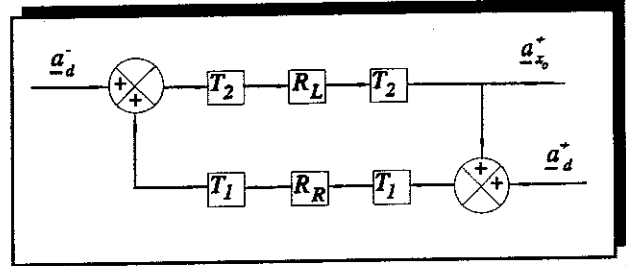


Figure A2.8 Pictorial Representation of Equation (A2.24)

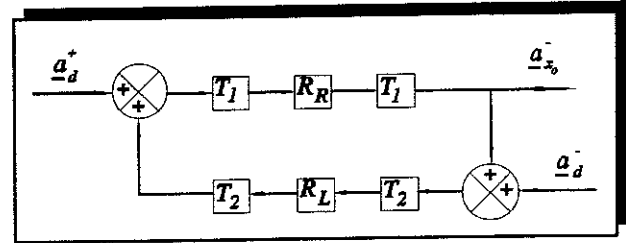


Figure A2.9 Pictorial Representation of Equation (A2.25)

For $-l_2 \leq x \leq 0$

$$\begin{aligned} A_1 &= A_{1r} + A_{1d} \\ A_2 &= A_{2r} \\ A_3 &= A_{3r} + A_{3d} \\ A_4 &= A_{4r} \end{aligned}$$

For $0 < x \leq l_1$

$$\begin{aligned} A_1 &= A_{1r} \\ A_2 &= A_{2r} + A_{2d} \\ A_3 &= A_{3r} \\ A_4 &= A_{4r} + A_{4d} \end{aligned}$$

It can be seen that the reflected waves propagate throughout the whole of the beam but only the direct A_1 and A_3 waves are generated to the left of x_0 , and the direct A_2 and A_4 waves to the right of x_0 .

In the longitudinal case, where the lateral force in **figure A2.7** is replaced with an in plane force such as that shown in **figure A2.5**, equations (A2.24) and (A2.25) can still be used to describe the reflected waves, but now there is only a propagating wave in each direction. Thus

$$a_d^+ = A_{rd} ; \quad a_d^- = A_{ld}$$

where the subscript d refers to a direct or generated wave rather than a reflected wave. Boundary reflection coefficients are +1 for a free end and -1 for a fixed end, and the transmission matrix reduces to $T_l = e^{-jk_l x}$. Equation (A2.15) gives the axial displacement of the beam, where the wave amplitudes are given by:

For $-l_2 \leq x \leq 0$

$$\begin{aligned} A_l &= A_{lr} + A_{ld} \\ A_r &= A_{rr} \end{aligned}$$

For $0 < x \leq l_1$

$$\begin{aligned} A_l &= A_{lr} \\ A_r &= A_{rr} + A_{rd} \end{aligned}$$

APPENDIX 3

A3 VIBRATIONAL POWER FLOW IN BEAMS

A3.1 Introduction

This appendix describes active vibration control strategies that use power as a controlling parameter. Two control strategies are discussed; that of maximising the power absorbed by a secondary force array and the minimization of the total power supplied by both primary and secondary forces. However, before the principle behind these strategies is outlined, the general concept of vibrational power flow into and along a beam is discussed, and power supplied by various actuators is compared. Finally the conditions for power absorption by a force actuator are examined.

A3.2 Power Supplied by Various Actuators

Power flow into and along a beam is discussed at length other researchers, for example [111]. Only the results of this work relevant to the thesis are summarized in this appendix. Consider first a general case where a force, f with a harmonic time dependence acting at a point on a structure causes a phase shifted harmonic response (velocity, v) at

the same frequency as the excitation force. This is shown pictorially in figure A3.1.

The time averaged input power P is given by [111]:

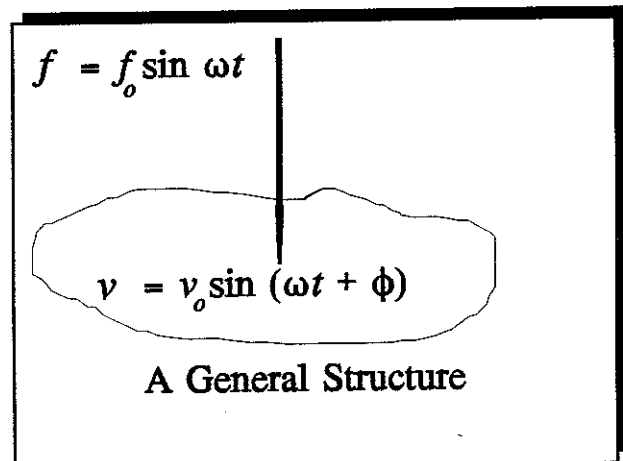


Figure A3.1 Force Excitation of a General Structure

$$P = \frac{1}{T} \int_0^T f_o v_o \sin \omega t \sin(\omega t + \phi) dt \quad (\text{A3.1})$$

Integrating this expression leads to alternative forms:

$$P = \frac{1}{2} f_o v_o \cos \phi = \frac{1}{2} \text{Re} \{ f v^* \} = \frac{1}{2} |f|^2 \text{Re} \{ M \} = \frac{1}{2} |v|^2 \text{Re} \{ Z \} \quad (\text{A3.2a-d})$$

where ω is the circular frequency of excitation, ϕ is the phase angle between the force and the response, $*$ denotes a complex conjugate, M is the point mobility of the structure and Z is the point impedance. Re stands for the real part. Equation (A3.2c) can be used to determine the power input when the structure is excited by a force source, and equation (A3.2d) used when the structure is excited by a velocity source.

The dynamic behaviour of a beam at acoustic frequencies can be described in terms of waves which are generally written in terms of displacement rather than velocity. An alternative representation of equation (A3.2b), which is relevant to this thesis is:

$$P = \frac{\omega}{2} \text{Im} \{ f w^* \} = -\frac{\omega}{2} \text{Im} \{ f^* w \} \quad (\text{A3.3a,b})$$

where Im stands for the imaginary part. Consider now an infinite uniform beam excited by a point force f , as shown in figure A3.2. The power supplied to the beam is given by equation (A3.3). Now the displacement at x_o is the superposition of the near-field wave, A_2 and the propagating wave, A_4 as discussed in Appendix 2 and is given by:

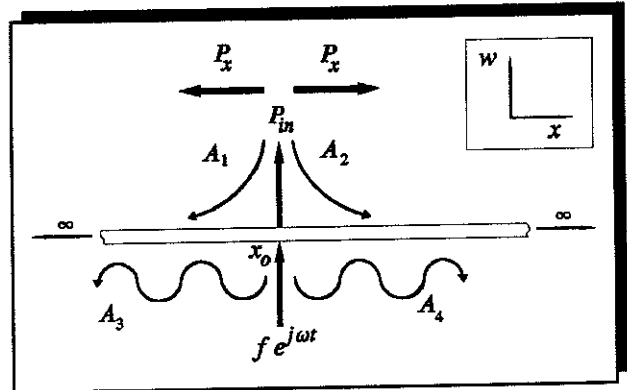


Figure A3.2 Power Input into an Infinite Uniform Beam by a Point Force

$$w(0) = -\frac{f}{4EI k_b^3} (1 + j) \quad (\text{A3.4})$$

where E is the Young's modulus, I is the second moment of area about the neutral axis and k_b is the flexural wavenumber discussed in Appendix 1. Substituting for $w(0)$ into equation (A3.3b) gives the expression for the power supplied to the beam by a lateral point force.

$$P_{in} = \frac{\omega |f|^2}{8EI k_b^3} \quad (\text{A3.5})$$

As the flexural wave number, k_b is proportional to ω^2 , P_{in} is proportional to $\omega^{-1/2}$ and hence decreases with increasing frequency. At any point along the beam there is an internal bending moment and shear force, and both of these transmit power away from the source. Goyder and White [111] showed that the power supplied by the driving force is transferred to the beam's internal shear force at the point of excitation. As the distance from the driving force increases, the power is transferred from the internal shear force to the internal bending moment until the power transmitted by these two components is equal. *The nearfield wave, therefore, is seen to couple the two components of the power flow and does not itself transmit power unless it impinges on a discontinuity or interacts with another nearfield wave.* In the far field the power is transmitted by the propagating waves, and in either direction is equal to:

$$P_x = \frac{\omega |f|^2}{16EI k_b^3} \quad (\text{A3.6})$$

It should be noted that in a finite undamped beam with lossless boundary conditions such as free, fixed and simply supported, no net power flows into the beam. The power is reactive and flows back and forth between the source and the boundaries. In a damped, finite system the energy is dissipated through internal losses only.

Consider now an infinite uniform beam excited by a point harmonic moment M , as shown in **figure A3.3**. The mechanism of power input by a moment is similar to that

of a point force. In this case, however, the power is transferred from the applied moment to an internal bending moment at the point of excitation, and the nearfield wave again couples the shear force and the bending moment. However, power is transferred from the bending

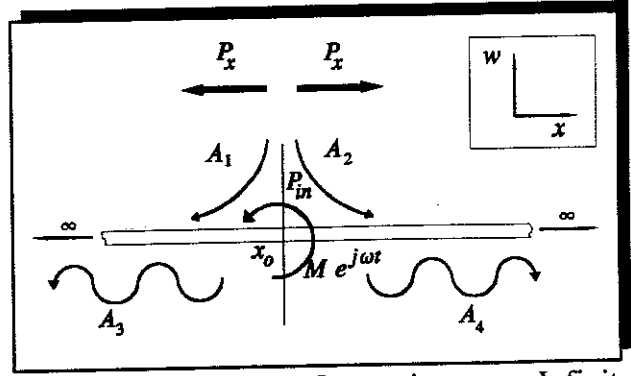


Figure A3.3 Power Input into an Infinite Uniform Beam by a Point Moment

moment component to the shear force component so that in the far-field the power is transmitted in equal proportions between the internal shear force and bending moment by the propagating wave, as in the case of a force source. The alternative versions of equations (A3.3a,b) for moment excitation of a beam are:

$$P_{in} = \frac{\omega}{2} \text{Im} \{M(w')^*\} = -\frac{\omega}{2} \text{Im} \{M^* w'\} \quad (\text{A3.7a,b})$$

where M is the harmonic moment applied and $(w')^*$ is the complex conjugate of the spatial derivative of the transverse displacement (slope). The slope of a beam as a result of an applied moment at $x = 0$ is:

$$w'(0) = \frac{M}{4EI k_b} (1 - j) \quad (\text{A3.8})$$

and hence the power supplied by a moment is:

$$P_{in} = \frac{\omega |M|^2}{8EI k_b} \quad (\text{A3.9})$$

The power carried in a propagating wave in the far field is half the power supplied and is given by:

$$P_x = \frac{\omega |M|^2}{16EI k_b} \quad (\text{A3.10})$$

It should be noted that for a moment source the power supplied to a beam is

proportional to $\omega^{1/2}$ and hence a moment is better at exciting a beam at high frequencies.

The third type of source considered in this appendix consists of a pair of moments a distance l apart which is the action of a PZT flexural vibration actuator of length l as discussed by Crawley and de Luis [32]. Consider such a source applied to an infinite beam as shown in **figure A3.4**. The slope of the beam at $x = 0$ is given by:

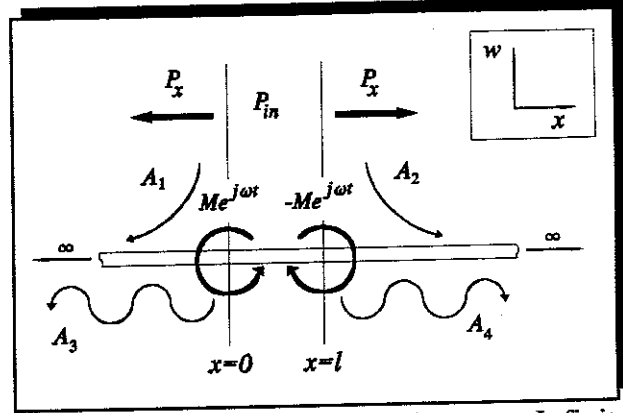


Figure A3.4 Power Supplied to an Infinite Uniform Beam by a Pair of Moments

$$w'(0) = \frac{M}{4EI k_b} \{ 1 - e^{-k_b l} - j + j e^{-j k_b l} \} \quad (\text{A3.11})$$

which can be substituted into equation (A3.7b) to give the power supplied by the moment at the left-hand end of the actuator:

$$P_{left} = \frac{\omega |M|^2}{8EI k_b} (1 - \cos k_b l) \quad (\text{A3.12})$$

The slope of the beam at $x = l$ is given by:

$$w'(l) = \frac{-M}{4EI k_b} \{ 1 - e^{-k_b l} - j + j e^{-j k_b l} \} \quad (\text{A3.13})$$

which can be substituted into equation (A3.7b) to give the power supplied by the moment at the right-hand end of the actuator:

$$P_{right} = \frac{\omega |M|^2}{8EI k_b} (1 - \cos k_b l) \quad (\text{A3.14})$$

The total power supplied by a pair of moments a distance l apart is the sum of the powers supplied by the moments at each end of the actuator and is thus given by:

$$P_{in} = \frac{\omega |M|^2}{4EI k_b} (1 - \cos k_b l) \quad (A3.15)$$

The power carried in the propagating wave in the far field is half of this and is given by:

$$P_{in} = \frac{\omega |M|^2}{8EI k_b} (1 - \cos k_b l) \quad (A3.16)$$

Unlike the force and moment actuators, the power supplied by this actuator has a complicated frequency dependence. To compare these actuators the power supplied to an infinite beam by a force, a moment and a pair of moments per unit input force and moment are plotted as a function of l/λ (frequency) in **figure A3.5**, where λ is a flexural wavelength.

It can be seen that at low frequencies the force actuator supplies more power than the other two actuators, but the power that other actuators supply increases with frequency. However, at frequencies where the length of the PZT actuator equals an integral number of flexural wavelengths, the power supplied by this actuator reduces to zero. It is clear that the actuator should ideally be operated in higher frequency regions, close to where the length of the actuator equals odd integral numbers of half flexural wavelengths.

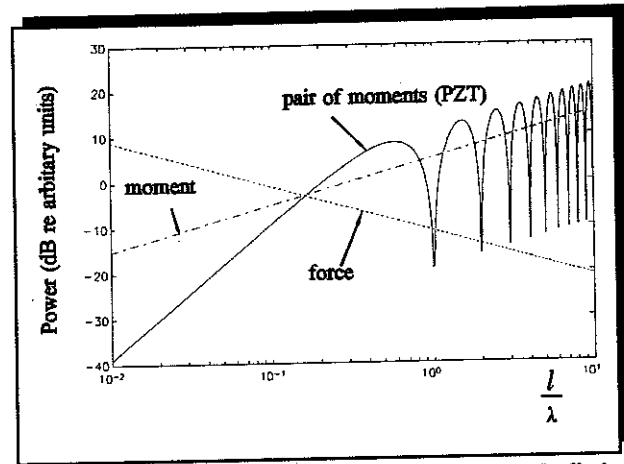


Figure A3.5 Power Supplied to an Infinite Beam by Different Actuators

A PZT actuator can also be used to generate longitudinal waves as discussed in Appendix 2. It is

modelled as a pair of forces applied at each end of the actuator as shown in **figure**

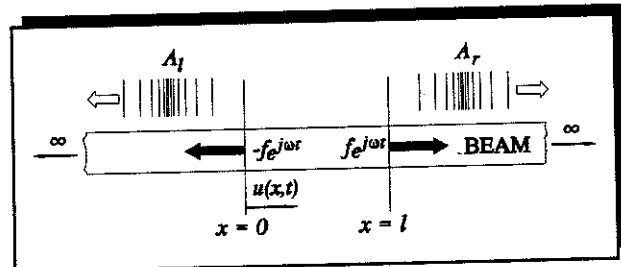


Figure A3.6 Power Supplied to an Infinite Uniform by a Pair of In-Plane Forces

A3.6. The forces at each end of the actuator supply power to the beam, and the power can be calculated using the equation:

$$P = -\frac{\omega}{2} \text{Im}\{f^* u\} \quad (\text{A3.17})$$

The displacement of the beam at each end of the actuator can be determined from equation (A3.17), which gives

$$u(0) = \frac{jf}{2k_l ES} (1 - e^{jk_l l}) \quad (\text{A3.18})$$

and

$$u(l) = \frac{jf}{2k_l ES} (1 - e^{-jk_l l}) \quad (\text{A3.19})$$

where k_l is the longitudinal wavenumber and S is the cross-sectional area of the beam. These can be substituted into equation (A3.17) and summed to give the total power supplied by the actuator:

$$P = \frac{\omega |f|^2}{2k_l ES} (1 - \cos k_l l) \quad (4.33)$$

This is plotted in **figure A3.7** which should be compared with **figure A3.5**. The trend is similar at low frequencies, starting very small and increasing with frequency until the length of the actuator equals half a longitudinal wavelength. The power then reduces to zero when the length of the actuator equals a whole wavelength. This pattern then

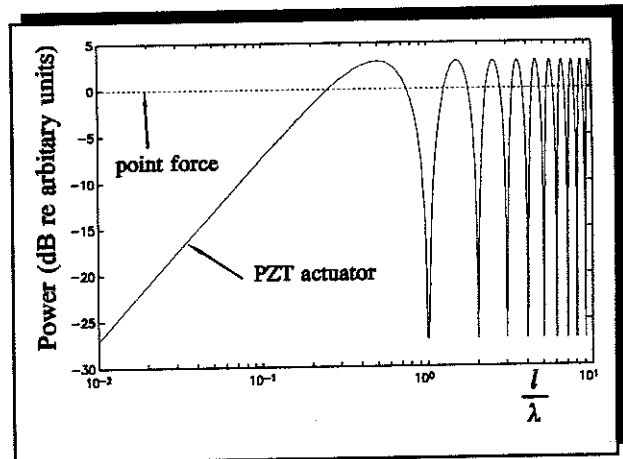


Figure A3.7 Power Supplied to an Infinite Beam by a Longitudinal PZT Actuator

repeats with increasing frequency but the power supplied does not steadily increase like the flexural actuator as longitudinal waves travel at constant speed. Also plotted in **figure A3.7** is the power supplied by a single point in-plane force. It can be seen

that this supplies much more power than a PZT actuator at low frequencies, but at higher frequencies the maximum power supplied by the PZT actuator is 3 dB greater than this.

A3.3 Power Based Control Strategies

Two power based control strategies of maximizing the acoustic power absorbed by secondary sources and minimizing the total acoustic power supplied to a system have been comprehensively described by Elliott *et al* [36], and are discussed in this Appendix. Although the strategies were derived generally, they were written in terms of acoustic impedances, and it is more appropriate in the structural case to cast the problem in terms of forces and displacements using dynamic stiffnesses and receptances. In this section, general expressions are derived for the secondary forces required to (a) maximize the power absorbed by a secondary force array, and (b) to minimize the total power supplied to the beam by the primary and secondary forces. The expressions are quite general and can be applied to any one dimensional structure.

Consider a section of beam with a primary force array \underline{F}_p and a secondary force array \underline{F}_s , as shown in figure A3.8. No restrictions are placed on the number of forces in that can be placed in each array and no restrictions are placed on the nature of the system boundaries. The vector of primary forces can be written as:

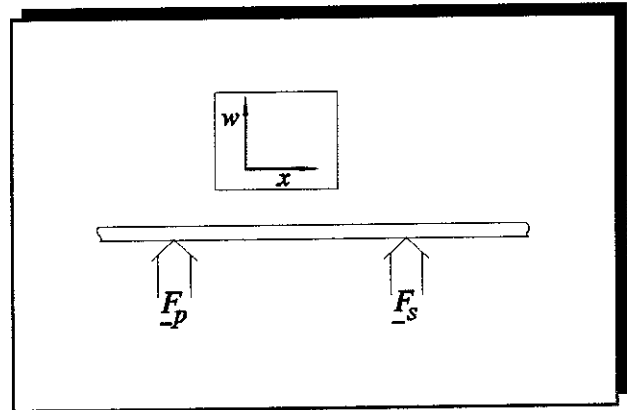


Figure A3.8 A Primary and Secondary Array Positioned on a Beam

$$\underline{F}_p = [f_{p1}, f_{p2}, \dots, f_{pn}]^T \quad (\text{A3.21})$$

and the transverse displacements at the points of application of the primary forces can

be written as:

$$\underline{w}_p = [w_{p1}, w_{p2}, \dots, w_{pn}]^T \quad (\text{A3.22})$$

The vector of secondary forces can be written as:

$$\underline{F}_s = [f_{s1}, f_{s2}, \dots, f_{sn}]^T \quad (\text{A3.23})$$

and the transverse displacements at the points of application of the secondary forces can be written as:

$$\underline{w}_s = [w_{s1}, w_{s2}, \dots, w_{sn}]^T \quad (\text{A3.24})$$

Now the displacement vectors can also be written as:

$$\underline{w}_p = \underline{\alpha}_{pp} \underline{F}_p + \underline{\alpha}_{ps} \underline{F}_s \quad (\text{A3.25})$$

and

$$\underline{w}_s = \underline{\alpha}_{sp} \underline{F}_p + \underline{\alpha}_{ss} \underline{F}_s \quad (\text{A3.26})$$

where $\underline{\alpha}_{pp}$ is the receptance matrix relating the displacements at the primary force positions to the primary forces and $\underline{\alpha}_{ss}$ is the receptance matrix relating the displacements at the secondary force positions to the secondary forces. $\underline{\alpha}_{sp}$ and $\underline{\alpha}_{ps}$ are the transfer receptance matrices relating the displacements at the primary/secondary force positions to the secondary/primary forces. Now, the power outputs of the primary and secondary force arrays can be written as:

$$P_p = -\frac{\omega}{2} \text{Im} \{ \underline{F}_p^H \underline{w}_p \} \quad (\text{A3.27})$$

$$P_s = -\frac{\omega}{2} \text{Im} \{ \underline{F}_s^H \underline{w}_s \} \quad (\text{A3.28})$$

which are the vector equivalents of (A3.3b). P_p and P_s are the power outputs of the primary and secondary force arrays, and H denotes the transpose of the complex conjugate (hermitian transpose). Using the relationships for the displacements at the array positions given in equations (A3.25) and (A3.26), the power outputs can be written as:

$$P_p = -\frac{\omega}{2} \text{Im} \left\{ \underline{F}_p^H \underline{\alpha}_{pp} \underline{F}_p + \underline{F}_p^H \underline{\alpha}_{ps} \underline{F}_s \right\} \quad (\text{A3.29})$$

and

$$P_s = -\frac{\omega}{2} \text{Im} \left\{ \underline{F}_s^H \underline{\alpha}_{sp} \underline{F}_p + \underline{F}_s^H \underline{\alpha}_{ss} \underline{F}_s \right\} \quad (\text{A3.30})$$

A3.3.1 Maximizing the Power Absorbed by the Secondary Force Array

With this control strategy, the power absorbed by the secondary force array given by equation (A3.30), has to be minimized. Noting that:

$$\text{Im} \left\{ \underline{F}_s^H \underline{\alpha}_{sp} \underline{F}_p \right\} = -\frac{j}{2} \left\{ \underline{F}_s^H \underline{\alpha}_{sp} \underline{F}_p - \left(\underline{F}_s^H \underline{\alpha}_{sp} \underline{F}_p \right)^* \right\} \quad (\text{A3.31})$$

and letting $\underline{X}_{ss} = \text{Im} \left\{ \underline{\alpha}_{ss} \right\}$, equation (A3.30) can be written as:

$$P_s = -\frac{\omega}{2} \left\{ \underline{F}_s^H \underline{X}_{ss} \underline{F}_s + \underline{F}_s^H \left\{ -\frac{j}{2} \underline{\alpha}_{sp} \right\} \underline{\alpha}_{ss} \underline{F}_p + \underline{F}_p^H \left\{ \frac{j}{2} \underline{\alpha}_{sp}^H \right\} \underline{F}_s \right\} \quad (\text{A3.32})$$

This is an equation of Hermitian quadratic form as described by Nelson *et al* [35], which has a general form:

$$P_s = \underline{F}_s^H \underline{A} \underline{F}_s + \underline{F}_s^H \underline{b} + \underline{b}^H \underline{F}_s \quad (\text{A3.33})$$

where:

$$\underline{A} = -\frac{\omega}{2} \underline{X}_{ss}, \quad \underline{b} = \frac{j\omega}{4} \underline{\alpha}_{sp} \underline{F}_p$$

Now, provided \underline{A} is positive-definite there will be a unique global minimum of P_s and thus maximizing the power absorption of the secondary force array. This can be argued [37] by the physical reasoning that the power input due to the control forces alone, must always be positive and so \underline{A} is positive-definite. Power absorption can

thus be maximized with respect to the secondary forces. The optimum set of secondary forces which give a global minimum of P_s can be shown to be [35]:

$$\underline{F}_{sa} = -\underline{A}^{-1}\underline{b} \quad (\text{A3.34})$$

which in this case is:

$$\underline{F}_{sa} = \frac{j}{2} \underline{X}_{ss}^{-1} \underline{\alpha}_{sp} \underline{F}_p \quad (\text{A3.35})$$

It should be noted that the strategy of maximizing the power absorbed by the secondary force array is a local control strategy. Examination of equation (A3.35) shows that the secondary forces can be calculated with knowledge of only the displacements at the secondary force positions in the absence of control and the point and transfer dynamic stiffnesses associated with the secondary force array (\underline{X}_{ss}^{-1})

A3.3.2 Minimizing the Total Power Supplied by the Primary and Secondary Force Arrays

This control strategy involves minimizing the total power supplied by the primary and secondary force arrays. The total power P_t , supplied to the beam by both arrays is given by:

$$P_t = P_p + P_s \quad (\text{A3.36})$$

Substituting for P_p and P_s from equations (A3.29) and (A3.30) gives:

$$P_t = -\frac{\omega}{2} \text{Im} \left\{ \underline{F}_p^H \underline{\alpha}_{pp} \underline{F}_p + \underline{F}_p^H \underline{\alpha}_{ps} \underline{F}_s + \underline{F}_s^H \underline{\alpha}_{sp} \underline{F}_p + \underline{F}_s^H \underline{\alpha}_{ss} \underline{F}_s \right\} \quad (\text{A3.37})$$

Now,

$$\text{Im} \left\{ \underline{F}_p^H \underline{\alpha}_{pp} \underline{F}_p \right\} = -\frac{j}{2} \left\{ \underline{F}_p^H \underline{\alpha}_{pp} \underline{F}_p - \left(\underline{F}_p^H \underline{\alpha}_{pp} \underline{F}_p \right)^* \right\} \quad (\text{A3.38})$$

As $\left(\underline{F}_p^H \underline{\alpha}_{pp} \underline{F}_p \right)^*$ is a scalar it is equal to $\underline{F}_p^H \underline{\alpha}_{pp}^H \underline{F}_p$, its transpose. Also

$\alpha_{pp} = \alpha_{pp}^T$ due to reciprocity, therefore $\alpha_{pp}^H = \alpha_{pp}^*$. Thus equation (A3.38)

becomes:

$$\begin{aligned} \text{Im} \left\{ \underline{F}_p^H \alpha_{pp} \underline{F}_p \right\} &= -\frac{j}{2} \left\{ \underline{F}_p^H \alpha_{pp} \underline{F}_p - \underline{F}_p^H \alpha_{pp}^* \underline{F}_p \right\} \\ &= \left\{ \underline{F}_p^H \left(-\frac{j}{2} (\alpha_{pp} - \alpha_{pp}^*) \right) \underline{F}_p \right\} \end{aligned}$$

Therefore

$$\text{Im} \left\{ \underline{F}_p^H \alpha_{pp} \underline{F}_p \right\} = \underline{F}_p^H \text{Im} \{ \alpha_{pp} \} \underline{F}_p \quad (\text{A3.39})$$

Hence the total power into the beam can be written as:

$$P_t = -\frac{\omega}{2} \left\{ \underline{F}_s^H \underline{X}_{ss} \underline{F}_s + \underline{F}_s^H \underline{X}_{sp} \underline{F}_p + \underline{F}_p^H \underline{X}_{sp}^T \underline{F}_s + \underline{F}_p^H \underline{X}_{pp} \underline{F}_p \right\} \quad (\text{A3.40})$$

where $\underline{X}_{sp}^T = \underline{X}_{ps}$ due to reciprocity, and

$$\underline{X}_{ss} = \text{Im} \{ \alpha_{ss} \}, \quad \underline{X}_{sp} = \text{Im} \{ \alpha_{sp} \}, \quad \underline{X}_{pp} = \text{Im} \{ \alpha_{pp} \}$$

This is an equation of Hermitian quadratic form which has a general form:

$$P_t = \underline{F}_s^H \underline{A} \underline{F}_s + \underline{F}_s^H \underline{b} + \underline{b}^H \underline{F}_s + c \quad (\text{A3.41})$$

where:

$$\underline{A} = -\frac{\omega}{2} \underline{X}_{ss}, \quad \underline{b} = -\frac{\omega}{2} \underline{X}_{sp} \underline{F}_p, \quad c = -\frac{\omega}{2} \underline{F}_p^H \underline{X}_{pp} \underline{F}_p$$

Provided \underline{A} is positive-definite, which can be argued in the same manner as in the power absorption strategy, then there will be a unique global minimum of P_t . Power can thus be minimised with respect to the secondary forces and the optimum set of secondary forces which give a global minimum of P_t is:

$$\underline{F}_{so} = -\underline{A}^{-1} \underline{b} \quad (\text{A3.42})$$

which in this case is:

$$\underline{F}_{so} = -\underline{X}_{ss}^{-1} \underline{X}_{sp} \underline{F}_p \quad (\text{A3.43})$$

A3.4 Mechanisms of Power Absorption by a Force Actuator

Section A3.3 discussed the concept of power absorption by a force actuator. This section examines the physical conditions that must exist at the interface between a force actuator and a beam for vibrational power to flow from the beam to the actuator. Consider a section of uniform beam with a force applied at $x = 0$, as shown in **figure A3.9**.

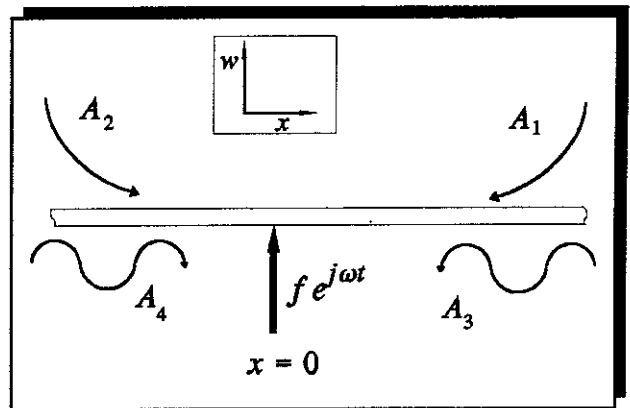


Figure A3.9 Excitation of a Beam by a Lateral Force

A_1 , A_2 , A_3 and A_4 are waves incident on the force actuator caused by disturbances or discontinuities elsewhere on the beam. The transverse displacement at $x = 0$ is made up of these waves and the direct displacement caused by the force (the principle of superposition). The actuator generating the force f , can either;

- Supply power to the beam
- Absorb power from the beam
- Neither supply nor absorb power from the beam.

These conditions are investigated in turn. The power supplied by a lateral force is given by equation (A3.3), which can be expanded to give:

$$P_{in} = |f||w| \operatorname{Im} \{ \cos \phi - j \sin \phi \} \quad (\text{A3.44})$$

which reduces to:

$$P_{in} = -|f||w| \sin \phi \quad (\text{A3.45})$$

where ϕ is the phase angle between the transverse displacement of the beam at $x = 0$ and the applied force f . A positive angle means the displacement leads the force. A graph of power input into the beam against phase angle is shown in **figure A3.10**. Examination of this figure shows that:

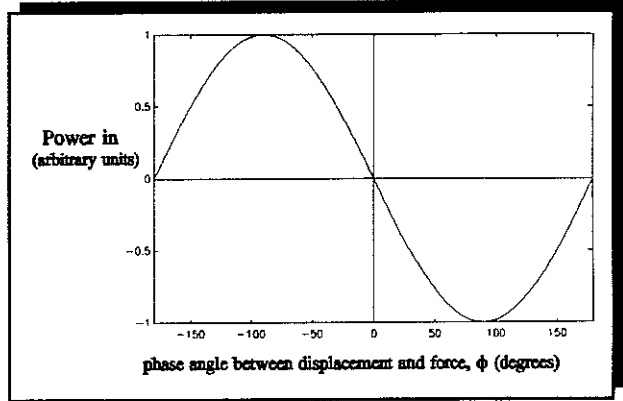


Figure A3.10 Power Supplied to- and Absorbed from the Beam as a Function of Phase Angle between the Displacement and the Force Applied

- a. When $-180^\circ < \phi < 0$, that is when the transverse displacement at $x = 0$ lags the force, power is supplied to the beam by the force actuator.
- b. When $0^\circ < \phi < 180^\circ$, that is when the transverse displacement at $x = 0$ leads the force, power is absorbed by the force actuator.
- c. When $\phi = 0$ or 180° , that is when the force and displacement at $x = 0$ are either in phase or out of phase, no power is supplied to the beam.
- d. Maximum power is supplied to the beam when $\phi = -90^\circ$ and maximum power is absorbed by the force actuator when $\phi = 90^\circ$.

In the absence of any waves present which are *not* generated by the force f , power will *always* be supplied to the beam by the force actuator.

APPENDIX 4

A4 EXPERIMENTAL APPARATUS

This appendix contains details of the experimental equipment and materials used during the project.

A4.1 Beam Experiments

A4.1.1 Experimental Equipment

Accelerometers, Brüel and Kjær

Type 4368 (mass 30 g), Serial No 801055, sensitivity 4.6 pC m s^{-2}

Type 4369 (mass 14 g), Serial No 361782, sensitivity 1.98 pC m s^{-2}

Type 4369 (mass 14 g), Serial No 320345, sensitivity 1.94 pC m s^{-2}

Force Transducers, Brüel and Kjær

Type 8200 Serial No 942231, sensitivity 4.03 pC N^{-1}

Type 8200 Serial No 556082, sensitivity 3.58 pC N^{-1}

Conditioning Amplifiers, Brüel and Kjær

Type 2626, Serial No 1029097 (Mechs No 325)

Type 2626, Serial No 1130092 (Mechs No 333)

Type 2626, Serial No 1429099 (Mechs No 411)

Type 2626, Serial No 1429098 (Mechs No 410)

Type 2626, Serial No 1429097 (Mechs No 409)

Analyzer Hewlett Packard Frequency Response Analyzer, type 3566A, Serial No A619046.0.

TI'KO PCX433 Personal Computer

Wayne Kerr Capacitance Probe Amplifier Serial Number 138

Wayne Kerr Capacitance Probes

E1 1210 and ME1 172 (lateral motion)

MC1 176 (longitudinal motion)

1.98 gauge factor Strain Gauges

2 x Strain Gauge Indicators, Measurements Group P-3500 Serial Nos 50518 & 53300

Strain Gauge Amplifier type Sangamo Western Controls Modular Carrier Amplifier
C56 Serial No 100608

Transformers

1:125 Transformer manufactured by Quad Electronics

1:5 Transformer

Variable Capacitor manufactured by Muirhead Co Ltd.

LVDT

weights and carrier

Oscilloscope

Power Amplifiers

Derritron Type 25 W Power Amplifier

Derritron Type 300 W Power Amplifier

2 x Derritron Type VP2 Electrodynamic Shaker

Phase Controller for Sinusoidal Signals

Calibrated frequency range 10 Hz - 1 kHz

Max. input voltage - 3 V

Gain $0.93 \pm 7\%$

Phase control range 360°

Capacitance Meter RS Components CM 20A Serial No 90703240

A4.1.2 Beam and PZT Elements

The beam used in the experiments conducted in this project was an aluminium beam with the following specification:

Aluminium Bar	Alloy 5083
	Density 2670 kg m^{-3}
	Young's modulus $71 \times 10^9 \text{ N m}^{-2}$
	nominal width 30 mm
	nominal thickness 6 mm
	nominal length 4 m

The aluminium bar was tapered at one end to progressively reduce the flexural rigidity, and enveloped in a piece of exponentially shaped rubber to provide some damping. These measures were taken to give an anechoic termination for flexural waves. The beam with the PZT elements attached, which was suspended by four lengths of light cord and is shown in **figure A4.1**

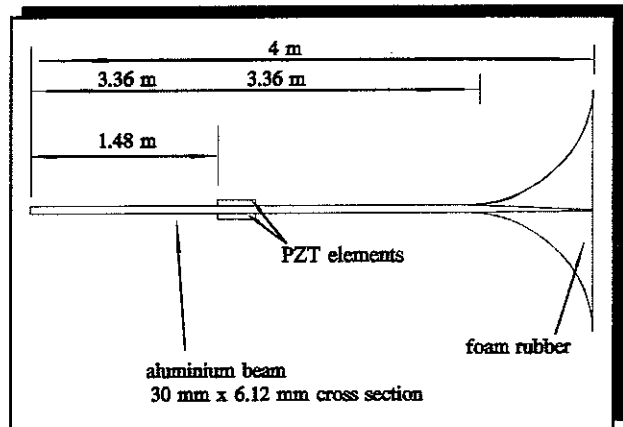


Figure A4.1 Beam Used in Experiments - Plan View

The PZT elements, (Matroc Unilator PC5H) used as sensors and actuators were fixed to the beam using a conductive glue (Planned Products 2400 Circuit Works Conductive Epoxy) and are shown schematically in **figure**

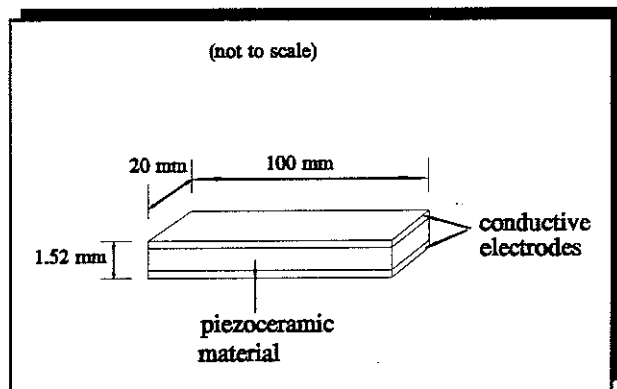


Figure A4.2 A Piezoceramic Element

A4.2. A detailed drawing of the PZT elements fixed to the beam is shown in **figure A4.3**. 2 x 100 mm x 120 mm x 1.52 mm PC5H Piezoceramic (PZT) Elements (see data sheet in **figure A4.4**)

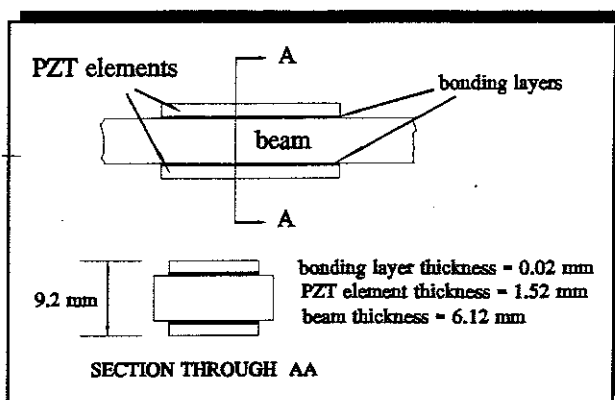


Figure A4.3 PZT Elements Fixed to the Beam

		Macro Uniaxial Materials and Nearest Equivalent Navo Type from DDUSTD-1376A (SH)									
Parameter	Symbol	Unit	PC3 Type IV	PC4 Type III	PC4A Type I	PC4D Type I	PC5 Type II	PC5H Type VI	PC6 Type VI		
Electrical-Low field											
Relative permittivity	ϵ'_{33}		1100	1075	1100	1325	1800	2900	225		
Dielectric Loss	$\tan \delta$.008	.002	.002	.002	.02	.027	.024		
Resistivity	ρ_{el}	$\Omega \cdot m$	10^{10}	10^{13}	10^{12}	10^{10}	10^{12}	10^{13}	10^{10}		
Electrical-High field											
Increase in ϵ'_{33} @ 2KV		%	2.7	1.9	3.8	5.1	—	—	—		
Dielectric Loss @ 2KV		%	.007	.004	.007	.010	—	—	—		
Increase in ϵ'_{33} @ 4KV		%	7.25	4.68	9.63	12.68	—	—	—		
Dielectric Loss @ 4KV		%	.015	.01	.018	.021	—	—	—		
Electro-Mechanical											
Coupling Factors											
k_p			.26	.53	.51	.55	.58	.58	.08		
k_{31}			.15	.31	.30	.32	.34	.34	.04		
k_{33}			.44	.71	.68	.67	.67	.68	.47		
k_t			.31	.45	.49	.45	.45	.48	.47		
Charge Constants											
d_{31}		$\times 10^{-12} C/N$	-42	-104	-103	-123	-178	-212	-4		
d_{33}		$\times 10^{-12} C/N$	127	287	296	335	409	529	65		
d_{tt}		$\times 10^{-12} C/N$	43	79	90	89	58	104	56		
Voltage Constants											
g_{31}		$\times 10^{-3} V/mN$	4.3	-10.9	-10.5	-10.5	-11.0	-8.3	-2.2		
g_{33}		$\times 10^{-3} V/mN$	13.0	30.2	30.4	28.6	25.7	20.8	32.6		
g_t		$\times 10^{-3} V/mN$	4.4	8.3	9.2	7.6	3.6	4.1	28.2		
Frequency Constants											
N_p		$Hz \cdot m$	3177	2292	2252	2257	2002	2094	2841		
N_{31}		$Hz \cdot m$	2373	1576	1581	1636	1375	1497	2192		
N_{33}		$Hz \cdot m$	2371	1570	1549	1576	1415	1483	2004		
N_t		$Hz \cdot m$	1800	1000	1780	1800	1470	1430	—		
N_c		$Hz \cdot m$	1505	1020	1000	1030	830	940	—		
N_i		$Hz \cdot m$	2715	2082	2046	2168	1944	1968	2176		
Quality Factor	Q_m		600	1200	600	600	60	60	1200		
Mechanical											
Compliances											
s_{33}^E		$\times 10^{-12} m^2/N$	8.1	14.7	15.0	14.4	17.2	16.8	9.1		
s_{11}^E		$\times 10^{-12} m^2/N$	7.8	11.7	12.1	12.3	16.7	15.1	7.5		
s_{12}^E		$\times 10^{-12} m^2/N$	-2.4	-3.6	-3.8	-3.8	-5.2	-4.7	-2.3		
s_{33}^D		$\times 10^{-12} m^2/N$	6.5	7.4	8.1	8.0	9.4	9.1	7.8		
s_{11}^D		$\times 10^{-12} m^2/N$	7.6	10.8	11.0	10.7	15.0	13.3	7.5		
s_{12}^D		$\times 10^{-12} m^2/N$	-2.6	-4.8	-5.1	-5.1	-7.1	-6.4	-2.3		
s_{66}^D		$\times 10^{-12} m^2/N$	20.4	30.7	31.7	32.2	43.7	39.6	19.7		
Density	ρ	kg/m^3	5800	7600	7600	7650	7750	7300	6800		
Curie Temperature	T_c	$^{\circ}C$	130	300	320	330	370	210	220		
Time Stability											
Coupling Factor	k_p		-3.5	-2.1	-2.0	-1.7	-0.4	-2.5	-1.7*		
Capacitance	C	Relative change per decade %	-3.6	-4.1	-5.3	-4.6	-1.8	-0.7	-2.3		
Frequency	f		0.7	1.1	1.2	1.0	0.2	0.2	0.2		

Figure A4.4 Data Sheet For Piezoceramic Elements

A4.2 Pipe Experiments

A4.2.1 Experimental Equipment

Steel Plates Density 7800 kg m^{-3}

 Young's modulus $208 \times 10^9 \text{ N m}^{-2}$

 Thick plate $1.25 \text{ m} \times 1.25 \text{ m} \times 3/8"$

 Thin plate $1.25 \text{ m} \times 1.25 \text{ m} \times 3/16"$

Perspex Pipe 2.17 m long, 150 mm outside diameter, 140 mm inside diameter

Solartron 1254 4 Channel Frequency Response Analyzer, Serial No 200122 and 8

Channel expansion box, Serial No 000133

Solartron 1200 Signal Processor, Serial No 200174

Hydrophone, Brüel and Kjær Type 8103, Serial No 1565849 sensitivity 98 pC Pa^{-1}

Oscilloscope

Force Transducers, Brüel and Kjær

 Type 8200 Serial No 942231, sensitivity 4.03 pC N^{-1}

 Type 8200 Serial No 556090, sensitivity 3.98 pC N^{-1} (hammer)

Accelerometers

 ATOCHEM, ACH-01-03 W (mass 4 g), Serial No 023692, sensitivity 9.2 mV g^{-1} with matching charge amplifier

 Endevco Type 2250A M1-10 with built in charge amplifier (mass 0.4 g)

 #1 sensitivity 10.98 mV g^{-1}

 #2 sensitivity 10.68 mV g^{-1}

 #3 sensitivity 10.83 mV g^{-1}

 #4 sensitivity 10.93 mV g^{-1}

 Brüel and Kjær, Type 4368 (mass 30 g), Serial No 801055, sensitivity 4.6 pC m s^{-2} (plate test)

Conditioning Amplifiers, Brüel and Kjær

 Type 2626, Serial No 1029097 (Mechs No 325) (force gauge)

 Type 2626, Serial No 1130092 (Mechs No 333) (accelerometer)

 Type 2626, Serial No 1429099 (Mechs No 411) (hydrophone)

2 x Derritron Type 25 W Power Amplifier

Shakers

Goodmans Model 390A Electrodynamic Shaker (primary)

Derritron Type VP2 Electrodynamic Shaker (secondary)

Fluid Actuator

Phase Controller

PVDF Film manufactured by KYNAR, type DT052K/L (7 in No)

Young's modulus $2.5 \times 10^9 \text{ Nm}^{-2}$

Density 1728 kg m^{-3}

70 mm x 15 mm x 52 μm

Piezoelectric constant $23 \times 10^{-12} \text{ V m}^{-1}$

A4.2.2 Fluid Actuator Drawings

This section contains the engineering drawings for the actuator used to control pressure waves in a pipe

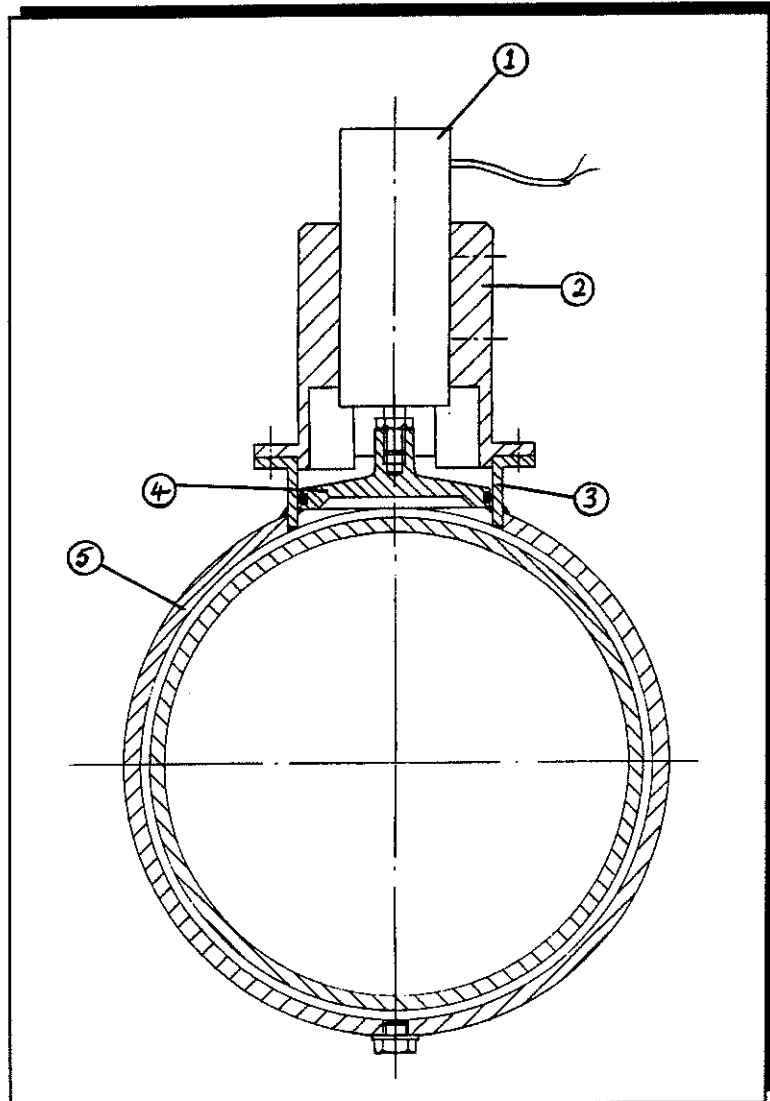


Figure A4.5 Fluid Actuator Assembly

- All dimensions are in millimetres
- Tolerances are not shown

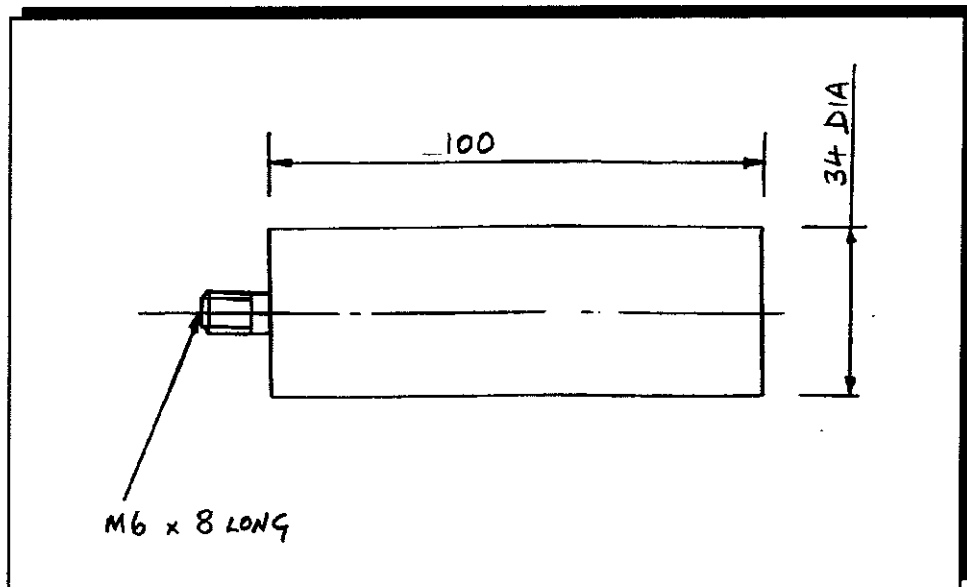


Figure A4.6 Item 1 Magnetostrictive Actuator Outline Drawing

Notes

1. Supplier: Edge Technologies, inc
ETREMA Products Division
306 South 16th Street
Ames, IA 50010, USA

2. Actuator Type: 50/6-MP

3. Data (abbreviated from data sheet)

Max Displacement (peak-to-peak)	50 μ m
Rated Load	490 N
Current input	± 1.5 A
Coil Resistance	6.4 Ω
Magnetic Bias	yes
Mechanical pre-stress	yes

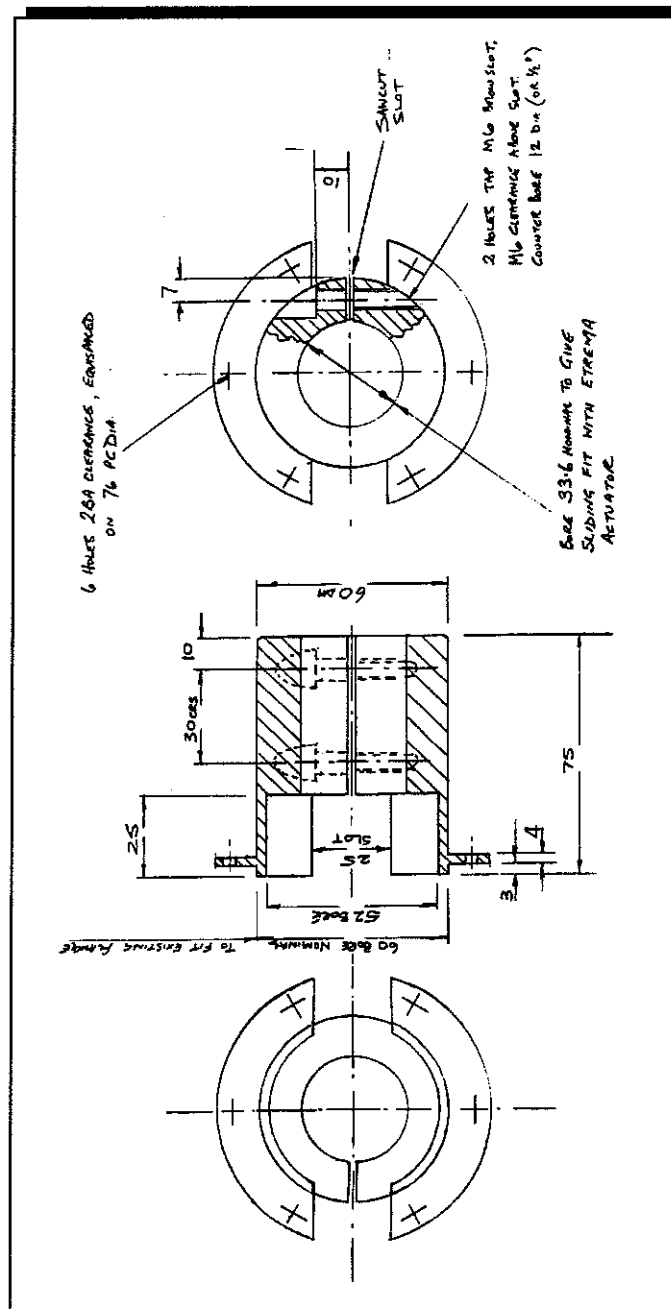


Figure A4.7 Item 2 Actuator Clamp

Notes

1. Material Aluminium.
2. Make 1 off.

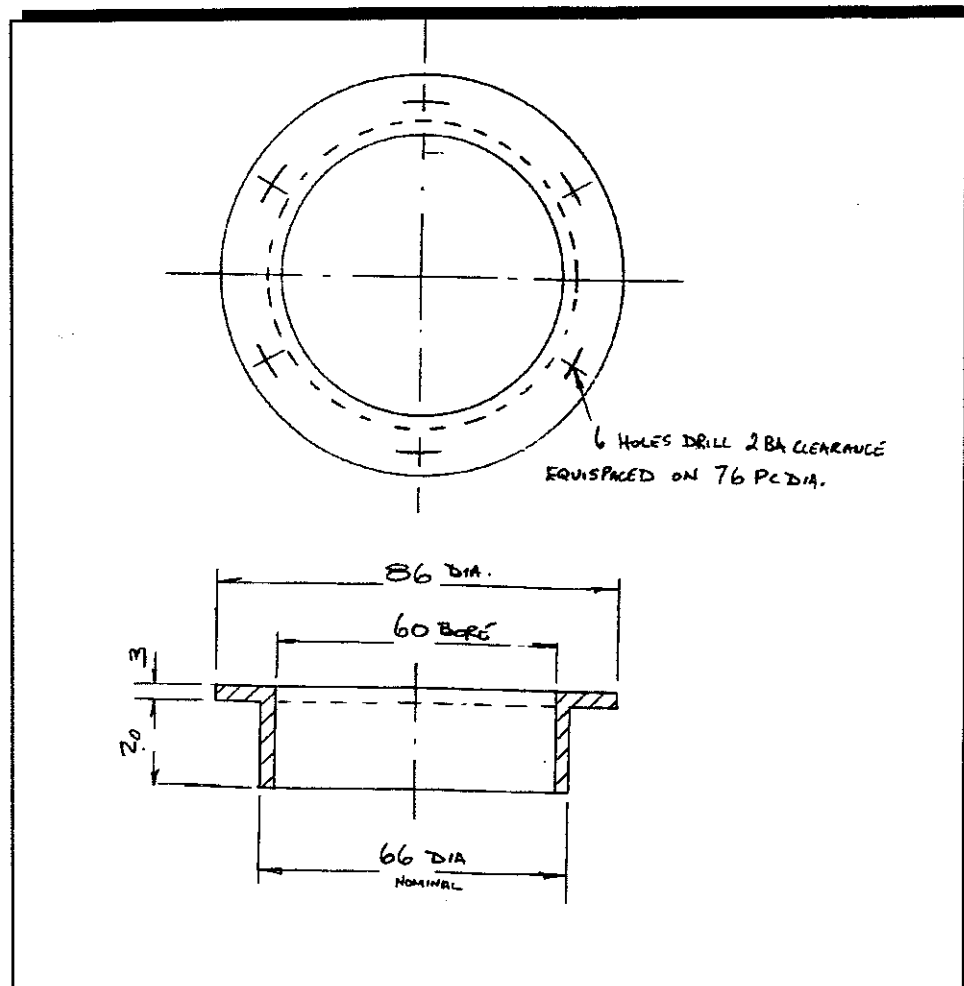


Figure A4.8 Item 3 Cylinder

Notes

1. Material Mild Steel.
2. The lower part of cylindrical section that mates with the cylinder ring is to be shaped to that section so that it does not protrude.
3. Make 1 off.

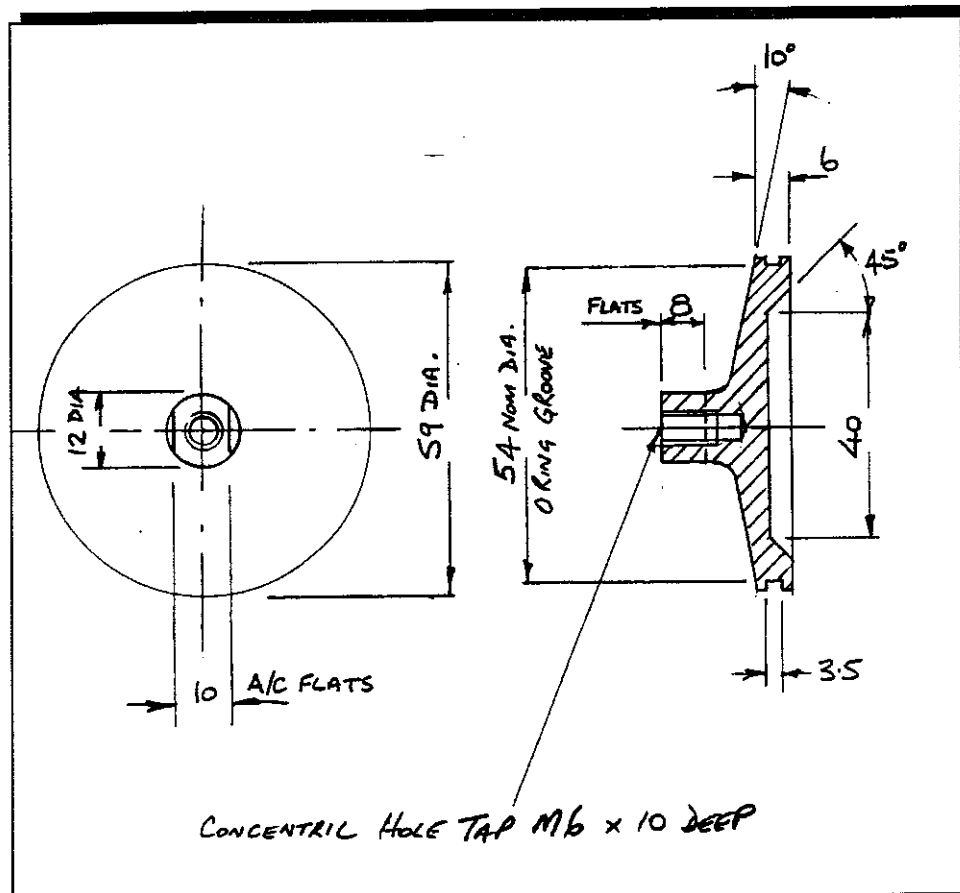


Figure A4.9 Item 4 Piston

Notes

1. Material Aluminium
2. Make 1 off

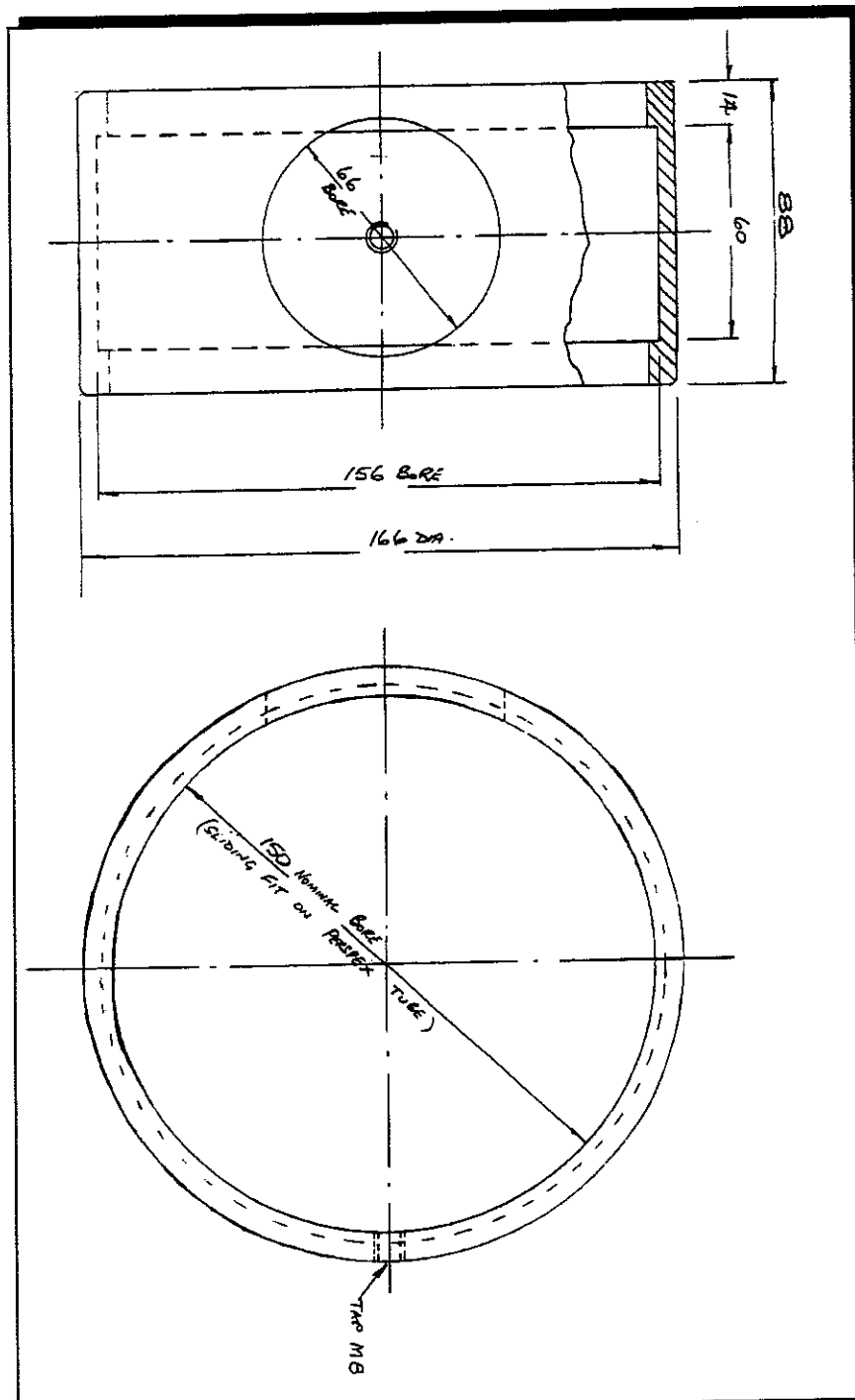


Figure A4.10 Item 5 Cylinder Ring

Notes

1. Material Mild Steel.
2. Make 1 off.

GLOSSARY OF TERMS

A_1	=	negative-going nearfield flexural wave
A_2	=	positive-going nearfield flexural wave
A_3	=	negative-going propagating flexural wave
A_4	=	positive-going propagating flexural wave
A_l	=	negative-going longitudinal wave
A_r	=	positive-going longitudinal wave
\underline{a}	=	vector of waves
a, h	=	mean radius and thickness of a pipe
B	=	fluid bulk modulus of elasticity
C	=	capacitance
c_f	=	speed of sound in a fluid
c_o	=	speed of sound in air
c_s	=	speed of sound in the shell
d_{31}	=	piezoelectric constant
D	=	dielectric displacement
e_1	=	energy in the $s = 1$ wave
e_2	=	energy in the $s = 2$ wave
E	=	electrical field
E_s	=	Young's modulus of elasticity of the shell
E_p	=	Young's modulus of elasticity of piezoelectric material
f	=	force
\underline{F}	=	vector of forces
G	=	shear modulus
\underline{h}	=	state vector
j	=	$\sqrt{(-1)}$
I	=	second moment of area
k_1	=	predominantly fluid based wave number
k_2	=	predominantly shell based wave number
k_a	=	sound in a air wavenumber

k_b	=	flexural wavenumber on an Euler-Bernoulli beam
\underline{k}_b	=	real part of the complex flexural wavenumber
k_{inf}	=	longitudinal wavenumber in an infinite medium
k_f	=	fluid wavenumber
k_{pl}	=	longitudinal wavenumber in a flat plate
k_s	=	shear wavenumber
k_{plate}	=	flexural wavenumber in a flat plate
K	=	dynamic stiffness
M	=	moment
p	=	fluid pressure
q	=	electrical charge
P	=	vibrational power
R	=	radius of curvature, electrical resistance
\underline{R}	=	wave reflection matrix
S	=	cross-sectional area
\underline{T}	=	transmission matrix
t_p	=	thickness of piezoelectric element
t_b	=	thickness of beam
T	=	t_p/t_b (thickness ratio of PZT element to beam)
u	=	axial displacement of a beam
u, w	=	shell displacements in the axial and radial directions
u_f	=	axial displacement of fluid
ν	=	Poisson's ratio
V	=	voltage
w	=	lateral displacement of a beam
z	=	mechanical impedance
α	=	receptance
β	=	fluid loading term
ϵ	=	strain
$\mu\epsilon$	=	microstrain
μ	=	Lagrange multiplier
λ	=	wavelength

κ	=	Timoshenko's shear coefficient
Λ	=	piezoelectric strain
ϕ	=	phase angle
ρ_f	=	density of fluid
ρ_s	=	density of shell
ρ_p	=	density of piezoelectric material
σ	=	stress
θ	=	slope of beam
ω_o	=	ring frequency of a pipe
ω	=	frequency
Ω	=	frequency normalised to the ring frequency

REFERENCES

1. M.J. BRENNAN, S.J. ELLIOTT and R.J. PINNINGTON 1994. *Accepted for publication by the American Society of Mechanical Engineers (Journal of Acoustics and Vibration)*. Mechanisms of Noise Transmission through Helicopter Gearbox Support Struts.
2. C.E. CREDE and J.E. RUZICKA 1987. *Shock and Vibration Handbook (Chapter 30) edited by C.M. HARRIS. 3rd Edition McGraw Hill*. Theory of Vibration Isolation.
3. D.A. CROLLA and M.B.A. ABDEL-HADY 1991. *Transactions of the Society of Automobile Engineers*, Vol 100, 1660-1666. Semi-Active Suspension Control for a Full Vehicle Model.
4. D. KARNOPP, M.J. CROSBY and R.A. HARWOOD 1974. *Transactions of the ASME, Journal of Engineering for Industry*, May, **96**(2), 619-626. Vibration Control Using Semi-Active Force Generators.
5. T. KOBORI, M. SAKAMOTO, M. TAKAHASHI, N. KOSHIKA and K. ISHI 1990. *The 8th Japan Earthquake Engineering Symposium*. Shaking Table Experiment of Multi-Story Seismic Response Controlled Structure with Active Variable Stiffness (AVS) System.
6. N.K. PETEK, R.J. GOUDIE and F.P. BOYLE 1989. *Proceedings of the Second International Conference on ER Fluids*, North Carolina, USA 7-9 August. Actively Controlled Damping in Electrorheological Fluid-Filled Engine Mounts.
7. M.J. BRENNAN, R.J. RANDALL and M.J. DAY 1994. *Submitted for publication to the Journal of Smart Materials and Systems*. An Electro-Rheological Vibration Damper.
8. K. SETO 1992. *Proceedings of the 1st International Conference on Motion and Vibration Control*, Yokohama, Japan, Vol 1, 1-11. Trends on Active Vibration Control in Japan.
9. T. LONG, M.J. BRENNAN, M.J. DAY and S.J. ELLIOTT 1994. *Proceedings of the Tenth International on Systems Engineering*, Coventry, Vol 2, 741-748, 6-8 September. Adaptive Control of Pneumatic Vibration Absorbers.
10. C.A. ROGERS 1992. *Proceedings of the 1st European Conference on Smart Structures and Materials*, Glasgow, 12-14 May, 163-175. Mechanics Issues of Induced Strain Actuation.

11. P.LEUG 1934. *US Patent Application 204316*. Process of Silencing Sound Oscillations.
12. P.A. NELSON and S.J. ELLIOTT 1992. *Active Control of Sound*. Academic Press.
13. L. CREMER, M. HECKL and E.E. UNGAR 1988. *Structure-borne Sound*. 2nd Edition, Springer-Verlag, Heidelberg.
14. D. J. EWINS 1986. *Modal Testing: Theory and Practice*. Research Studies Press Ltd.
15. D.J. MEAD 1982. *Chapter 9 of Noise and Vibration*. (Edited by R.G. White and J.G.Walker). Ellis Horwood, Chichester. Structural Wave Motion.
16. B.R. MACE 1984. *Journal of Sound and Vibration* **97**(2), 237-246. Wave Reflection and Transmission in Beams.
17. M.J. BALAS 1978. *Journal of Optimisation Theory and Applications* **25**, 415-435. Active Control of Flexible Systems.
18. E. LUZZATO AND M. JEAN 1983. *Journal of Sound and Vibration* **86**, 455-473. Mechanical Analysis of Active Vibration Damping in Continuous Structures.
19. A.H. VON FLOTOW 1988. *Large Space Structures: Dynamics and Control*. (edited by S.N. Atluri and A.K. Amos). Springer-verlag, Heidelberg. The Acoustic Limit of Control in Structural Dynamics.
20. C.R. FULLER and F.J. FAHY 1982. *Journal of Sound and Vibration* **81**(4), 501-518. Characteristics of Wave Propagation and Energy Distributions in Cylindrical Elastic Shells Filled with Fluid.
21. D.W. MILLER, S.R. HALL and A.H. VON FLOTOW 1990. *Journal of Sound and Vibration* **140**(3), 475-497. Optimal Control of Power Flow at Structural Junctions.
22. D.J. PINES and A.H. VON FLOTOW 1990. *Journal of Sound and Vibration* **142**(3), 391-412. Active Control of Bending Propagation at Acoustic Frequencies.
23. X. PAN and C.H. HANSEN 1993. *Journal of Sound and Vibration* **165**(3), 497-510. The Effect of Error Sensor Location and Type on the Active Control of Beam Vibration.

24. X. PAN and C.H. HANSEN 1993. *Journal of Sound and Vibration* **168**(3), 429-448. The Effect of End Conditions on the Active Control of Beam Vibration.
25. B.R. MACE 1987. *Journal of Sound and Vibration* **114**(2), 253-270. Active Control of Flexural Vibrations.
26. R.J. McKINNELL 1989. *Proceedings of the Royal Society of London, A* **421**, 357-393. Active Vibration Isolation by Cancelling Bending Waves.
27. J. SCHEUREN 1985. *Proc. Inter-Noise* 85, 591-595. Active Control of Bending Waves in Beams.
28. J. SCHEUREN 1988. *Proc. Inter-Noise* 88, 1065-1068. Non-Reflecting Termination for Bending Waves in Beams by Active Means.
29. S.J. ELLIOTT and L. BILLET 1993. *Journal of Sound and Vibration* **163**(2), 295-310. Adaptive Control of Flexural Waves Propagating in a Beam.
30. R.J. McKINNELL 1989. *Proceedings of the Royal Society of London, A* **421**, 357-393. Active Vibration Isolation by Cancelling Bending Waves.
31. M.J. BRENNAN, S.J. ELLIOTT and R.J. PINNINGTON 1992. *Royal Naval Engineering College Research Report, RNEC-RR-92029*. An investigation into Different Strategies for Controlling Flexural Waves in an Infinite Beam.
32. E.F. CRAWLEY and J. de LUIS 1987. *American Institute of Aeronautics and Astronautics Journal*, Vol 25, No 10, 1373-1385. Use of Piezoelectric Actuators as Elements of Intelligent Structures.
33. B.D. BUNDAY 1985. *Basic Optimisation Methods*. Edward Arnold Ltd, London.
34. P.A. NELSON and S.J. ELLIOTT 1986. *Journal of Sound and Vibration* **105**, 173-178. The Minimum Power Output of a Pair of Free Field Monopole Sources.
35. P.A. NELSON, A.R.D. CURTIS, S.J. ELLIOTT and A.J. BULLMORE 1986. *Journal of Sound and Vibration* **116**(3), 397-414. The Minimum Power Output of Free Field Point Sources in the Active Control of Sound.
36. S.J. ELLIOTT, P. JOSEPH, P.A. NELSON and M.E. JOHNSON 1991. *Journal of the Acoustical Society of America* **90**(5). Power Output Minimization and Power Absorption in the Active Control of Sound.

37. A.R.D. CURTIS 1988. *PhD Thesis, University of Southampton*. The Theory and Application of Quadratic Minimization in the Active Reduction of Sound.
38. W. REDMAN-WHITE, P.A. NELSON and A.R.D. CURTIS 1987. *Journal of Sound and Vibration* **112**(1), 187-191. Experiments on the Active Control of Flexural Wave Power Flow.
39. D. GUICKING, J. MELCHER and R. WIMMEL 1989. *Acustica*, Vol 69, 39-52. Active Impedance Control in Mechanical Structures.
40. G. PAVIC 1993. *Proceedings of the Institute of Acoustics* Vol 15 Part 3 (1993) 395-402. Input Power Suppression of Vibrating Infinite Beams and Plates by Secondary Sources.
41. M.E. JOHNSON and S.J. ELLIOTT 1993. *Journal of the Acoustical Society of America* **93**(3), 1453-1459. Measurement of Acoustic Power Output in the Active Control of Sound.
42. M.J. BRENNAN, S.J. ELLIOTT and R.J. PINNINGTON 1993. *Royal Naval Engineering College Research Report, RNEC-RR-93011*. Active Control of Flexural Waves on Euler-Bernoulli Beams by Power Absorption and Minimization.
43. D.G. MACMARTIN and S.R. HALL 1991. *Journal of Sound and Vibration* **148**(2), 223-241. Structural Control Experiments Using an H_∞ Power Flow Approach.
44. N. HIRAMI 1992. *IDEE-Force 1992 "Eur'acoustics" Workshop on the Active Control of Noise, Flow Instabilities and Vibrations*, held in Lyon, France, 2-3 July. Is the Optimal Damper a Good attenuator?
45. M.J. BRENNAN, S.J. ELLIOTT and R.J. PINNINGTON 1993. *Royal Naval Engineering College Research Report, RNEC-RR-93017*. Decomposition of Propagating Flexural Waves.
46. M.J. DAY 1989. *Royal Naval Engineering College Technical Report, RNEC-TR 89007*. A Phase Controller for Sinusoidal Signals.
47. *The First European Conference on Smart Structures and Materials*, held at the Forte Crest Hotel, Glasgow, 12-14 May 1992.
48. *1995 North American Conference on Smart Structures and Materials*, to be held in San Diego, USA, 26 Feb-3 Mar 1995.
49. *The Journal of Intelligent Material Systems and Structures*. Published by Technomic Publishing Co, Inc, 851 New Holland Ave., Box 3535, Lancaster, PA 17604, USA.

50. *Journal of Smart Materials and Structures*. Published by the Institute of Physics, IOP Publishing Ltd., Techno House, Redcliffe Way, Bristol, BS1 6NS.
51. P. CURIE and J. CURIE 1880, *Comptes Rendus* **91**, 294.
52. W.P. MASON 1981. *Journal of the Acoustical Society of America*, **70**(6) 1561-1566. Piezoelectricity, its History and Applications.
53. H.F. TIERSTEN 1981. *Journal of the Acoustical Society of America*, **70**(6) 1567-1576. Electroelastic Interactions and the Piezoelectric Equations.
54. B.A. AULD 1981. *Journal of the Acoustical Society of America*, **70**(6) 1577-1585. Wave Propagation and Resonance in Piezoelectric Materials.
55. D. BERLIN COURT 1981. *Journal of the Acoustical Society of America*, **70**(6) 1586-1595. Piezoelectric Ceramics: Characteristics and Applications.
56. G.M. SESSIER 1981. *Journal of the Acoustical Society of America*, **70**(6) 1596-1608. Piezoelectricity in Polyvinylidene fluoride.
57. N.F. FOSTER 1981. *Journal of the Acoustical Society of America*, **70**(6) 1609-1614. Piezoelectricity in Thin Film Materials.
58. *Morgan Matroc Limited*. Unilator Division, Vauxhall Industrial Estate, Ruabon, Wrexham, Clwd, LL14 6HY.
59. *Focas Ltd*. Unit Four, Cheney Manor Industrial Estate, Swindon, Wiltshire, SN2 2PJ. (Vibetek piezowire)
60. G.P GIBBS, C.R FULLER and R.J. SILCOX 1993. *2nd Conference on Recent Advances in the Active Control of Sound and Vibration*, Blacksburg, VA, 28-30 April 1993, 909-925. Active Control of Flexural and Extensional Power Flow in Beams Using Real Time Wave Vector Sensors.
61. J. REX 1991. *MSc Dissertation, University of Southampton*. The Use of Integrated Transducers for the Active Control of Structural Vibration.
62. S.E. BURKE and J.E. HUBBARD 1986. *Control of Distributed Parameter Systems, Proceedings of the Forth IFAC Symposium of Control of Distributed Parameter Systems*, 161-166, Held in Los Angeles, edited by H Rauch (Pergamon, New York 1987). Distributed Parameter Control Design for Vibrating Beams using Generalized Functions.
63. C.K. LEE and F.C. MOON 1990. *Journal of Applied Mechanics, Transactions of the American Society of Mechanical Engineers*, **57**, 434-441. Modal Sensors/Actuators.

64. M.E. JOHNSON and S.J. ELLIOTT 1993. *Proceedings of the Institute of Acoustics*, Vol 15 part 3 (1993) 411-420. Volume Velocity Sensors for Active Control.
65. C. LARSON and P.N. LARSON 1993. *Inter-Noise 93*, held in Leuven, Belgium, August 24-26, 815-820. Active Control of Radiation from Plates by use of Modal Sensors.
66. S. LEFEBVRE, C. GUIGOU and C.R. FULLER 1992. *Journal of Sound and Vibration* **155**(1), 177-184. Experiments on Active isolation using Distributed PVDF Error Sensors.
67. J. REX and S.J. ELLIOTT 1992. *The First International Conference on Motion and Vibration Control, Yokohama*, September 1992, Vol 1 339-343. The QWSIS - A New Sensor for Structural Radiation Control.
68. A.R. BRISCOE and R.J. PINNINGTON 1993. *Proceedings of the Institute of Acoustics*, Vol 15 part 3, 959-966. Structural and Fluid Power Transmission Measurement in Empty and Fluid Filled Pipes.
69. G.P. GIBBS and C.R. FULLER 1992. *AIAA Journal*, vol 30, No 2 February 1992, 457-463. Experiments on Active Control of Vibrational Power Flow using Piezoceramic Actuators/Sensors.
70. C.R. FULLER, G.P. GIBBS and R.J. SILCOX 1990. *International Congress on Recent Developments in Air- and Structure-Borne Sound and Vibration*, 657-662. Held at Auburn University, USA, Mar 6-8, 1990. Simultaneous Active Control of Flexural and Extensional Power Flow in Beams.
71. J. DOSCH, D.J. INMAN and GARCIA 1992. *Journal of Intelligent Materials, Systems and Structures*, vol 3 Jan 1992, 166-185. A Self-Sensing Actuator for Collocated Control.
72. J. PAN, C.H. HANSEN and S.D. SNYDER 1992. *Journal of Intelligent Materials, Systems and Structures*, vol 3, January 1992, 3-16. A Study of the Response of a Simply Supported Beam to Excitation by a Piezoelectric Actuator.
73. E.F. CRAWLEY and E.H. ANDERSON 1989. *Proceedings of the 30th Structures, Structural Dynamics and Materials Conference*, Mobile, Alabama, US. 2000-2010. Detailed Models of Piezoceramic Actuation of Beams.
74. B.T. WANG and C.A. ROGERS 1991. *Journal of Intelligent Materials, Systems and Structures* vol 2, January 1991, 38-57. Modelling of Finite-Length Spatially Distributed Induced Strain Actuators for Laminate Beams and Plates.

75. R.L CLARK, J. PAN and C.H. HANSEN 1992. *Journal of the Acoustical Society of America* **92** (2), Pt 1, August 1992, 871-876. An Experimental Study of the Active Control of Multiple Wave Types in an Elastic Beam.
76. D.J. PINES and A.H. VON FLOTOW 1990. *Journal of Sound and Vibration* **142**(3), 391-412. Active Control of Bending Wave Propagation at Acoustic Frequencies.
77. J.L. FANSON and J.K. CAUGHEY 1987. *Proceedings of the 28th AIAA/ASME/ASCE/AHS Structures, Structural Dynamics and Materials Conference AIAA Paper 87-0902*. 588-598. Positive Position Feedback Control of Precision Structures.
78. M.J. BALAS 1978. *Journal of Optimization Theory and Applications*. Vol 25, No3, 415-436. Active Control of Flexible Systems.
79. J. de LUIS AND E.F. CRAWLEY 1990. *Proceedings of the 31st Structures, Structural Dynamics and Materials Conference*. Held at Long Beach CA, AIAA -90-1163-CP, 2340-2350. Experimental Results of Active Control on a Prototype Intelligent Structure.
80. E.K. DIMITRIADIS, C.R. FULLER and C.A. ROGERS 1991. *Transactions of the ASME, Journal of Vibration and Acoustics*, vol 113 January 1991, 100-107. Piezoelectric Actuators for Distributed Vibration Excitation of Thin Plates.
81. A.B. PALAZZOLO, R.R. LIN, R.M. ALEXANDER, A.F. KASCAK and J. MONTAGUE 1989. *Transactions of the ASME, Journal of Vibration, Acoustics, Stress, and Reliability in Design*, Vol 111, 298-305, July 1989. Piezoelectric Pushers for Active Vibration Control of Rotating Machinery.
82. C.C. SUNG, V.V. VARADAN, X.Q. BAO and V.K. VARADEN 1990. *Proceedings of the AIAA/ASME/ASCE/AHS/ASC 31st Structures, Structural Dynamics and Materials Conference*, 2317-2322. Active Control of Torsional Vibration.
83. T. BAILEY and J HUBBARD 1985. *Journal of Guidance and Control* **8**, 605-611. Distributed Piezoelectric Polymer Active Vibration Control of a Cantilever Beam.
84. H.S. TZOU and M. GADRE 1989. *Journal of Sound and Vibration* **132**(3), 433-450. Theoretical Analysis of a Multi-Layered Thin Shell Coupled with Piezoelectric Shell Actuators for Distributed Vibration Control.
85. W. CHARON, G. LINDNER and H.ROTH 1992. *First European Conference on Smart Structures and Materials*, Glasgow 1992 329-332. Smart Structures with Piezopolymers for Space Applications.

86. M. HARPER and R. LEUNG 1993. *Proceedings of Inter-Noise 93*, held in Leuven, Belgium, August 24-26, 1993, 871-874. Active Vibration Control in Pipes.
87. IEEE Standard on Piezoelectricity. ANSI/IEEE Std 176-1987 (January 1988).
88. M.J. BRENNAN, M.J. DAY, S.J. ELLIOTT and R.J. PINNINGTON 1993. *Royal Naval Engineering Research Report, RNEC-RR-93034*. Distributed Piezoelectric Actuators and Sensors.
89. M.J. BRENNAN, S.J. ELLIOTT and R.J. PINNINGTON 1992. *First International Conference on Motion and Vibration Control, Yokohama, Japan, September 1992*, 605-609. Active Control of Vibrations Transmitted Through Struts.
90. NoiseBuster, Noise Cancellation Technologies, Inc. 800 Summer Street, Stamford, CT 0691, USA.
91. L. MEIROVITCH 1990. *Dynamics and Control of Structures*. John Wiley and Sons.
92. S.J. ELLIOTT, M.J. BRENNAN and R.J. PINNINGTON 1993. *Proceedings of Inter-Noise 93*, Vol II, 842-846, held in Leuven, Belgium. Feedback Control of Flexural Waves in a Beam.
93. M.G. HARRIS, W.J. BURMEISTER, R.J. MARTIN and F.M. ARANGIO. *Proceedings of the Midwest Symposium on Circuits and Systems* (IEEE Cat No. 91CH2819-1) 88-91. Vibration Cancellation Effectiveness using a Second Order Piezoelectric Actuator Model.
94. C.R. FULLER, C.A. ROGERS and H.H. ROBERTSHAW 1989. *Proceedings of the SPIE Conference 1170 on Fiber Optic Smart Structures and Skins II*, Boston, MA, August 5-8 1989. Active Structural Acoustics Control with Smart Structures.
95. A. BARBERIS, P.ESCOBAR ROJO, V.GUSMEROLI and C.MARIOTTINI 1992. *Proceedings of the 1st European Conference on Smart Structures and Materials*, Glasgow 1992. Elastic Curve Recovery by a Quasi-Distributed Polarimetric Fiber Optic Sensor.
96. B.J. BRÉVART and C.R. FULLER 1993. *Journal of the Acoustical Society of America*, **94** (3), Pt 1. Active Control of Coupled Wave Propagation in Fluid-filled Elastic Cylindrical Shells.
97. M.J. BRENNAN, S.J. ELLIOTT and R.J. PINNINGTON 1993. *Royal Naval Engineering College Research Report, RNEC-RR-93035*. Waves in Fluid-Filled Pipes.

98. R.J. PINNINGTON and A.R. BRISCOE 1994. *Journal of Sound and Vibration* **173**(4), 503-516. Externally Applied Sensor for Axisymmetric Waves in a Fluid Filled Pipe.
99. G. PAVIC 1992. *Journal of Sound and Vibration* **154**(3), 411-429. Vibroacoustical Energy Flow through Straight Pipes.
100. F.J. FAHY 1987. *Sound and Structural Vibration: Radiation, Transmission and Response*. Academic press Inc. (London) Ltd.
101. L.E. KINSLER, A.R. FREY, A.B. COPPENS and J.V. SANDERS 1982. *Fundamentals of Acoustics*. John Wiley and Sons Inc.
102. T.C. LIN and G.W. MORGAN 1956. *Journal of the Acoustical Society of America*, Vol 28 No 6, 1165-1176. Wave Motion through Fluid Contained in a Cylindrical Elastic Shell.
103. W. FLÜGGE 1973. *Stresses in Shells*. 2nd Edition, Springer-Verlag, Berlin, Heidelberg, New York.
104. E.H. KENNARD 1953. *Journal of Applied Mechanics*, 33-40. The New Approach to Shell Theory: Circular Cylinders.
105. AMP of Great Britain Ltd, Merrion Ave, Terminal House, Stanmore, Middlesex, UK. Kynar Piezo Film Application Notes
106. J. HORNER 1990. *PhD Thesis, University of Southampton*. Vibrational Power Transmission Through Beam-Like Structures.
107. L.C. CHOW and R.J. PINNINGTON 1987. *Journal of Sound and Vibration* **118**(1) 123-139. Practical Industrial Method of Increasing Structural Damping in Machinery, 1: Squeeze Film Damping with Air.
108. M.A. HECKL 1992. *Course Notes for a Short Course on Structure-borne Sound*, held at Penn. State University 22-24 July 1992.
109. G.B. WARBURTON 1976. *The Dynamical Behaviour of Structures*, 2nd Edition, Pergamon Press Ltd.
110. G.R. COWPER 1966. *Journal of Applied Mechanics*, Vol 33, 335-340. The Shear Coefficient in Timoshenko's Beam Theory.
111. H.G.D. GOYDER and R.G. WHITE 1980. *Journal of Sound and Vibration* **68**, 59-75. Vibrational Power Flow from Machines into Built Up Structures, Part I: Introduction and Approximate Analysis of Beam and Plate-like Foundations.